Self-Consistent ICRH Distribution Functions and Equilibria in Magnetically Confined Plasmas

PAR

Martin JUCKER

ÉCOLE POLYTECHNIQUE
FÉDÉRALE DE LAUSANNE

Suisse
2010

to infinity and beyond

Abstract

The deployment of high power radio frequency waves in the ion cyclotron range (ICRF) constitutes an important operational facility in many plasma devices, including ITER. Any charged particle describes a helical motion around a given magnetic field line, the so-called cyclotron motion. ICRF relies on the interaction between charged particles and an injected Radio Frequency (RF) wave, tuned to be at the same frequency as the helical cyclotron motion. It is applied not only for pure heating of the plasma, i.e. Ion Cyclotron Resonant Heating (ICRH), but also for the generation of non-inductive current through Ion Cyclotron Current Drive (ICCD). The numerical code package SCENIC has been developed for self-consistently simulating the effects of ICRH on the resonant ion species within the plasma, the resulting changes in the plasma equilibrium, and finally the back reaction onto the injected wave field. SCENIC is an iterated scheme, which advances the resonant ions' distribution function, the equilibrium and the wave field iteratively until a converged solution, representing a steady state, is reached. The constituents of SCENIC are the MagnetoHydroDynamic (MHD) equilibrium code VMEC,[1] the full wave code LE-Man[2] and the Hamiltonian guiding centre drift following code VENUS.[3] All of these codes are capable of dealing with 3D geometries, and have recently been updated to handle pressure anisotropy, where the energy density parallel and perpendicular to the magnetic field differ. This is important since the RF field resonates mainly with the particle's motion perpendicular to the magnetic field, thus creating pressure anisotropy. After the introduction and description of the different codes and their interfaces, this work verifies the consistency of the numerical results with expected results for simple cases, and a benchmarking effort against the similar code package SELFO is shown. After this validation, SCENIC is applied to different heating scenarios, which are relevant to present (Joint European Torus, JET) and future (ITER) devices. Low power heating simulations with a 1% helium-3 minority in background deuterium plasmas demonstrate that a pressure anisotropy is induced. We show that the hot particle distribution function can be adequately approximated with a particular bi-Maxwellian for the equilibrium and wave field computations. For high power, 3% hydrogen minority heating scenarios, the heating scheme alters the background equilibrium state. This justifies one of the main novelties introduced in this work, namely the inclusion of the equilibrium computation in the self-consistent scheme. Effects due to asymmetric wave injection and different heating locations on the hot particle distribution function, the hot dielectric tensor and the equilibrium will be studied. Here, the emergence of a high energy tail in the minority species distribution function is shown explicitly, and some of its exotic features are observed via the RF driven current, the density and the pressure evolution.

Keywords: Plasma physics, Ion cyclotron range of frequencies, Ion cyclotron resonance heating, Ion cyclotron current drive, Integrated modeling, Monte Carlo simulations

Version abrégée

L'injection d'ondes électromagnétiques à haute puissance dans la bande des fréquences radio constitue un important outil opérationnel dans de nombreuses expériences, notamment ITER. Cette technique se base sur l'interaction entre le mouvement naturel hélicoïdal de toute particule chargée autour d'une ligne de champ magnétique donnée (mouvement cyclotronique) et une onde radio dont la fréquence correspond à la fréquence cyclotronique. Cette méthode n'est pas seulement appliquée pour le chauffage du plasma, mais aussi pour la génération de courant non-inductif. Le code numérique SCENIC a été développé pour simuler de manière cohérente les effets du chauffage par ondes cyclotroniques sur les ions résonnants dans le plasma, les changements résultants dans l'équilibre du plasma, et finalement les effets sur le champ d'onde lui-même. En calculant l'évolution de la fonction de distribution des ions résonnants, de l'équilibre ainsi que du champ d'ondes de manière itérative, SCENIC permet l'obtention d'une solution convergeante vers un nouvel état d'équilibre. SCENIC est composé du code d'équilibre MagnetoHydroDynamique (MHD) VMEC,[1] du code d'ondes LEMan,[2] et du code Hamiltonien VENUS[3] suivant les centre de guidage des particules chargées. Ces trois codes sont capables de gérer des géométries tridimensionnelles et ont été mis à jour récemment pour inclure l'anisotropie de la pression, état où la densité d'énergie varie entre les directions parallèle et perpendiculaire au champ magnétique. L'intégration de l'anisotropie est importante car le champ d'ondes radio résonne principalement avec le mouvement des particules perpendiculaire au champ magnétique, créant ainsi une anisotropie de la pression. Après l'introduction et la description des différents codes et de leurs interfaces, la cohérence des résultats numériques avec les résultats attendus sera vérifiée dans des cas simples, et une étude comparative avec le code similaire SELFO sera présentée. Suite à cette validation, SCENIC sera appliqué à différents scenarii de chauffage récurrents dans les expériences présentes (Joint European Torus, JET) et futures (ITER). Les simulations de chauffage à basse puissance avec une minorité de $1\,\%$ d'hélium-3 dans un plasma de deuterium démontreront qu'une anisotropie de pression est induite. Nous montrerons que la fonction de distribution des particules chaudes peut être estimée de manière adéquate avec une bi-Maxwellienne particulière développée pour le calcul de l'équilibre et du champ d'onde. Dans les cas de chauffage à haute puissance avec une minorité de $3\,\%$ d'hydrogène, l'équilibre magnétique du plasma est altéré. Cela justifie une des principales nouveautés présentés dans cette thèse, à savoir le calcul cohérent de l'équilibre. Les effets d'un spectre asymétrique d'ondes sur la fonction de distribution des particules chaudes, sur le tenseur diéléctrique et sur l'équilibre seront étudiés dans des cas d'injection d'ondes à des endroits différents dans le plasma.

Mots clés: Physique des plasmas, Ondes dans la gamme de fréquence ion cyclotron, Chauffage par ondes cyclotroniques, Simulations numériques intégrées, Simulations Monte Carlos

Notations used in this thesis

e	Elementary charge $e = 1.622 \times 10^{-19}$
Z	Atomic number
Q	Electric charge, $Q = Ze$ for an ion, $Q = -e$ for an electron
q	Safety factor
m	Particle mass
n	Number density
B	Magnetic field strength with B_0 value at magnetic axis
$\mathbf{E}$	Electric field
E	Energy
T	Temperature
Ω	Cyclotron frequency $\Omega = QB/m$
ρ_L	Larmor radius $\rho_l = v_\perp / \Omega$
B_c	Critical magnetic field
ω	Frequency of injected wave $\omega = QB_c/m$
ψ	Poloidal flux function
Φ	Toroidal flux function
χ	Scalar potential
s	Radial Boozer coordinate, related to toroidal flux
I	Poloidal current flux
J	Toroidal current flux
φ	Toroidal angle
p	Pressure
P	Power
R	Major radius with R_0 location of magnetic axis
r	Local minor radius
a	Minor radius $a = \max(r)$
$\mathcal{E}$	Dielectric tensor
ICRF	Ion Cyclotron Range of Frequencies
ICRH	Ion Cyclotron Resonance Heating
ICCD	Ion Cyclotron Current Drive
RF	Radio Frequency
LFS	Low Field Side: $R < R_0$
OA	On Axis: $R = R_0$
HFS	High Field Side: $R > R_0$
FLR	Finite Larmor Radius

Contents

1. A few words about fusion

A few years ago, scientists working in fusion had difficulty showing why it is important to move away from fossil fuels towards renewables and non-polluting ways of energy production. Every thesis and presentation had to be started with historical atmospheric CO^2 concentration plots, world primary resource consumption, etc. In the last few years, the general attitude has changed a lot, especially since the recent change of administration in the White House and Al Gore's world tour showing exactly those plots every plasma physicist had been showing in the introduction of every presentation for years. We will therefore assume the reader understands that fossil fuels are problematic and that another way of producing energy has to be found.

Virtually every renewable energy source's efficiency depends on the environmental conditions (geography, weather, etc) at the location where it is exploited. Obviously, wind turbines need enough wind, solar panels sufficient radiation, water turbines large amounts of water flow and so on, and thus research and development efforts have to be split into the different ways of generating power, virtually each country developing what is best for its latitudes, weather conditions and other geographic conditions. The intrinsic non-universality of these sources of energy might well be one of the main reasons why these technologies take a long time to develop and are still rather inefficient and expensive. A second important difficulty is the storage of energy produced, as for instance solar power is mainly generated during the summer, whereas more power is needed in winter for heating. Another strategy for organising research in the field is to unite scientific efforts internationally and use the resulting large financial and scientific resources to work on something much more difficult but, once operational, beneficial for all countries in the same way. Such a philosophy is the basis of one of the largest international scientific programs, the International Thermonuclear Experimental Reactor (ITER), being built at the time of writing in Cadarache, France. The basic idea sounds very simple: The sun is constantly producing vast amounts of energy. So why not try and create the same reactions producing this energy directly on earth instead of recollecting tiny fractions of the sun's energy using solar panels? The reactions in the core of the sun are what we call thermonuclear fusion. Light chemical elements, mostly hydrogen, are being pressed together and combine to create new, heavier elements (helium). None of these elements are poisonous or radioactive and all are very common on earth - two of the biggest advantages of these reactions. The total mass of the heavier element created is lower than the sum
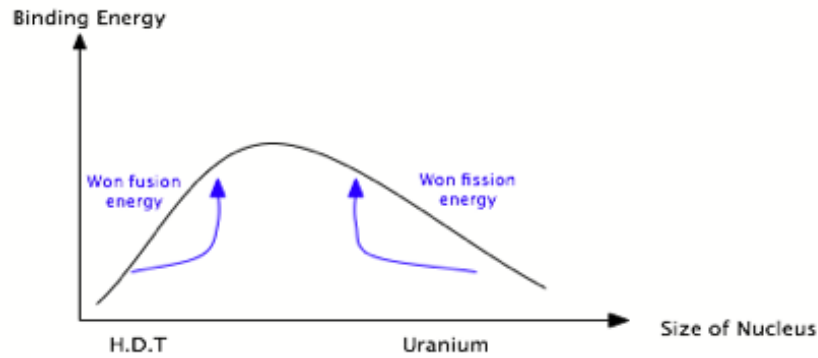
Figure 1.1.: Fusing light elements releases energy just as splitting very heavy elements. The difference in binding energy between the initial and the final elements of reach reaction can be seen as gained energy.

of its light constituents, and the mass difference is converted into energy after Einstein's famous formula $E = mc^2$. It is worth noting that the conversion of mass into energy is at the very heart of present nuclear fission power plants. Here, very heavy elements are split into lighter elements, but the effect is exactly inverted: the sum of the masses of the new lighter elements is lower than the mass of the initial heavy element, and the missing mass is again converted into energy. One could also explain the energy gain using the measured binding energies for all different elements, as schematically shown in Fig. 1.1. The difference in binding energy between the initial (e.g. hydrogen, deuterium, tritium for fusion, uranium for fission) and the final elements can be interpreted as energy gain from the reaction.

Now, any nucleus of any element contains protons, i.e. positively charged particles. Two positive charges repel each other. For fusion, this electromagnetic force has to be overcome, which is why the pressure has to be very high for fusion to occur. In the sun, its huge mass guarantees an enormous pressure due to gravitational forces. On earth, the absence of this mass has to be compensated with even higher temperature. One can expect that on earth a temperature of 100 million degrees has to be attained for fusion to take place. At this temperature, any natural element is neither solid not liquid nor in gas form, but in the fourth state of matter, plasma. In this state, the electrons are no longer bound to the atomic nucleus (as in the case of a solid, fluid, or gas), but are free to move away from the latter, now called "ion" because of its net positive charge. The gas (or plasma) is ionised, i.e. composed of particles carrying positive and negative electric charges. Any particle that carries an electric charge is subject to electromagnetic forces, which gives rise to a special kind of physical behaviour, described by plasma physics. Any kind of research conducted for nuclear fusion has to be done in the frame of plasma physics. Consequently, the rest of this thesis will entirely focus on plasma physics, and the next chapter will introduce the mathematical tools and description needed.

2. Theoretical background

We have seen that the theoretical background for nuclear fusion has to come from plasma physics. We will now introduce basic notions, principles and notations which will be used throughout the thesis. Starting from a description of the most widely operated type of machine, the tokamak, we will introduce the underlying equations describing the global equilibrium, discuss the fundamental trajectories of the charged particles inside a plasma, and establish a statistical description, the so-called kinetic description. We will conclude the chapter with some details on wave physics, in particular in relation to the ion cyclotron range of frequencies, which will be of great importance to this thesis.

2.1. Magnetic equilibrium

2.1.1. The tokamak

Consider for the time being we can create such a plasma with the required temperature for fusion to be possible. What would a fusion power plant look like? Hot particles move very fast, and the most important question is: How can we force these very fast particles to stay where we want them long enough so that they can collide with other particles and fuse? A deuterium ion with an energy equivalent to the required temperature of one hundred million degrees ($\sim 10\,\mathrm{keV}$) moves at a speed of about one thousand kilometers per second. Such a particle can be expected to have a collision with another particle about every 100 milliseconds (for the densities considered in this thesis), such that the deuterium ion would have to travel one hundred kilometers before colliding the first time with another particle. Moreover, every particle has to suffer a high number of collisions before an efficient collision causes two nuclei to fuse. We cannot even dream of building devices long enough for that to happen. There is another way. Namely, we can build closed loops, like donuts or tires, where the particles can move in circles and therefore travel a virtually infinite distance without ever leaving the device. This is the idea of the toroidal fusion devices, which have been in the centre of fusion research since the 1960s (Fig. 2.1).

Such toroidally shaped devices can still differ quite a lot in size and form. If there is no difference in toroidal direction (along the torus) in any of the quantities defining the plasma, the plasma can be considered to be two dimensional, since we do not need to

Magnetic circuit
(iron transformer core)

Inner poloidal field coils
(primary transformer circuit)

Toroidal field coils

Outer Poloidal field
coils (for plasma
positioning and shaping)

Poloidal field

Toroidal field

Plasma with plasma current I_p
(secondary transformer circuit)

Resultant helical magnetic field
(exaggerated)
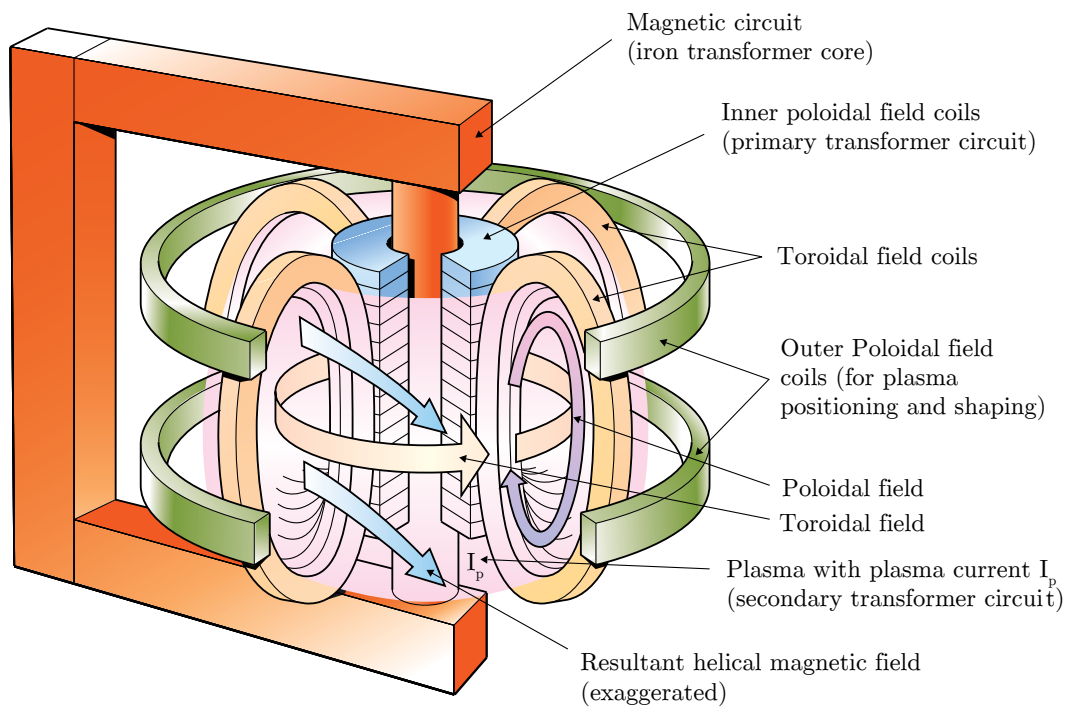
(a) Sketch of the current and magnetic field generation in a Tokamak. The central column (red) acts as a transformer and creates toroidal current in the plasma, and thus also a poloidal magnetic field, whereas the toroidal field coils (yellow) generate the toroidal magnetic field. The green coils are responsible for shaping the plasma.
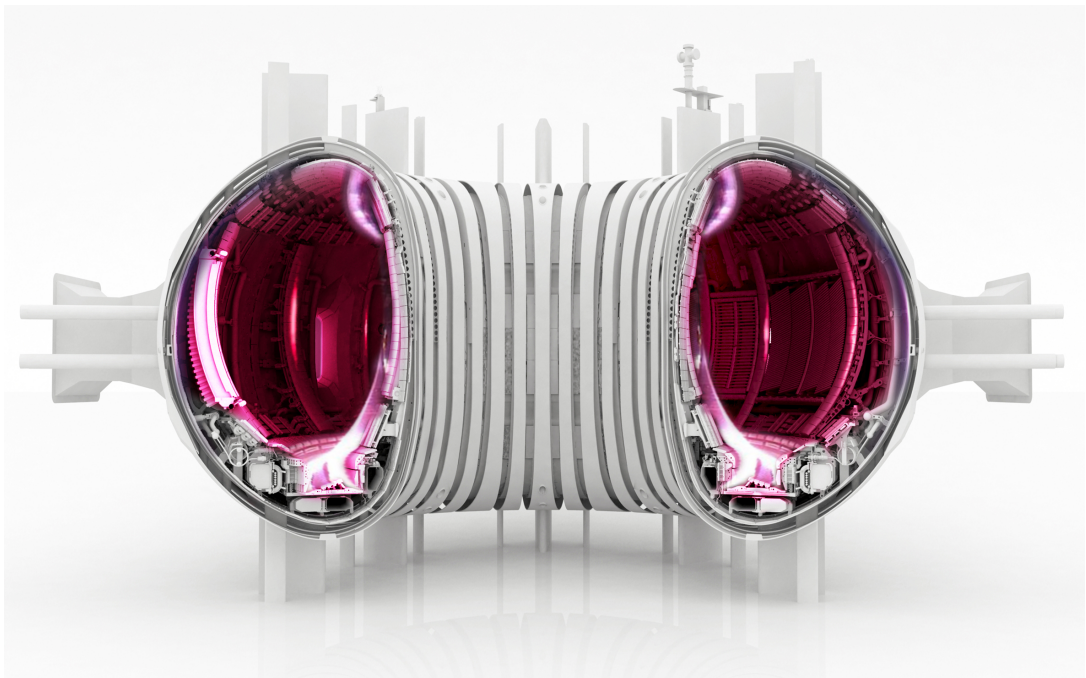
(b) Computer generated slice of the Joint European Torus (JET) plasma vessel, together with 3D imagery of the inside of the vessel.

Figure 2.1.: Sketch of the outer coils of a tokamak (in reality there are many more field coils), and an artist's view of the Joint European Torus (JET), at present the largest fusion device in the world. *both figures from jet.efda.org*
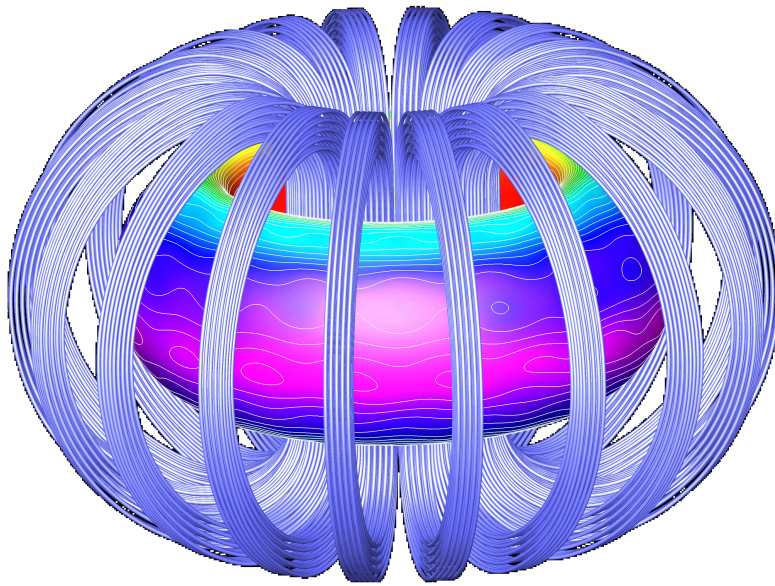
Figure 2.2.: Numerical representation of the toroidal field coils in ITER and their 3D ripple effect on the magnetic field strength inside the plasma. The coloring shows the magnetic field strength in the plasma, showing the characteristic $1/R$ dependence of Eq. (2.1) with the maximum (red) on the inside and the minimum (violet) on the outside of the vessel. *oakridgelabnews on flickr.com*

consider the third dimension along the torus. In that case we call the device a tokamak. We shall concentrate on such configurations in this thesis. In reality, however, even if we intend to build such a device, it will never be perfectly symmetric, be it only because the magnetic field coils are separated by a finite distance and the resulting toroidal magnetic field can therefore not be completely constant, causing what is called magnetic ripple effects, as illustrated in Fig. 2.2. More complicated devices are stellarators, where the magnetic configuration is truly three dimensional in that the magnetic field is voluntarily twisted. In such machines, one is forced to apply three dimensional theory for their description. Although the code package described in this thesis has been developed for being able to treat such geometries, we will not consider stellarators, since computations are much more time consuming and testing is more complicated due to the fact that the results are less intuitive.

Hence, we come back to the tokamak, where (ideally) all parameters are constant in the toroidal direction, i.e. along the torus. This direction is parametrised by the angle φ. We have learned that the charged particles within the plasma basically follow the magnetic field lines. Thus, if we want to make these particles circle around the torus in a tokamak, the magnetic field must be along the toroidal direction, $B \sim B_\varphi$. However, the toroidal field is created using toroidal field coils, as schematically highlighted in yellow in Fig. 2.1(a) and in blue in Fig. 2.2. Especially the latter figure shows that due to the form of
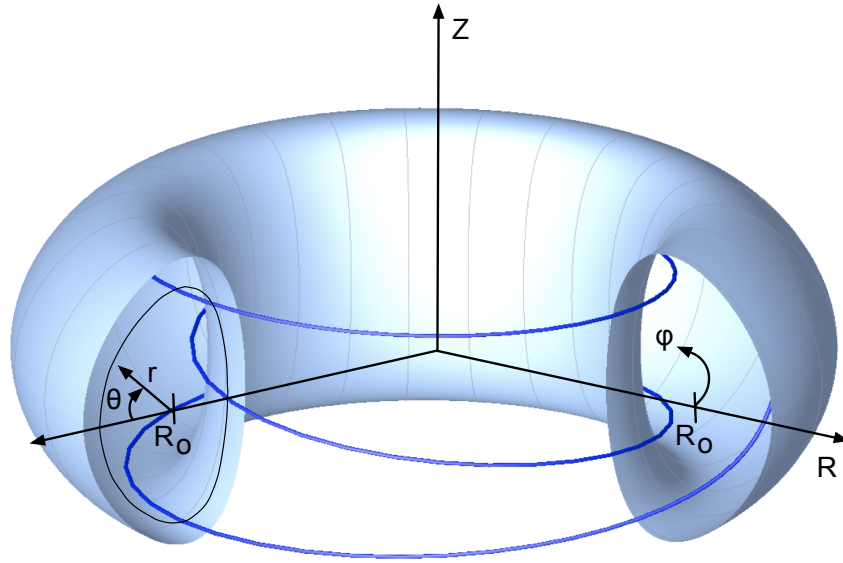
Figure 2.3.: The toroidal coordinates (R, φ, Z) make use of the fact that the tokamak is essentially two dimensional. The dependence on the toroidal angle φ can be neglected and the Cartesian coordinates (R, Z) are sufficient for the equilibrium description (right hand side). R_0 defines the magnetic axis of the torus. Another possible set of coordinates are the polar coordinates (r, θ) as shown on the left hand side. θ is the poloidal angle, r the local minor radius. The blue 3D line shows a magnetic field line with $q \approx 3$ and the black line on the left side the corresponding flux surface in the (R, Z) poloidal plane.

the torus, these magnetic coils are closer together on the inboard side, thus strengthening the magnetic field on that side. As a result, the toroidal magnetic field strength decreases with major radius R, which denotes the radial distance from the centre of the torus, as can be seen from the coloring of the plasma inside the coils in Fig. 2.2, red denoting high, violet low value. We can therefore write

$$B_\varphi \approx \frac{B_0 R_0}{R}, \qquad (2.1)$$

where R_0 denotes the position of the centre of the toroidal volume, the magnetic axis, and B_0 the magnetic field strength at $R = R_0$. The coordinates are illustrated in Fig. 2.3. B is therefore not constant in the plasma, and in the presence of a gradient of the magnetic field, the particles start drifting across the field lines. These drifts are responsible for the particle orbits leaving given magnetic field lines ("drifting" through the magnetic field), with characteristic velocities of

$$\mathbf{v}_D^{\nabla B} = \frac{m_\alpha v_\perp^2}{2 Q_\alpha B^3} \left(\nabla B \times \mathbf{B} \right), \qquad (2.2)$$

with α denoting the particular species, m_α the mass and Q_α the particle charge. This term is dependent on charge, and therefore electrons and ions move into opposite directions.

The resulting charge separation results in an electric field $\mathbf{E}$, corresponding to the electric Coulomb force between particles of opposite charge. This electric field gives rise to another drift velocity, which is independent of the charge of the particles, and therefore ions and electrons move together in the same direction. The complete drift velocity is then

$$\mathbf{v}_D = \frac{\mathbf{E} \times \mathbf{B}}{B^2} + \frac{m_\alpha v_\perp^2}{2 Q_\alpha B^3} \left(\nabla B \times \mathbf{B} \right),$$
(2.3)

We see from Eq. (2.1) that a magnetic field gradient, and therefore the particle drifts of Eq. (2.3) are always present in a tokamak. In order to compensate those drifts, one can add another component to the magnetic field, usually much weaker and this time in the poloidal direction, i.e. along the angle θ. This gives the total magnetic field a helical structure around the torus, similar to a screw driver in toroidal direction (blue 3D line in Fig. 2.3). The particles, which are mainly following the magnetic field lines, are then describing helical trajectories as well, and the drifts which are directed towards the plasma edge on the upper half of the torus ("up") are directed away from the edge on the lower half of the torus (still "up") and vice versa. The most basic particle drifts can therefore be avoided with this kind of magnetic field structure. As a result of the addition of a poloidal component of the magnetic field, the field lines describe what is called magnetic flux surfaces in the poloidal RZ-plane. One example is shown in Fig. 2.3, where the helical field (blue 3D line) describes the flux surface at the minor radius r (black line, left). In order to quantify the twisting of the field lines, the safety factor can be defined

$$q = \frac{1}{2\pi} \oint \frac{1}{R} \frac{B_\varphi}{B_\theta} \mathrm{d}l,$$
(2.4)

where the integration is performed over one loop along a flux surface in the poloidal cross section. The safety factor quantitatively stands for the number of toroidal loops a magnetic field line performs to complete one poloidal loop. If that number is rational, $q = m/n$, the magnetic field lines close after m toroidal and n poloidal loops. The name safety factor then comes from the fact that if the magnetic field lines close on themselves, any magnetic perturbation can easily grow into an instability since it can propagate along the magnetic field lines and always come back to where it has been created, such that global deformations of the field lines can arise. This is especially important for the regions where $q \leq 1$, i.e. where the field lines close on each other after less than one toroidal rotation. Since for most of the particles the motion along the field lines is much faster than across it, most of the characteristics of the plasma are approximatively constant around one given flux surface, and their values can appropriately be represented as functions of a radial variable proportional to the magnetic flux inside a given surface. In order to define the magnetic flux, let us write the magnetic field in the contravariant representation as[4]

$$\mathbf{B} = \nabla \varphi \times \nabla \psi + \nabla \Phi \times \nabla \theta,$$
(2.5)

with ψ the poloidal and Φ the toroidal flux function. Indeed, the total poloidal flux is

$$\Psi_P(\rho) = \int_{A_P} d\boldsymbol{\sigma} \cdot \mathbf{B} = \int_{A_p} \sqrt{g} d\rho' d\varphi \nabla\theta \cdot \nabla\varphi \times \nabla\psi = \int_0^{2\pi} d\varphi \int_0^\rho d\rho' \frac{\psi(\rho')}{d\rho'} = 2\pi\psi(\rho),$$

$$(2.6)$$

where $\sqrt{g} = (\nabla\rho \times \nabla\theta \cdot \nabla\varphi)^{-1}$ is the Jacobian and ρ an arbitrary radial variable. The same reasoning yields the toroidal flux

$$\Psi_T(\rho) = \int_{A_T} d\boldsymbol{\sigma} \cdot \mathbf{B} = \int_0^{2\pi} d\varphi \int_0^\rho d\rho' \frac{\Phi(\rho')}{d\rho'} = 2\pi\Phi(\rho). \qquad (2.7)$$

One popular radial coordinate is the normalised radius

$$\rho_p = \sqrt{\frac{\psi}{\psi_a}}, \qquad (2.8)$$

where ψ_a is the poloidal flux function at the plasma edge. In this thesis, we will not use the poloidal but rather the toroidal flux Φ enclosed by a given flux surface. We introduce the radial coordinate

$$s = \frac{\Phi}{\Phi_a} \qquad (2.9)$$

in the numerical codes. The minor radius as defined in Fig. 2.3 is then approximately

$$r \approx a\sqrt{s}, \qquad (2.10)$$

where a is the maximum minor radius of the machine. It follows that we can define the normalised radius

$$\rho = r/a \approx \sqrt{s}. \qquad (2.11)$$

This is only approximately true because, as one can see in Fig. 2.3, the plasma does in general not have a circular cross section. Indeed, it is possible to shape the plasma in the poloidal plane. One possible description of the shaping can be done when expanding the coordinates (R, Z) into an infinite sum of shaping coefficients, reading

$$R = R_0 + r\cos\theta - \Delta(r) + \sum_{m\geq 2} S_m(r)\cos(m-1)\theta \qquad (2.12a)$$

$$Z = r\sin\theta - \sum_{m\geq 2} S_m(r)\sin(m-1)\theta, \qquad (2.12b)$$

where $S_m(r)$ are the shaping coefficients and $\Delta(r)$ is the Shafranov shift and corresponds to a displacement of the magnetic axis with respect to the geometric centre of the plasma. This is an important quantity related to global stability of the plasma as we will see later on. The expansion (2.12) is the expression which will be relevant for interpretation of results and discussions related to stability. However, in the equilibrium code VMEC the

coordinates are implemented differently.

$$\bar{R} = \sum_{n \geq 0} \bar{R}_n(s) \cos n\theta \tag{2.13a}$$

$$\bar{Z} = \sum_{n \geq 1,} \bar{Z}_n(s) \sin n\theta. \tag{2.13b}$$

The two expansions can be compared, such that the relation between the VMEC coordinates (2.13) and the definition for the analytical studies (2.12) becomes more clearly apparent, yielding

$$r(s) = \frac{\bar{R}_1(s) + \bar{Z}_1(s)}{2}, \tag{2.14a}$$

$$R_0 = \bar{R}_0(0), \tag{2.14b}$$

$$\Delta = \bar{R}_0(0) - \bar{R}_0(s), \tag{2.14c}$$

$$S_2 = \frac{\bar{R}_1(s) - \bar{Z}_1(s)}{2}, \tag{2.14d}$$

$$S_{m \geq 3} = \bar{R}_{m-1}. \tag{2.14e}$$

One can, however, define other expansions. A popular alternative is mainly applied when restricting shaping to elongation κ and triangularity δ as defined in Fig. 2.4. These definitions of elongation and triangularity are well established, and the expansion then is of the form

$$R = \hat{R}_0 + \hat{r} \cos{(\theta + \delta \sin \theta))} \tag{2.15a}$$

$$Z = \hat{Z}_0 + \hat{r} \kappa \sin \theta. \tag{2.15b}$$

Again, we can compare the different expansions, and find that the elongation κ and the triangularity δ are related to the shaping coefficients in (2.12) as follows:

$$\kappa = \frac{r - S_2}{r + S_2}, \tag{2.16a}$$

$$\delta = \frac{4S_3}{r}. \tag{2.16b}$$

These relations are considered when setting the boundary conditions for the fixed boundary version of the equilibrium code VMEC, given an elongation κ, a triangularity δ and a magnetic axis at R_0.
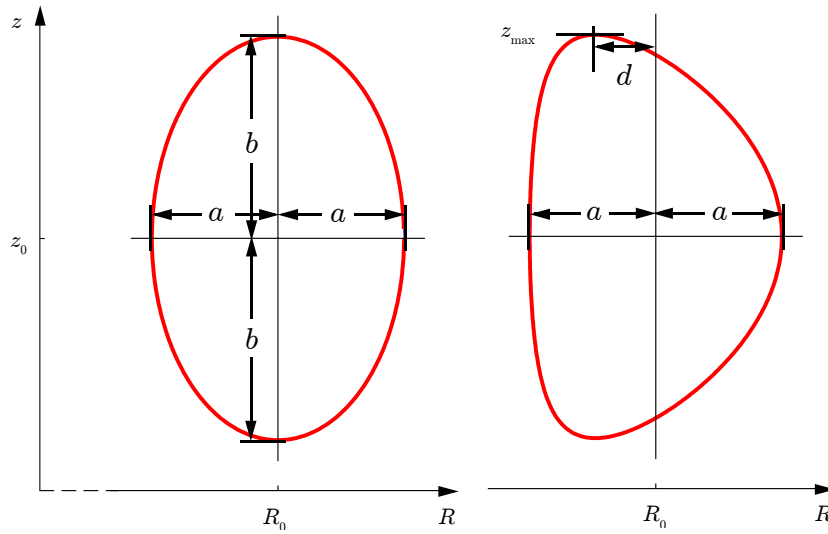
Figure 2.4.: Definitions of the elongation $\kappa = b/a$ and triangularity $\delta = d/a$ for a shaped plasma.

2.1.2. Magnetohydrodynamics (MHD)

Magnetohydrodynamics (MHD) is a combination of hydrodynamics and electromagnetism. Instead of describing every particle separately, the whole plasma is treated as a fluid subject to the pressure and Lorentz forces. The connection to electromagnetism is done through Ohm's law, as we shall see later. The core of hydrodynamics is the momentum or Euler equation, which is a form of Newton's law. As it considers the complete plasma as one fluid with macroscopic properties such as density or pressure, MHD is very powerful in the description of plasma equilibria and global stability, since it does not include complicated small scale behaviour, but treats the complete plasma as a whole. The velocity $\mathbf{v}$ entering this equation is then not the velocity of one given particle but the average velocity of all particles within a considered volume of mass m. The momentum conservation in this model reads

$$mn\frac{\mathrm{d}\mathbf{v}}{\mathrm{d}t} = mn\left(\frac{\partial}{\partial t} + \mathbf{v} \cdot \nabla\right)\mathbf{v} = \mathbf{j} \times \mathbf{B} - \nabla \cdot \mathbf{P}, \qquad (2.17a)$$

where n is the number density, $\mathbf{j}$ the current density, $\mathbf{B}$ the magnetic field and $\mathbf{P}$ the pressure tensor. The left hand side (LHS) denotes the total fluid velocity time derivative, being the sum of the partial time and the convective derivative, whereas the right hand side (RHS) denotes the force applied to it. In general, the pressure tensor has diagonal terms corresponding to pressure, and off-diagonal terms related to stress. In this thesis, we will neglect stress terms, but consider pressure anisotropy, such that the pressure tensor includes different pressures parallel and perpendicular to the magnetic field. We will use the Chew-Goldberger-Low expansion[5] and the pressure tensor then takes the

form

$$\mathbf{P} = p_\perp (\mathbf{I} - \epsilon_{ij}) + p_\parallel \epsilon_{ij}. \tag{2.17b}$$

$\mathbf{I}$ is the unit dyadic and $\epsilon_{ij} = B_i B_j / B^2$. For isotropic pressures ($p_\parallel = p_\perp$), this term becomes simply ∇p, with the total pressure

$$p = \frac{p_\parallel + 2p_\perp}{3}. \tag{2.17c}$$

In this section, we will consider both anisotropic and isotropic pressures. The reason for this lies in the set up of the numerical scheme developed in this thesis, which is described in detail in Chapters 4-7. Namely, the equilibrium will contain two different plasma populations, one constituting the majority of the plasma, and considered thermal Maxwellian, and thus isotropic, and one minority, which will resonate with the injected wave and be considered bi-Maxwellian and anisotropic. This separation of the total pressure into a parallel and a perpendicular contribution for the resonant plasma population will be an important addition in this work as compared to using one scalar total pressure. The last fluid-like equation is the continuity equation

$$\frac{\partial}{\partial t} n + \nabla \cdot (n\mathbf{v}) = 0, \tag{2.17d}$$

and makes sure that the total number of particles is conserved. In order to close the system of equations, equation of state yields a relation between the mass density and the pressure,

$$\frac{\mathrm{d}}{\mathrm{d}t} \left(\frac{p}{(mn)^\gamma} \right) = 0, \tag{2.17e}$$

where γ is the ration of specific heats, usually taken to be $\gamma = 5/3$. For the electromagnetic fields, the evolution is governed by Maxwell's equations

$$\nabla \cdot \mathbf{E} = 0 \tag{2.18a}$$

$$\nabla \times \mathbf{E} = -\frac{\partial \mathbf{B}}{\partial t} \tag{2.18b}$$

$$\nabla \cdot \mathbf{B} = 0 \tag{2.18c}$$

$$\nabla \times \mathbf{B} = \mu_0 \mathbf{j} \tag{2.18d}$$

Finally, the electromagnetic fields and the fluid motion are linked by Ohm's law,

$$\mathbf{E} + \mathbf{v} \times \mathbf{B} = \eta \mathbf{j}, \tag{2.18e}$$

where we introduced the resistivity η. In the case of the so-called ideal MHD, where the plasma is considered a perfect conductor, $\eta = 0$ and Ohm's law states that, in the local frame of the moving fluid, no electric field can exist. Eqs. (2.17 and 2.18) represent the most basic description usually employed to model plasmas. It is nevertheless a closed model and contains extremely rich physics. As we are interested in magnetic equilibria without mean flow, total and partial time derivatives must vanish ($\partial_t = 0$ and $\mathbf{v} = 0$).

For anisotropic plasmas described in this thesis, one has to introduce an effective current density $\mathbf{K}$ defined in such a way that Eq. (2.18d) writes[4,6]

$$\nabla \times (\sigma \mathbf{B}) \equiv \mu_0 \mathbf{K}, \qquad (2.19a)$$

where

$$\sigma \equiv 1 - \frac{\mu_0}{B} \left.\frac{\partial p_\parallel}{\partial B}\right|_s = 1 - \mu_0 \frac{p_\parallel - p_\perp}{B^2} \qquad (2.19b)$$

is related to the firehose stability criterion,[6] which states that σ must be positive everywhere. The momentum equation (2.17a) yields then the force balance in equilibrium state as

$$\left.\frac{\partial p_\parallel}{\partial s}\right|_B \nabla s = \mathbf{K} \times \mathbf{B}, \qquad (2.19c)$$

where the radial coordinate s has been defined in Eq. (2.9). We see from this that $\mathbf{K} \cdot \nabla s = 0$, stating that the effective current density lines lie on constant flux surfaces. Finally, the equilibrium magnetic field has to satisfy

$$\nabla \cdot \mathbf{B} = 0. \qquad (2.19d)$$

Equations (2.19) define the anisotropic MHD equilibrium. We will turn again to the isotropic limit, since the background thermal plasma will always be treated isotropic, and it is also more straightforward to derive some basic relations we will need for qualitative understanding later on in this thesis. In the isotropic case, $\sigma = 1$, and thus $\mathbf{K} = \mathbf{j}$, and the pressure $\nabla \cdot \mathbf{P} \rightarrow \nabla p$. In that case, Eqs. (2.17) and (2.18) reduce to

$$\mathbf{j} \times \mathbf{B} = \nabla p, \qquad (2.20a)$$
$$\nabla \times \mathbf{B} = \mu_0 \mathbf{j}, \qquad (2.20b)$$
$$\nabla \cdot \mathbf{B} = 0, \qquad (2.20c)$$

From these equations we can derive some fundamental properties. For instance, in the isotropic equilibrium the pressure and the current lie on magnetic flux surfaces, since $\mathbf{B} \cdot \nabla p = 0$ and $\mathbf{j} \cdot \nabla p = 0$. In other words, in the isotropic limit, the surfaces on which the field lines lie are also surfaces of constant pressure, and the current lies on these surfaces as well. Inspecting Eqs. (2.20), the force balance in this model is quadratic in magnetic field strength and linear in pressure as seen if we combine the first two equations of Eqs. (2.19). This is why the parameter

$$\beta \equiv \frac{p}{B^2/2\mu_0}, \qquad (2.21)$$

giving information about the ratio between pressure and magnetic force, is very useful for classifying any given magnetic equilibrium. It is not only an important parameter of the equilibrium, but it also gives information about the efficiency of a given configuration, since one wants to achieve high pressure p but the magnetic field B has to be generated,

such that β to some extent gives the ratio of the obtained force (pressure in the plasma) divided by the cost (in terms of magnetic field strength created by the external coils). Eqs. (2.19) and also (2.20) show clearly that for any given configuration, the magnetic field, the pressure and the current are linked. These equations are in vector form, such that not only the amplitudes of these quantities are linked, but more generally their vector components. One can therefore also find a relation between the current and the safety factor defined in Eq. (2.4). One can define the local inverse aspect ratio

$$\epsilon \equiv \frac{r}{R_0},$$
(2.22)

which in standard tokamaks can be considered small. Then, for a large aspect ratio, i.e. $\epsilon \ll 1$, and a circular cross section, the expression for the safety factor, Eq. (2.4) can be simplified to read

$$q = \frac{rB_\varphi}{R_0 B_\theta}.$$
(2.23)

Then, defining the current inside the flux surface at r as

$$I(r) = 2\pi \int_0^r j(r')r'\mathrm{d}r',$$
(2.24)

one can find the relation between the current, the magnetic field and the safety factor using Eqs. (2.20) as

$$q(r) = \frac{2\pi r^2 B_\varphi}{\mu_0 I(r)R}.$$
(2.25)

This relation shows that there is a direct relation between the current and the safety factor, and this will be important for the results in this thesis. We will locally change the current using wave-particle interactions, and therefore change the safety factor profile. With a change in the safety factor profile the magnetic topology can be changed without changing the amplitude of the field. Therefore, acting on the current within the plasma can have an important direct effect on the equilibrium, and this is one of the motivations for this thesis, i.e. for including the equilibrium evolution in the self-consistent computations.

The magnetic equilibrium is defined by the state which minimises the energy with the given constraints of current and pressure profiles and the boundary conditions. In a general three dimensional geometry, and the anisotropic pressure given by $p_\perp$ and $p_\parallel$, the required energy functional is of the form[7]

$$W = \int_V \mathrm{d}V \left(\frac{B^2}{2\mu_0} + \frac{p_\parallel(s,B)}{\Gamma - 1} \right),$$
(2.26)

where V is the real space volume of the plasma and Γ the adiabatic index ($\Gamma = 0$ in all of this work). In a tokamak, this reduces to the generalised Grad-Shafranov equation given e.g. in Ref. 8. Here we will only give the relations showing the effects of the perpendicular pressure on the shaping coefficients and point the interested reader to the above mentioned reference. The effect of the anisotropic pressure on the Shafranov shift

and the shaping coefficients is defined by[8]

$$\Delta'' + \left(\frac{2(rf_1)'}{rf_1} - \frac{1}{r}\right)\Delta' - \frac{1}{R_0} + \frac{r(\bar{p}_{\perp,2} + p_{\parallel,2})'}{R_0 B_0^2 f_1^2} - \frac{r p'_{\perp,2,(2)}}{2R_0 B_0^2 f_1^2} \quad = \quad 0 \quad (2.27a)$$

$$S''_{m,2} + \left(\frac{2(rf_1)'}{rf_1} - \frac{1}{r}\right)S'_{m,2} - \frac{m^2 - 1}{r^2}S_{m,2}$$

$$+ \frac{p_{\perp,2,(m+1)}(m+1) + p_{\perp,2,(m-1)}}{2R_0 B_0^2 f_1^2 m} - \frac{r\left[p'_{\perp,2,(m-1)} - p'_{\perp,2,(m+1)}\right]}{2R_0 B_0^2 f_1^2 m} = 0. \quad (2.27b)$$

The notations are as follows: f and g are the normalised poloidal and toroidal magnetic fields, using $\mathbf{B} = R_0 B_0 \left[f(r)\nabla\varphi \times \nabla r + g(r,\theta)\nabla\varphi\right]$, the numbered subscript corresponds to the order in the inverse aspect ration expansion $O(\epsilon)$, prime denotes derivative with respect to r, and the perpendicular pressure has been Fourier expanded using $p_{\perp,2}(r,\theta) = \bar{p}_{\perp,2}(r) + \sum_{n\geq 1} p_{\perp,2,(n)}(r)\cos n\theta$. S_m are the shaping coefficients as defined in Eq. (2.12). Note that this notation includes anisotropy in the way $\sigma\mathbf{B}$ appears in Eqs. (2.19), in that the toroidal magnetic field component g depends also on poloidal angle θ. In isotropic equilibria, g is a function of minor radius r only. Eqs. (2.27) show that the Shafranov shift Δ and the shaping coefficients S_m, and thus the elongation and triangularity, depend on the magnetic field strength and that the dependence on the perpendicular pressure is much stronger than the dependence on the parallel pressure. Indeed, the authors in Ref. 8 showed that when $p_\perp/p_\parallel \sim \epsilon^{-1}$, the poloidal derivative of the perpendicular pressure can be of the same order as the perpendicular pressure itself, i.e. $\partial p_\perp/\partial\theta \sim p_\perp$. Thus, in the simulations in this thesis, the Fourier amplitudes $p_{\perp,2,(n)}$ in Eqs. (2.27) can be quite large. The reason why perpendicular pressure is more important than parallel pressure can be understood when considering the particle orbits, in particular the difference between what is called passing and trapped particles. We will therefore turn to these orbits now.

2.2. Particle orbits

2.2.1. Gyro motion and cyclotron frequency

The equation of motion for a single charged particle in a homogeneous magnetic field and without electric field is

$$m\frac{d\mathbf{v}}{dt} = Q\mathbf{v} \times \mathbf{B}, \quad (2.28)$$

where m and Q are the particle's mass and charge respectively. The term $\mathbf{v} \times \mathbf{B}$ is responsible for the division of the motion into dynamics perpendicular and parallel to the magnetic field, since in the parallel direction $\mathbf{v} \times \mathbf{B}|_\parallel = 0$, and the particle does not feel any force in that direction, and therefore $\mathbf{v}_\parallel = \mathbf{v}_{0\parallel} = \text{const}$. In the perpendicular direction, however, there is an acceleration causing the particle to spin or gyrate around
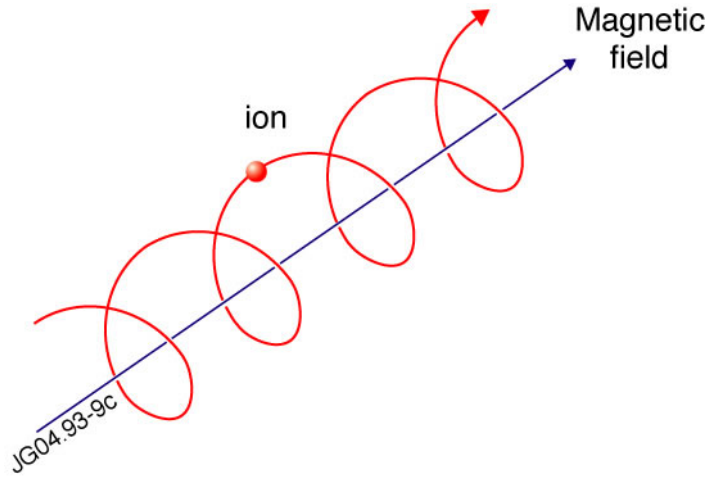
Figure 2.5.: A charged particle (an ion shown) moves along the magnetic field in a helical motion.
figure from jet.efda.org

a given magnetic field line, as illustrated in Fig. 2.5. Indeed, solving in (x, y, z), where $\mathbf{B} = (0, 0, B)$, one can find evolution equations of the form

$$x(t) = \rho_L \cos \Omega t \tag{2.29a}$$
$$y(t) = \rho_L \sin \Omega t \tag{2.29b}$$
$$z(t) = v_{0\parallel} t. \tag{2.29c}$$

This describes the so-called cyclotron or gyro motion, defined by the cyclotron frequency

$$\Omega = \frac{QB}{m}. \tag{2.30}$$

and the Larmor radius

$$\rho_L = \frac{v_\perp}{\Omega}. \tag{2.31}$$

There are two important points to be made. In this thesis, we will study wave-particle interactions which take place when the cyclotron frequency of a given particle matches the frequency of the injected wave, allowing for energy exchange between the particle and the wave. The other effect is that one can average over this fast motion of the particles and only consider the motion of the centre of the helix-like orbit, the so-called guiding centre. The basic influence of the gyro motion will still be present through the so-called magnetic moment of the particle, defined as

$$\mu = \frac{m v_\perp^2}{2B}. \tag{2.32}$$

The magnetic moment is related to the charged particle describing a helical orbit, and by doing so creating a current loop around the magnetic field line, and is an adiabatic

invariant in the guiding centre description. The resulting guiding centre trajectories are faster to solve, since instead of integrating the complete Lorentzian orbits, one retains only the magnetic moment and evolves the average position of the particle in time. The guiding centre orbits will be described in more detail in the following section, and are the basis of the VENUS code, which is part of the numerical scheme developed in this thesis.

2.2.2. Guiding centre drifts

Trap cone

As we have already seen, particles mainly follow the magnetic field lines, and are bound in their perpendicular motion by the cyclotron gyration. One constant of motion is of course the particle energy $E = 0.5mv^2 = 0.5m(v_\parallel^2 + v_\perp^2)$. The already mentioned magnetic moment is defined as $\mu = mv_\perp^2/2B$ and is an adiabatic invariant. The magnetic field lines are not straight in a tokamak, but assume a helical form, describing magnetic flux surfaces in the poloidal plane. We also know from Eq. (2.1) that the magnetic field strength has roughly a $1/R$ dependence. Thus, when a particle moves along the field line starting on the low field side of the torus ($R > R_0$) with a given constant energy and magnetic moment, it will see the field increase as it moves over to the high field side, that is when R decreases. With increasing B and constant μ and E, the parallel velocity

$$v_\parallel^2 = 2(E - \mu B)/m \tag{2.33}$$

decreases and can even vanish. But, $v_\parallel^2 \geq 0$, such that, when $B = E/\mu$, the particle cannot move on. The only possibility for the particle is then to reverse (i.e. change sign of $v_\parallel$). This is called the magnetic mirror, as the particles are reflected at $B = E/\mu$. Such particles are called trapped, since they are no longer free to move along the magnetic field lines. The particles with low enough μ do not suffer the mirroring and are thus called passing, as for those particles the mirror condition is never satisfied in the plasma, and they can therefore continue to follow the magnetic field lines. Fig. 2.6 shows one example of a trapped and a passing particle in three and two dimensions (i.e. in the poloidal plane). In the poloidal cut to the right of Fig. 6.2, the colored shading shows the magnetic field strength. The trapped particle describes in the two dimensional poloidal plane a banana-like form, which is why trapped orbits are also called banana orbits. The equations of motion for the guiding centre orbits will be given later in Chapter 6. Nevertheless, for the description the following simple demonstration is adequate. One can define the trap cone, which is the region in velocity space inside which the particles are trapped, and outside which they are passing. The trapped-passing boundary at a given flux surface is given by a ratio of $v_\parallel/v_\perp$ such that the parallel velocity just vanishes at the maximum field strength on that flux surface. Explicitly, let us define the minimum (maximum) field strength along a given guiding centre orbit as $B_{\min}$ ($B_{\max}$). Now, we want to find the transition from passing to trapped orbits in velocity space. Therefore, we consider a particle which is exactly on that transition, the trapped-passing boundary. This means that the maximum magnetic field is just strong enough to reflect the particle on the midplane, i.e. at $\theta = \pi$.
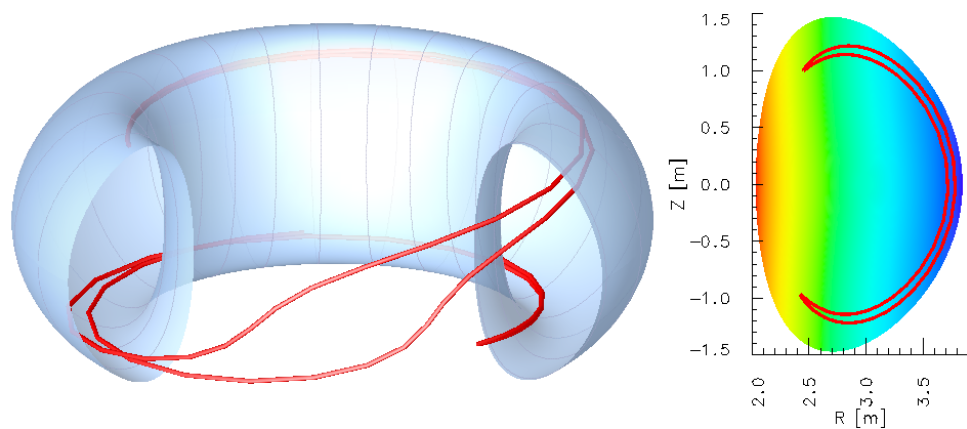
(a) Trapped particle or banana orbit. The particle has a large enough magnetic moment for it to be reflected by strong B. One can clearly see the difference in toroidal angle between the two passings of the orbit on the midplane $\theta = 0$, corresponding to the toroidal precession.
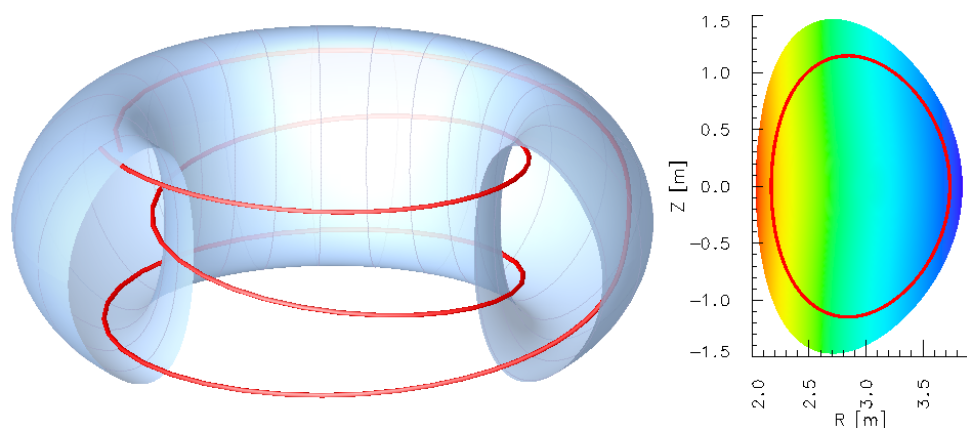
(b) Passing particle orbit. The magnetic moment is low and the particle follows the magnetic field lines closely around the complete orbit.

Figure 2.6.: A trapped and a passing particle orbit. The trapped particle describes a banana shaped curve in the poloidal plane, hence the name banana orbit. The passing particle is following the magnetic field lines closely, which is why the orbit resembles the mangetic field line in Fig. 2.3.

We denote the perpendicular and parallel velocities at the minimum magnetic field, i.e. at $\theta = 0$, as $v_{\perp,0}$ and $v_{\parallel,0}$, whereas the parallel velocity vanished at the point of maximum field strength, and we denote the perpendicular velocity $v_{\perp,t}$. By virtue of conservation of magnetic moment μ, we can then write

$$\frac{v_{\perp,t}^2}{B_{\max}} = \frac{v_{\perp,0}^2}{B_{\min}}, \tag{2.34}$$

since the mass if of course conserved as well. Since at the bounce point $v_{\parallel,t} = 0$, the conservation of energy implies

$$v_{\perp,t}^2 = v_{\perp,0}^2 + v_{\parallel,0}^2 \equiv v_0^2, \tag{2.35}$$

and therefore

$$\frac{v_0^2}{B_{\max}} = \frac{v_{\perp,0}^2}{B_{\min}}. \tag{2.36}$$

It follows that $v_{\parallel,0}^2 = v_0^2(1 - B_{\min}/B_{\max})$ and $v_0^2 = v_{\perp,0}^2 B_{\max}/B_{\min}$, and finally we obtain

$$\frac{v_{\parallel,0}^2}{v_{\perp,0}^2} = \frac{B_{\max}}{B_{\min}} - 1. \tag{2.37}$$

For a tokamak, we can approximate $B \approx B_0 R_0 / R$, as seen before, $R \approx R_0 + r\cos\theta$, and assume large aspect ratio, $\epsilon = r/R_0 \ll 1$, such that $R_0/R \approx 1/(1 + \epsilon\cos\theta)$. It follows that $B_{\min} = B(\theta = 0) \approx B_0(1 - \epsilon)$ and $B_{\max} = B(\theta = \pi) \approx B_0(1 + \epsilon)$. Eq. (2.37) then gives $v_{\parallel,0}^2/v_{\perp,0}^2 \approx 2\epsilon/(1 - \epsilon)$. If we invoke once again $\epsilon \ll 1$, we see that

$$\frac{v_{\parallel,0}}{v_{\perp,0}} \approx \sqrt{2\epsilon}. \tag{2.38}$$

If we further assume an isotropic distribution (e.g. a Maxwellian), the fraction of trapped particles is determined by $v_{\parallel,0}/v_0$ on the trap cone, and thus the fraction of trapped particles for such distributions has the same dependence of $\sqrt{2r/R_0}$. Thus, the further away from the magnetic axis, the larger the fraction of trapped particles. Fig. 2.7 illustrates the trap cone in velocity space for a better understanding. If, at the position of minimum magnetic field strength along its orbit, a particle has a ratio of $v_\parallel/v_\perp$ which is smaller than the one defined in Eq. (2.37), the particle is inside the trap cone, and it will be reflected, i.e. describe a banana orbit. The lower the parallel with respect to the perpendicular velocity, the closer $B_{\max}$ and $B_{\min}$, which means that the particle is reflected at lower θ. The extreme case where $v_{\parallel,0} \to 0$, $B_{\max} \to B_{\min}$ is called stagnation orbit, since the particle is not moving at all in poloidal direction, since the point of reflection coincides with the point of departure. Such orbits will only move in toroidal direction. Particles with rather low parallel velocity, such that $B_{\max}$ is not far from $B_{\min}$, and thus the maximum poloidal angle of the particle orbit is considerably smaller than $\pi/2$ are called deeply trapped, and particles which are close to the trapped-passing boundary but still inside
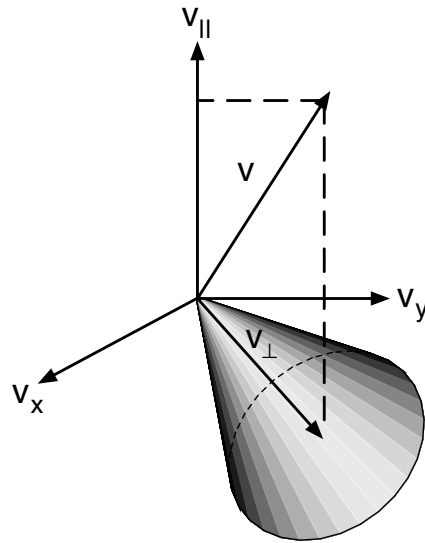
Figure 2.7.: Definition of the trap cone in velocity space. Particles with parallel and perpendicular velocities inside the cone are trapped, outside the cone are the passing particles.

the trap cone are called barely trapped. Finally, particles close to the trapped-passing boundary but outside the trap cone are barely passing and particles with almost vanishing perpendicular velocity are deeply passing.

In later Chapters, contour plots of the distribution function as a function of $v_\parallel$ and $v_\perp$ will be an important tool for interpretation of the simulation results. We can then recall Eq. (2.37) in order to estimate where in these contour plots particles are trapped or passing. The distinction is important, since trapped and passing particles do not have the same effects. For instance, we will see that, since trapped particles have in general higher μ and thus higher perpendicular velocity than passing particles, a high number of trapped particles means a high perpendicular pressure and vice versa. Now, trapped particles cannot complete a poloidal circuit around a given flux surface, and thus the trapped population cannot contribute to the fast equalisation of the characteristics along one given flux surface. Therefore, one can expect that perpendicular pressure cannot be treated as a flux surface quantity, and the poloidal dependence will have to be retained for consistent computations. This is one important reason why the dependence of the Shafranov shift and the shaping coefficients (2.27) on the perpendicular pressure is more important than one the parallel pressure. We can already see why it will be important to retain the anisotropic pressure ($p_\perp \neq p_\parallel$) and the poloidal dependence of the macroscopic quantities in what follows.

Finite orbit width

As can be seen in Fig. 2.6(a), trapped particles do not exactly follow the field lines, and the inner and outer leg of the banana orbits do not lie on each other. The difference in radius of the inner and the outer leg is called orbit width. For a simple explanation, we again place ourselves into the axisymmetric tokamak geometry. Here, the symmetry in toroidal φ direction implies, along the particle orbit, conservation of the canonical angular momentum

$$P_\varphi = Rmv_\varphi + Q\psi, \tag{2.39}$$

where as before R is the major radius, Q the particle's charge and ψ the poloidal flux function. Now, if we place ourselves at one given R and look at the orbit of a trapped particle as in Fig. 2.6(a), we see that the sign of the velocity in toroidal direction changes from the inner to the outer part of the orbit. This is of course no surprise, since the particle is mirrored when $v_\parallel \to 0$, and it simply moves back to where it came from. But then, the toroidal moment P_φ must be conserved, and therefore

$$\psi_2 - \psi_1 = \frac{Rm}{Q} \left(v_\varphi^1 - v_\varphi^2 \right). \tag{2.40}$$

From our observations we expect that v_φ changes sign between points 1 and 2, and therefore the right hand side of Eq. (2.40) is either negative or positive, but never zero (except if the toroidal velocity is zero of course). This is the proof that a trapped particle cannot have a zero orbit width. In the poloidal cut in Fig. 2.8(a) we chose the inner leg with label 1 and the outer to have label 2, such that $\psi_2 - \psi_1 > 0$, and therefore $v_\varphi^1 - v_\varphi^2 > 0$. Now, at the same position R, the magnetic field has approximately the same strength at positions 1 and 2, and from the magnetic moment and energy conservation and what we found before follows that $0 < v_\varphi^1 \approx -v_\varphi^2$. Within this approximation, let us define $v_\varphi = v_\varphi^1 \approx -v_\varphi^2$, such that we can write the orbit width $\delta\psi = \psi_2 - \psi_1$ as

$$\delta\psi \approx 2\frac{Rm}{Q}|v_\varphi|. \tag{2.41}$$

Trapped particles travel along the toroidal coordinate φ on the inner leg of a trapped orbit ($v_\varphi^1 > 0$), and opposite φ on the outer leg ($v_\varphi^2 < 0$). In all simulations presented in this work, the toroidal current is chosen in the direction opposite the coordinate φ. We can therefore already state that in our simulations, trapped ions will move in counter-current direction on the inner leg, and in the co-current direction on the outer leg. Furthermore, the toroidal velocity $v_\varphi \to 0$ at the turning points, and therefore the orbit width vanishes, meaning that the average radial position of a trapped particle $\overline{\psi}_t$ corresponds to the position at the turning points $\psi_{t.p.}$,

$$\overline{\psi}_t = \psi_{t.p.}. \tag{2.42}$$

These considerations will become important in the discussion of the RF induced current in the following chapters. Eq. (2.41) shows that the orbit width scales with the toroidal velocity, and thus with $\sqrt{E}$ for a given pitch angle v_φ/v. Highly energetic particles have
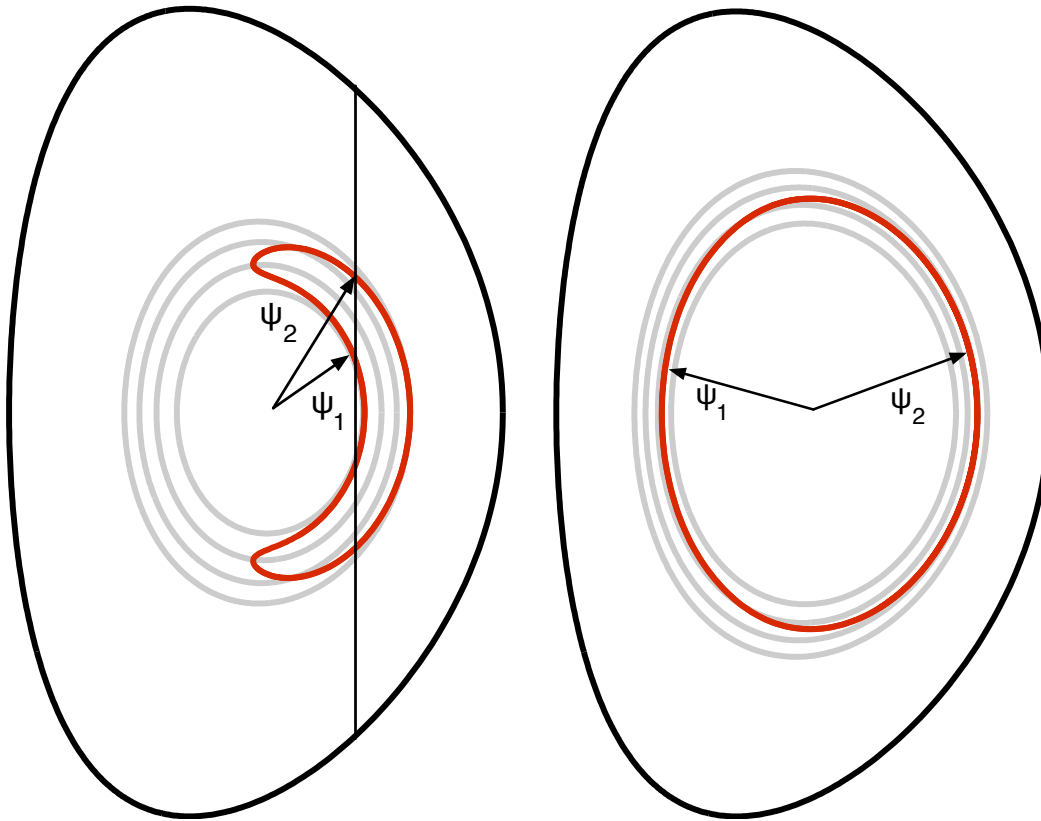
(a) Poloidal trapped particle orbit. The trapped parti-
cle describes a banana orbit with a finite orbit width
$\Delta\psi = \psi_2 - \psi_1$ given by Eq. (2.41) for $\psi_{1,2}$ at the
same major radius R (vertical line).

(b) Poloidal passing particle orbit. The passing par-
ticle orbit can also depart form a given flux surface
as given in Eq. (2.45). For the here shown orbit with
$v_\varphi < 0$, the orbit is shifted to the right with respect
to the flux surfaces, for the opposite sign of v_φ the
shift is to the left in the poloidal plane.

Figure 2.8.: Finite orbit widths in a tokamak for passing and trapped orbits. The departure from
the flux surfaces depends on the toroidal velocity. The maximum orbit width at one
given flux surface, occurring on the trapped-passing boundary, is twice as large for
passing than for trapped particles. Grey lines show flux surfaces in the vicinity of the
respective orbits.

larger orbit widths than thermal particles, which will be of great importance when we discuss the orbits of the high energy particles heated with radio frequency waves. Also, barely trapped particles (trapped particles which describe an almost complete poloidal orbit) will have larger orbit widths than deeply trapped particles (particles which are almost stationary and oscillate close to the midplane), since the toroidal velocity is usually greater for the first than for the latter. For passing particles, the orbit does also depart from a given flux surface. There is, however, an important difference, which is that the toroidal velocity does not change sign. Hence, for a given major radius R and toroidal moment P_φ, the orbit always passes through the same point. However, there is a departure as a function of poloidal angle, as the magnetic field still increases between $\theta = 0$ and $\theta = \pi$ and decreases for $\theta = \pi$ to $\theta = 2\pi$. Again using the toroidal moment, and expressing the poloidal flux function yields along the orbit

$$\psi = \frac{P_\varphi}{Q} - \frac{Rm}{Q}v_\varphi = C - \frac{Rm}{Q}v_\varphi. \tag{2.43}$$

This looks similar to the case of trapped particles, Eq. (2.41). However, the toroidal velocity does not change sign, and we can define the orbit width of a passing particle as the difference in ψ between $B_{\min}$ and $B_{\max}$ of a complete poloidal orbit, i.e. in the usual tokamak configuration between $\theta = 0$ and $\theta = \pi$. Assuming that both the toroidal and total magnetic fields depend on $1/R$, we can compare the poloidal flux function at two different values of R, say $\psi_1 = \psi(R_1)$ and $\psi_2 = \psi(R_2)$,

$$\psi_2 - \psi_1 = \delta\psi = \frac{m}{Q}\left(R_1 v_\varphi^1 - R_2 v_\varphi^2\right), \tag{2.44}$$

Note that for a passing particle, the signs of $v_\varphi^{1,2}$ are the same, whereas for a trapped particle, $v_\varphi^2 = -v_\varphi^1$ and at $R_1 = R_2$, and we obtain again Eq. (2.41). For a barely passing particle on the trapped-passing boundary, and taking the major radii $R_2 = R = R(\theta = 0)$ and $R_1 = R(\theta = \pi)$, we obtain the maximum orbit width for a passing particle with $v_\varphi = v_\varphi^2$ and $v_\varphi^1 \to 0$, namely

$$\psi_1 - \psi_2 = \delta\psi = \frac{mR}{Q}v_\varphi, \tag{2.45}$$

which is in absolute value exactly half the orbit width for a barely trapped particle on the trapped-passing boundary, i.e. with the same v_φ, but the orbit width given by Eq. (2.41). There is, however, another difference between passing and trapped particles. The orbit width $\delta\psi$, and thus the departure from the average radial position, depends on the sign of v_φ. Fig. 2.8(b) shows a passing particle orbit with $v_\varphi < 0$. Choosing the subscripts as in the derivation of Eq. (2.45), we see that $\psi_1 - \psi_2 < 0$, i.e. $\psi_1 < \psi_2$, meaning that in the poloidal plane, the passing orbit is shifted to the right with respect to the flux surfaces. Had we considered a particle with $v_\varphi > 0$, the passing orbit would have been shifted to the left with respect to the flux surfaces. If we want to have a qualitative understanding of the average radial position of a passing particle orbit, i.e. where along the orbit $\delta\psi = 0$

as for the trapped particles, we can consider a deeply passing particle, i.e. $\mu = 0$. In this case, $v_\varphi \approx v_\parallel = v$, and the orbit width $\delta\psi$ is given by

$$\delta\psi \approx \frac{m}{Q} v_\varphi (R_1 - R_2). \tag{2.46}$$

If we further neglect flux surface shaping, such a deeply passing particle will describe a circle with $R_{\min} = R_0 - \Delta r$ and $R_{\max} = R_0 + \Delta r$, where Δr is the radius of the circular orbit. Now, if we choose $R_2 = R_{\max}$, we see that the orbit width increases (in absolute value) linearly with the distance $|R_1 - R_2|$, being exactly twice as large at $R_1 = R_{\min}$ compared to $R_1 = R_0$, i.e. the magnetic axis. The average radial position of the deeply passing orbit $\overline{\psi}_{\mathrm{d.p.}}$ is therefore at

$$\overline{\psi}_{\mathrm{d.p.}} = \psi(R_0) = \psi(\theta = \pi/2). \tag{2.47}$$

If we allow for finite perpendicular velocity, the average radial position will move towards $R_{\min}$, and for barely passing particles ($\overline{\psi}_{\mathrm{b.p.}}$) and barely trapped particles ($\overline{\psi}_{\mathrm{b.t.}}$) at the trapped passing boundary,

$$\overline{\psi}_{\mathrm{b.p.}} = \overline{\psi}_{\mathrm{b.t.}} = \psi(\theta = \pi). \tag{2.48}$$

We will come back to this discussion when we introduce the model bi-Maxwellian distribution function in Chapter 4 and the loading of the marker distribution in Chapter 6. There are many other types of orbits than the standard two we have briefly shown here.[9] In particular, it is possible to have trapped particles encircling the magnetic axis or passing particles which stay entirely on the low field side of the magnetic axis. The latter will become important when we study the low field side heating cases in Chapters 11 and 12, and the effect of non-standard orbits in ICRH scenarios has also been documented e.g. in Refs. 10,11. An excellent review on orbit classification can be found in Ref. 12.

Another difference for trapped or passing particles is what is called toroidal precession. One can very clearly distinguish a toroidal motion of the trapped particle in Fig. 2.6(a) between the two passings through the midplane ($\theta = 0$) in the section of the 3D plot where the tokamak has been cut open. This difference in toroidal angle as the particle orbit evolves is called toroidal precession drift and is present for passing particles as well. But since the passing particles follow the magnetic field lines, the toroidal precession is only a small contribution to the toroidal propagation of the particles. For trapped particles however, the precession is the only cause for toroidal propagation of the particles, and this inherent frequency of particle motion automatically present in the plasma can resonate with perturbations within the plasmas and it can therefore play an important role of global stability of the plasma. We will study the characteristics of this motion in detail in Chapter 8.

2.3. Kinetic description

We have so far explained two different possible descriptions of a plasma. When dealing with global quantities and equilibrium, looking at the plasma as one single fluid, thus using MHD, is appropriate. If one wants to study in detail what happens to single particle orbits, one should consider a guiding centre drift description. There are, however, phenomena where a great number of particles are involved, but each particle is affected differently according to its position in the $(\mathbf{x}, \mathbf{v})$ phase space. For such phenomena, it is much more appropriate to use a statistical approach, such as kinetic theory. Here, it is necessary to know the distribution function in phase space, $f(\mathbf{x}, \mathbf{v}, t)$, which gives (depending on its normalisation) the total number of particles or unity when integrated over the six-dimensional phase space. f must be a continuous function of its arguments, positive and finite at any instant of time, and must tend to zero as the velocity becomes infinitely large. For instance, in a highly collisional plasma, the thermal equilibrium state takes the form of a Maxwellian distribution with density and temperature profiles $n(s)$ and $T(s)$ of the form

$$f_M(s, E) = \frac{n(s)m}{2\pi T(s)} e^{-E/T(s)}. \tag{2.49}$$

Here, the normalisation is chosen such that the integral over velocity space yields the density. The evolution equation for the distribution function is the Boltzmann equation

$$\frac{\mathrm{d}f}{\mathrm{d}t} = \frac{\partial f}{\partial t} + \mathbf{v} \cdot \nabla f + \frac{\mathbf{F}}{m} \cdot \frac{\partial f}{\partial \mathbf{v}} = \left. \frac{\partial f}{\partial t} \right|_c, \tag{2.50}$$

where the LHS denotes the total time derivative and the RHS dissipation due to collisions. Again the force is the Lorentz force, $\mathbf{F} = Q(\mathbf{E} + \mathbf{v} \times \mathbf{B})$. If there are different species inside the plasma with different mass and charge, Eq. (2.50) has to be satisfied for each species separately. However, the electromagnetic fields in the Lorentz force are the same for all species, thus linking the state of the different species together into a set of equations. Often, the collisional term is neglected, and the resulting equation is the Vlasov equation

$$\frac{\mathrm{d}f}{\mathrm{d}t} = \frac{\partial f}{\partial t} + \mathbf{v} \cdot \nabla f + \frac{\mathbf{F}}{m} \cdot \frac{\partial f}{\partial \mathbf{v}} = 0. \tag{2.51}$$

An important difference to MHD is the distinction between particles with different velocities. With the distribution function, the whole velocity range is covered, whereas the fluid description only takes into account an average velocity of a fluid element (consisting of many particles). The most striking difference is in the investigation of the stability of different excitations, where the kinetic theory can "resolve" instabilities due to a difference in velocity of the particles within the plasma. The link between the two descriptions can be made through the global quantities like density, pressure and current. In the kinetic descriptions, these are defined as moments of the distribution function. Explicitly, we can

write for every species i

$$n_i(\mathbf{x}, t) = \int f_i(\mathbf{x}, \mathbf{v}, t) \mathrm{d}^3\mathbf{v}, \tag{2.52a}$$

$$\mathbf{j}_i(\mathbf{x}, t) = Q_i \int \mathbf{v} f_i(\mathbf{x}, \mathbf{v}, t) \mathrm{d}^3\mathbf{v}, \tag{2.52b}$$

$$p_i(\mathbf{x}, t) = \frac{m_i}{3} \int v^2 f_i(\mathbf{x}, \mathbf{v}, t) \mathrm{d}^3\mathbf{v}, \tag{2.52c}$$

$$p_{\perp i}(\mathbf{x}, t) = \frac{m_i}{2} \int v_\perp^2 f_i(\mathbf{x}, \mathbf{v}, t) \mathrm{d}^3\mathbf{v}, \tag{2.52d}$$

$$p_{\parallel i}(\mathbf{x}, t) = m_i \int v_\parallel^2 f_i(\mathbf{x}, \mathbf{v}, t) \mathrm{d}^3\mathbf{v}. \tag{2.52e}$$

The factors of one third and one half in the definitions of the thermal and perpendicular pressures come from the fact that there are three indistinguishable directions in the isotropic, and two perpendicular and one parallel directions in the anisotropic case.

The evolution of the system due to heating effects can only be dealt with using kinetic theory, since the wave-particle interactions, and especially the so-called Landau damping, depend on the relative velocities of the particles with respect to the wave propagation. As a consequence, the wave propagation and the time evolution of the system subject to ICRF wave injection is computed using distribution functions. However, solving the Boltzmann equation (2.50) directly is very difficult, if not impossible, due to the large variety of spatial and temporal scales involved. Usually, the drift kinetic approach is applied, where the Boltzmann equation is averaged over the fast gyro motion. In velocity, space, a spherical coordinate system is then introduced with $(v_\perp \cos\alpha, v_\perp \sin\alpha, v_\parallel)$, where α is the gyroangle, over which the equation is averaged. Then, the distribution function is usually expanded, separating terms of different spatial scales, where mostly the gyroradius serves as small parameter compared to the orbit width.[13,14] Especially for ICRF, the wave-particle interactions take place on a scale of the order of the gyroradius, and codes trying to solve the drift kinetic equation directly in terms of f therefore usually have to make approximations in longer spatial scales, as for example neglecting finite orbit width effects. However, these effects can be very important, and we therefore chose a different approach. If we want to retain full finite orbit width effects, we have to follow the particles by integrating their equations of motion. However, the gyroradius is very small with respect to the orbit scale, and in a first approach we have to neglect gyro motion effects, and find equations of motion for the guiding centre. An unperturbed system will conserve energy, if no electromagnetic fields (other than the equilibrium magnetic field) or collisions are present. The wave kinetic equation for such systems reduces to[15]

$$\mathbf{v} \cdot \nabla f = 0, \tag{2.53}$$

with the distribution function depending only on the constants of motion. The guiding centre trajectories can be described in the Hamiltonian formulation. However, the equations of motion have to be in the correct form, such that the resulting drift velocity $\mathbf{v}$ satisfies Liouville's theorem. Thus, the evolution of the guiding centre drift orbits must be such

that[16,17]

$$\mathbf{v} = \frac{v_\parallel}{B} \frac{\sigma \left[\mathbf{B} + \nabla \times (\rho_\parallel \sigma \mathbf{B}) \right]}{1 + \rho_\parallel \mu_0 \mathbf{K} \cdot \mathbf{B} / B^2}, \tag{2.54}$$

where $\rho_\parallel = m v_\parallel / QB$ is the parallel gyroradius and $\mathbf{K}$ and σ have been introduced in Sec. 2.1.2. Most authors neglect the term $\rho_\parallel \mu_0 \mathbf{K} \cdot \mathbf{B} / B^2$, departing from the strict Hamiltonian formulation. Additionally, the retention of pressure anisotropy by retaining σ and $\mathbf{K}$ is a complete novelty, and the isotropic relation can be found setting $\sigma = 1$ and $\mathbf{K} = \mathbf{j}$. The corresponding equations of motion implemented in VENUS are given in Chapter 6. Note that these equations of motion include terms related to electromagnetic perturbations happening in the same time and length scales as the guiding centre orbits. This represents a generalisation of Eq. (2.53), but those terms are not considered in this thesis. In order to solve for the evolution of the distribution function, we have to add the perturbations corresponding to the collisions and RF wave-particle interactions. This is done using a Monte Carlo approach, which will simulate the Coulomb collisions, i.e. the RHS of Eq. (2.50), and the action of the wave on the distribution, i.e. the term $Q/m\mathbf{E} \cdot \partial f / \partial \mathbf{v}$. The latter operator will link the dynamics on the gyro time and spatial scale to the evolution on the orbit time scale, and will be derived in the frame of quasilinear theory in Chapter 6. Finally, our approach will be to represent the distribution function by a certain number of particles, then called markers, whereof each samples a part of the distribution function in phase space. Then, we can evolve the marker or particles' guiding centre orbits together with the constraints coming from collisions with background plasma and wave-particle interactions, and simulate in this way the evolution of the distribution function by retaining full orbit width effects.

2.4. Electromagnetic waves

If we want to profit from the inherent cyclotron motion of charged particles as described above, by injecting electromagnetic waves matching the cyclotron frequency, we need to know more about creation, propagation and absorption of such waves. We have to deal with the characteristics of the plasma in which the waves have to propagate, since the waves will be influenced by the presence of the plasma and not propagate in the same way as in a vacuum. Furthermore, an external antenna will have to be added, in which a certain current is exciting the waves. The appropriate equations are then Maxwell's equations in a medium,

$$\nabla \times \mathbf{E} = -\frac{\partial B}{\partial t} \tag{2.55a}$$

$$\nabla \cdot \mathbf{D} = \rho_{\text{ant}} \tag{2.55c}$$

$$\nabla \times \mathbf{B} = \mu_0 \left(\frac{\partial \mathbf{D}}{\partial t} + \mathbf{j}_{\text{ant}} \right) \tag{2.55b}$$

$$\nabla \cdot \mathbf{B} = 0 \tag{2.55d}$$

Here, c is the vacuum speed of light. $\mathbf{D}$ is the so-called displacement field, and is directly

related to the internal behaviour of the plasma. It equals the electric field in a vacuum. $\mathbf{j}_{\mathrm{ant}}$ is the antenna current and ρ_{ant} its charge density, i.e. these terms are related to the source of the electromagnetic fields. The excitation from the antenna is periodic, and we can therefore write the temporal dependency as $x(\mathbf{r}, t) = \hat{x}(\mathbf{r}) \exp(-i\omega t)$. We can then define the vacuum wave number and use Eqs. (2.55a) and (2.55b) to obtain

$$\nabla \times \nabla \times \mathbf{E} - \omega^2 \mu_0 \mathbf{D} = i\omega \mu_0 \mathbf{j}_{\mathrm{ant}}. \tag{2.56}$$

Now, we need to introduce a relation between the displacement field $\mathbf{D}$ and the electric field $\mathbf{E}$. This is done introducing the dielectric tensor $\mathcal{E}$ such that

$$\mathbf{D} = \epsilon_0 \mathcal{E} \cdot \mathbf{E}. \tag{2.57}$$

Note that this is in general a dimensionless tensor, which equals the unit dyadic in a vacuum. The constant ϵ_0 then defines the vacuum permitivity. Now, the wave equation for the electric field reads

$$\nabla \times \nabla \times \mathbf{E} - \frac{\omega^2}{c^2} \mathcal{E} \cdot \mathbf{E} = i\omega \mu_0 \mathbf{j}_{\mathrm{ant}}, \tag{2.58}$$

with $c^2 = 1/\epsilon_0 \mu_0$ the vacuum speed of light. This equation can be solved for finding the electric field once we know the dielectric tensor. As said above, the latter describes the action of the medium on the wave field, and we therefore have to derive the dielectric tensor from the description of the plasma. In Eq. (2.55b) we separated internal and external terms on the right hand side. If we now concentrate on the internal terms for finding the dielectric tensor, we have to include an internal current just as we have added the external current $\mathbf{j}_{\mathrm{ant}}$. Thus, the displacement field in Eq. (2.55b) contains a current term

$$\nabla \times \mathbf{B} = \mu_0 \frac{\partial \mathbf{D}}{\partial t} = \mu_0 \left(\epsilon_0 \frac{\partial \mathbf{E}}{\partial t} + \mathbf{j} \right). \tag{2.59}$$

Assuming again the $\exp(-i\omega t)$ dependence, we find

$$\mathbf{D} = \epsilon_0 \mathbf{E} + \frac{i}{\omega} \mathbf{j}. \tag{2.60}$$

We have already defined the dielectric tensor in Eq. (2.57), and looking at the last equation, we see that the current $\mathbf{j}$ has to be proportional to the electric field for our definition of $\mathcal{E}$ to hold. We therefore define the conductivity σ as

$$\mathbf{j} = \sigma \cdot \mathbf{E}, \tag{2.61}$$

and then obtain

$$\mathbf{D} = \epsilon_0 \left(\mathbf{I} + \frac{i}{\epsilon_0 \omega} \sigma \right) \cdot \mathbf{E} = \epsilon_0 \mathcal{E} \cdot \mathbf{E}, \tag{2.62}$$

such that the dielectric tensor now takes the form

$$\mathcal{E} = \mathbf{I} + \frac{i}{\epsilon_0 \omega} \sigma. \tag{2.63}$$

If we further decompose the electric field into a sum of plane waves $\exp(-\mathbf{k} \cdot \mathbf{x} - i\omega t)$, Eq. (2.58) becomes inside the plasma (where $\mathbf{j}_{\mathrm{ant}} = 0$)

$$\mathbf{k} \times \mathbf{k} \times \mathbf{E} + \frac{\omega^2}{c^2} \mathcal{E} \cdot \mathbf{E} = 0. \tag{2.64}$$

Nontrivial solutions can be found by setting the determinant to zero, which yields

$$D(\mathbf{k}, \omega) = \det \left[\mathbf{k}\mathbf{k} - k^2 \mathbf{I} + \frac{\omega^2}{c^2} \mathcal{E} \right] = 0. \tag{2.65}$$

This equation relates the wave vector $\mathbf{k}$ to the frequency ω. Such equations are called dispersion relations. If we define without loss of generality the coordinates such that $\mathbf{k}$ is in the xz plane, define the refraction index $\mathbf{n} = \mathbf{k}c/\omega$ and decompose Eq. (2.65) into the parallel and perpendicular directions, we obtain

$$- \mathcal{E}_{xy}\mathcal{E}_{yx}(n_\perp^2 - \mathcal{E}_{zz}) + (n^2 - \mathcal{E}_{yy}) \left[n_\parallel^2 \mathcal{E}_{zz} + (n_\perp^2 - \mathcal{E}_{zz})\mathcal{E}_{xx} \right] = 0. \tag{2.66}$$

If we know the dielectric tensor, the dispersion relation (2.66) yields the refraction index, and thus the wave vector, and we can finally find the electric field with Eq. (2.64). It is interesting to note a few properties of the dielectric tensor. First of all, the real part of the dielectric tensor is related to the propagation of the wave, whereas the imaginary part describes the absorption of the wave by the plasma. An intuitive way of seeing this is its direct relation to the wave number in Eq. (2.66). Recalling that the electric field has a dependence $\exp(i\mathbf{k} \cdot \mathbf{x})$, we see that the real part of $\mathbf{k}$ is related to a sinusoidal behaviour (propagation), whereas the imaginary part of $\mathbf{k}$ will result in exponential growth, or rather exponential decay, which is more physical since exponential growth needs infinite energy. Decay of the wave inside the plasma means, by virtue of energy conservation, absorption of the wave by the plasma, through the so-called Landau damping, which describes the damping (decay) of the wave due to wave-particle interactions. Other interesting phenomena take place in the limits where $n \to \infty$ or $n \to 0$. The first case is called resonance. This is where most wave-particle interactions happen. The latter case is called cut-off, and it means that the plasma is unable to support the wave. Propagation is impossible and the wave is reflected.

If we want to find the dielectric tensor, we need to find the conductivity σ. By its definition, Eq. (2.61), we have to find the relation between the current and the electric field. This can be done using the kinetic description, in particular the Vlasov equation, Eq. (2.51). As described earlier, the electric field is contained in this equation through the Lorentz force $\mathbf{F} = Q(\mathbf{E} + \mathbf{v} \times \mathbf{B})$. This description is especially useful for finding the dielectric tensor since the current is defined as the first moment of the distribution function f as given in Eq. (2.52b). Indeed, the distribution function yields the description of the plasma

and Eq. (2.61) together with the current defined as a moment of the distribution function allow us to find the dielectric tensor, which in turn allows the resolution of the wave equation (2.58). We will show in the Chap. 5 and Appendix A the detailed computations for the specific distribution function we implemented in the code.

2.4.1. The Ion Cyclotron Range of Frequencies (ICRF)

In order to heat the plasma to the needed temperatures for fusion devices, auxiliary heating (i.e. additional to the Ohmic heating generated by the toroidal plasma current) has to be applied. One promising possibility is to profit from the cyclotron motion of the particles, as described in Sec. 2.2.1, and couple an electromagnetic wave with a similar frequency to the plasma. One advantage is that, as described in Sec. 2.1.1, the magnetic field shows a dependence on the inverse of the major radius, $B \sim 1/R$, and therefore the cyclotron frequency of a given ion species (i.e. given charge over mass ratio) also has a $1/R$ dependence. An injected wave with a fixed frequency will therefore interact with the resonant species at one given major radius, where $\omega \approx \Omega(R)$. A localised heating of the plasma is therefore possible, which can be a great advantage.

In the ion cyclotron range of frequencies, $\omega \sim \Omega_i = ZeB_c/m_i$, the electrons can short circuit the parallel electric field, since they move much faster than the wave, due to their much lower mass. Here chose a system of coordinates where $\mathbf{B} = B\hat{z}$ and $\mathbf{k} = k\hat{x}$. The dispersion relation (2.66) then simplifies to

$$n_\perp^2 = \mathcal{E}_{yy} - n_\parallel^2 - \frac{\mathcal{E}_{xy}\mathcal{E}_{yx}}{\mathcal{E}_{xx} - n_\parallel^2}, \tag{2.67}$$

where in the cold approximation (i.e. no thermal contribution from the plasma)

$$\mathcal{E}_{xx} = \mathcal{E}_{yy} = (\mathcal{E}^+ + \mathcal{E}^-)/2 \tag{2.68a}$$

$$\mathcal{E}_{yx} = -\mathcal{E}_{xy} = i(\mathcal{E}^+ - \mathcal{E}^-)/2 \tag{2.68b}$$

$$\mathcal{E}^\pm = 1 - \sum_s \frac{\omega_s^2}{\omega(\omega \pm \Omega_s)}. \tag{2.68c}$$

ω_s and Ω_s are the plasma and the cyclotron frequencies of species s. We consider the cold approximation here just for obtaining a simple overview. The dielectric tensor developed in this thesis containing the thermal effects of a strongly anisotropic population will be shown later in Chapter 5. Stix[18] has shown that the electric field polarisation, i.e. if one decomposes the electric field into two circularly polarised fields $E^\pm = (E_x \pm iE_y)/2$, is given as

$$\frac{E^+}{E^-} = -\frac{\mathcal{E}_{xx} + i\mathcal{E}_{xy} - n_\parallel^2}{\mathcal{E}_{xx} - i\mathcal{E}_{xy} - n_\parallel^2} = [\text{cold approx.}] = -\frac{\mathcal{E}^+ - n_\parallel^2}{\mathcal{E}^- - n_\parallel^2}. \tag{2.69}$$

One can see that at the cyclotron resonance of any species in the plasma, $\mathcal{E}^- \to \infty$, and therefore $E^+ \to 0$. This is true for the cold approximation. In the warm approximation, including finite temperature or pressure, $\mathcal{E}^-$ remains finite, but the qualitative

behaviour is similar. Unfortunately, the left handed component of the electric field E^+ is the more important one, since it rotates in the same direction as the ions around the magnetic field lines. Thus, if one tries to heat the plasma using cyclotron waves in a single species plasma at $\omega \sim \Omega$, the wave-particle interactions become very inefficient due to the (nearly) vanishing of E^+. However, there are two main solutions to the problem: One is to apply a wave with a frequency of an integer multiple of the cyclotron frequency, $\omega \sim n\Omega$, so-called n*th* harmonic heating, or one can apply the heating at the fundamental harmonic ($n = 1$) to a small minority species, such that E^+ can be sufficiently strong at the resonance in the warm model. The first possibility has the disadvantage that at high concentrations of a second ion species, the so-called ion-ion hybrid resonance appears besides the cyclotron resonance and, especially, a corresponding cut-off limits the propagation of the injected wave. If the ion-ion hybrid resonance is reached, mode conversion takes place, which is the transition of the initially injected wave into another type of wave (like e.g. Bernstein waves). We will concentrate on minority heating, where no mode conversion takes place, and no cut off exists in the plasma. Here, the left handed component E^+ will still show a slight local minimum along the cold resonance, but it will also show a local maximum at the high field side of that layer (if injected from the low field side). If the minority ions are warm, and thus show a non-zero Doppler shift proportional to $k_\parallel v_\parallel$, maximum power deposition will be located slightly displaced from the cold resonant layer, on the high field side. We will show that this is the case, e.g. in Fig. 5.2. One reason why we choose minority scenarios is that mode conversion can only be modelled with finite Larmor radius models, whereas our wave code, LEMan, is limited to a zero Larmor radius model. The advantage of minority heating is that the ion species, and thus the charge over mass ratio, can be chosen, and therefore the choice of a cyclotron resonance position $\omega \sim ZeB_c/m$ is possible not simply by choosing a wave frequency. It might be enough to locally heat the minority species using rather low power wave injection, e.g. for generating a localised current which acts on the safety factor profile as described in Sec. 2.1.1. Note that even if the final goal is to heat the background plasma, minority heating is a reasonable alternative, since once the power has been absorbed by the minority species, the latter are describing large orbits, and are slowing down along these orbits through Coulomb collisions with the background ions and electrons. It is then possible to heat the background plasma indirectly, and in a much larger region than the initial ion cyclotron power deposition. We will study both effects, i.e. Ion Cyclotron Current Drive (ICCD) and Ion Cyclotron Resonance Heating (ICRH) in detail in this thesis.

3. Motivations for this work

3.1. Ion Cyclotron Range of Frequencies

In the introduction we have learned that temperatures of about one hundred million degrees have to be attained for fusion to be possible. But how can we obtain such high temperatures? A first mechanism to exploit is Ohmic heating. In a tokamak, the poloidal magnetic field is generated with a current inside the plasma column along the toroidal direction. A current inside a resistive material generates heat automatically due to Ohm's law. In particular, heat comes from the dissipative effects of electric resistivity. One can therefore exploit this feature not only to create the poloidal magnetic field, but also for heating the plasma. The only problem with this is that Ohmic heating only works if the medium carrying the current is resistive, and in a plasma the resistivity decreases with temperature. Ohmic heating therefore becomes less and less efficient the higher the temperature, and other possibilities have to be found. One very promising possibility is to exploit the cyclotron motion of a charged particle around a given field line, and inject an electromagnetic wave matching this inherent frequency. In this case, resonant wave-particle interactions can occur at the position in the plasma where the Doppler shifted wave frequency $\omega - k_{\parallel} v_{\parallel}$ as seen by a given particle equals the eigenfrequency of the particle, $\Omega = ZeB/m$. We have already described this in Sec. 2.2.1. This type of heating in the ion cyclotron range of frequencies (ICRF) has been and still is installed in major fusion devices all over the world, and it is considered to be one of the major contributors to additional heating in ITER.[19] As noted before, ICRF is not only important for pure heating of the plasma, i.e. Ion Cyclotron Resonance Heating (ICRH), but also for the generation of non-inductive current through Ion Cyclotron Current Drive (ICCD). Applied to plasma species with low concentrations (minority scheme), highly localised heating effects can be generated, and ICCD can thereby be applied to control MHD instabilities, e.g. sawteeth as in Ref. 20. The physics involved spans broad spectrum that encompasses MHD equilibrium, wave propagation and absorption, kinetic effects from wave-particle interactions and also wide orbit effects. As a result, observations include many mutual interactions and the effects of single ingredients are difficult to filter out from measurements. It is therefore important to develop numerical tools which include as many physical mechanisms as possible to simulate Radio Frequency (RF) scenarios accurately.

3.2. Self-consistency

Ion cyclotron resonant wave-particle interaction is the coupling of the rotating electric fields $E^{\pm}$ and the charged particle's gyro motion around the field lines. Both are purely perpendicular to the magnetic field, and the interaction therefore takes place mainly in that perpendicular plane. The only exceptions are a small change in parallel velocity for satisfying momentum and energy conservation, and the pitch angle (the angle the velocity vector describes with respect to the magnetic field) scattering on the background plasma. These preferentially perpendicular interactions result in a distorted distribution function of the resonant minority species, a distortion increasing the value in the perpendicular direction, causing the distribution function to become non-Maxwellian.[21,22]

As discussed in Sec. 2.4, the form of the distribution function has a direct effect on the dielectric tensor and thus the wave propagation and absorption. However, as discussed in Sec. 2.3, the distribution function is affected by the electromagnetic field through the Lorentz force in the Vlasov equation (2.51), and the system becomes nonlinear, since the distribution function affects the fields, which in turn affect the distribution function. It has therefore been understood that in order to solve this nonlinear problem, a numerical description is crucial. And if one attempts to simulate ICRF scenarios numerically, a self-consistent algorithm has to be found, such that the interconnections between fields and distribution function can be resolved. Several such numerical schemes have been developed, each with its specialisations, advantages and, necessarily, deficiencies. Many research groups have concentrated on the accurate development of the wave computations, neglecting some of the essential particle orbit effects. For example, the full-wave code TORIC[23,24,25] has been developed to include higher order Finite Larmor Radius (FLR) effects and can be applied to mode conversion scenarios and heating at higher harmonic frequencies, ($\omega = n\Omega$ with $n \geq 1$). It has then been coupled to the Fokker-Planck code SSFPQL[26,27,28] for advancing the distribution function. The Fokker-Planck approach, however, assumes zero orbit widths, and is therefore a very restricted model as we will see in this thesis. A similar approach is the coupling of the wave code AORSA,[29,30,31] where all orders in FLR are included, to the Fokker-Planck code CQL3D.[32] Again, the wave code is very developed, but the zero orbit width approximation in the Fokker-Planck code is an important limitation. Accepting this, a new package has been developed very recently, coupling AORSA to the guiding centre orbit following code ORBIT-RF.[33] In this new package, full harmonic ICRF can be modelled, and finite orbit width effects included. Ref. 34 reports on the achievement of two iterations for a complete simulation of about one slowing down time, which, depending on the chosen scenario, is not enough in both number of iterations and total simulation time, as will we show here. Also, the RF induced particle pinch, as discussed in Sec. 6.2.2, is not included since no change in parallel velocity due to wave-particle interactions is included. A slightly different approach has been adopted when coupling the wave code LION[35,36] to the orbit averaged Monte Carlo code FIDO,[37,38] giving the code package SELFO.[39,40,41,10] LION includes higher harmonic resonances, and FIDO full orbit effects. The distribution function evolution is simulated including full particle orbit effects and is described in the frame of the three constants of motion in an axisymmetric torus. However, the guiding centre orbits are not

followed in real space, but an orbit averaged scheme is implemented, allowing for much lighter and thus faster computation. SELFO is based on fully centered and circular flux surfaces, thus neglecting shaping and pressure effects like Shafranov shift.

Recalling the discussion in Sec. 2.3 about the different possibilities of solving the Boltzmann equation in the presence of radio frequency fields, we feel that a drift kinetic description, including finite orbit width effects, constitutes an adequate approach for integrated modelling of ICRH heating. Neglecting finite orbit widths represents a severe restriction to the applicability of such a model, whereas more sophisticated models such as gyrokinetic or full Lorentzian approaches provide a small improvement in the physics description compared to the much higher cost in terms of computational resources needed.

All of the above mentioned codes are built for 2D axisymmetric tokamaks. Even in a tokamak, the toroidal magnetic field is not exactly axisymmetric in reality, since the magnetic coils are not perfect, and not continuous around the torus, as already shown in Fig. 2.2. The resulting so-called magnetic ripple can have effects like toroidal trapping of particles etc., which cannot be considered in these codes. Also, more advanced geometries without Ohmic currents, so-called stellarators, have a fully developed three dimensional structure. If we want to be able to study ICRH in such geometries, we need codes which are built for non-axisymmetric plasmas. One code package consisting of the wave code TASK/WM[42] and the drift-kinetic code GNET[43,44] has been developed for the Large Helical Device (LHD), which is a three dimensional stellarator. Here, finite orbit width effects are included, but the dielectric tensor is based on the the cold approximation,[45,46,47] which does not include warm effects such as the Doppler broadened resonance.

If we apply ICRF to a given plasma, we do this with the aim of changing at least the resonant minority's distribution function, either creating a hot tail (heating, ICRH) or asymmetries with respect to the sign of the parallel velocity (current drive, ICCD) or both. In any case, ICRF is applied to induce a change. If the applied power is sufficiently high, the (mainly perpendicular) temperature of the resonant species will rise considerably and might have the effect that the minority pressure (again, mainly perpendicular) becomes important in the equilibrium computations, i.e. a change in magnetic equilibrium may be the result of the applied heating. Furthermore, if the RF induced current is important enough, the safety factor profile, and thus the magnetic shear defined as the radial safety factor derivative, can change sufficiently to displace e.g. the $q = 1$ surface to move out of the resonance layer, which is important for sawtooth control. In both cases, the magnetic equilibrium can be changed and it is therefore important to re-evaluate it during the simulation. Additionally to a shift of the $q = 1$ surface, a changed equilibrium can have the effect that the resonant layer, where the RF power is absorbed, moves in real space due to variations in magnetic field strength (in turn due to increased pressure), and particle orbits can change drastically, if e.g. a magnetic well develops and particles become trapped and describe non-standard orbits[48] (see Sec. 8.2).

It is therefore important to account for the effects of applied RF power not only on the distribution function of the resonant plasma species, and thus the dielectric tensor, but also on the equilibrium. But once the equilibrium and/or the wave field change, the distribution function of the heated species will change again, inducing further change in equilibrium and wave field and so on. These non-linear effects can best be included in

a numerical model using an iterated scheme, taking into account all changes due to the applied power, and finding in that way a self-consistent solution of the chosen heating scenario, including equilibrium, dielectric tensor and distribution function. This is the philosophy we have chosen to pursue in this thesis by developing the new 3D self-consistent ICRH code package SCENIC, where we couple the MHD equilibrium code VMEC[49] to the full-wave code LEMan[2] and the guiding centre orbit code VENUS.[3] As opposed to most of the other existing code packages, the emphasis lies on correctly dealing with the orbits of highly energetic orbits in three dimensions, and on the self-consistent generation of the equilibrium. The limiting component is the wave code LEMan, which does not include FLR effects. We will therefore be limited to fundamental minority heating scenarios. It is important to note that within these scenarios where no mode conversion occurs, the model is very extensive and accurate as we will show in what follows. We will start by describing SCENIC in the next part containing Chapters 4 to 7.

SCENIC: Self-Consistent Ion Cyclotron

After introducing the subject, we will now turn to a basic description of the numerical model. The new code package SCENIC has been created for self-consistent simulations. Here, a converged result corresponds to a steady state, where the input RF power absorbed by a heated minority species equals the power lost to the background plasma. Self-consistency is achieved by updating the equilibrium and wave field a number of times during the simulation, such that mutual effects between the wave field and equilibrium can be included. Fig. 3.1 shows a schematic view of the code package. The three compo-
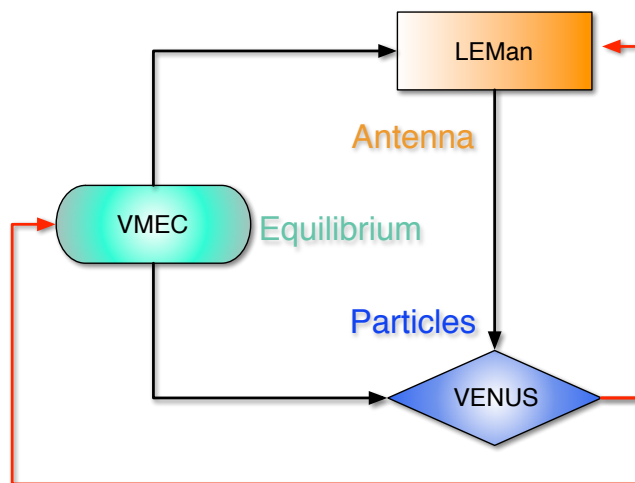

Figure 3.1.: Schematic view of the code package SCENIC. Black arrows show dependencies for one iteration, red arrows the re-creation of new inputs for the following iteration.

nents will be described in the following chapters. The discussion of VMEC and LEMan will be rather brief because they have been developed and described mainly elsewhere (except the new features involving anisotropy in LEMan), whereas most of the numerical development of this thesis was concentrated on VENUS, and thus the section devoted to its description will be somewhat longer.

4. VMEC: Equilibrium

The plasma equilibrium is determined by a fixed boundary version of VMEC, which includes an anisotropic hot particle pressure. This version is described in detail in Refs. 50 and 49, and we will only describe the features which are important for this thesis. VMEC uses Boozer coordinates (s, θ, φ), where the radial coordinate s has been introduced in Eq. (2.9), and the poloidal and toroidal angles (θ, φ) are chosen such that the magnetic field lines describe straight lines in that particular set of variables. VMEC is based on magnetohydrodynamics (MHD) as described in Sec. 2.1.2 and finds magnetic equilibria with nested flux surfaces (no magnetic islands) by minimising the energy functional, Eq. (2.26). Within the description, two fluids are included, one with an isotropic pressure $p(s)$ and temperature $T(s)$, which is based on a Maxwellian distribution. For this thermal species, pressure and density are flux surface quantities. The second fluid represents the hot, anisotropic species, with the pressure as defined in Eq. (2.17b). Here, the underlying distribution function includes two different temperature profiles parallel ($T_\parallel$) and perpendicular ($T_\perp$) to the magnetic field. From the Vlasov equation (2.51) one can show that any equilibrium distribution function f has to satisfy $\mathbf{B} \cdot \nabla f = 0$ to lowest order in Larmor radius. Now, if we were to consider a pure bi-Maxwellian of the form $\exp\left[-mv_\perp^2/2T_\perp - mv_\parallel^2/2T_\parallel\right]$, it would violate that condition, since the perpendicular and parallel velocities depend on the magnetic field strength as described in Sec. 2.2.2 and Eq. (2.33). It has been shown, e.g. in Ref. 21, that such a simple bi-Maxwellian has important deficiencies if applied to RF heating scenarios. It is therefore imperative to find another form of the bi-Maxwellian. If we recall that we will be interested in ICRH, where the cold resonance is defined by a layer of one given value of magnetic field strength, we can introduce a constant value of the magnetic field B_c, along which the (cold) resonance will take place. The second requirement for a distribution function is that it shall be written in terms of constants of motion. For unperturbed orbits, three constants are the energy $E = mv^2/2$, the magnetic moment $\mu = mv_\perp^2/2B$ and the orbit averaged radial position $\bar{s}$. Note that we do not use the toroidal momentum P_φ since this is not a constant of motion if the axisymmetry along φ is broken, e.g. in a stellarator. We can then replace $mv_\perp^2/2 \rightarrow mv_\perp^2 B_c/2B = \mu B_c$ and $v_\parallel^2 = 2m(E - \mu B) \rightarrow 2m|E - \mu B_c|$. Note that for the last term, the absolute value has to be taken, since the term can go negative, depending on B_c/B. Finally, our bi-Maxwellian model, which satisfies the Vlasov equation and

represents a good model for anisotropic plasmas,[22,51] reads

$$F_h(\bar{s}, E, \mu) = \mathcal{N}(\bar{s}) \left(\frac{m_h}{2\pi T_\perp(\bar{s})} \right)^{3/2} \exp\left[-m_h \left(\frac{\mu B_c}{T_\perp(\bar{s})} + \frac{|E - \mu B_c|}{T_\parallel(\bar{s})} \right) \right] \qquad (4.1)$$

The great advantage of writing F_h in terms of the orbit averaged radial position $\bar{s}$ is that in this way, F_h includes finite orbit width effects, as we will see later in this thesis. Recalling the orbit width discussion from Sec. 2.2.2, we define the average radial position by

$$\bar{s} \equiv \frac{\int s(t)\mathrm{d}t}{\int \mathrm{d}t}, \qquad (4.2)$$

where the integral is performed over one complete unperturbed poloidal orbit. Especially for trapped particles, this temporal average is equivalent to a weighted spatial average, where the turning points are more heavily weighted than the inner and outer legs of the orbit, since the velocity vanishes and the particle spends more time at those points than on any other point along the orbit. Thus, for trapped particles, $\bar{s} \approx s(\theta_b)$, with the turning points at $\theta = \theta_b$, whereas for passing particles, $\bar{s} \approx s(\theta = \pi/2)$. This corresponds to some of the considerations in Sec. 2.2.2, in particular Eqs. (2.42), (2.47), (2.48) and Fig. 2.8.

A very important property of this particular distribution function is that the moments of the distribution function, i.e. the macroscopic quantities like pressure and density, can be obtained analytically in terms of B and other relevant parameters.[51] These moments are no longer flux surface quantities but functions of the radial variable $\bar{s}$ and the magnetic field strength B. In a 2D configuration like an axisymmetric tokamak, this description is equivalent to using $(\bar{s}, \theta)$. But since VMEC is capable of dealing with more complicated 3D geometries, B is more general. The density-like amplitude factor $\mathcal{N}$ is linked to the physical hot particle density n^h through

$$n^h(\bar{s}, B) = \mathcal{N}(\bar{s}) \sqrt{\frac{T_\parallel}{T_\perp}} \mathcal{C}(\bar{s}, B), \qquad (4.3a)$$

with

$$\mathcal{C}(\bar{s}, B) = \begin{cases} \frac{B/B_c}{1 - T_\perp/T_\parallel(1 - B/B_c)} & , B > B_c \\ 1 & , B = B_c \\ \frac{B}{B_c} \frac{1 + T_\perp/T_\parallel(1 - B/B_c) - 2\left[T_\perp/T_\parallel(1 - B/B_c)\right]^{3/2}}{1 - \left[T_\perp/T_\parallel(1 - B/B_c)\right]^2} & , B < B_c \end{cases} \qquad (4.3b)$$

The total parallel and perpendicular pressures $p_\parallel$, $p_\perp$ are (where $p(\bar{s})$ denotes the thermal pressure)

$$p_\parallel(\bar{s}, B) = p(\bar{s}) + \mathcal{N}(\bar{s}) T_\parallel(\bar{s}) H(\bar{s}, B) \qquad (4.4a)$$

with

$$H(\bar{s}, B) = \begin{cases} \frac{B/B_c}{1-T_\perp/T_\parallel(1-B/B_c)} & , B > B_c \\ 1 & , B = B_c \\ \frac{B}{B_c}\frac{1+T_\perp/T_\parallel(1-B/B_c)-2\left[T_\perp/T_\parallel(1-B/B_c)\right]^{5/2}}{1-\left[T_\perp/T_\parallel(1-B/B_c)\right]^2} & , B < B_c, \end{cases} \qquad (4.4b)$$

and

$$p_\perp(\bar{s}, B) = p_\parallel(\bar{s}, B) + B \left.\frac{\partial p_\parallel}{\partial B}\right|_s. \qquad (4.4c)$$

Now, we introduce the hot parallel pressure amplitude $p_h(\bar{s})$, such that

$$\mathcal{N}(\bar{s})T_\parallel(\bar{s}) = p(\bar{s})p_h(\bar{s}) \qquad (4.5)$$

and from (4.4a), the hot parallel pressure reads

$$p_\parallel^h(\bar{s}, B) = p(\bar{s})p_h(\bar{s})H(\bar{s}, B) \qquad (4.6)$$

The input profiles for VMEC are now the flux surface quantities $p(\bar{s}), p_h(\bar{s}), T_\perp/T_\parallel(\bar{s}), B_c$ and either the total toroidal current enclosed in a given flux surface $J(\bar{s})$ or the inverse safety factor $\iota(\bar{s}) = 1/q$. Two omnipresent quantities related to pressure anisotropy are the in Eq. (2.19b) already introduced σ and

$$\tau \equiv \left.\frac{\partial(\sigma B)}{\partial B}\right|_s = 1 + \frac{\mu_0}{B}\left.\frac{\partial p_\perp}{\partial B}\right|_s. \qquad (4.7)$$

These quantities will appear e.g. in the equations of motion (6.4). In the equilibrium, they are useful to monitor the firehose and the mirror stability criteria[6] $\sigma > 0$ and $\tau > 0$. If one or both of them are negative, the determined equilibrium from VMEC should not be considered physical. Especially if $\tau < 0$, the equilibrium problem is no longer elliptic.[4] Note that in the isotropic limit $T_\perp = T_\parallel$, $\tau = \sigma = 1$.

The equilibrium is of course the basis of the numerical model. VMEC's output is read by both LEMan and VENUS and the scenario is almost completely chosen by fixing the inputs for VMEC. Indeed, with the choice of the critical magnetic field B_c, even the location of the resonant layer is defined by $R_c = B_0 R_0/B_c$ in the large aspect ratio approximation. The only other free parameters left are the minority species (i.e. its mass and charge), the toroidal wave spectrum and the deposited power. B_c, the mass and the charge of the minority species then define the antenna frequency through $\omega = qB_c/m$. Fig. 4.1 shows symbolically VMEC's role in the package: define the plasma geometry and the magnetic equilibrium. Fig. 4.2 shows three example outputs in poloidal plots. The magnetic field strength as shown in Fig. 4.1, and the perpendicular pressure for two different scenarios, one with the resonant layer (white line) on the high field side of the magnetic axis (Fig. 4.2(b)) and one with the resonant layer on the low field side of the magnetic axis (Fig. 4.2(c)). For the latter two plots an anisotropy of $T_\perp/T_\parallel = 10$ was assumed.

The first component of the package is introduced, and we will now turn to the second input required by VENUS, the radio frequency wave field.
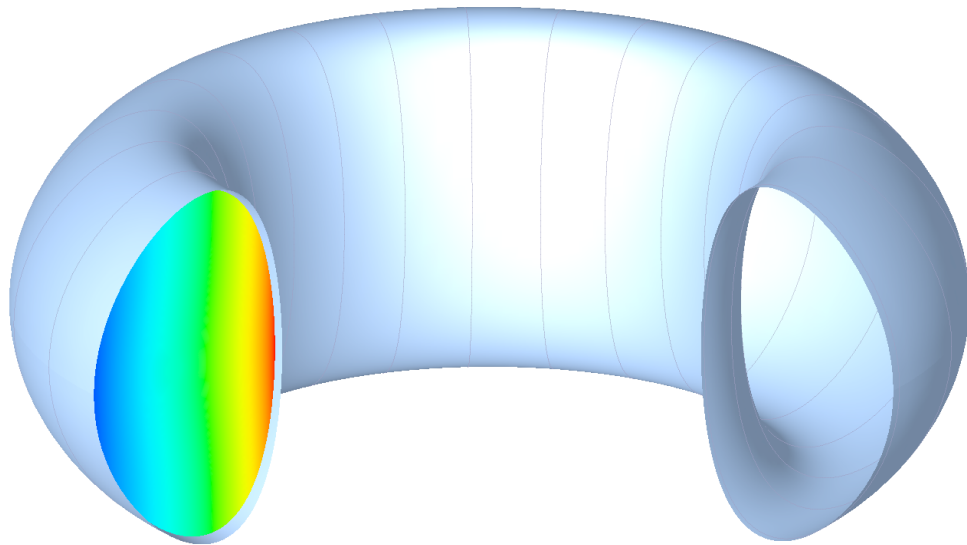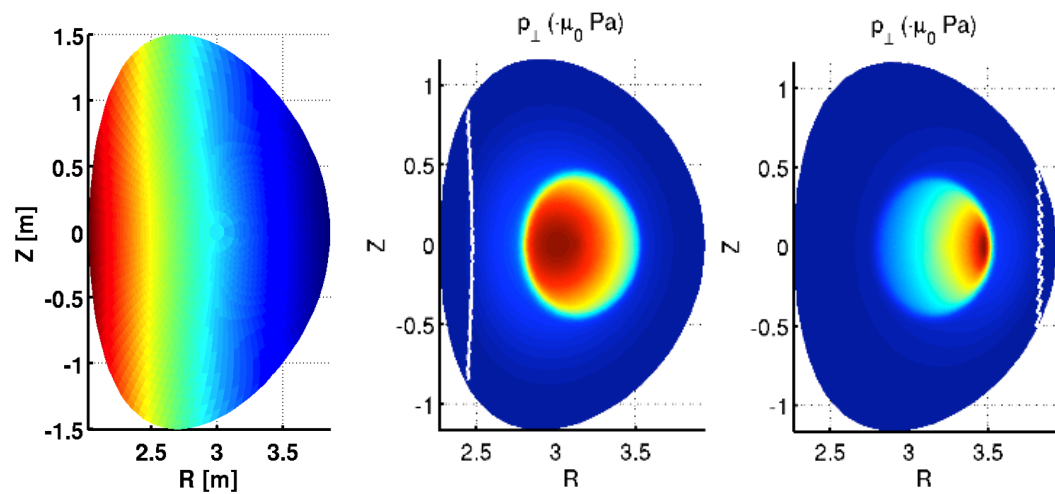
Figure 4.1.: VMEC computes the equilibrium, and is thus defining the machine we are looking at, and to a large extent even the complete simulated scenario. The poloidal cut to the left shows the magnetic field strength.

(a) Magnetic field strength B.

(b) $P_\perp$ for a high field side resonance ($B_c > B_0$, white line).

(c) $P_\perp$ for a low field side resonance ($B_c < B_0$, white line).

Figure 4.2.: Main VMEC outputs: 3D Magnetic field and pressures, constructed from the input profiles and external plasma shape. We show here examples of perpendicular pressure, once for $B_c > B_0$ and once for $B_c < B_0$.

5. LEMan: Radio frequency wave field

The Low-frequency ElectroMagnetic wave propagation code was initially developed for the study of Alfvén wave propagation computations.[2] Recently, it has been extended to work in the ion cyclotron range of frequencies,[52] including a hot dielectric tensor based on the bi-Maxwellian (4.1) model employed here.[53] The derivation of the latter is part of this thesis, and we will therefore start this chapter giving its analytical expression. For the Monte Carlo operators implemented in VENUS, the parallel and perpendicular wave numbers have to be passed from LEMan to VENUS. This computation had to be added specifically for SCENIC. Although the parallel wave number is used in LEMan, it is not the same definition of $k_\parallel$ which is needed in VENUS, and $k_\perp$ is not present at all in LEMan. This is why we will describe the form of these wave numbers in this chapter before moving on to the description of VENUS.

5.1. Dielectric tensor

In principle, we can find the dielectric tensor by finding the distribution function f solving the Vlasov equation (2.51), integrating the function for finding the current, solving for the conductivity using $\mathbf{j} = \sigma \cdot \mathbf{E}$ and finally the dielectric tensor using (2.63). Then, once we found the dielectric tensor, we can find the electric field solving the wave equation (2.58). There is, however, a problem: The solution of the distribution function depends on the electric field in the first place. In order to solve this problem, one either has to implement a self-consistent calculation just for finding the electric field, or one assumes a certain distribution function and can then solve for the dielectric tensor and the electric field accordingly. Since the equilibrium is already based on the bi-Maxwellian distribution function F_h given in Eq. (4.1), and our numerical model already is rather sophisticated and computationally demanding, the second possibility seems by far the more appropriate.

Following Refs. 54 and 55, we have derived the dielectric tensor for the fast particles modelled by the distribution function (4.1) to zeroth order in both $\epsilon_e = \rho_L/L$ and $\epsilon_p = \rho_L/\lambda_\perp$, where ρ_L is the Larmor radius defined in Eq. (2.31), L a characteristic length scale of the stationary plasma and $\lambda_\perp$ a characteristic wave length of the perturbing electromagnetic field in the direction perpendicular to the equilibrium magnetic field. An example of the detailed calculations can be found in Appendix A and we will give here only the final expressions, which are different for $B \geq B_c$ and $B < B_c$. They read

- For $B \geq B_c$:

$$\mathcal{E}_{nn} = 1 - \frac{1}{2\omega} \frac{\sqrt{T_\parallel/T_\perp}}{C_+} \sum_k (\tilde{Z}_1^\parallel + \tilde{Z}_{-1}^\parallel) \tag{5.1aa}$$

$$\mathcal{E}_{nb} = -\frac{i}{2\omega} \frac{\sqrt{T_\parallel/T_\perp}}{C_+} \sum_k (\tilde{Z}_1^\parallel - \tilde{Z}_{-1}^\parallel) = -\mathcal{E}_{bn} \tag{5.1ab}$$

$$\mathcal{E}_{\parallel\parallel} = 1 + \frac{2}{(k_\parallel v_{\parallel T})^2} \frac{\sqrt{T_\parallel/T_\perp}}{C_+} \sum_k \left(\tilde{\omega}_p^2 - \omega \tilde{Z}_0^\parallel \right), \tag{5.1ac}$$

- For $B < B_c$:

$$\mathcal{E}_{nn} = \mathcal{E}_{nn}^{B \geq B_c} - \frac{1}{2\omega} \frac{C_+ - C_-}{C_+ C_-} \sum_k (\tilde{Z}_1^\perp + \tilde{Z}_{-1}^\perp) \tag{5.1ba}$$

$$\mathcal{E}_{nb} = \mathcal{E}_{nb}^{B \geq B_c} - \frac{i}{2\omega} \frac{C_+ - C_-}{C_+ C_-} \sum_k (\tilde{Z}_1^\perp - \tilde{Z}_{-1}^\perp) = -\mathcal{E}_{bn} \tag{5.1bb}$$

$$\mathcal{E}_{\parallel\parallel} = \mathcal{E}_{\parallel\parallel}^{B \geq B_c} - \frac{C_+ + C_-}{C_+ C_-} \sum_k \left(\sqrt{\frac{B_c - B}{B_c}} \tilde{\omega}_p^2 - \omega \tilde{Z}_0^\perp \right), \tag{5.1bc}$$

Here, $v_{\parallel T}^2 = 2T_\parallel/m$ is the fast particles' thermal parallel velocity and

$$C_\pm = \frac{B_c}{B} \pm \frac{T_\perp}{T_\parallel} \left(1 - \frac{B_c}{B} \right) \tag{5.2a}$$

$$Z^{Sh}(z) = \frac{z}{\sqrt{\pi}} \int_{-\infty}^\infty \frac{1}{z-x} e^{-x^2} \mathrm{d}x, \qquad \mathrm{Im}\, z > 0 \tag{5.2b}$$

$$\tilde{Z}_l^\parallel = \frac{\tilde{\omega}_p^2}{\omega - l\Omega_c} Z^{Sh} \left(\frac{\omega - l\Omega_c}{k_\parallel v_{\parallel T}} \right) \tag{5.2c}$$

$$\tilde{Z}_l^\perp = \sqrt{\frac{B_c - B}{B_c}} \frac{\tilde{\omega}_p^2}{\omega - l\Omega_c} Z^{Sh} \left(\sqrt{\frac{B_c}{B_c - B}} \frac{\omega - l\Omega_c}{k_\parallel v_{\parallel T}} \right), \tag{5.2d}$$

and $\tilde{\omega}_p^2 = Q_k^2 \mathcal{N}_k / \epsilon_0 m_k$ the plasma frequency of species k. The subscripts n, b and $\parallel$ denote the normal, bi-normal and parallel components relative to the magnetic field. In addition to the discussion in Ref. 53, we can highlight a few observations: First of all, one can see that we exactly recover the zeroth order results obtained in Refs. 55 and 54 (Maxwellian distribution) in the limit where $T_\perp/T_\parallel \to 1$ and $B_c \to 0$ (i.e. $F_h \to F_M$). However, the additional parameter B_c in the distribution function has the effect that, even if we consider the isotropic case $T_\perp = T_\parallel$, some of the additional terms proportional to B_c ($\neq 0$) do not vanish and introduce poloidally dependent corrections to the dielectric tensor. This reflects the speciality of ICRF interactions, where the resonance lies mainly along

one layer of constant major radius, and thus cuts through the flux surfaces. This naturally introduces poloidal dependences. Finally, the plasma frequency $\tilde{\omega}_p$ in expressions (5.2) does not involve the physical density but rather the density factor $\mathcal{N}(s)$ defined in the distribution function (4.1) and related to the physical density through Eq. (4.3), which can be considerably higher than the physical density if $T_\perp / T_\parallel \gg 1$.

5.2. Wave numbers for VENUS

Besides the wave field, parallel and perpendicular wave numbers have to be passed to VENUS for the quasilinear diffusion coefficients. The perpendicular wave number is not used in any of the computations of LEMan. But also the parallel wave number passed to VENUS does not necessarily coincide with the parallel wave number determined for the internal computations of LEMan. In the latter, an iterative method assures that the consistent parallel wave number is computed for every toroidal and poloidal mode pair, and all modes present in the plasma are treated correctly.[53,56] In contrast, the Monte Carlo operators in VENUS, simulating the wave-particle interactions and described in the next Chapter, are derived for the interaction of one wave with one value for $k_\parallel$ and $k_\perp$ for each toroidal mode number n_φ (including all poloidal modes) in the axisymmetric case, or for the complete toroidal and poloidal mode spectrum in the three dimensional case. We will therefore have to find equivalent wave numbers which represent the complete wave field present in the plasma, but take only one value at one given place in real space. In many numerical codes, the solution of the problem is simply to neglect the poloidal modes for one given toroidal mode, and approximate the parallel wave number by $k_\parallel \approx n_\varphi / R$. This may be an acceptable approximation in a 2D geometry like a tokamak, where the different toroidal modes decouple and can therefore be treated independently. But, if the condition $n_\varphi \gg mq$ (with m the poloidal mode and q the safety factor) does not hold, this approximation has its deficiencies. In SCENIC, we not only want to be able to treat 3D cases, but we also want to include the so-called upshift, which is the correction to the parallel wave vector due to poloidal modes. If we recall that the wave vector $\mathbf{k}$ in the dispersion relation corresponds to a differential operator (in Fourier space), we can find a form of $k_\parallel$ and $k_\perp$ which is closer to its original nature. We adopted in this thesis the solution that we directly differentiate the scalar potential for finding the wave numbers. The derivation of the new relations for finding the parallel and perpendicular wave numbers is given in Appendix B. The final form of the parallel wave number passed to the Monte Carlo operators in VENUS reads

$$|k_\parallel| = \left| \frac{1}{\chi B \sqrt{g}} \left(\psi' \frac{\partial \chi}{\partial \theta} + \Phi' \frac{\partial \chi}{\partial \varphi} \right) \right|. \tag{5.3a}$$

$\sqrt{g}$ is the Jacobian and g^{ss} the first metric element. I and J are the poloidal and toroidal current fluxes, the prime denotes the derivative with respect to the radial variable s, and all other notations are as defined earlier in this thesis. For $k_\parallel$, only derivatives with respect to the poloidal and toroidal angles are present. Thus, for every toroidal and poloidal mode pair, a parallel wave number can be computed at the end of each LEMan sim-

ulation, by directly differentiating the corresponding scalar potential. Then, a weighted summation over all modes (again, for axisymmetric cases over all poloidal modes for one given toroidal mode), where the weight of each mode is proportional to the corresponding Fourier amplitude, is performed, yielding one mean parallel wave number. As for the parallel wave number, we have derived a new way of determining the perpendicular wave number based on differentiating the scalar potential χ. The details of the computation are given in Appendix B as well, and the perpendicular wave number passed from LEMan to VENUS is

$$|k_\perp|^2 = \left| g^{ss} \left(\frac{1}{\chi} \frac{\partial \chi}{\partial s} \right) \right|^2 + \left| \frac{1}{g^{ss}} \left[\frac{1}{\chi \sigma B \sqrt{g}} \left(\mu_0 J \frac{\partial \chi}{\partial \varphi} + \mu_0 I \frac{\partial \chi}{\partial \theta} \right) \right] \right|^2. \qquad (5.3b)$$

Note that due to the radial derivative in this relation, it is not possible to perform an average over all modes as for the parallel wave number. Here, we perform the differentiation once on the complete scalar potential, thus finding an effective perpendicular wave number for the total wave field in the plasma. Most other codes determine $k_\perp$ with the dispersion relation for the fast magnetosonic wave,

$$\omega^2 = \frac{k^2}{2} \left[v_s^2 + v_A^2 + \sqrt{\left(v_s^2 + v_A^2 \right)^2 + 4 v_s^2 v_A^2 \cos^2 \theta} \right], \qquad (5.4)$$

with the sound speed $v_s^2 = \gamma p / \rho$, where $\gamma = 5/3$, p is the pressure and ρ the mass density. The Alfvén velocity is defined by $v_A^2 = c^2 / (1 + \omega_{pi}^2 / \Omega_i^2) \approx B / (\mu_0 n_i m_i)$, where c is the speed of light, ω_p the plasma frequency, and subscript i denotes the background ions. θ is the angle spanned between the magnetic field and the total wave vector, such that $k_\parallel^2 = k^2 \cos^2 \theta$. As this dispersion relation is an approximation, the value for $k_\perp$ cannot be precise, and it is even possible that $k_\perp^2 < 0$ due to the approximations made. Therefore, the form of the wave numbers given in Eqs. (5.3) are implemented for passing $k_\parallel$ and $k_\perp$ to the Monte Carlo operators in VENUS. With the wave code added to the numerical model, we have now not only an equilibrium, but also the means of heating the plasma and deposit power coming from radio frequency field. The artist's view is given in Fig. 5.1 and a representation of the newly added information in Fig. 5.2 All that is left to add is a means of computing the change of the minority distribution function as a result of the applied heating and the slowing down on the background plasma. This is what we will describe next in the chapter about VENUS.
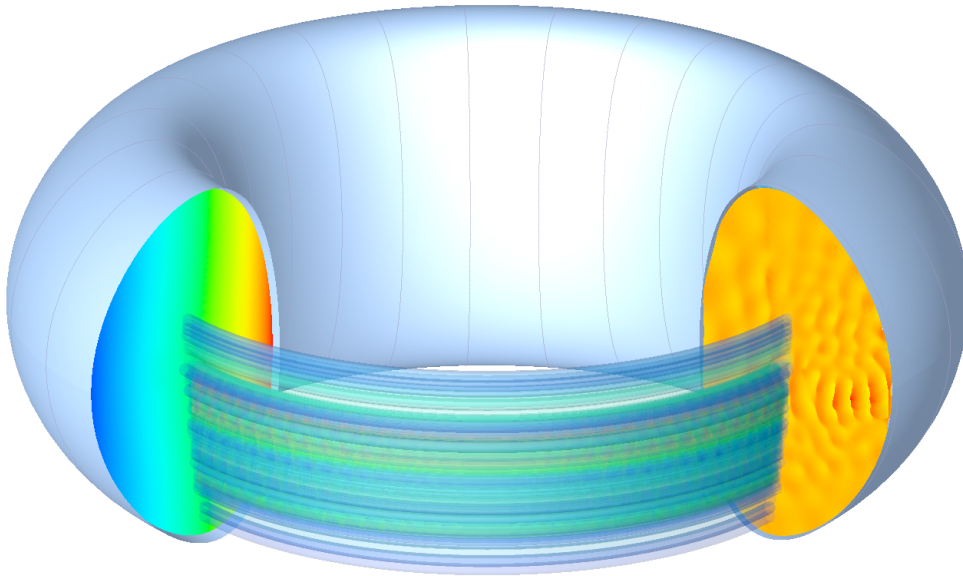
Figure 5.1.: LEMan adds the radio frequency field to the equilibrium defined by VMEC. Shown is the torus as in Fig. 4.1 with the additional 3D power deposition and $\Re(E^+)$ computed by LEMan.
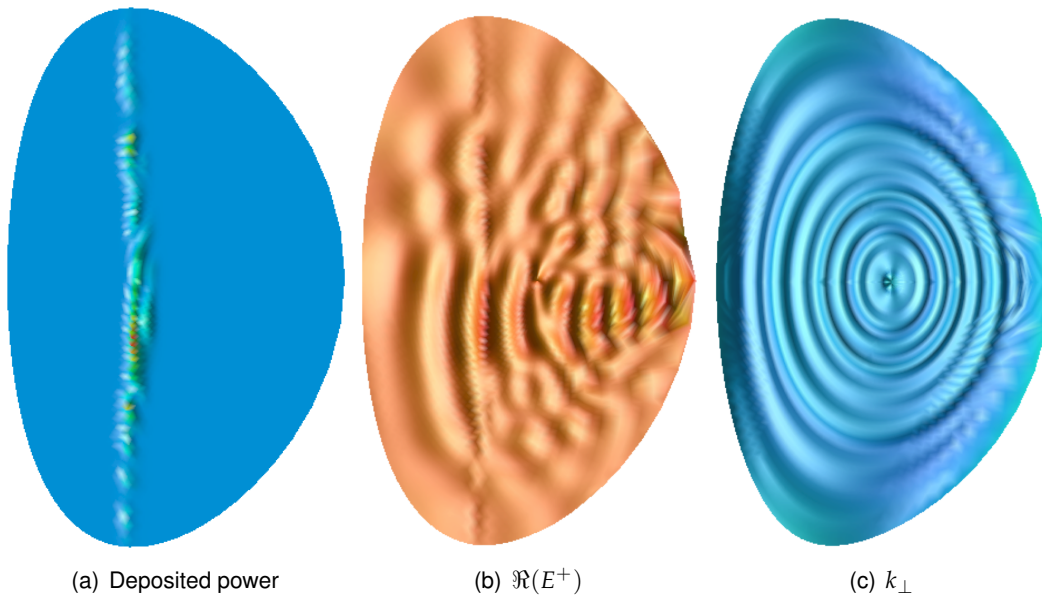

(a) Deposited power   (b) $\Re(E^+)$ (c) $k_\perp$

Figure 5.2.: LEMan computes the deposited power, wave fields E^+ and E^- and the wave vectors $k_\perp$ and $k_\parallel$ for VENUS' Monte Carlo operators. As described in Sec. 2.4.1, the left handed electric field E^+ has a local minimum along the resonant layer, and the maximum power deposition is therefore slightly to the high field side (left) of the cold resonance.

6. VENUS

Most of the work of this thesis was devoted to further developing the single particle Hamiltonian code VENUS. It has initially been developed as a transport δf code[3] and was transformed into a full-f ICRH code for this thesis. Thus, the particle loading had to be changed, the equations of motion have been extended for including additional terms derived in Ref. 17, Monte Carlo operators for the wave-particle interaction were added as well as statistics modules for the integration of the distribution function and for the creation of new inputs to VMEC and LEMan for the iterated scheme. We will in this chapter describe the workings of VENUS during the temporal integration of the particle orbits, whereas the statistics modules will be dealt with in the next chapter.

6.1. Equations of motion

The equations of motion are based on a Hamiltonian formulation of the orbits of charged particles in an electromagnetic field. They have been derived in Refs. 17 and 4 and only the main results will be shown here. For guiding centre particles, the relativistic drift Hamiltonian (written for Boozer coordinates) reads

$$H = \gamma m_0 c^2 + Q\chi(s, \theta, \varphi, t), \tag{6.1}$$

where, as always, Q and m_0 is the particles charge and rest mass, c the speed of light and χ is the electrostatic potential. Denoting the magnetic moment μ and the momentum parallel to the magnetic field $P_\parallel$, we can write γ as

$$\gamma = \sqrt{1 + \frac{2\mu B}{m_0 c^2} + \frac{P_\parallel^2}{m_0^2 c^2}}. \tag{6.2}$$

Note that for our simulations of ions, relativistic corrections are negligible and the Hamiltonian is $H = 2\mu B + P_\parallel^2 + Q\chi$. The equations of motion are, however, also valid for (relativistic) electrons, and we show therefore the general form of the equations of motion. In the vector potential, we can deal with a parallel perturbation, Υ, and still retain the

canonical structure of the variables. We thus write

$$\mathbf{A} = \Phi(s)\nabla\theta - \psi(s)\nabla\varphi + \Upsilon\sigma\mathbf{B},\tag{6.3}$$

with the standard notations of this thesis. For practical reasons, the equations of motion are not written in terms of the canonical variables $(\theta, \varphi, P_\theta, P_\varphi)$ but in terms of $(s, \theta, \varphi, \rho_\parallel)$, where we introduced the parallel gyroradius $\rho_\parallel = P_\parallel/(Q\sigma B)$:

$$\dot{s} = +\frac{\mu_0 I(s)}{D}\left[\left.\frac{\partial\chi}{\partial\theta}\right|_{s,\varphi,t} + \frac{1}{\gamma}\left(\frac{\mu}{Q} + \sigma\tau\Omega_0\rho_\parallel^2\right)\frac{\partial B}{\partial\theta} - \frac{\Omega_0}{\gamma}\sigma^2 B\rho_\parallel\left.\frac{\partial\Upsilon}{\partial\theta}\right|_{s,\varphi,t}\right]$$

$$+\frac{\mu_0 J(s)}{D}\left[\left.\frac{\partial\chi}{\partial\varphi}\right|_{s,\theta,t} + \frac{1}{\gamma}\left(\frac{\mu}{Q} + \sigma\tau\Omega_0\rho_\parallel^2\right)\frac{\partial B}{\partial\varphi} - \frac{\Omega_0}{\gamma}\sigma^2 B\rho_\parallel\left.\frac{\partial\Upsilon}{\partial\varphi}\right|_{s,\theta,t}\right]\tag{6.4a}$$

$$\dot{\theta} = -\frac{\mu_0 I(s)}{D}\left[\left.\frac{\partial\chi}{\partial s}\right|_{\theta,\varphi,t} + \frac{1}{\gamma}\left(\frac{\mu}{Q} + \sigma\tau\Omega_0\rho_\parallel^2\right)\frac{\partial B}{\partial s} + \frac{\Omega_0}{\gamma}\sigma B\rho_\parallel^2\left.\frac{\partial\sigma}{\partial s}\right|_B\right]$$

$$+\frac{\Omega_0\sigma^2 B}{\gamma D}\rho_\parallel\left[\psi'(s) + (\rho_\parallel + \Upsilon)\mu_0 I'(s) + \mu_0 I(s)\left.\frac{\partial\Upsilon}{\partial s}\right|_{\theta,\varphi,t}\right]$$

$$+\frac{\Omega_0\sigma^2 B}{\gamma D}\rho_\parallel(\rho_\parallel + \Upsilon)\frac{\partial(\sigma B_s)}{\partial\varphi}$$

$$-\frac{\sigma B_s}{D}\left[\frac{\partial\chi}{\partial\varphi} + \frac{1}{\gamma}\left(\frac{\mu}{Q} + \Omega_0\sigma\tau\rho_\parallel^2\right)\frac{\partial B}{\partial\varphi} - \frac{\Omega_0}{\gamma}\sigma^2 B\rho_\parallel\frac{\partial\Upsilon}{\partial\varphi}\right]\tag{6.4b}$$

$$\dot{\varphi} = -\frac{\mu_0 J(s)}{D}\left[\left.\frac{\partial\chi}{\partial s}\right|_{\theta,\varphi,t} + \frac{1}{\gamma}\left(\frac{\mu}{Q} + \sigma\tau\Omega_0\rho_\parallel^2\right)\frac{\partial B}{\partial s} + \frac{\Omega_0}{\gamma}\sigma B\rho_\parallel^2\left.\frac{\partial\sigma}{\partial s}\right|_B\right]$$

$$+\frac{\Omega_0\sigma^2 B}{\gamma D}\rho_\parallel\left[\Phi'(s) + (\rho_\parallel + \Upsilon)\mu_0 J'(s) + \mu_0 J(s)\left.\frac{\partial\Upsilon}{\partial s}\right|_{\theta,\varphi,t}\right]$$

$$-\frac{\Omega_0\sigma^2 B}{\gamma D}\rho_\parallel(\rho_\parallel + \Upsilon)\frac{\partial(\sigma B_s)}{\partial\theta}$$

$$+\frac{\sigma B_s}{D}\left[\frac{\partial\chi}{\partial\theta} + \frac{1}{\gamma}\left(\frac{\mu}{Q} + \Omega_0\sigma\tau\rho_\parallel^2\right)\frac{\partial B}{\partial\theta} - \frac{\Omega_0}{\gamma}\sigma^2 B\rho_\parallel\frac{\partial\Upsilon}{\partial\theta}\right]\tag{6.4c}$$

$$\dot{\rho}_\parallel = - \left. \frac{\partial \Upsilon}{\partial t} \right|_{s,\theta,\varphi}$$

$$- \frac{1}{D} \left[\psi'(s) + (\rho_\parallel + \Upsilon)\mu_0 I'(s) + \mu_0 I(s) \left. \frac{\partial \Upsilon}{\partial s} \right|_{\theta,\varphi,t} \right] \left[\left. \frac{\partial \chi}{\partial \theta} \right|_{s,\varphi,t} + \frac{1}{\gamma} \left(\frac{\mu}{Q} + \sigma\tau\Omega_0 \rho_\parallel^2 \right) \frac{\partial B}{\partial \theta} \right]$$

$$- \frac{1}{D} \left[\Phi'(s) + (\rho_\parallel + \Upsilon)\mu_0 J'(s) + \mu_0 J(s) \left. \frac{\partial \Upsilon}{\partial s} \right|_{\theta,\varphi,t} \right] \left[\left. \frac{\partial \chi}{\partial \varphi} \right|_{s,\theta,t} + \frac{1}{\gamma} \left(\frac{\mu}{Q} + \sigma\tau\Omega_0 \rho_\parallel^2 \right) \frac{\partial B}{\partial \varphi} \right]$$

$$+ \frac{\mu_0}{D} \left[I(s) \left. \frac{\partial \Upsilon}{\partial \theta} \right|_{s,\varphi,t} + J(s) \left. \frac{\partial \Upsilon}{\partial \varphi} \right|_{s,\theta,t} \right] \left[\left. \frac{\partial \chi}{\partial s} \right|_{\theta,\varphi,t} + \frac{1}{\gamma} \left(\frac{\mu}{Q} + \sigma\tau\Omega_0 \rho_\parallel^2 \right) \frac{\partial B}{\partial s} + \frac{\Omega_0}{\gamma} \sigma B \rho_\parallel \left. \frac{\partial \sigma}{\partial s} \right|_B \right]$$

$$- \frac{1}{D} \left[(\rho_\parallel + \Upsilon) \frac{\partial(\sigma B_s)}{\partial \varphi} + \sigma B_s \frac{\partial \Upsilon}{\partial \varphi} \right] \left[\frac{\partial \chi}{\partial \theta} + \frac{1}{\gamma} \left(\frac{\mu}{Q} + \Omega_0 \sigma \rho_\parallel^2 \right) \frac{\partial B}{\partial \theta} \right]$$

$$+ \frac{1}{D} \left[(\rho_\parallel + \Upsilon) \frac{\partial(\sigma B_s)}{\partial \theta} + \sigma B_s \frac{\partial \Upsilon}{\partial \theta} \right] \left[\frac{\partial \chi}{\partial \varphi} + \frac{1}{\gamma} \left(\frac{\mu}{Q} + \Omega_0 \sigma \rho_\parallel^2 \right) \frac{\partial B}{\partial \varphi} \right] \tag{6.4d}$$

with $\Omega_0 = QB/m_0$ and

$$D = \psi'(s)J(s) - \Phi'(s)I(s) + (\rho_\parallel + \Upsilon) \left[J(s)I'(s) - I(s)J'(s) + I(s)\frac{\partial(\sigma B_s)}{\partial \theta} + J(s)\frac{\partial(\sigma B_s)}{\partial \varphi} \right].$$

$$\tag{6.5}$$

The terms containing σB_s assure the canonical properties and are, together with the factors σ and τ related to anisotropy, neglected in all other codes to our knowledge. However, they ensure that the drift velocity satisfies Liouville's theorem by matching the required drift velocity, Eq. (2.54), and they can make a difference as shown in Fig. 6.1. In this figure, the particle orbit is integrated using the exact same initial conditions, once with the newly introduced terms, once without. The differences are especially important for tight aspect ratio and high pressure (high β). Even though Eqs. (6.4) are implemented in VENUS, we will, as already indicated, concentrate on 2D configurations in this thesis. Furthermore, the interactions with the RF field are implemented using Monte Carlo operators described in the next section and these fields are therefore not present in the equations of motion. We will not consider electromagnetic perturbations other than the RF fields. Thus, all terms containing Υ, χ, and derivatives with respect to φ will be zero.

With the equations of motion (6.4) and the equilibrium, we can already study single particle orbits, as shown in Figs. 6.1 and 6.2. This is the configuration implemented for a first physical study in Chapter 8, where we look at one single particle orbit and derive the effect of pressure gradients on the toroidal precession drift.

For integrated modeling as shown in Fig. 3.1, interactions with the background plasma and the injected wave field have to be added. Since all of these parts are applied to the particle orbits in phase space, they are included in VENUS and described here. Furthermore, the modules for creating new inputs for VMEC and LEMan must be included. These are needed at the end of every VENUS run, once the orbits have been advanced in time. They represent an interface to VMEC and LEMan and are therefore separately treated in the next chapter.
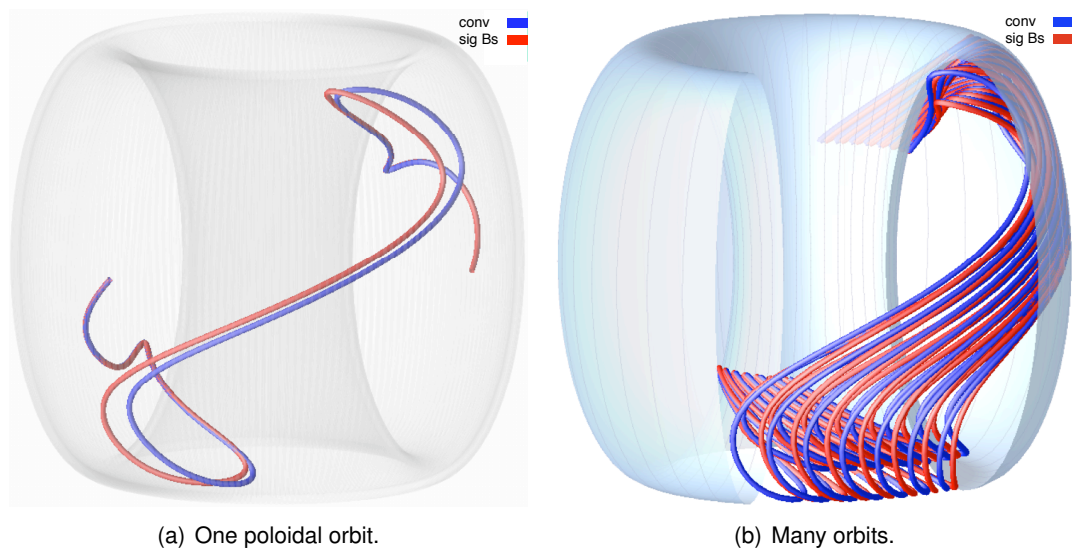
(a) One poloidal orbit.   (b) Many orbits.

Figure 6.1.: Orbit difference with (red) and without (blue) the terms in σB_s plotted for a tight aspect ratio high β tokamak ($B_0 = 5.6\,\mathrm{T}$, $R_0 = 1.1\,\mathrm{m}$, $a = 0.9\,\mathrm{m}$, $\delta = 2.5$) with $\beta = 19\,\%$ and a $10\,\mathrm{MeV}$ trapped particle.[17]
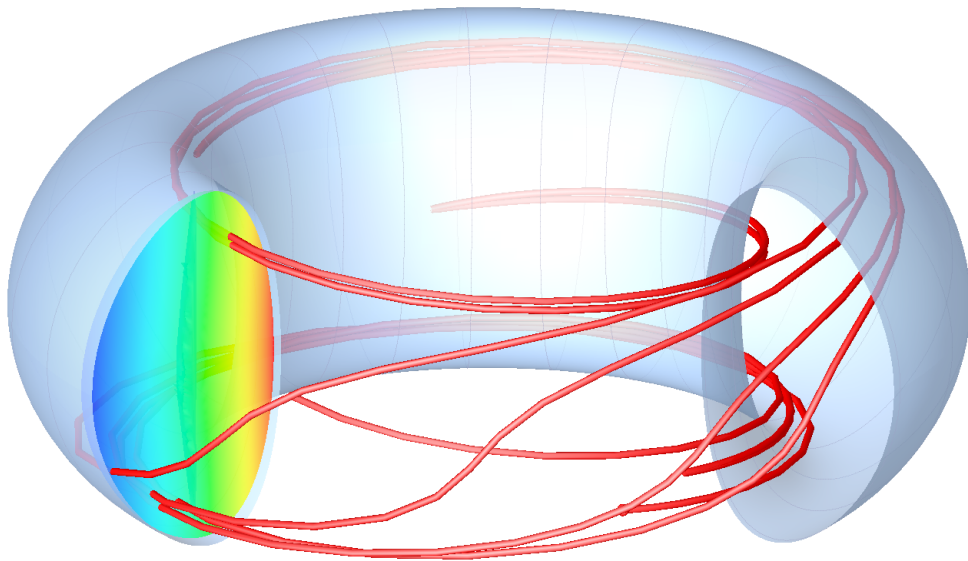
Figure 6.2.: VENUS can be run without any interaction operators for independent single particle studies. It reads the equilibrium from VMEC and integrates the equations of motion in time. The orbit is sometimes not very smooth because not every integration time step is plotted.

6.2. Monte Carlo interaction operators

We now want to include in the trajectories of the hot particles the effects of Coulomb collisions and the injected electromagnetic field. While we know everything we need for the followed particles, we do not have the information of the speed, pitch angle and exact position of each and every one of the 10^{19} or so background particles present in every cubic meter. In addition, if we wanted to know the exact phase of every particle's gyro motion with respect to the RF field at the time of wave-particle interaction, we would have to follow the full Lorentzian particle orbits instead of the guiding centre orbits, which would be much too expensive. However, such interactions take place in great numbers, and we can therefore rely on statistical methods to model the mentioned interactions in a way which gives physically correct results. Furthermore, from a physical point of view, the wave-particle interactions introduce a non-reversible component into the evolution of the particle orbit. This is included in the dielectric tensor through the Z-functions defined in Eq. (5.2), and it has to be included in the particle orbits. The numerical modules describing the wave-particle interactions implemented in VENUS contain therefore random numbers, such that irreversibility is ensured. These methods are summarised under the term Monte Carlo method. Here, we apply many times per simulation operators in phase space with random components, and choose these operators such that they do indeed model the physical processes. In mathematical terms, we need to model the right hand side of the Boltzmann equation (2.50), namely the term $\partial f/\partial t|_c$, and the non-linear wave-particle interactions in the force term. We write these two contributions on the right hand side of the equation as one term coming from the Coulomb collisions with the background ions and electrons, denoted C, and one due to the wave-particle interactions with the RF field. The latter will have a quasilinear form and we introduce therefore the symbol Q_L. The evolution equation of the distribution function takes now the form of the Fokker-Planck equation

$$\left(\frac{\partial}{\partial t} + \mathbf{v} \cdot \nabla\right) f = C + Q_L. \tag{6.6}$$

The first term (C) will be described next, and Q_L in Sec. 6.2.2.

6.2.1. Coulomb collisions

Coulomb collisions describe the energy diffusion (slowing down) and change of direction (deflection) of the simulated particles due to the Coulomb force originating from background charged particles (thermal ions and electrons). As usual, we denote the test particle's mass m and charge Q, the background particle's mass m_1 and charge Q_1. The characteristic time scales for these processes are derived e.g. by Stix[57] and can be written[58]

$$\tau_s = \frac{v_{th,1}^2 v}{(1 + m/m_1) A_D \Psi(x)} \tag{6.7a}$$

$$\tau_d = \frac{v^3}{A_D \left[\text{Er}(x) - \Psi(x)\right]}, \tag{6.7b}$$

where we defined

$$A_D = \frac{n_1 Q^2 Q_1^2 \ln \Lambda}{2\pi \epsilon_0^2 m^2} \tag{6.8}$$

$$x = \frac{v}{v_{th,1}} \tag{6.9}$$

$$\mathrm{Er}(x) = \mathrm{erf}(x) \equiv \frac{2}{\sqrt{\pi}} \int_0^x e^{-y^2} \mathrm{d}y \tag{6.10}$$

$$\Psi(x) = \frac{\mathrm{Er}(x) - x\mathrm{Er}'(x)}{2x^2} \tag{6.11}$$

Fig.6.3 shows the deflection and slowing down times as functions of the test particle's energy for a helium-3 or hydrogen ion on deuterium background ions and electrons with $T_e = 5\,\mathrm{keV}$, $T_D = 1.8\,\mathrm{keV}$, $n_D = 3.3 \times 10^{19}\,\mathrm{m}^{-3}$. We can note a few important points from these plots: For low energy, collisions on ions are more important, whereas for high energies, slowing down on electrons is dominant. The differences are greater for larger test particle mass, which has the effect that the switch between slowing down on ions and electrons is at lower energy for hydrogen than for helium-3. Also, deflection can be negligible at very high energies and thus pressure anisotropy is expected to be more important the higher the energy.

With these time scales we can construct our Monte Carlo Coulomb collision operators in energy and pitch angle. They are written in terms of collision frequencies

$$\nu_d = \sum_f \nu_d^f = \sum_f \frac{1}{\tau_d^f} \tag{6.12a}$$

$$\nu_s = \sum_f \nu_s^f = \sum_f \frac{1}{\tau_s^f}, \tag{6.12b}$$

where f denotes the background ion species or electrons, applied at every time step, and take the form[59]

$$\lambda_{n+1} = \lambda_n(1 - \nu_d\tau) + \mathcal{R}\sqrt{(1 - \lambda_n^2 \nu_d \tau)} \qquad \lambda \equiv v_\parallel / v \tag{6.13a}$$

$$E_{n+1} = E_n - (2\nu_s\tau)\left[E_n - \left(\frac{3}{2} + \frac{E_n}{\nu_s}\frac{\mathrm{d}\nu_s}{\mathrm{d}E} \right) T_p \right] + 2\mathcal{R}\sqrt{T_p E_n \nu_s \tau}. \tag{6.13b}$$

We wrote $\lambda \equiv v_\parallel / v$ for the pitch angle, τ for the time step, T_p for the background (thermal) temperature and n enumerates the time steps. $\mathcal{R}$ is a random number with zero mean value and unity variance.
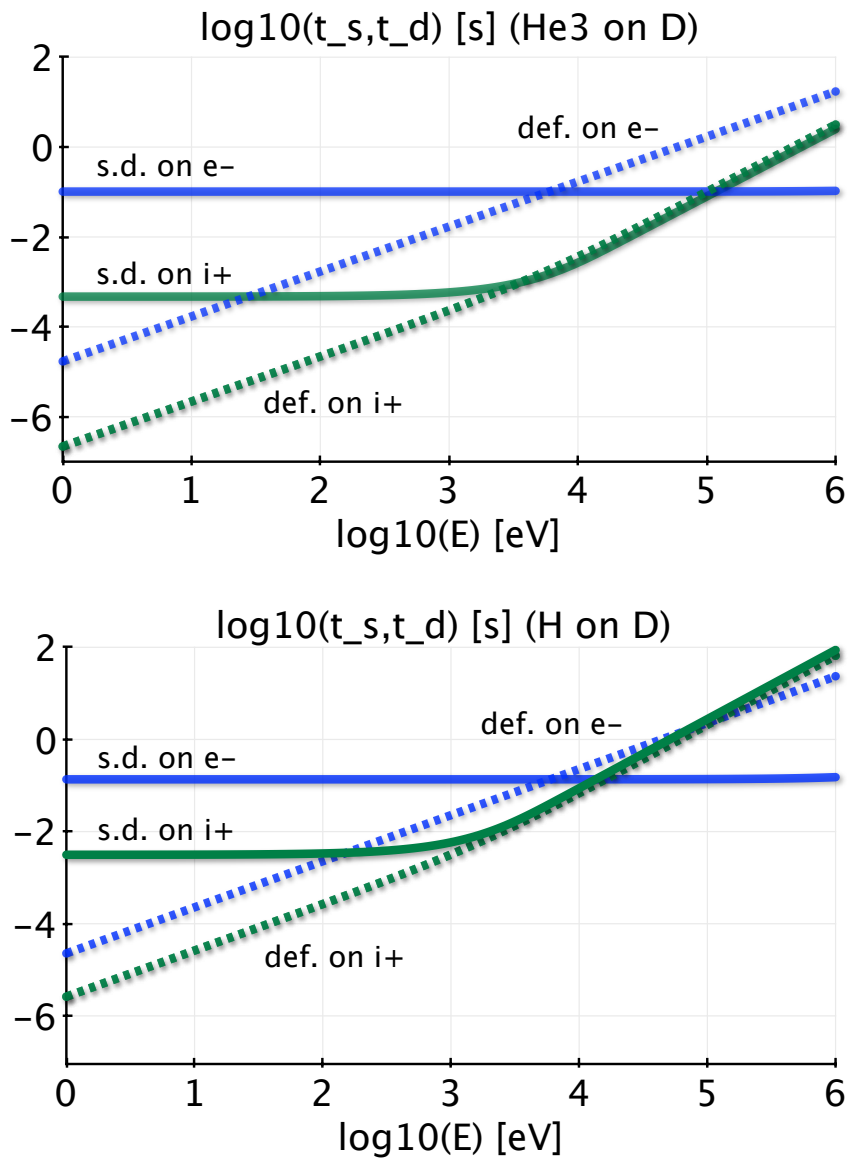
Figure 6.3.: Coulomb slowing down (t_s,s.d.) and deflection (t_d,def.) times of He^3 (top) and H (bottom) ions on background electrons (e-) and background deuterium ions (i+). The electron temperature is $T_e = 5\,keV$.

6.2.2. ICRH operators

Ion Cyclotron Resonant Heating consists of launching an electromagnetic (EM) wave (radio frequency wave) into the plasma. The frequency of this wave is chosen to be a multiple of the ion cyclotron frequency at a given magnetic field for a given ion population in the plasma. Ions (positive charge) and electrons (negative charge) have opposite sign in the definition of the cyclotron frequency (2.30). Physically, this means that in a right-handed system, ions are rotating clockwise and electrons counter-clockwise around the magnetic field lines. This will become important later on in this section. First, we want to see how the electric field from the EM wave interacts with the particles in the plasma.

Single particle dynamics

Following Stix'[57,18] derivation, or similarly the overview of Ref. 60, we can include the effect of the microwave on single particles in the plasma. Some of these computations are not very illuminating and therefore given in Appendix C. We introduce a system of coordinates where the magnetic field is $B_0(z)\hat{\mathbf{z}}$ and $\hat{\mathbf{x}}, \hat{\mathbf{y}}$ are perpendicular to that direction. For the passage through a cyclotron resonance (given by a sinusoidal wave field with frequency ω), the equations of motion write

$$\frac{\mathrm{d}v_x}{\mathrm{d}t} - \frac{QB_0(t)}{m}v_y = \frac{Q}{m}A\cos(-\omega t) \tag{6.14a}$$

$$\frac{\mathrm{d}v_y}{\mathrm{d}t} + \frac{QB_0(t)}{m}v_x = \frac{Q}{m}B\sin(-\omega t) \tag{6.14b}$$

One can write $B_0(t)$, since $v_\parallel$ is approximately constant along $B_0(z)$ and we can thus substitute t for z using $z \approx v_\parallel t$. The cyclotron frequency of the particle is now a function of time, and we Taylor expand it around t_{res}, the time at which the particle crosses the resonance, i.e. the time at which $\Omega = \omega$:

$$\Omega(t) \equiv \frac{QB_0(t)}{m} = \omega + (t - t_{\mathrm{res}})\Omega' + ... \tag{6.15}$$

Let us further introduce the velocity u and electric field amplitude $E^\pm$

$$u = v_x + iv_y \tag{6.16}$$

$$E^\pm = \frac{1}{2}(A \pm B), \tag{6.17}$$

such that the equations of motion combine into one equation, namely

$$\frac{\mathrm{d}u}{\mathrm{d}t} + i\Omega(t)u = \frac{Q}{m}\left(E^+ e^{-i\omega t} + E^- e^{+i\omega t}\right). \tag{6.18}$$

We are dealing with a resonance with the ions, and neglect thus for this illustration the non-resonant E^-. The solution to this differential equation is

$$u(t) \exp\left[i \int_{t_0}^t dt' \Omega(t')\right] \cong u(t_0) + \frac{Q}{m} E^+ e^{-i\theta} \sqrt{\frac{2\pi}{|\Omega'|}}, \tag{6.19}$$

where $\theta = \omega t_0 + \frac{\Omega'}{2}(t_{\text{res}} - t_0)^2 - \frac{\pi}{4}\text{sgn}(\Omega')$. Note that for the case of $v_\parallel \to 0$ (turning point), $\Omega(t)$ has to be expanded to second order, which makes an Airy function appear.[57] We can now easily find the average change of (perpendicular) energy per transit

$$W_\perp = \frac{m}{2}\langle u(t)u(t)^* - u(t_0)u(t_0)^*\rangle = \frac{m}{2}\left|\frac{Ze}{m}\right|^2 |E^+|^2 \frac{2\pi}{|\Omega'|}, \tag{6.20}$$

with $Q = Ze$. The rate of power absorption given to $\langle mv_\perp^2/2\rangle$ per unit volume can be written as

$$P_\perp = \frac{\pi Z^2 e^2}{m|k_\parallel|} |E^+|^2 n_{res}\left(\mathbf{x}, v_\parallel^{res}\right), \tag{6.21}$$

where n_{res} is the density of resonant particles.

Note that for these simplified considerations we did not include the Doppler shifted frequency of the field the particle sees. Indeed, one should include the Doppler shift such that the frequency in Eqs. (6.14) ω changes to $\omega - k_\parallel v_\parallel$. This Doppler shift will be included in the next section, since it will be rather important in what follows.

Quasilinear electromagnetic theory

After this first study of single particle dynamics, which gives a first approximation to the problem, we derive the quasilinear operators more consistently (still following Stix[57,18]), i.e. using the Vlasov equation

$$\frac{\partial f}{\partial t} + \mathbf{v} \cdot \nabla f + Q\nabla_{\mathbf{p}} \cdot [(\mathbf{E} + \mathbf{v} \times \mathbf{B}) f] = 0, \tag{6.22}$$

with $\nabla_{\mathbf{p}} = \partial/\partial \mathbf{p}$. Passing into Fourier space (with $\mathbf{k} = k_\perp cos\theta\hat{\mathbf{x}} + k_\perp \sin\theta\hat{\mathbf{y}} + k_\parallel\hat{\mathbf{z}}$) and linearising as well as averaging over the gyroangle α yields

$$\frac{\partial f_0}{\partial t} = -\lim_{V\to\infty} Q \int \frac{d^3\mathbf{k}}{V} \int_0^{2\pi} \frac{d\alpha}{2\pi} \nabla_{\mathbf{p}} \cdot [(\mathbf{E}_k + \mathbf{v} \times \mathbf{B}_k) f_{-k}], \tag{6.23}$$

with V the volume in $\mathbf{k}$ space. The average over the gyroangle can be done using Bessel functions of the first kind J_n:

$$\frac{\partial f_0}{\partial t} = \lim_{V\to\infty} \pi Q^2 \sum_{n=-\infty}^{n=+\infty} \int \frac{d^3\mathbf{k}}{V} L p_\perp \delta(\omega_{kr} - k_\parallel v_\parallel - n\Omega)|\psi_{n,k}|^2 p_\perp L f_0, \tag{6.24a}$$

with

$$L = \left(1 - \frac{k_\parallel v_\parallel}{\omega_{kr}}\right) \frac{1}{p_\perp} \frac{\partial}{\partial p_\perp} + \frac{k_\parallel v_\perp}{\omega_{kr}} \frac{1}{p_\perp} \frac{\partial}{\partial p_\parallel} \tag{6.24b}$$

$$\psi_{n,k} = \frac{1}{2}\left(E_{kx} + iE_{ky}\right) e^{-i\theta} J_{n-1}(z) + \frac{1}{2}\left(E_{kx} - iE_{ky}\right) e^{i\theta} J_{n+1}(z)$$
$$+ \frac{p_\parallel}{p_\perp} E_{kz} J_n(z), \tag{6.24c}$$

ω_{kr} the real part of the frequency ω_k and the argument of the Bessel functions $z = k_\perp v_\perp / \Omega$. If we now remember that $v_\parallel$ effects are of order $k_\parallel v_\parallel / \Omega \sim k_\parallel \rho_L \to 0$ and that the parallel E_z effects are negligible, we can write Eqs. (6.24) as

$$\frac{\partial f_0}{\partial t} \cong \frac{\pi Q^2}{2|k_\parallel|} \sum_{n=-\infty}^{n=+\infty} \frac{1}{p_\perp} \frac{\partial}{\partial p_\perp} p_\perp \left|E^+ J_{n-1} + E^- J_{n+1}\right|^2 \delta\left(v_\parallel - \frac{\omega - n\Omega}{k_\parallel}\right) \frac{\partial f_0}{\partial p_\perp}, \tag{6.25a}$$

with

$$E^\pm \equiv \frac{1}{2}\left(E_x \pm iE_y\right) e^{\pm i\theta}, \quad E_{x,y} \in \mathbb{C}. \tag{6.25b}$$

By definition, the diffusion coefficient in perpendicular velocity relates the temporal derivative of f_0 to its second derivative with respect to perpendicular velocity,

$$\frac{\partial f_0}{\partial t} = Q_{L\perp} \frac{\partial^2 f_0}{\partial v_\perp^2}, \tag{6.26}$$

and one can extract the diffusion coefficient from Eqs. (6.25) as

$$Q_{L\perp} = \frac{\pi}{2} \frac{Q^2}{m^2} \left|E^+ J_{n-1} + E^- J_{n+1}\right|^2 \delta\left(\omega - k_\parallel v_\parallel - n\Omega\right). \tag{6.27}$$

Since we are following particle orbits, we are interested in the change of perpendicular velocity during a time t, which is given by

$$(\Delta v_\perp)^2 = 4tQ_{L\perp} = 2\pi t \frac{Q^2}{m^2} \left|E^+ J_{n-1} + E^- J_{n+1}\right|^2 \delta\left(\omega - k_\parallel v_\parallel - n\Omega\right). \tag{6.28}$$

If we apply the change in velocity (6.28) only where the resonance condition $\omega = k_\parallel v_\parallel - n\Omega$ is satisfied, we can approximate $t \sim \tau$ and $\delta\left(\omega - k_\parallel v_\parallel - n\Omega\right) \sim \tau/2\pi$, with τ the interaction time of the particle with the wave. For the construction of the Monte Carlo operator, we need a mean value and standard deviation of the perpendicular velocity, which follow directly from (6.28) and can be written[45]

$$\langle \Delta v_\perp^2 \rangle = \alpha \frac{Q^2}{m^2} \tau^2 |E^+ J_{n-1} + E^- J_{n+1}|^2 \tag{6.29a}$$

$$\langle \Delta v_\perp \rangle = \frac{\langle \Delta v_\perp^2 \rangle}{2v_\perp}. \tag{6.29b}$$

The constant factor α depends on the definition of $E^{\pm}$ and will automatically be adjusted during the simulation for a constant deposited power and will be described further in Sec. 9.1.2. From this, we get the operator[45,61]

$$\Delta v_{\perp} = \frac{\langle \Delta v_{\perp}^2 \rangle}{2 v_{\perp}} + \mathcal{R} \sqrt{2 \langle \Delta v_{\perp}^2 \rangle} \tag{6.29c}$$

where $\mathcal{R}$ is a random number with zero mean value and unity variance. Introducing the phase

$$\nu(t) \equiv \int^t (\omega - k_{\parallel} v_{\parallel} - n\Omega) \mathrm{d}t', \tag{6.30}$$

the interaction time τ corresponds to the phase integral[62,63,64]

$$\tau = \int^t \mathrm{d}t' e^{i\nu}. \tag{6.31}$$

We can expand the phase around the resonance (when $\dot{\nu} = \omega - k_{\parallel} v_{\parallel} - n\Omega = 0$) and write

$$\tau \approx \int_{-\infty}^{\infty} \mathrm{d}t \exp i \left(\nu + \frac{1}{2} \ddot{\nu} t^2 + \frac{1}{6} \dddot{\nu} t^3 \right) \Big|_{\dot{\nu}=0}, \tag{6.32}$$

where a dotted variable is a derivative with respect to time. In most cases, the expansion to the second order is sufficient, yielding

$$\tau_1 = \sqrt{\frac{2\pi}{|\ddot{\nu}|}}. \tag{6.33a}$$

However, when $\ddot{\nu} \to 0$, one has to retain the third order term in (6.32), and one obtains[62]

$$\tau_2 = 2\pi \left(\frac{2}{\dddot{\nu}} \right)^{1/3} \mathrm{Ai} \left(-\frac{\ddot{\nu}^2}{2^{2/3} \dddot{\nu}^{4/3}} \right), \tag{6.33b}$$

where Ai is the Airy function. τ_1 is the default interaction time, but τ_2 has to be used when $\ddot{\nu} \to 0$, in which case $\tau_1 \to \infty$. More precisely, one can show that $(\tau_2/\tau_1)^2 = 1$ if $\dddot{\nu}^2 = 69.65 \ddot{\nu}^3$, so that we switch to τ_2 if $\dddot{\nu}^2 > 69.65 \ddot{\nu}^3$.

As noted by Stix, one can show that the operator L in Eq. (6.24) acts on $F = v_{\perp}^2 + (v_{\parallel} - \omega/k_{\parallel})^2$ such that $LF = 0$. Thus, one can understand L as a gradient along the line in phase space where

$$v_{\perp}^2 + \left(v_{\parallel} - \frac{\omega}{k_{\parallel}} \right)^2 = \mathrm{const.} \tag{6.34}$$

One can see this as a local description of the conservation of energy during the wave-particle interaction, and is known as the Kennel-Engelmann constraint.[65] The variation in

perpendicular velocity then reads,

$$\Delta\left(v_\perp^2\right) = -\Delta\left(v_\parallel - \frac{\omega}{k_\parallel}\right)^2, \tag{6.35}$$

which yields for a small change

$$2v_\perp\Delta v_\perp = -2\left(v_\parallel - \frac{\omega}{k_\parallel}\right)\Delta v_\parallel, \tag{6.36}$$

such that

$$-\frac{v_\perp\Delta v_\perp}{v_\parallel - \omega/k_\parallel} = \Delta v_\parallel. \tag{6.37}$$

But, at the resonance (at which this operator is only applied), $v_\parallel = (\omega - \Omega)/k_\parallel$, and we can finally write our Monte Carlo operator for the parallel velocity

$$\Delta v_\parallel = \frac{k_\parallel}{\Omega} v_\perp \Delta v_\perp \tag{6.38}$$

Eqs. (6.29), (6.33) and (6.38) are the operators implemented in VENUS. These operators are valid for fundamental harmonic heating, and they neglect the instantaneous radial displacement of the guiding centre due to the change in perpendicular velocity and the resulting variation in Larmor radius. More general Monte Carlo operators have been derived in Ref. 78, including both higher harmonics and the instantaneous radial guiding centre displacement. Those operators are, however, rather complicated and need further development for direct application in VENUS. The operators are applied every time a particle crosses the Doppler shifted resonance $\omega = k_\parallel v_\parallel + \Omega$. It is important to include the change in parallel velocity $\Delta v_\parallel$ in the wave-particle interactions, even if the interaction is mainly in the perpendicular direction. First of all, it corresponds to a conservation of energy and should therefore not be omitted. But, more importantly, the change in parallel velocity changes the particle orbit in that it induces a RF-induced radial transport of resonant particles. The corresponding theory has been derived in Ref. 66 and observations reported in Ref. 67. If we look at the case of an axisymmetric tokamak, we can make use of the conservation of toroidal momentum P_φ defined in Eq. (2.39) to understand the workings of this drift. Indeed, the change in parallel velocity during the wave-particle interaction induces a change in toroidal momentum as

$$\Delta P_\varphi = \left(Rmv_\varphi^{\text{after}} + Q\psi\right) - \left(Rmv_\varphi^{\text{before}} + Q\psi\right) \approx RmB_\varphi\Delta v_\parallel/B, \tag{6.39}$$

This displacement is small and usually included by invoking the conservation of toroidal momentum in axisymmetric geometries, and it is not clear how one should include it in the general three-dimensional case. After the interaction, the new toroidal moment is conserved along the unperturbed orbit, and its change due to the previous interaction means that, considering a trapped particle, at the turning points the poloidal flux ($\sim$ radial

variable)

$$\Delta \psi_t = \frac{\Delta P_\varphi}{Q} \approx \frac{R m B_\varphi}{QB} \Delta v_\|, \tag{6.40}$$

such that the turning points move in real space proportionally to the change in parallel velocity due to the RF interactions. We can express this drift in terms of energy change by using the Kennel-Engelmann constraint (6.34) or (6.38) and $\Delta E = 0.5 m \Delta (v_\perp^2 + v_\|^2)$, giving

$$\Delta \psi_t \approx \frac{R B_\varphi}{QB\omega} k_\| \Delta E. \tag{6.41}$$

Recall that a positive parallel wave vector, i.e. in the direction along the toroidal variable φ, means counter-current injection. Since we apply the RF waves for heating, ΔE will be positive on average, such that $\mathrm{sgn}(\Delta \psi) = \mathrm{sgn}(k_\|)$, and thus, there will be a net inward drift for co-current wave injection ($k_\| < 0$), and a net outward drift for counter-current injection ($k_\| > 0$). These RF induced particle pinches cannot be included if one neglects the change in parallel velocity. We will come back to this drift in later chapters.

6.3. Initial loading of marker distribution

The model distribution function (4.1) is defined using an orbit averaged radial position, whereas the guiding centre orbits in VENUS are complete and the particles have to be loaded somewhere well defined in phase space. Thus, for attributing the correct weights to each particle when loading the distribution, the code needs to know the average radial position $\bar{s}$ of the unperturbed orbit, given the initialised position in phase space. For this, VENUS can be run in a different mode, allowing for the creation of a lookup table. Figure 6.4 shows a passing or trapped orbit respectively (blue and solid line), each with the corresponding $\bar{s}$ flux surface (red and dashed). This lookup table will then give the average radial position of an orbit as a function of the pitch angle $\lambda = v_\|/v$, energy E, and the three-dimensional position in real space. The creation of this lookup table works as follows:

(i) Load many particles uniformly distributed in complete phase space

(ii) Save initial $s_0, \theta, \varphi, \lambda$ and E

(iii) Run every particle for one orbit and determine average radial position using Eq. (4.2)

(iv) Create lookup table of the form

s_0	θ	φ	λ	E	$\bar{s}$
⋮	⋮	⋮	⋮	⋮	⋮

Once the lookup table is created, we can load the particles by choosing $\bar{s}, \theta, \varphi, \lambda$ and E according to F_h given in Eq. (4.1), and then determine the initial radial position s_0 by inverting the lookup table. A step by step description would be

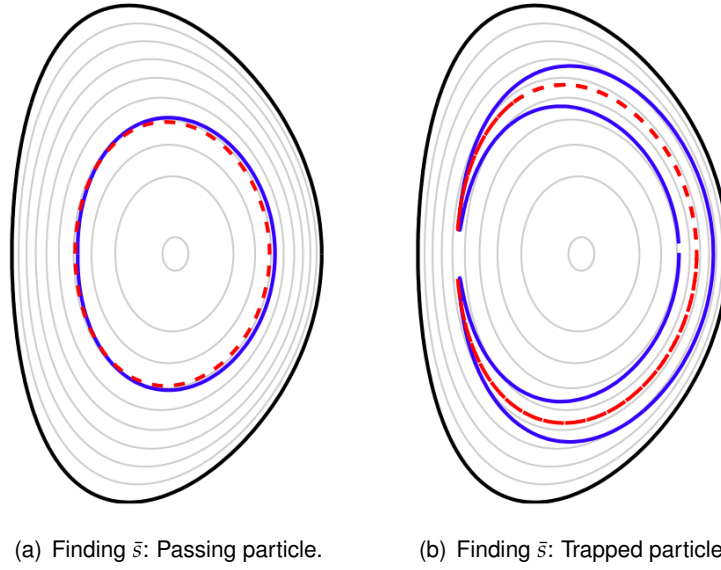(a) Finding $\bar{s}$: Passing particle.   (b) Finding $\bar{s}$: Trapped particle.

Figure 6.4.: Finding $\bar{s}$: The orbit of a passing (trapped) particle in blue and solid, with the corresponding $\bar{s}$ flux surface in red and dashed. For passing particles, orbits cross the $\bar{s}$ flux surface close to $\theta = \pi/2$, for trapped particles, $\bar{s} \approx s(\theta_b)$.

(i) Load according to F_h by choosing $\bar{s}, \theta, \varphi, \lambda$ and E.

(ii) Invert lookup table and determine initial s_0

$\bar{s}$	θ	φ	λ	E	s_0
$\vdots$	$\vdots$	$\vdots$	$\vdots$	$\vdots$	$\vdots$

(iii) Start the particle at (s_0, θ, φ)

Although the particle distribution function in terms of the constants of motion $F_h(\bar{s}, \mu, E)$, and for a given set $(\bar{s}, \mu, E.\sigma)$, where $\sigma = \text{sign}(v_\parallel)$, the corresponding particle orbit is defined, it is more practical to load the particles in terms of $\bar{s}, \theta, \varphi, \lambda$ and E, and then invert the lookup table for finding s_0. Indeed, with this choice we can load $\bar{s} \in [0,1]$, $\theta \in [0, 2\pi]$, $\varphi \in [0, 2\pi]$ and $\lambda \in [-1, 1]$. Then, we can determine s_0 and finally $\mu = E(1 - \lambda^2)/B(s_0, \theta, \varphi)$. Moreover, if we were to construct the lookup table in terms of μ, E, σ instead of $\theta, \varphi, \lambda, E$, the poloidal and toroidal positions of the actual orbit (corresponding to s_0 and the constants of motion) would not be determined.

Note that for axisymmetric cases, the toroidal angle φ does not have any effect on $\bar{s}$. Furthermore, this loading procedure has to be executed only once at the beginning of any given self-consistent simulation. Every subsequent iteration, VENUS reloads the particle distribution exactly as it was at the end of the previous iteration. In this way, we make sure that no approximation is done to the distribution contained in VENUS. Although only needed once per simulation, this lookup table is also very useful for comparing the
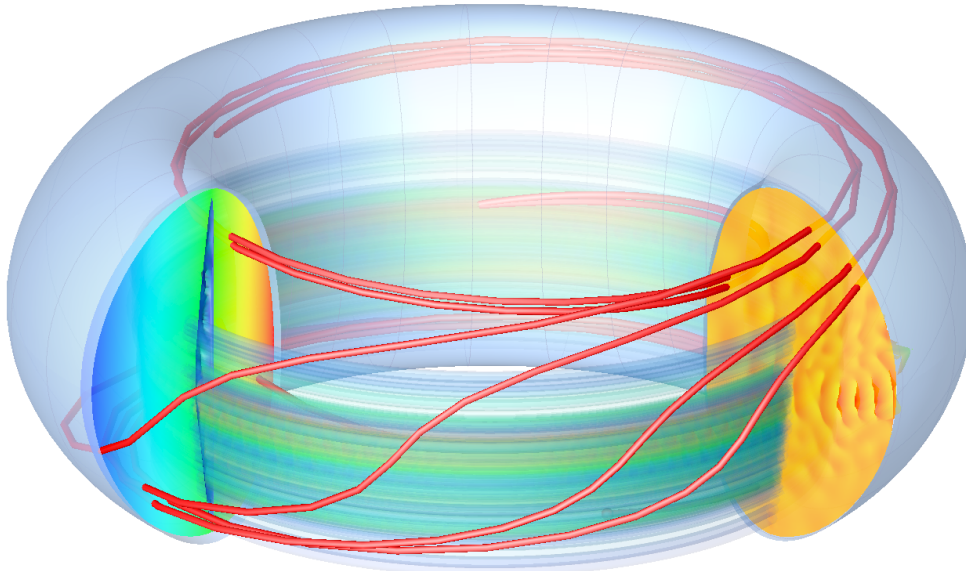
Figure 6.5.: Artist's view of the SCENIC package, including the equilibrium from VMEC (represented by the magnetic field,left), the wave field from LEMan (E^+, right) and a particle orbit including power deposition from VENUS (red orbit, 2D and 3D power deposition).

model distribution function with the distribution from VENUS, in order to check if the bi-Maxwellian is an appropriate model. We will perform such comparisons in Chapters 11 and 12, and show that the inclusion of the finite orbit widths through $\bar{s}$ is indeed a crucial improvement with respect to other analytical models.

Fig. 6.5 shows an artist's view of the package described so far. VMEC provides the equilibrium and geometry, represented as the shape of the confined plasma and the magnetic field strength on the left poloidal cut, LEMan then computes the wave field (orange 2D plots within the cross section), and VENUS follows particle orbits including Coulomb collisions on the background (not represented) and ICRH heating (green, showing regions of power deposition). We now are able to complete one iteration of the SCENIC package. What remains to be described is the re-creation of inputs at the end of every iteration for the self-consistent iterated scheme to be working. We have finished building the package for one complete iteration VMEC-LEMan-VENUS. The only missing part is then the generation of new input files for VMEC and LEMan for the next iteration. This will be described in the next chapter.

7. Self-consistency modules

Once the Monte Carlo operators are implemented, we need tools to interpret the resulting distribution of particles. All Monte Carlo operators have been derived from the Fokker-Planck equation (6.6) and yield thus first of all the evolution of the underlying distribution function. There are two different kinds of output to construct at the end of every VENUS run: One for the iteration of the model VMEC-LEMan-VENUS-VMEC-etc, and one for the physical quantities we are interested in, e.g. for diagnostics purposes or physical studies.

7.1. Mean energy

In order to check if the iterative method achieves convergence and to determine when the simulation can be stopped, a criterion which is easy to implement and observe has to be identified. Preferably it would be a global quantity, which does not depend on any position in phase space but which shows when a steady-state has been achieved. A steady-state is reached when the deposited power by the RF field is balanced by the power loss of the minority species to the background species. When that happens, the total energy content of the minority species will remain constant. Therefore, a relevant quantity to observe is the total energy content of the minority species, or, equivalently, the mean energy

$$\langle E \rangle \equiv \frac{1}{N} \int_V \frac{1}{2} m v^2 f \mathrm{d}V, \tag{7.1}$$

where f is the minority distribution function in VENUS and V is the total phase space volume, $\mathrm{d}V = \mathrm{d}^3 x \mathrm{d}^3 v$, and $N = \int_V f \mathrm{d}V$. We will still concentrate on only one iteration, i.e. describe here how VENUS re-creates new inputs to VMEC and LEMan at the end of one given run. We will study the convergence of the SCENIC model with respect to the number and length of the iterations when we will do iterated simulations in Chapter 11.

7.2. Splitting mechanism

The background electron and ion profiles (density and temperature) are considered static, i.e. constant in time during the simulation. Only the simulated minority is dynamically changing. But out of this minority population, especially for low to moderate heating power scenarios, only a certain portion is effectively heated to higher energies, depending on background profiles, heating location, type of minority etc. It is then convenient to divide the minority population into a thermal and a hot species, and compute the moments of the distribution function for each of these two separately. Then, the thermal minority species can be treated as second isotropic species in the dielectric tensor, and the thermal minority pressure added to the background pressure in the equilibrium. Only the energetic minority population is treated as hot and therefore bi-Maxwellian in VMEC and LEMan. Table 7.1 introduces a nomenclature which will be used throughout this thesis, denoting the different populations present in the simulation. We note that depending on the injected RF power, a large part of the minority species will become energetic, and thus a δf scheme would not be appropriate anymore, since the condition δf$\ll$f would not be satisfied. This is why we chose a full-f description in VENUS, and indeed, we will show simulations where the hot tail is as high as almost $50\,\%$ of the total minority.

One way of determining the thermal and hot parts of the minority distribution is to create the total distribution, and determine the thermal Maxwellian temperature by differentiating the distribution with respect to energy. Indeed, inspecting the Maxwellian (2.49), it is easy to see that $\partial_E f_M(s, E) = -f_M(s, E)/T(s)$. Once the temperature profile is found, the radial derivative can give the density profile as $\partial_s \ln f_M(s) = \partial_s \ln n(s) - \partial_s \ln T(s)[1 - E/T(s)]$. With density and temperature the Maxwellian is determined and one can subtract that distribution from the total distribution in VENUS, leaving only the non-Maxwellian parts. This approach has, however, some practical deficiencies. First of all, all operations occur on the distribution at the lower energy range. We know that a Monte Carlo scheme can be rather noisy, and therefore operations on the distribution directly are at least as noisy as the distribution itself. Moreover, we are interested in the tail of the distribution, using more markers in that region than in the less interesting thermal part, decreasing the exactness of statistical measures on the thermal part. Furthermore, we do not actually need to resolve the exact distribution function itself in SCENIC, but only the integrated moments like density, current and pressure. In the above outlined scheme, these quantities would be found by integrating the approximated Maxwellian instead of the actual distribution as it is in VENUS. We now propose another automated splitting of the distribution function, which is simpler, less noisy and uses the non-approximated raw distribution function from VENUS.

The basic idea can be understood from Fig. 6.3, where the slowing down and deflection times are plotted against the particle energy. Deflection means randomisation of the pitch angle, which is why this process is usually called pitch angle scattering, and leads to isotropic distributions. The higher the deflection time, the lower the deflection frequency and thus the weaker the isotropisation, and the more anisotropic the distribution. For low energies, the deflection time is lower than the slowing down time, and it is dominated by ion-ion collisions. For intermediate energies, ion-ion collisions still dominate, but the pitch

Designation	Population	Species	Model	Evolution
Background	Majority plasma	D & e$^-$	Maxwellian	static
Thermal	Minority, $E < E_c(s)$	He^3 or H	Maxwellian	dynamic
Hot	Minority, $E > E_c(s)$	He^3 or H	bi-Maxwellian	dynamic

Table 7.1.: Nomenclature of the different populations present in all simulations.

angle scattering is equally important as slowing down. For high energies, however, slowing down on electrons becomes dominant before the pitch angle scattering and slowing down on ions, and anisotropy will not be equalised as efficiently as for lower energies. The passage from the regime where ion-ion collisions are dominant to the regime where ion-electron collisions are more important coincides with the passing from equal pitch angle scattering and slowing down to slowing down dominated, and is defined by the critical energy[58]

$$E_{\text{crit}}(s) = 14.8 \frac{A_h}{A_i^{2/3}} T_e(s),\tag{7.2}$$

where $A_{i,h}$ is the atomic number of the background and hot ions respectively, and $T_e(s)$ the electron temperature. This critical energy is defined as follows: for particles with energy below E_{crit}, pitch angle scattering is important and the pitch angle distribution is equalised, whereas for particles above this energy, slowing down is dominant, such that the pitch angle distribution remains anisotropic. For hydrogen or helium-3 in deuterium, $E_{\text{crit}}^{(\text{H,He3})} = (9.3, 28)T_e$, and the example case shown in Fig. 6.3, $T_e = 5\,\text{keV}$, giving critical energies of $46\,\text{keV}$ and $140\,\text{keV}$ respectively. These values correspond to the intersection of the green and blue curves in Fig. 6.3. Now, we do not want to split the distribution into thermal and hot parts based entirely on the nature of the Coulomb collisions. While this certainly gives us a good indication of how it could be done based on physical processes, it is clear that even a thermal Maxwellian, with electron temperature T_e, will contain some high energy particles, with energies above E_{crit}. Furthermore, if we only consider the particles with energy $E > E_{\text{crit}}$, it might be that the hot parallel temperature will be estimated too low, since the very highly energetic particles are the resonant ones, interacting strongly with the RF field in the perpendicular direction. We apply the splitting mechanism to each particle in the simulation instead of the distribution function, but retain a maximum flexibility in the splitting of the distribution function. We achieve this by introducing a critical energy E_c and constructing the splitting criterion

$$\begin{aligned} E_c(s) &= & xT_e(s) \\ \text{if particle energy } E < E_c(s) &\Rightarrow & \text{thermal} \\ \text{else} &\Rightarrow & \text{hot,} \end{aligned}\tag{7.3}$$

with s the particle's radial position and x a coefficient generalising Eq. (7.2). The parameter x, and its consequences, will be explored in Chap. 9, and Fig. 7.1 give a schematic view of splitting the distribution function in to a thermal part and a hot tail. This test is applied to every particle at the end of any VENUS simulation. If the particle is consid-
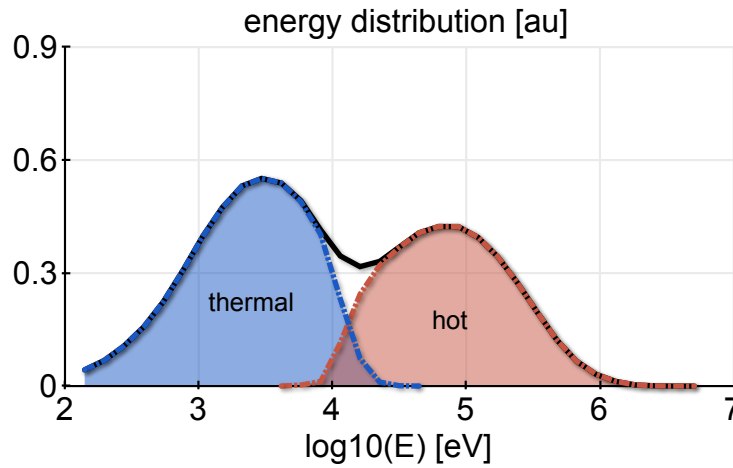
Figure 7.1.: Schematic view of the splitting mechanism. The total minority distribution function (black line) is split into an isotropic thermal (blue) and an anisotropic hot (red) minority part according to Eq. (7.3).

ered thermal, it will be considered in the integration of the thermal (isotropic) moments, if not its contribution will be included in the (anisotropic) hot moments. The details of the integration are given in the next section. Here we already state that the computed moments are then n_{th}^h, n^h, p_{th}^h, $p_\perp^h$ and $p_\parallel^h$, where the subscript th means that it is due to the minority population, but contains only contributions from particles with a lower energy than $E_c(s)$. Quantities without that subscript are computed with the particles having an energy $E > E_c$ only. Note that the induced currents, j_t (trapped) and j_p (passing), have to be taken from the complete distribution, since the total toroidal current has to be passed to VMEC. As stated above, this is a straightforward means of splitting the distribution function, and makes sure that the complete distribution in VENUS is being considered. Moreover, the Monte Carlo scheme's inherent noise is reduced to a minimum, since only the integrated moments are needed for the iterative scheme of SCENIC.

7.3. Computing the distribution function and its moments

For computing the distribution function and its moments, a standard particle-in-cell (PIC) procedure is implemented. Each particle is initialised at the start of the first iteration with a weight w_p, corresponding to the value of the model distribution function at the position in phase space at which the particle is loaded. If the particle is loaded according to the exact bi-Maxwellian from the equilibrium, the weight is unity. If not, it is determined by the ratio of that bi-Maxwellian over the distribution function after which the particles are loaded. At the end of each run, the integrals for the moments of the distribution function are approximated by sums over all particles inside a given cell in phase space. In what follows, we denote $\mathcal{J}$ the Jacobian, Δx the bin width in variable x, $ip \in \Delta x$ means that

particle i is located inside the bin Δx. In particular, $\Delta V = \Delta s \times \Delta \theta \times \Delta \varphi$. The integrated moments then are

- Density

$$n_{th}^h(s) \;=\; 2\pi \sum_{\substack{ip \in \Delta s \\ E_p < E_c}} 1 \frac{w_p}{\mathcal{J} \Delta s 2\pi 2\pi} \tag{7.4aa}$$

$$n^h(s,\theta,\varphi) \;=\; 2\pi \sum_{\substack{ip \in \Delta V \\ E_p > E_c}} 1 \frac{w_p}{\mathcal{J} \Delta s \Delta \theta \Delta \varphi} \tag{7.4ab}$$

- Toroidal current density

$$j_\varphi^h(s) = Ze2\pi \sum_{ip \in \Delta s} v_\parallel \frac{\Phi'(s)}{\sigma B(s,\theta)} \frac{w_p}{\mathcal{J} 2 \Delta s 2\pi 2\pi} \tag{7.4b}$$

- Pressures

$$p_{th}^h(s) \;=\; 2\pi \sum_{\substack{ip \in \Delta s \\ E_p < E_c}} \frac{v^2}{3} \frac{w_p}{\mathcal{J} \Delta s 2\pi 2\pi} \tag{7.4ca}$$

$$p_\parallel^h(s,\theta,\varphi) \;=\; 2\pi \sum_{\substack{ip \in \Delta V \\ E_p > E_c}} v_\parallel^2 \frac{w_p}{\mathcal{J} \Delta s \Delta \theta \Delta \varphi} \tag{7.4cb}$$

$$p_\perp^h(s,\theta,\varphi) \;=\; 2\pi \sum_{\substack{ip \in \Delta V \\ E_p > E_c}} \frac{v_\perp^2}{2} \frac{w_p}{\mathcal{J} \Delta s \Delta \theta \Delta \varphi} \tag{7.4cc}$$

We write these quantities in terms of (s, θ, φ), not (s, B). Although (s, B) has been used in Chapter 4 and reduces the number of variables to two even in the general 3D cases, we found that writing it in terms of (s, θ, φ) is more intuitive to understand. Moreover, in the two dimensional case (tokamak), using (s, θ) and $\Delta \varphi = 2\pi$ is exactly equivalent to (s, B). As noted above, with this procedure, the (potentially noisy) Monte Carlo distribution function is not directly used for the iterations, but rather the integrated moments. This represents an initial smoothing of the distribution function. One can smooth the obtained profiles additionally with an appropriate interpolation mechanism if required.

7.4. Iteration outputs

As described in Sec. 4 and Ref. 50, the inputs to the equilibrium code VMEC are $p(\bar{s})$, $p_h(\bar{s})$, $T_\perp/T_\parallel(\bar{s})$, B_c and either the toroidal current $J(\bar{s})$ or the inverse safety factor $\iota(\bar{s}) \equiv 1/q(\bar{s})$. In order to create new inputs to VMEC and LEMan, we have to pass from the radial position of the particles s to the orbit averaged radial variable $\bar{s}$ as defined in Eq. (4.2). Without Monte Carlo interaction operators, the distribution function does not evolve in time, and, equivalently, the particle orbits do not change in shape. In this case, finding the moments in terms of the orbit averaged radial position is equivalent to time averaging the integrated moments (7.4) over many orbit revolutions. Therefore, at the end of a given VENUS run, we switch the action of the Monte Carlo interaction operators off, and perform the time average of the integrated moments. Note that for this, all bins in phase space are kept constant during this averaging, and thus $\Delta s \to \Delta \bar{s}$, and finally $s \to \bar{s}$ in Eqs. (7.4). Density and pressure from the thermal contribution of the minority population, Eqs. (7.4aa) and (7.4ca), can be directly passed to VMEC and LEMan. The thermal pressure is added to the background pressure in VMEC, whereas the density and temperature (using $p = nT$ for Maxwellian distributions) are read by LEMan as second (warm Maxwellian) background species. We are left with the computation of the hot parallel pressure amplitude $p_h(\bar{s})$, the anisotropy $T_\perp/T_\parallel(\bar{s})$ and the total toroidal current $J(\bar{s})$ for VMEC. For LEMan, the density-like factor $\mathcal{N}(\bar{s})$ and the hot parallel temperature have to be found additionally.

From the relations given in Ref. 50 and Section 4, we can find the quantities we are looking for in a straightforward way. First, we find the anisotropy $A(\bar{s}) \equiv T_\perp/T_\parallel(\bar{s})$ (denoted A in what follows for simplicity) from the integrated moments of the distribution function:

$$\frac{p_\perp^h(\bar{s},\theta,\varphi)}{p_\parallel^h(\bar{s},\theta,\varphi)} = M(\bar{s},A,B), \tag{7.5a}$$

where

$$M(\bar{s},A,B) = \begin{cases} A\frac{B}{B_c}\left[1 - A\left(1 - B/B_c\right)\right]^{-1} & ,B > B_c \\ A\frac{B}{B_c}\frac{[1+A(1-B/B_c)]^2 - 5[A(1-B/B_c)]^{3/2} + [A(1-B/B_c)]^{7/2}}{\{1-A^2(1-B/B_c)^2\}\{1+A(1-B/B_c) - 2[A(1-B/B_c)]^{5/2}\}} & ,B < B_c \end{cases} \tag{7.5b}$$

$p_\perp^h(\bar{s},\theta,\varphi)$ and $p_\parallel^h(\bar{s},\theta,\varphi)$ are known from the distribution function, $B(\bar{s},\theta,\varphi)$ is known from the equilibrium, and B_c is an input parameter. For the regions where $B > B_c$, the anisotropy $A(\bar{s})$ can be computed directly, whereas a root finding algorithm has to be applied in the case $B < B_c$. In VENUS a simple secant method is implemented to that end. The second quantity to be determined is the hot parallel pressure amplitude p_h, which can be found using the definition in Eq. (4.6). The hot parallel pressure is known from (7.4c) and the thermal pressure from the background, so that we can simply invert the equation for the hot parallel pressure to find $p_h(\bar{s})$. For the density-like amplitude factor $\mathcal{N}(\bar{s})$, Eq. (4.3) gives the relation to the physical density found in Eq. (7.4a) which can again be inverted once the anisotropy has been found. The hot parallel temperature

$T_{\parallel}(\bar{s})$ is finally found using its relation to the previously found $\mathcal{N}(\bar{s})$, $p_h(\bar{s})$ and the thermal pressure $p(\bar{s})$, Eq. (4.5). As a summary and for more clarity, we give the explicit relations once more with the geometrical factors $\mathcal{C}(\bar{s}, B)$ and $H(\bar{s}, B)$ given in Eqs. (4.3b) and (4.4b):

$$p_h(\bar{s}) = \left\langle \frac{p_{\parallel}^h(\bar{s}, \theta, \varphi)}{p(\bar{s}) H(\bar{s}, B)} \right\rangle \tag{7.6}$$

$$\mathcal{N}(\bar{s}) = \left\langle \sqrt{A(\bar{s})} \frac{n^h(\bar{s}, \theta, \varphi)}{\mathcal{C}(\bar{s}, B)} \right\rangle \tag{7.7}$$

$$T_{\parallel}(\bar{s}) = \left\langle \frac{p_{\parallel}^h(\bar{s}, \theta, \varphi)}{\mathcal{N}(\bar{s}) H(\bar{s}, B)} \right\rangle . \tag{7.8}$$

The angular brackets $\langle \cdot \rangle$ have been added for the following reason: Eqs. (7.5) to (7.8) are fitting the arbitrary distribution function from VENUS onto the bi-Maxwellian implemented in VMEC and LEMan. Indeed, in the frame of the bi-Maxwellian (4.1), the factors $p_{\parallel}^h(\bar{s}, \theta, \varphi)/H(\bar{s}, B)$, $n^h(\bar{s}, \theta, \varphi)/\mathcal{C}(\bar{s}, B)$ and $A(\bar{s})$ in Eq. (7.5) do not depend on any variable other than $\bar{s}$. But, since the pressures and density are not evaluated on the basis of the bi-Maxwellian, this is not true. The fitting is done in such a way that $A(\bar{s})$, $p_h(\bar{s})$, $\mathcal{N}(\bar{s})$ and $T_{\parallel}(\bar{s})$ are computed in each poloidal and toroidal cell for one given radial cell, and a poloidal and toroidal average is performed (thus the angular brackets). As a result, the radial profiles needed for the equilibrium and wave computations correspond to the analytical model implemented in the corresponding codes. Finally, the current computed as in Eq. (7.4b) does not include the reaction of the background ions and electrons. This reaction has to be included in the equilibrium computations. Indeed, the accelerated fast ions drag electrons with them due to the charge separation and the resulting electric field. Also, if more fast ions are circulating in one toroidal direction than into the other, total angular momentum conservation has to be invoked. This has the effect that bulk ions will move in the inverse direction. Both of these effects diminish the effective current and have to be considered for the equilibrium current. Momentum conservation and quasi-neutrality and the balance of collision rates then yield,[68,69]

$$
\begin{aligned}
j_{\text{VMEC}}^{\text{RF}} = \quad & j_{\text{VENUS}}^{\text{RF}} \left[1 - \frac{Z_h}{Z_{\text{eff}}} - \frac{m_h \sum_i Z_i n_i (1 - Z_i/Z_{\text{eff}})}{Z_h \sum_i n_i m_i} \right. \\
& \left. + \quad 1.46 \sqrt{\frac{r}{R_0}} A(Z_{\text{eff}}) \left(\frac{Z_h}{Z_{\text{eff}}} - \frac{m_h \sum_i n_i Z_i^2}{Z_h Z_{\text{eff}} \sum_i n_i m_i} \right) \right],
\end{aligned}
\tag{7.9}
$$

where the $1 - Z_h/Z_{\text{eff}}$ term comes from the electron drag, and the third term from the bulk ions moving in the opposite way. Both effects are diminished by the fraction of trapped particles, which is proportional to $\sqrt{r/R_0}$ as discussed earlier in Eq. (2.37). The RF induced current density (7.9) can be integrated over space and added to the Ohmic toroidal current, allowing for a change in the safety factor profile due to ICCD. Obviously, we choose thus the total toroidal current $J(s)$ as input, and determine the corresponding safety factor profile from VMEC.

Eqs. (7.5) to (7.9) are implemented in VENUS for finding new inputs to VMEC and LEMan at the end of each iteration. The resulting radial profiles are then smoothed out over s using an advanced cubic spline.[70] For refining the statistical results even further, the spatial binning can be adjusted, as explained in the following section.

7.5. Spatial binning

For more useful binning, several advancements have been introduced into the way VENUS treats the bins for the statistics. In the poloidal direction, the binning is in the interval $[-\pi, \pi]$ instead of $[0, 2\pi]$, such that if one chooses an odd number of poloidal bins nbinspol, the center of bin number (nbinspol+1)/2 is exactly along $\theta = 0$. This is especially useful when one wants to look at the distribution function at $\theta = 0$, which is traditionally the case. In the radial direction, a linear binning in s would be nonlinear in r and thus in terms of r not be very precise towards the magnetic axis (recall that $s \sim r^2$). A coefficient α has therefore been introduced, such that the radial interval borders $s_b(0 : \texttt{nbinsrad})$ for s are at

$$s_b(0) = s_b^0 \tag{7.10}$$

$$s_b(n) = s_b^0 + (s_b^{\texttt{nbinsrad}} - s_b^0) \left(\frac{n}{\texttt{nbinsrad}}\right)^\alpha \tag{7.11}$$

Every time the statistics module is called, these interval borders are used (fixed in the beginning once and for all) for the radial binning. The value of $s(n)$ is then computed every time as the mean value of all the particles' radial position s counted within that bin. This means that $s(n)$ is not exactly at the mid-value between $s_b(n-1)$ and $s_b(n)$, but at the position weighted by the density variation within the bin. Also, the Boozer poloidal grid is not equidistant in real poloidal angle. The LFS has indeed (much) less poloidal grid points than the HFS. In order to correct that, the number of poloidal grid points has been made dependent of the radial position in the following way:

$$N_\theta(n) = \left[\frac{\texttt{nbinspol}}{\beta} + \texttt{nbinspol}(1 - 1/\beta)\frac{n-1}{\texttt{nbinsrad} - 1}\right] \tag{7.12}$$

where $[\cdot]$ denotes integer part. It now follows that, for $\beta > 1$ ($\beta < 1$), there are fewer (more) poloidal bins in the centre ($N_\theta(1) = \texttt{nbinspol}/\beta$, $N_\theta(\texttt{nbinsrad}) = \texttt{nbinspol}$), which can enhance statistics by ensuring large enough bins, and therefore enough particles per bin, (good resolution) also in the centre. Fig. 7.2 shows the effect of the parameters α and β on the 2D grid. For simplicity, we chose $\alpha = \beta$ for these plots, but the two parameters are of course independent.

(a) $\alpha = \beta = 2.0$ (b) $\alpha = \beta = 1.5$ (c) $\alpha = \beta = 1.0$ (d) $\alpha = \beta = 0.75$ (e) $\alpha = \beta = 0.5$
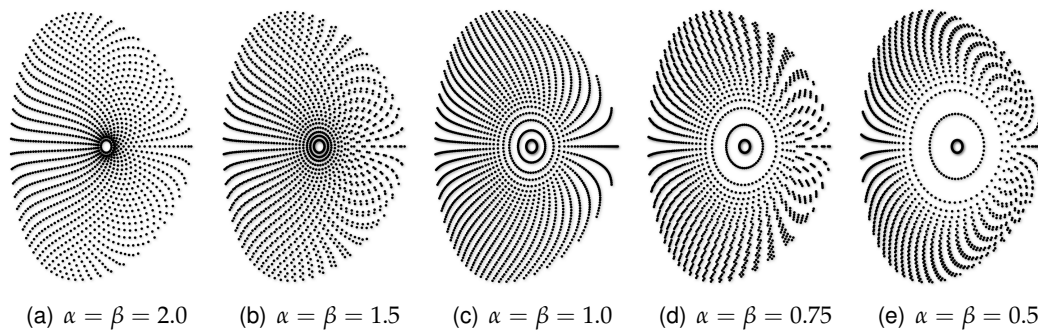
Figure 7.2.: Effect of the binning exponent α and the poloidal parameter β on the 2D grid in the poloidal plane. $\alpha = \beta = 1$ follows the Boozer coodinates, $\alpha = 2$ yields equidistant minor radius grid. Here, `nbinsrad=36`, `nbinspol=55`.

Numerical simulations

After the description of the numerical model, we now use SCENIC for numerical simulations. First of all, single particle dynamics will be studied in Chapter 8. LEMan is not required in this chapter, and the simulated particles in VENUS are considered free of any interaction, such that the orbits are constrained purely to the equations of motion (6.4). This chapter allows for a study of how the equilibrium alone can act on the particle orbits, and as an example, the toroidal drift frequency of trapped particles is determined. Also, the power of VENUS can be made clear explicitly showing non-standard orbits, here represented by so-called tear drop orbits due to poloidal variation of the magnetic field.

Starting with Chapter 9, the newly introduced operators will be tested. Benchmarking against SELFO in Chapter 10 will represent the final tests and first results, before applying SCENIC independently to low and high power scenarios in Chapter 11 and 12 respectively. Here, we will be in a position to study the effects of ion cyclotron heating on the equilibrium and dielectric tensor, taking full advantage of the code package.

8. Single particle dynamics

As a first application, we consider the combination VMEC-VENUS, where all interaction operators in VENUS have been turned off. This allows for a detailed study of how the equilibrium influences the unperturbed particle orbits. In particular, we will show how the perpendicular pressure gradient acts on the toroidal drift frequency of trapped particles. The latter is an important quantity for MHD stability, besides the effect of the current, which will be studied in later chapters. Finally, non-standard orbits will be visualised at the end of the chapter in the form of tear drop orbits.

8.1. Toroidal drift frequency

Regions of unfavourable curvature can lead to instabilities such as collisionless trapped-electron modes, fishbones and many others. The stability of these modes is largely determined by the toroidal precession drift of trapped particles. Rosenbluth and Sloan[71] have shown that such modes can be affected in regions of bad curvature through plasma diamagnetism (i.e. the effect of the pressure gradient on the magnetic field strength), which can inverse the sign of the precession drift frequency ω_D of a single particle. Furthermore, Beer et $al.$[72] have shown the importance of the toroidal drift on trapped electron modes using a $s - \alpha$ model and concentrated on the effects of the local and global shear on ω_D in enhanced reverse-shear discharges, where it was found that the dominant stabilising effect was the reversal of the toroidal precession drifts of barely trapped electrons. We note here that for a large aspect ratio, low to moderate β equilibrium, the local shear is defined by the second derivative of the Shafranov shift. Furthermore, a few years earlier, Wu et $al.$[73] studied the effects of trapped alpha particles on internal kink and fishbone modes, including shaping, local and global shear. It was found that elongation and the Shafranov shift can significantly reduce the magnitude of the precessional drift frequency and enhance the trapped particle drift reversal domain in pitch angle space. Finally, Connor et $al.$[74] investigated the effects of pressure gradients self-consistently by considering the diamagnetic well effect together with the effect of local and global shear. The latter study is nevertheless essentially restricted to equilibria which do not contain a significant auxiliary heated fast ions energy content. Indeed, the authors stress that a consistent treatment of the effect of finite β from energetic ions on the toroidal precession drift should in general involve an anisotropic pressure equilibrium.

In this section, we will concentrate on the effects of pressure anisotropy, both parallel dominated and perpendicular. Clearly this is also motivated by the fact that ICRH heating creates anisotropic equilibria where $p_\perp > p_\parallel$, while another well established heating possibility, tangential Neutral Beam Injection (NBI) heating, typically has parallel anisotropy $p_\perp < p_\parallel$. Deposition can be strongly localised, creating large gradients in local beta values ($\beta = 2p/B^2$), which in turn gives rise to a reduction or even reversal in the toroidal drift precession.

We know that in isotropic plasmas the effect of the pressure on the precession drift frequency enters through a local shear and a magnetic well effect.[74] The local shear is proportional to $r\Delta''$, where Δ denotes the Shafranov shift as defined in Eq. (2.12), and the effect of pressure on Δ'' is given in Eq. (2.27). The latter equation can be integrated to give[75,51]

$$\Delta'(r) = \frac{r}{R_0}\left(\frac{l_i}{2} + \langle \beta_p \rangle + \beta_{ph}^A\right),$$ (8.1)

with $\beta_{ph}^A = 2\mu_0 q^2 \langle p^h \cos 2\theta \rangle$, $p^h = (p_\parallel^h + p_\perp^h)/2, l_i = (2q^2/r^4)\int_0^r \mathrm{d}r^3/q^2$ is the internal inductance, and $\langle \beta_p \rangle = -(2\mu_0 q^2/B_0^2\epsilon^2)\int_0^r \mathrm{d}r(r/r_1)^2 \times \mathrm{d}\langle p \rangle/\mathrm{d}r$ the local poloidal beta. Angular brackets mean flux surface average. Thus, using the standard notation for this thesis, Eq. (2.27) is an equation for Δ'' only and reads

$$R_0\Delta'' = (2\hat{s} - 3)\left(\frac{l_i}{2} + \langle \beta_p \rangle\right) - 2r\langle \beta_p \rangle' + (2\hat{s} - 1)\beta_{ph}^A + r\beta_{ph}^{A'}.$$ (8.2)

with the magnetic shear $\hat{s} = (r/q)\mathrm{d}q/\mathrm{d}r$. The magnetic well effect in an isotropic plasma is described through the ballooning mode parameter

$$\alpha = -\frac{2R_0 q^2}{B_0^2}\frac{\mathrm{d}p}{\mathrm{d}r},$$ (8.3)

with standard notations. Given that we will study anisotropic pressure equilibria, it is convenient in this study to define a new parameter

$$\alpha_\perp = -\frac{2R_0 q^2}{B_0^2}\frac{\partial p_\perp}{\partial r},$$ (8.4)

thus depending only on the perpendicular pressure component. Note that in the isotropic limit, $\alpha = \alpha_\perp$, since $p_\parallel = p_\perp = p$.

In the following, we define a JET-like equilibrium with a major radius of $R_0 = 3.16\,\mathrm{m}$, edge minor radius $a = 1\,\mathrm{m}$, elongation $\kappa_a = 1.4$ and triangularity $\delta_a = 0.4$. The q-profile was chosen to be $q = q_0 + \Delta q(r/r_1)^2$, with $q_0 = 0.7, \Delta q = 1 - q_0$ and $r_1 = 0.4$. For the calculation of the drift frequency, we followed a test ion of $10\,\mathrm{eV}$ close to the location of maximum pressure gradient. We chose a rather low energy in order to ensure negligible banana orbit width. At each time step, local α and $\alpha_\perp$ are calculated and in the end averaged over the total simulation time. This gives a weighted orbit average of $\alpha_\perp$ similar to the computation of $\bar{s}$ for the equilibrium, where the turning points count more heavily

than the rest of the banana orbit, since the particle spends more time at those points than elsewhere. Mathematically, this corresponds to

$$\langle \alpha_\perp \rangle = \frac{\int \alpha_\perp(\theta)\mathrm{d}t}{\int \mathrm{d}t} \approx \alpha_\perp(\theta_b). \tag{8.5}$$

At the end of the simulation, the average toroidal drift frequency is calculated using the trivial relation

$$\langle \dot{\varphi} \rangle = \frac{\varphi_e - \varphi_i}{t_{tot}}, \tag{8.6}$$

where φ_e is the value of the toroidal angle φ at the last passing of the midplane, φ_i the toroidal angle at the first passing and t_{tot} the total simulation time in-between the first and the last passing of the particle at the midplane. Note that the toroidal angle is not restricted to the interval $[0, 2\pi]$ but can have any value on the real axis. Following Ref. 74, and generalising its expression for the drift frequency to include pressure anisotropy, Ref. 48 could show that the finite β correction to the drift frequency is of the form

$$\omega_D = \omega_D^{(\beta=0)} - \omega' \left(r\Delta'' G_3(\theta_b) + \frac{\langle \alpha_\perp \rangle}{2q^2} \right), \tag{8.7}$$

where $\omega' = qE/rR_0m\Omega_c$, $\Omega_c = eB_0/m$, $\cos(\theta_b) = 1 - 2k^2$ and $k^2 = ((1 - \mu B_0)/\epsilon + 1)/2$. The drift frequency excluding pressure effects $\omega_D^{(\beta=0)}$ has been defined in e.g. Ref. 74 and reads

$$\omega_D^{(\beta=0)} = \omega' \left[G_1(k^2) + 2\hat{s}G_2(k^2) \right]. \tag{8.8}$$

The factors G_{1-3} are defined using the elliptic integrals of the first and second type, $K(k^2) = \int_0^{\pi/2} \mathrm{d}\omega \, [1 - k^2 \sin^2 \omega]^{-1/2}$ and $E(k^2) = \int_0^{\pi/2} \mathrm{d}\omega \, [1 - k^2 \sin^2 \omega]^{1/2}$ to give,

$$G_1(k^2) = 2E(k^2)/K(k^2) - 1 \tag{8.9a}$$
$$G_2(k^2) = 2E(k^2)/K(k^2) + 2(k^2 - 1) \tag{8.9b}$$
$$G_3(k^2) = \frac{4}{3}[(2k^2 - 1)E(k^2)/K(k^2) + (1 - k^2)]. \tag{8.9c}$$

We recognise the first term within the parenthesis of Eq. (8.7) as the local shear effect, the second representing the diamagnetic effect. In the following sections, the approximation of Eq. (8.7) will assist qualitative comparisons between different regimes.

(a) $T_\perp / T_\parallel = 1/10$.   (b) $T_\perp / T_\parallel = 1$.   (c) $T_\perp / T_\parallel = 10$.
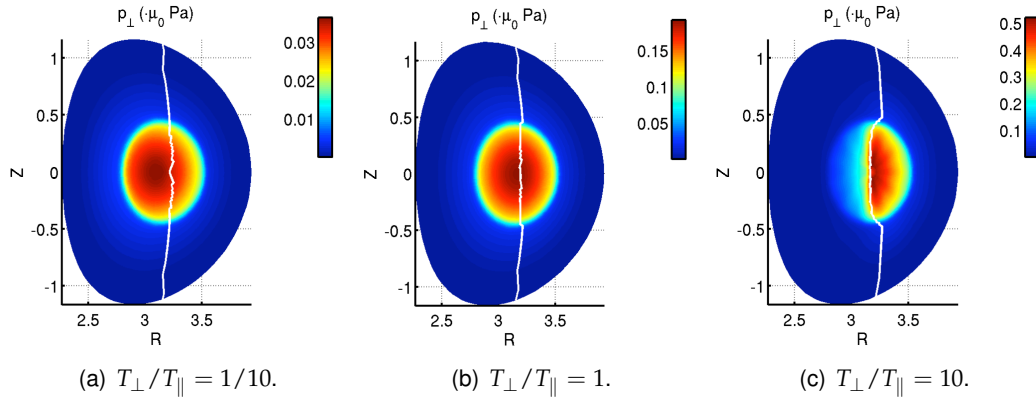
Figure 8.1.: The perpendicular pressure in the RZ plane for the different considered anisotropic cases. The white lines denote the locations of $B = B_c$.

8.1.1. Local shear effect

We first concentrate on the local shear effect, the term proportional to $r\Delta''$ in Eq. (8.7). We compare four equilibria, one with $\beta = 0$, and the other three having the same profile for the flux surface averaged α,

$$\bar\alpha = -\frac{R_0 q^2}{B_0^2} \frac{\int (p'_\parallel + p'_\perp)\mathrm{d}\theta}{\int \mathrm{d}\theta},\tag{8.10}$$

which at its peak (at $r/a = 0.4$, where all the simulations are done) is $\bar\alpha \approx 1.03$. The latter three cases however differ with respect to their values of $T_\perp / T_\parallel$, and are shown in Fig. 8.1 to have $T_\perp / T_\parallel = 1/10, 1$ and 10. In each it is seen that the hot particle deposition layer is chosen to pass close to the magnetic axis, i.e. $B_c \approx B_0 \approx 3.1\,\mathrm{T}$. Fig. 8.1(c) demonstrates the clearest departure from isotropy. It is seen that the pressure peak is elongated along the resonant layer $B = B_c$. This is due to the fact that hot particle deposition at that location generates preferential banana orbits with tips close to $\theta = \pm 90°$. Despite such spatial dependencies in Fig. 8.1, it turns out that by keeping $\bar\alpha(r)$ the same for all cases in Fig. 8.1, the profile for the Shafranov shift is almost the same for $\beta \neq 0$,[8] as shown in Fig. 8.2(a), where we plot $r\Delta''$. The only contrasting profile is that of the case with zero β. It follows that the local shear effect should lead to the same offset in ω_D for the three cases relative to the $\beta = 0$ case. The magnetic drift frequencies corresponding to the four equilibria, normalised to ω', are shown in Fig. 8.2(b). The differences between the lower three curves can be identified with the offset due to the diamagnetic effect (last term in Eq. (8.7)), and will be described in the next section. We can however most easily identify the local shear effect by comparing the top two curves in Fig. 8.2(b), i.e. the case with zero β, and the case with $T_\perp / T_\parallel = 1/10$. The reason for this is that both of the latter cases have small $\alpha_\perp$, the corresponding diamagnetic effect giving a small and almost constant offset for all bounce angles, the value being that of the differences of the curves

(a) Profiles of $r\Delta''$ for the four equilibria.

(b) The precession drift frequencies as functions of the bounce angle.
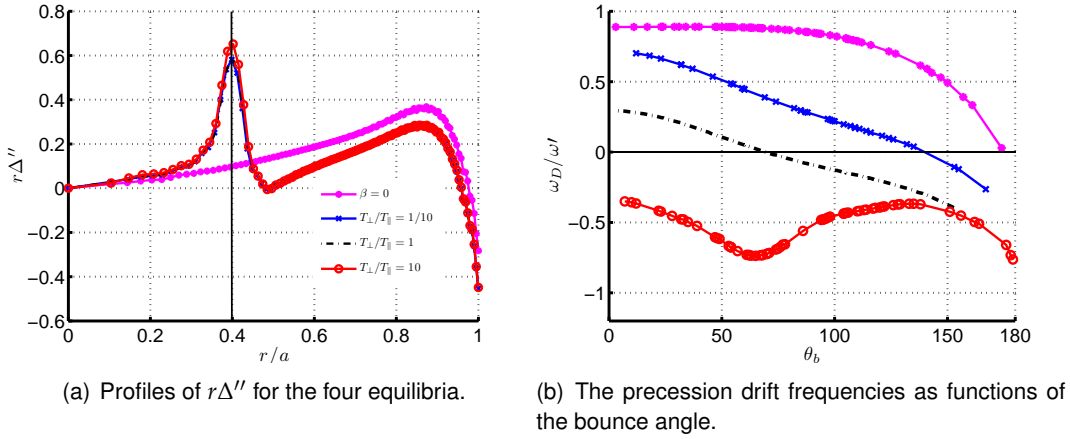
Figure 8.2.: The toroidal precession drift frequencies are different from one another, even if the local shear has the same effect in all cases. The line in (a) shows the radial location of the orbits. Starred (*) and magenta: $p = 0$, crosses (x) and blue: $T_\perp/T_\parallel = 1/10$, dots and black: $T_\perp/T_\parallel = 1$, circles (o) and red: $T_\perp/T_\parallel = 10$.

at $\theta_b = 0°$ or $\theta_b = 180°$ (since then $G_3 = 0$). Hence, the local shear effect is seen to reduce the drift for intermediate pitch angles, as is clear if one plots G_3 as a function of θ_b. If at the same time $\alpha_\perp$ is sufficiently large, the local shear effect can enable a wider region of pitch angle space where the direction of ω_D is reversed. This is the case for the isotropic finite β curve, and the $T_\perp/T_\parallel = 10$ curve in Fig. 8.2(b). Nevertheless, we see that the finite β effect in the perpendicular anisotropy case and the isotropic finite β case is dominated by the diamagnetic effects, and these are described next.

8.1.2. Diamagnetic effect

Figure 8.3 shows the same frequencies as before, though not including the $\beta = 0$ case, but now compared to the values of $\langle \alpha_\perp \rangle$ instead of $r\Delta''$. One can clearly see a bump appearing in the drift frequency for the case of perpendicular anisotropy ($T_\perp/T_\parallel = 10$), located at same bounce angle as the maximum of $\langle \alpha_\perp \rangle$. Also, ω_D is considerably higher for parallel anisotropy ($T_\perp/T_\parallel = 1/10$), where $\langle \alpha_\perp \rangle$ is much lower. Note that for the three different cases $T_\perp/T_\parallel = 10, 1$ and $1/10$, the flux surface averaged parameter $\bar{\alpha}$ at $r/a = 0.4$ was a constant value $\bar{\alpha} \approx 1.03$. From this, three different conclusions can be drawn: First, the diamagnetic effect is more important than the local shear effect for $T_\perp/T_\parallel \geq 1$ and $q \sim 1$. Second, the diamagnetic effect can also lower the toroidal precession drift frequency of deeply trapped particles, such that the frequency can be negative for all pitch angles. Third, anisotropy can introduce an important poloidal dependence of ω_D through a poloidal dependence of $\alpha_\perp$, i.e. of the perpendicular pressure and its gradient.

With off-axis heating, it is possible to shift the maximum pressure gradient in the RZ plane. Fig. 8.4 shows the pressure surfaces for high field side (HFS) and low field side (LFS) heating. As stated above, the deposition location can be chosen via the value of

(a) $\alpha_\perp$ as a function of the bounce angle.

(b) Toroidal magnetic drift frequency
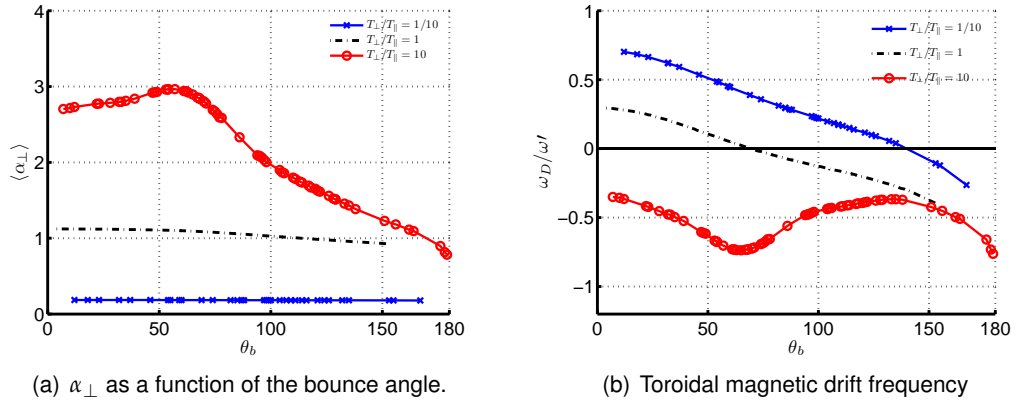
Figure 8.3.: The toroidal drift frequency depends on the parameter $\alpha_\perp = -2R_0 q^2 / B_0^2 (p'_\perp)$, which has a strong poloidal dependence.

the parameter B_c in the equilibrium code VMEC. Note that the peak of the pressure profile is not exactly at the locations of $B = B_c$. For all of the equilibria generated in this chapter, a sharp pressure gradient was imposed at the radial location $r/a = 0.4$. Outside this surface, the pressure is very low. The effect of LFS heating on the poloidal variation of $p_\perp$ is very strong, since in that case the deeply trapped particle fraction is higher than for HFS heating, where more barely trapped particles are created. More barely trapped particles tend then to average out a poloidal variation in $p_\perp$. The shifting of the pressure peak towards the inboard side (HFS heating) results in a shift in the maximum pressure gradient towards $\theta = \pi$, whereas the shifting of the pressure peak towards the outboard side (LFS heating) results in a shift in the maximum pressure gradient towards $\theta = 0$. As a result, one can see in Fig. 8.5 that the bump in precession drift frequency is shifted in the exact same way. For LFS heating, the toroidal drift frequency is even negative for deeply trapped particles, whereas it goes negative for large bounce angle in the case of HFS heating.

With these studies it becomes evident that the important parameter for determining the magnetic precession drift frequency is not the conventional diamagnetic term proportional to α, but rather its perpendicular analogue $\alpha_\perp(\theta_b)$ weighted close to the bounce angle θ_b.

8.1.3. Large orbit width relative to gradient length scales

If we now allow for an increase in the banana orbit width, we can study the case where the characteristic length scale of the pressure gradient is of the order of the banana width, $L_p \sim \Delta r$. Fig. 8.6 shows the effect on the case shown in Fig. 8.5 (LFS heating), but this time with an energy of $300\,\text{keV}$, such that the banana width is about the same as the pressure gradient length. The strong dependence on the bounce angle for deeply trapped particles can be understood as follows: For less deeply trapped orbits (higher θ_b), the particle sees a lower average pressure gradient, since its large banana width leads it into regions with lower $\alpha_\perp$, whereas deeply trapped particles do not see these

(a) Pressure surfaces for HFS heating.   (b) Pressure surfaces for LFS heating.
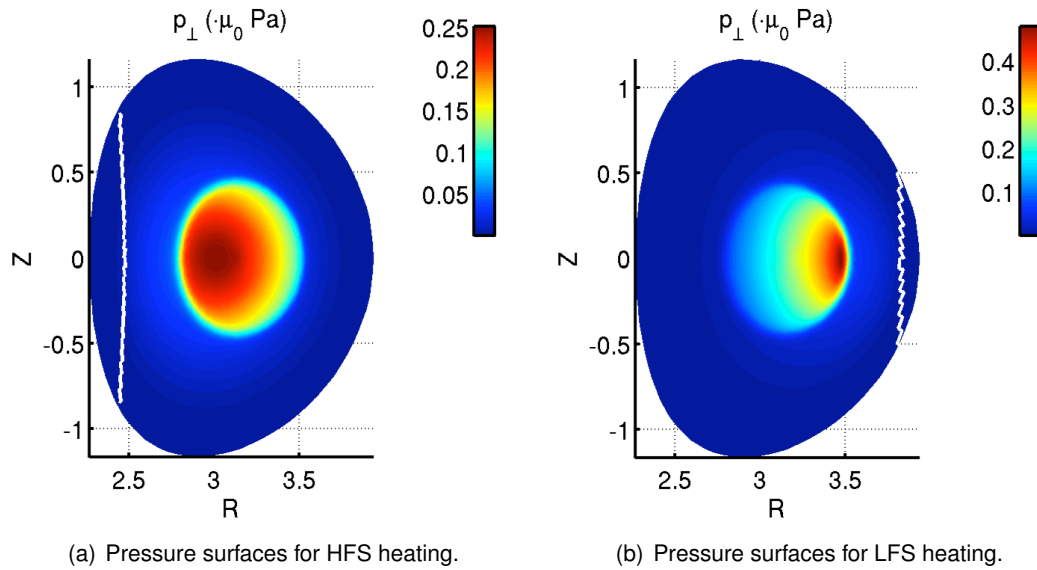
Figure 8.4.: $p_\perp$ in the RZ plane with resonant heating on (a) the HFS and (b) the LFS. In both $T_\perp/T_\parallel = 10$, and they can be compared with the reference equilibrium shown in Fig. 1(a), which has the resonant heating through the magnetic axis.

regions, since their orbit widths are much smaller, and thus their orbit averaged $\langle \alpha_\perp \rangle$ is considerably larger. A second effect is the poloidal variation of $\alpha_\perp$ with perpendicular anisotropy (as already seen above), which is responsible for the plateau in $\langle \alpha_\perp \rangle$ (red line) between 30 and 60 degrees. It is interesting to note that while the greatest effect is for perpendicular anisotropy, it is still considerable for the isotropic case, where $\alpha_\perp$ more than doubles.

8.2. Tear drop orbits

A particle is trapped if its parallel velocity vanishes due to high magnetic field strength, as can be seen in the relation

$$\frac{v_\parallel}{v} = \pm \sqrt{1 - \frac{\mu B}{E}}, \tag{8.11}$$

where μ and E are constant along an unperturbed orbit, such that $v_\parallel/v$ depends exclusively on the magnetic field strength. In a large aspect ratio isotropic plasma, the poloidal variation of B is given by $B \sim 1/R$, so that trapping is up-down-symmetric, and thus the particle passes through the outer midplane $\theta = 0$. If however B is non-monotonic with respect to $|\theta|$, particles can be locally trapped in the corresponding magnetic well. Two examples of non-monotonic B profiles are shown in Fig. 8.7 and will be described later. The trajectories of such trapped particles differ from conventional trapped orbits in that they stay either on the upper $(0 < \theta < \pi)$ or lower half $(\pi < \theta < 2\pi)$ of the plasma, and thus do not pass through the outer midplane. Such kinds of orbits are then called
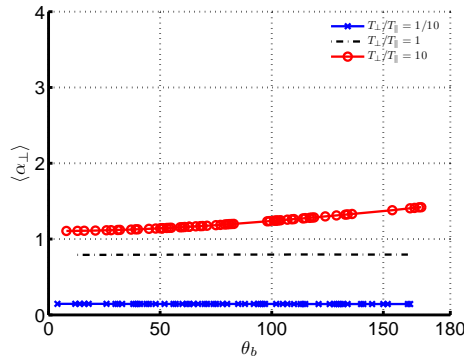
(a) HFS heating: $\langle \alpha_\perp \rangle$ as a function of the bounce angle.
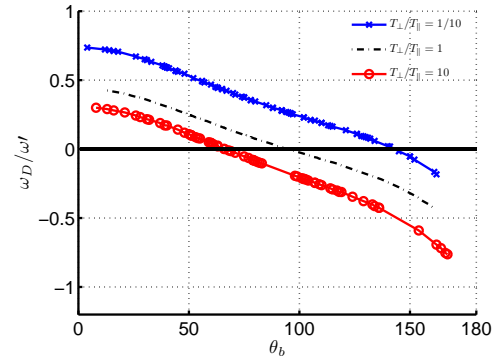
(b) HFS heating: Toroidal magnetic drift frequency
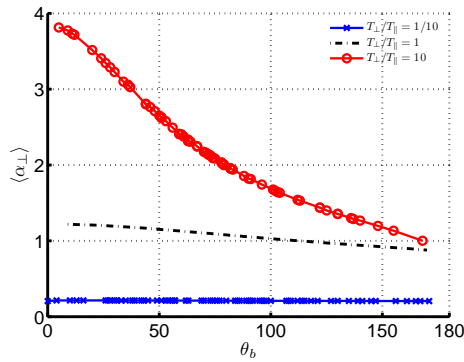
(c) LFS heating: $\langle \alpha_\perp \rangle$ as a function of the bounce angle.
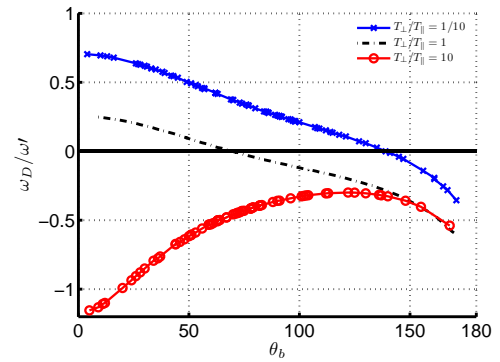
(d) LFS heating: Toroidal magnetic drift frequency

Figure 8.5.: As the peak in $\langle \alpha_\perp \rangle$ shifts to smaller or larger bounce angles for respectively LFS or HFS heating, the form of the drift frequency changes accordingly. The dependence on θ_b should be compared with the on-axis heating case of Fig. 8.3.
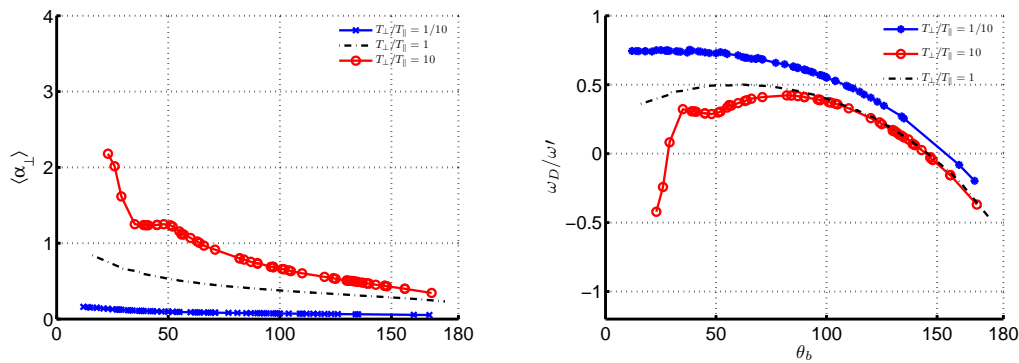
(a) LFS heating with wide banana orbits. Bounce averaged $\langle \alpha_\perp \rangle$ as a function of the bounce angle.

(b) LFS heating with wide banana orbits. Toroidal magnetic drift frequency

Figure 8.6.: Larger particle energies, and wider orbits, modify the magnetic drift frequency in equilibria with highly localised pressure gradients.

tear drop orbits, because of their trajectory in the RZ plane (see Fig. 8.9(a)). In isotropic plasmas, such orbits occur only in tight aspect ratio, because the toroidal and poloidal magnetic fields are of the same order. Nevertheless we point out that the localised trapping can be enhanced with perpendicular pressure anisotropy.

Having the possibility of poloidal dependence in the pressure and magnetic field due to anisotropy, we can enhance the variation of the magnetic field strength in the poloidal angle, as e.g. shown in the isotropic and anisotropic cases of Fig. 8.7. The corresponding perpendicular pressure for the latter two equilibria are shown in Fig. 8.8. In this part of our work, we considered a tight aspect ratio configuration with $R_0 = 1.16\,\mathrm{m}, a = 0.9\,\mathrm{m}$ and an elongation of $\kappa_a = 2.5$ at the edge. This was chosen such that tear drop orbits already can occur in the isotropic case as described above. The triangularity was zero and the safety factor profile unchanged from the previous section. For both the anisotropic and isotropic case, the volume averaged beta $\langle \beta \rangle \approx 1\%$ was kept constant and the flux averaged $\bar{\alpha}$ was similar with $\bar{\alpha} \approx 0.68$ for $T_\perp / T_\parallel = 10$ and $\bar{\alpha} \approx 0.75$ for $T_\perp / T_\parallel = 1$. However, as can be seen in Fig. 8.8, due to the LFS deposition employed, there are two sharp peaks in the anisotropic case compared to the isotropic equilibrium. These two sharp peaks are responsible for a deepened magnetic well shown Fig. 8.7. In the latter figure, the curves show the magnetic field strength as a function of poloidal angle at the radial location of the pressure peaks. The blue (upper) curve is the isotropic and the red (lower) curve is the anisotropic case. With the deepening of the magnetic well, i.e. lowering the minimum field, trapped particles at the well minimum achieve higher parallel velocities according to Eq. (8.11). Thus the particle orbits in isotropic and anisotropic equilibria are different in three dimensional space, and especially in the toroidal direction, as shown in Fig. 8.9. Here we show that the difference in the RZ plane (tear drop orbits) is rather small, whereas it is considerable in the toroidal angle, as shown by the s-like trajectory of the orbit in the 3D plot of Fig. 8.9(b) (red curve). This can be seen as an
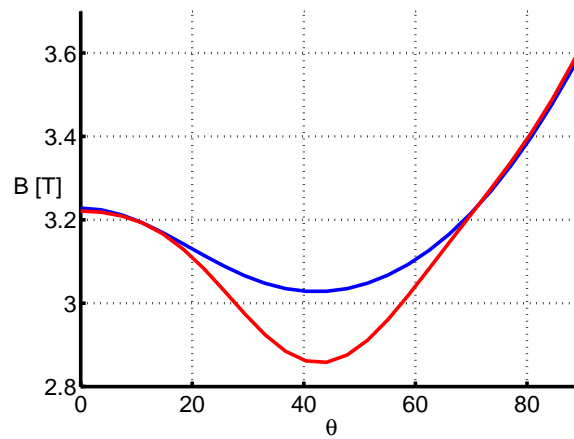
Figure 8.7.: Poloidal dependence of the pressure results in a stronger poloidal dependence of the magnetic field strength. The (upper) blue curve corresponds to $T_\perp/T_\parallel = 1$, the lower (red) curve to $T_\perp/T_\parallel = 10$.

indication that following the particle orbits in three dimensions can be crucial even in two dimensional equilibria. Note that the orbits were chosen in such a way that the turning points are at the same location (poloidally and radially) in both cases.

This concludes single particle orbit studies, and we will turn towards the study of the effect of ion cyclotron heating on equilibrium, dielectric tensor and distribution function for the rest of this thesis.
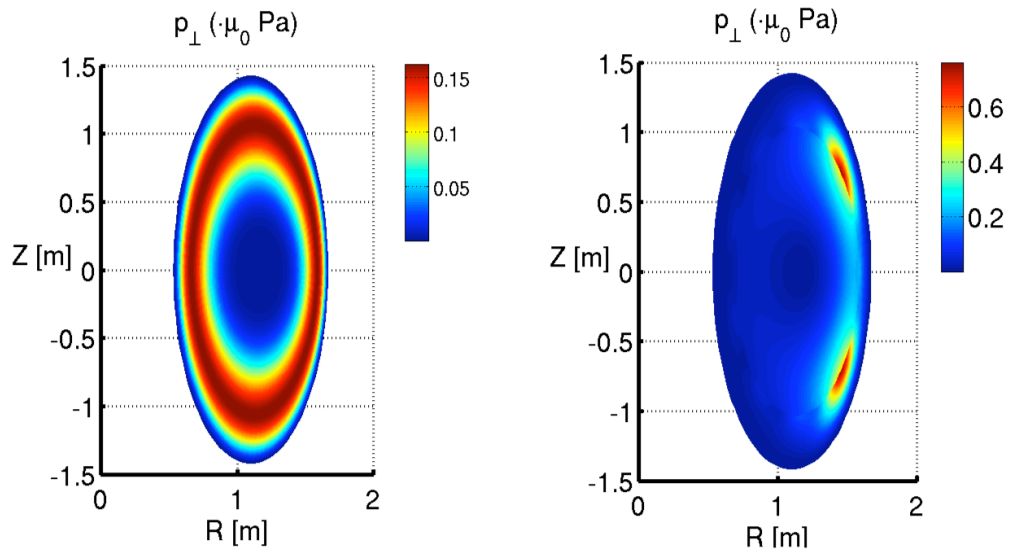
(a) Isotropic case: pressure is a flux surface quantity.

(b) Anisotropic case: pressure has now a poloidal dependence.

Figure 8.8.: Strong poloidal dependence of the pressure due to anisotropy and off-axis heating.
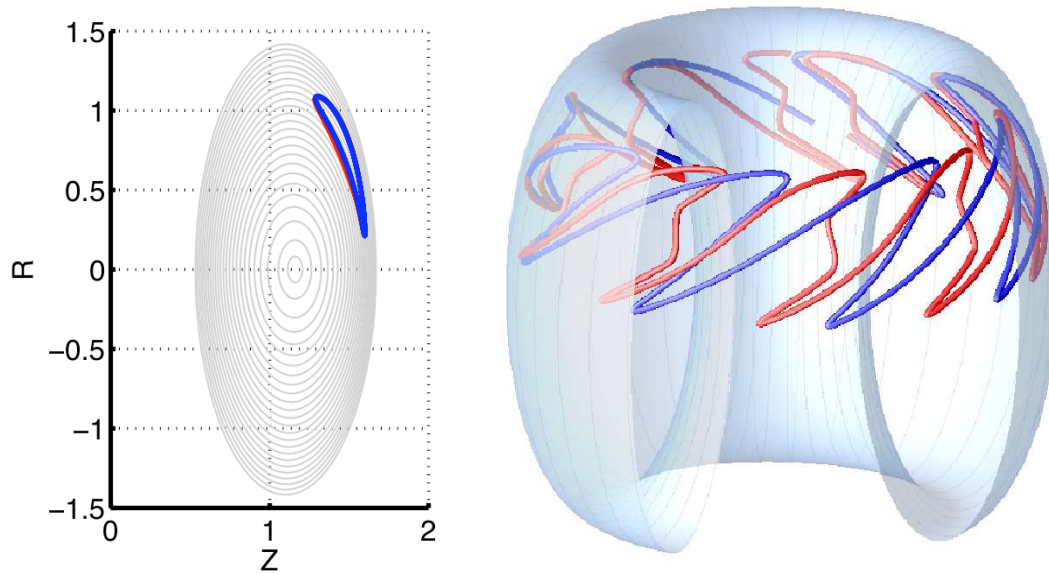
(a) Tear drop orbit in RZ: almost no difference.

(b) In 3D: one can clearly see a difference in toroidal direction.

Figure 8.9.: The deepened magnetic well has an impact mainly on the toroidal direction.

9. Testing with many particles

9.1. Monte Carlo operators

9.1.1. Coulomb collisions

After introducing the Monte Carlo operators described in Sec. 6.2, we will have to check their validity before putting too much confidence in the results. The Monte Carlo method is based on statistical behaviour including many particles. Thus, we will now have to increase the number of particles in the simulations. The Coulomb collision operators have to relax the hot particle distribution function to a Maxwellian with a temperature equal to that of the thermal background particles in the expected time scale. Fig. 9.1(a) shows the relaxation of the hot particle distribution function to a distribution equal to that of the thermal particles. In order to keep the problem as simple as possible, the initial hot particle distribution was chosen to be a Maxwellian ($B_c < B$ and $T_\perp / T_\parallel = 1$ everywhere) but with a temperature (constant in space) which was ten times higher than that of the thermal particles. The latter too where distributed with a constant temperature in space. The slight changes in temperature after saturation at about four slowing-down times can be explained with the fact that only 1'000 particles where used for this simulation and thus the integral of the distribution function cannot be expected to have a greater precision.

Another test of the Coulomb collision operators is to verify that the system becomes isotropic after an initially anisotropic state. Fig. 9.1(b) shows the evolution of the energy as before and the evolution of the radial profile of the anisotropy $T_\perp / T_\parallel$ is plotted in Fig. 9.1(c). The same equilibrium as before was used, with the difference that the parallel hot particle temperature was the same as the thermal temperature, whereas the perpendicular temperature was ten times higher in the beginning of the simulation. We can see in Figs. 9.1(b) and 9.1(c) that the anisotropy needs about five slowing-down times to saturate at the final (and expected) constant value of unity. The simple reason is that the relevant time scale here is not the energy-relaxation (i.e. slowing-down) time, but rather the typical time scale of Coulomb pitch angle scattering, which is longer at higher energy (as is the case for the starting energy in this simulation. See Fig. 6.3).

87
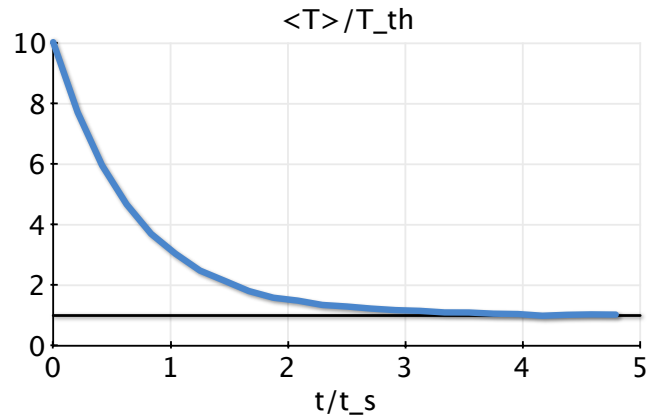
(a) The hot particle distribution relaxes to a Maxwellian with the same temperature as the background thermal distribution.
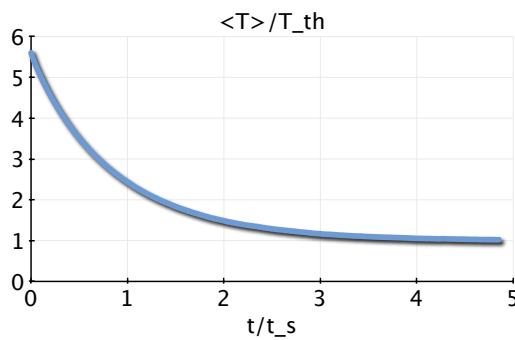
(b) Temperature evolution when initialised with $T_\perp = 10T_\parallel = T_{th}$.
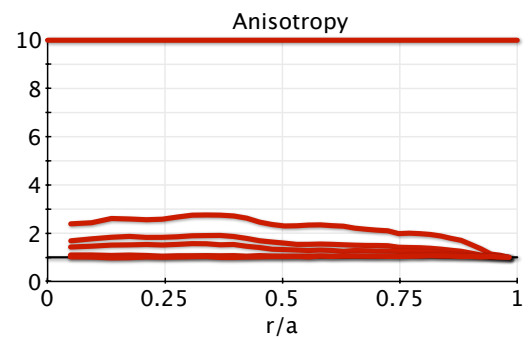
(c) Anisotropy $T_\perp / T_\parallel$ profile evolution when initialised with $T_\perp = 10T_\parallel = T_{th}$.

Figure 9.1.: Coulomb collisions have the effect that any minority distribution function will become isotropic and have the same temperature as the background species. Anisotropy denotes the factor $T_\perp / T_\parallel$. The simulations were conducted using one million particles on a 36x55 grid.
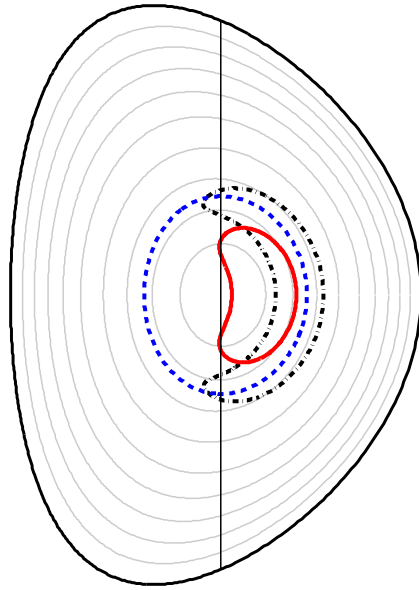
Figure 9.2.: Orbit evolution due to ICRH. Blue and dashed: Starting passing orbit. Black and dash-dotted: Banana orbit after $80\,\mathrm{ms}$. Red and solid: Banana orbit after $300\,\mathrm{ms}$. Note the alignment on the unshifted resonance (black vertical line) at $R = R_c$ as defined in Eq. (9.1). In grey a few selected flux surfaces.

9.1.2. ICRH operators

Particle orbit

A first check of the ICRH operators can be done by looking at one single particle orbit. From theory we expect that a trapped single particle's orbit changes due to the ICRH kicks in such a way that a passing particle (with a pitch angle not too far away from being a trapped particle) is first "converted" into a deeply trapped particle and from there its tip points move in real space towards the resonance and stay there, spending most of their time at the turning points along the resonance.[76] Fig. 9.2 shows an example of such an orbit under the effect of ion cyclotron heating. The resonant layer is at the magnetic axis, i.e. $B_c = B_0$, and the particle is initialised with a pitch angle of $\mu B_c/E = 0.48$ and an energy of $130\,\mathrm{keV}$, which defines in this case a passing orbit. During the simulation, the particle interacts with the background electrons and ions (Coulomb scattering) and receives random kicks in perpendicular and parallel velocity (ICRH interaction). Due to these interactions, after $300\,\mathrm{ms}$, the particle energy reaches $1\,\mathrm{MeV}$ and describes a large banana orbit with a pitch angle of $\mu B_c/E = 1$, i.e. with tip points aligned with the resonant layer. For this orbit, $5\,\mathrm{MW}$ of absorbed power was assumed, and a symmetric wave spectrum was injected with average (over all kicks and particles) parallel wave numbers on the resonance of $k_\parallel \sim \pm 8\,\mathrm{m}^{-1}$, and the average perpendicular wave number was $k_\perp \sim 38\,\mathrm{m}^{-1}$.

Doppler shift

The resonance is Doppler shifted due to the parallel wave length and the particle's parallel velocity. Indeed, for fundamental ICRH, the resonance condition is $\omega = \Omega + k_\parallel v_\parallel$, where we recall that $\omega = qB_c/m$ is the RF field frequency and $\Omega = QB/m$ the local cyclotron frequency at the particle's position. Now, in large aspect ratio tokamaks, one can approximate the magnetic field dependency with $B \approx B_0 R_0/R$ as described in Sec. 2.1.1, and define the (unshifted) resonant major radius using $\omega = \Omega$ as

$$R_c = \frac{QB_0 R_0}{m\omega} = \frac{\Omega_0}{\omega} R_0, \tag{9.1}$$

with Ω_0 the cyclotron frequency at the magnetic axis. The resonance condition then takes the form

$$\frac{1}{R_c} - \frac{1}{R} = \frac{mk_\parallel}{QB_0 R_0} v_\parallel = \frac{k_\parallel v_\parallel}{\Omega_0 R_0}, \tag{9.2}$$

where R denotes the major radius where the Doppler shifted resonance takes place. Defining a the maximum minor radius, the left hand side of Eq. (9.2) has extreme values $\pm 1/L \equiv a/(R_0^2 - a^2)$, such that if we multiply Eq. (9.2) by L, its values will be within the interval $[-1, 1]$ and (all other quantities fixed) depend linearly on $v_\parallel$. A straightforward test is then if for one given parallel wave vector the resonance is indeed linearly shifted as a function of $v_\parallel$. Fig. 9.3 shows this linear dependence of the shift on parallel velocity, as obtained by extracting the needed information from the Monte Carlo operator in VENUS. Note that the slight asymmetry in the y-axis (shift) comes from the fact that the unshifted resonant layer in the realistic magnetic equilibrium and the approximated R_c for creating the plot do not have exactly the same value, since $B_c = B_0 R_0/R_c$ is not exact.

Power deposition

LEMan only needs to provide VENUS with the wave vector and the electric fields. However, it also computes the deposited power, and it is therefore possible to compare the power deposition of LEMan and the power deposition within VENUS. First, we can compute the total energy gained by all the particles inside the plasma during a certain amount of time. Then, this total gained energy by the hot ions in VENUS must equal the total deposited power on the fast population needed for a given simulation (and given as input), multiplied by that same amount of time. This is a very quick and easy check and it can in fact be used as a regulator in VENUS: After regular time intervals Δt, the code checks the total absorbed power and compares it with the wanted absorbed power. If there is a difference, the electric field can be rescaled such that for the next time step the absorbed power should be closer to the expected value. This procedure ensures the correct normalisation of the electric field, and defines the parameter α in Eq. (6.29a).

Second, we can save the location and amplitude of the power deposition each time a kick is given in the Monte Carlo operator. At the end of the run, one can create a two dimensional plot of the deposited power and compare that to a similar plot from LEMan. This is done in Fig. 9.4 with flat temperature ($T = 5\,\text{keV}$) and density ($n_D =$
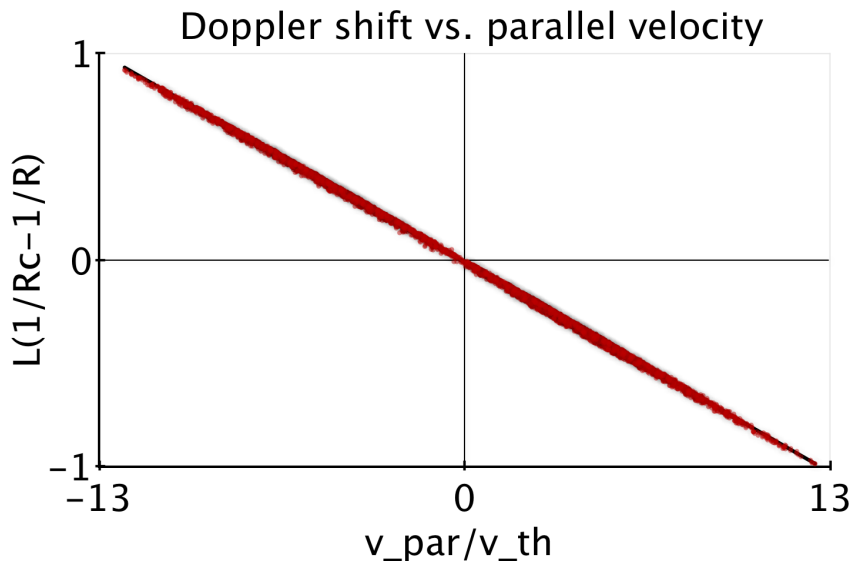
Figure 9.3.: Verification of the Doppler shifted resonant layer (9.2) as a function of $v_\parallel$. $n_\varphi = -27$ and $L = (R_0^2 - a^2)/a$.

$4 \times 10^{19}\,\mathrm{m}^{-3}$) profiles and a minority heating scenario of $2\,\%$ hydrogen in deuterium. The two dimensional power deposition plots and the power density profiles are very similar.

9.2. The statistics module

9.2.1. Splitting mechanism

In Chapter 7 we described how VENUS deals with the fact that the minority population is not entirely heated but evolves into a thermal part and a heated tail. Namely, a critical energy is defined, below which particles are considered Maxwellian (thermal), and above which they are considered bi-Maxwellian and hot, as described in Eq. (7.3). Fig. 9.5 shows a scan of the coefficient x in Eq. (7.3), i.e. different multiples of the electron temperature as critical energies. We chose to plot the energy distribution in terms of $f(E)\sqrt{E}$, corresponding to the number of particles at a given energy (i.e. integrated over real space and pitch angle). The energy is represented in a logarithmic scale, such that the thermal part and the tail are visible as two distinct local maxima. The black curve shows the initial (thermal) distribution and profile (same temperature as background and isotropic).

In Fig. 9.5(a), one can see that a critical energy of two and three times the electron temperature is too small. Too large a fraction of the thermal minority component (solid line) is assigned to the hot part, which is peaked far away from the tail (which is around $100\,\mathrm{keV}$ in that case). In that plot, a factor of five seems to be the correct choice for representing the thermal minority part. This is confirmed by the second plot, Fig. 9.5(b),

(a) LEMan   (b) VENUS

(c) Power density
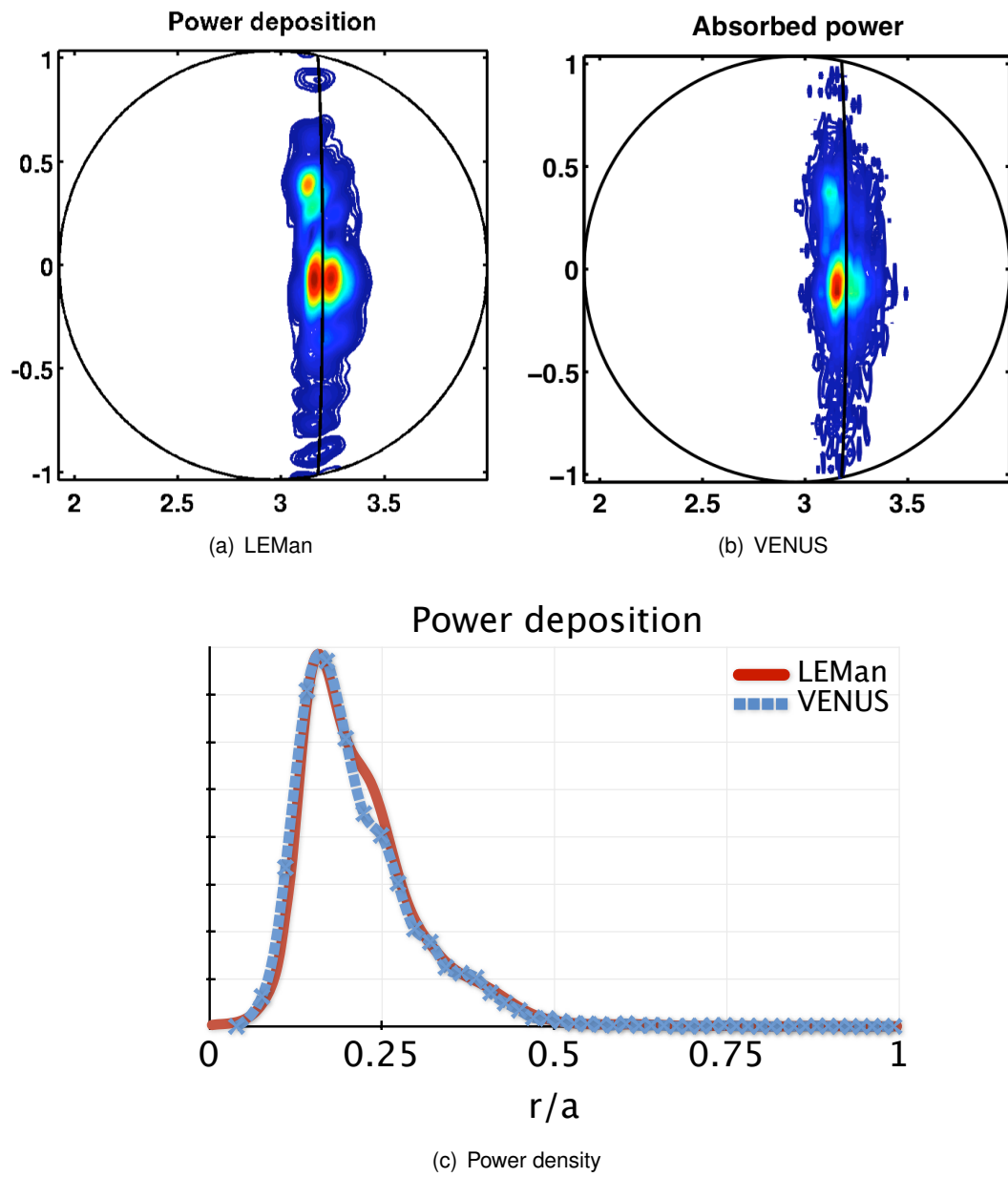
Figure 9.4.: Power deposition comparison between the wave code LEMan and the Monte Carlo
            code VENUS.
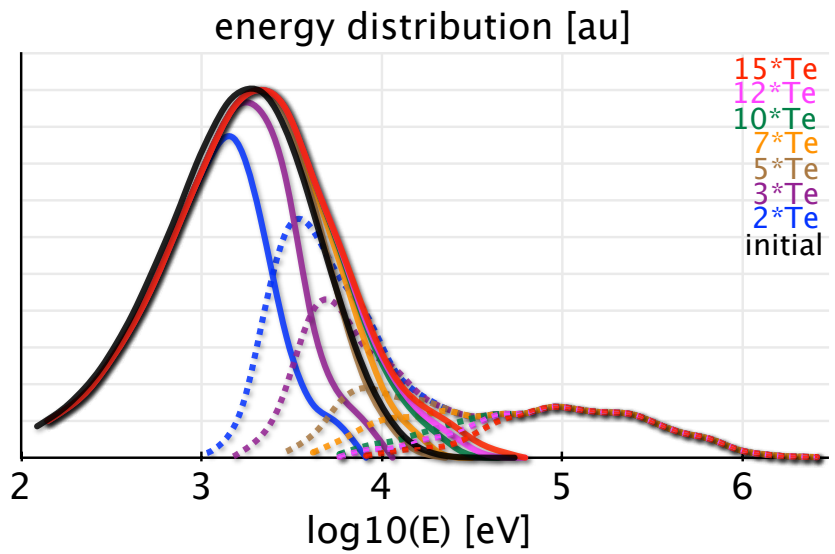
(a) Energy distribution $f(E)\sqrt{E}$ integrated over space and pitch angle. Thermal distribution in solid and tail in dotted lines.
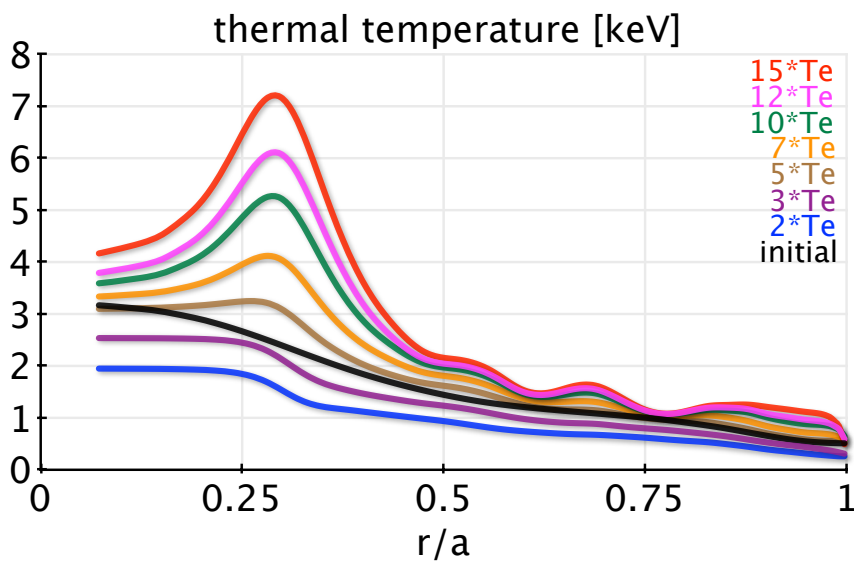
(b) The resulting thermal temperature profiles.

Figure 9.5.: Changing the critical energy for splitting the distribution function. Conditions (7.3) are used for the splitting and in the legends the value of the coefficient x indicated.
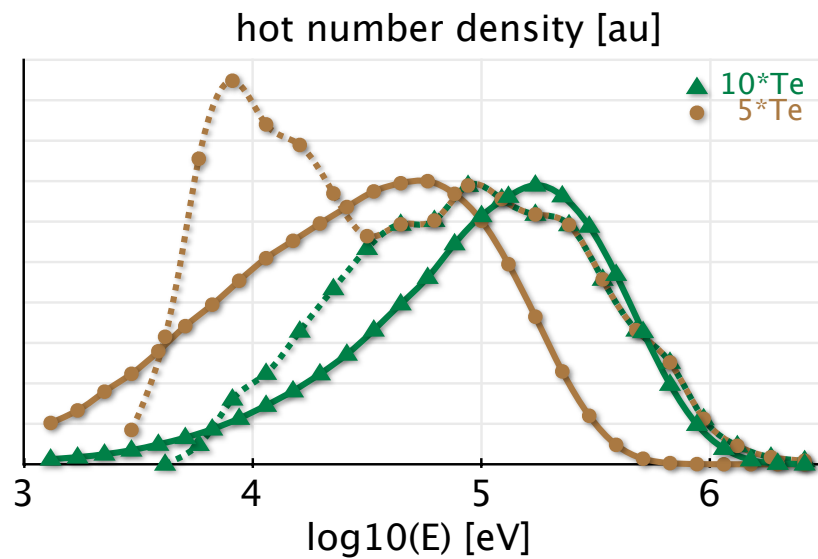
Figure 9.6.: VENUS output of the tail (dotted lines) compared to resulting analytical bi-Maxwellian. Clearly the factor of ten (green,triangles) is closer than the factor of five (brown,circles).

where the temperature profile for the factor of five is closest to the electron temperature (black). However, the main goal of this splitting is to be able to represent the tail as accurately as possible with the bi-Maxwellian model. As one can see from Fig. 9.5(a), the tail is peaked inside the initial thermal curve when using a factor of five, and representing the tail (outside the black curve) will be difficult with this splitting. This is what is shown in Fig. 9.6: The line representing the case of $E_c = 5T_e$ (brown,circles) incorporates a significant number of thermal particles (dotted line), and the analytical modeling for VMEC and LEMan (continuous lines) is further away from the form of the VENUS tail than the case $E_c = 10T_e$ (green,triangles). It becomes clear that choosing the value of E_c is a trade-off between keeping the thermal part at the same temperature as the background and trying to get the analytical model to agree as much as possible in the tail. It is important to remember here that the particle distribution in VENUS is not modified with the splitting and is re-loaded at every iteration the way it was at the end of the previous iteration (i.e. non-Maxwellian). With that, the exact choice of the critical energy is not as crucial as it seems, since the real minority distribution in VENUS is not changed. It is only the model distribution function applied to VMEC and LEMan which changes. Another note to make is that these checks were done for low power. For higher power, the tail will be more clearly separated from the bulk, and the choice for the critical energy should become much more obvious.
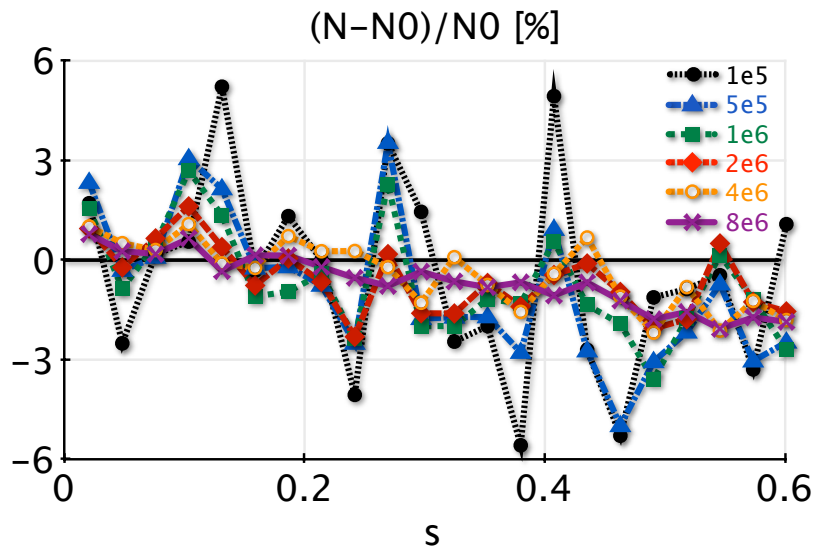
Figure 9.7.: Scan using different number of particles in VENUS. The density factor $\mathcal{N}(s)$ has been recreated directly after initial loading and compared to the input value $\mathcal{N}_0(s)$. The scan is performed from 10^5 to 8×10^6 particles with a grid size of 72x55.

9.3. Numerical behaviour of VENUS

9.3.1. Number of particles

The number of particles required in VENUS depends to a large extent on the chosen simulation. Depending on the heating scenario, pressure and density profiles (and thus also $T_\perp / T_\parallel$ and all other derived quantities) can show strongly localised maxima in both radial and poloidal direction. It is thus helpful to have a rather high number of grid points, up to $96\text{x}75$ (radial x poloidal). Additionally, when iterating between the codes, smooth profiles are needed at every iteration. This asks for a high number of particles. However, when studying a low power scenario, or a case where broad maxima can be expected in the profiles, fewer grid points can be used, decreasing the required number of particles. Fig. 9.7 shows a scan over the number of particles using a 72x55 grid. For this check, we loaded the particles and directly created the VENUS outputs, without advancing the orbits in time. The resulting outputs should be equal to the inputs. Fig. 9.7 then gives the relative difference between input and output of the density factor $\mathcal{N}(s)$ as an example, and we do not consider the values of the radial variable $s > 0.6$ for more clarity. The relative error diminishes for higher particle number, but the the curves of four and eight million particles are rather close to each other and not much different from two million, suggesting a certain saturation.
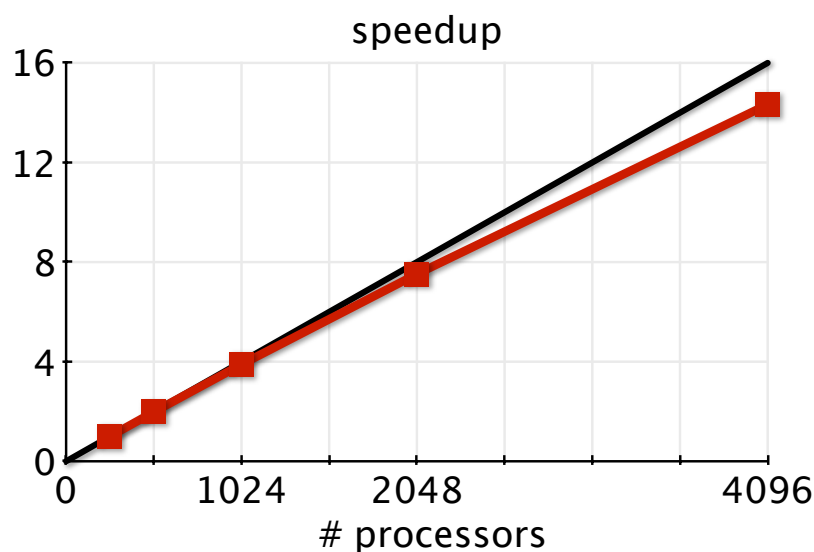
Figure 9.8.: Speedup of the VENUS code from 256 to 4096 processors (strong scaling). The straight line shows perfect scaling.

9.3.2. Scaling

Advancing the distribution function is the most time consuming part of SCENIC. Indeed, a two dimensional equilibrium takes a few seconds on one single processor for VMEC to compute. LEMan needs several minutes using two multicore compute nodes to add the wave field information. In contrast, VENUS requires of the order of tens of thousands of CPU hours for a converged solution (multiple iterations included), depending of course on the number of markers needed. In a typical run, five million markers had to be used and a total converged simulation took about 30'000 CPU hours. It is therefore important that VENUS scales well on high performance computers up to thousands of processors. The markers within VENUS do not interact with each other and thus the code is trivially parallelised by simply distributing the total number of markers among the processors. However, the simulation can of course not be done completely without communication among the processors. In the beginning, the equilibrium and wave field have to be read by all the processors. At the end of every VENUS simulation, the self-consistency modules (described in the next section) need the information of all the markers for integrating the distribution function and re-creating new inputs for VMEC and LEMan. Here, all information needed is given to the master processor and treated by the latter only. Again, the parts not parallelised use a few minutes of wall clock time compared with the tens of hours of the bulk of the simulation. Fig. 9.8 shows the speedup of parallelisation over thousands of processors and proves very satisfactory strong scaling. The reason why scaling is slightly deviating from perfect is that during the simulation, diagnostics are run at constant time intervals. These diagnostics involve communication among the processors, slowing down the simulation a little for the benefit of diagnostics information.

10. Benchmarking against SELFO

As described in Chapter 3, there are several other code packages developed for the numerical study of ICRH. An important test for a new code is always the comparison to other, well established codes, as a means of validation. SELFO[39] comprises a combination of the wave code LION[35,36] and the Monte Carlo code FIDO,[37] and has been applied to modelling JET experiments for many years. Its ability to deal with non-standard orbits of the highly energetic resonant ions has proved to be an essential part of its success. The similarity of the treatment of the particle orbits, including the Monte Carlo approach, makes that code package the perfect candidate for a benchmark of SCENIC.

10.1. SELFO vs. SCENIC

Even if the Monte Carlo and particle orbit approaches are similar, there are still differences between the two code packages SELFO and SCENIC. Three dimensional geometries can of course not be treated by SELFO, and we will only discuss differences for axisymmetric cases. Besides the fact that SCENIC is the only code evolving the equilibrium in the self-consistent loop, even the treatment of the initial equilibria is different from SELFO. In particular, SELFO is based on an axisymmetric, circular equilibrium with concentric flux surfaces without Shafranov shift, i.e.

$$R_{\text{SELFO}} = R_0 + r \cos \theta \qquad (10.1a)$$
$$Z_{\text{SELFO}} = r \sin \theta, \qquad (10.1b)$$

compared to the shaping expansion in Eq. (2.13). Therefore, if we want to create similar equilibria in SCENIC and SELFO, we will have to assume circular boundary conditions, and consider scenarios with small pressure gradients. Moreover, we will adjust the safety factor profile in order to minimise the Shafranov shift and higher order shaping coefficients as defined in the shaping expansion and the equilibrium relations (2.27). Another approximation in the SELFO equilibrium is that $B = B_0 R_0 / R$, such that the lines of constant magnetic field (and thus also the resonant layer) are exactly vertical in RZ coordinates. When it comes to the wave field calculations, the wave code LION included in SELFO contains Finite Larmor Radius (FLR) effects and can compute all higher harmonic resonances. Here, the coupling between LION and FIDO has been achieved in such a way

that the Monte Carlo code FIDO, which contains the full distribution function, treats the dielectric tensor kinetically, i.e. makes use of the full distribution function together with the parallel and perpendicular wave numbers to compute the warm dielectric tensor as described in Ref. 39. The value of the dielectric tensor is then fed to LION for updating the wave fields. Here, a parallel wave vector without upshift, $k_\parallel = n_\varphi/R$ is employed together with the dispersion relation of the fast magnetosonic wave, Eq. (5.4). With this, all harmonics can be included, i.e. the competition of multiple ion species with resonances at different harmonics is considered. However, LION does not include mode conversion, such that e.g. the ion-ion hybrid resonance cannot be modelled. For this reason, SELFO is, just as SCENIC, limited to minority (besides intrinsically inefficient fundamental majority) heating scenarios, where the ion-ion hybrid resonance does not appear. The inclusion of higher harmonic heating is, however, a feature which is not included in LEMan, and we will therefore limit this benchmark to fundamental minority heating. Finally, the Monte Carlo code FIDO does not follow the guiding centre orbits, but uses an orbit-averaged scheme with the three constants of motion E, μ, P_φ. Indeed, every point in this constants of motion space, plus the sign of $v_\parallel$, represents one orbit, and it is therefore not required to follow these orbits. The interactions with the background and the waves are then introduced with orbit-averaged operators,[77,78,37] acting on the three constants of motion, and assuming the simplified equilibrium given by Eq. 10.1). In order to treat realistic axisymmetric and non-axisymmetric shaped plasmas, VENUS instead follows guiding centre orbits. P_φ is not considered a constant of motion, since it is linked to the symmetry in toroidal direction, and not a constant of motion if one breaks axisymmetry. Moreover, the Monte Carlo operators are used in their local form, as described in Chapter 6. We will therefore in all stages have to check the results of the two code packages, instead of simply generating final results for comparison.

10.2. Finding an equilibrium

The magnetic equilibrium is the basis of everyone of our simulations. It not only defines the unperturbed particle orbits, but also the wave propagation and absorption. In order to compare simulation results from SCENIC and SELFO, we therefore need to define a suitable equilibrium. We have to find an equilibrium which is simple, and compares well between SELFO and SCENIC. For simplicity, the density and temperature (and thus the pressure) profiles are chosen to be constant, and thus the only free parameter to minimise the Shafranov shift is the safety factor. The numerical values are $n_e = 4 \times 10^{19}\,\mathrm{m^{-3}}$ and $T_e = T_i = 5\,\mathrm{keV}$. With the given pressure, the best safety factor was found to vary only very little from $q = 3$ on axis to $q = 2.7$ at the edge, such that the internal inductance contribution to the Shafranov shift is negligible. Note that we can only fix the values of q on the magnetic axis and at the plasma edge to be the same, but not the complete profile, due to a different treatment in the equilibrium calculations. The magnetic field strength is $B_0 = 3.45\,\mathrm{T}$ on axis. Note that the equilibrium is also described in Appendix D.1. With these profiles, the Shafranov shift in VMEC was $\Delta(a) = 4\,\mathrm{cm}$. We use a low field side (LFS) heating scenario and match the magnetic axis and the complete LFS of
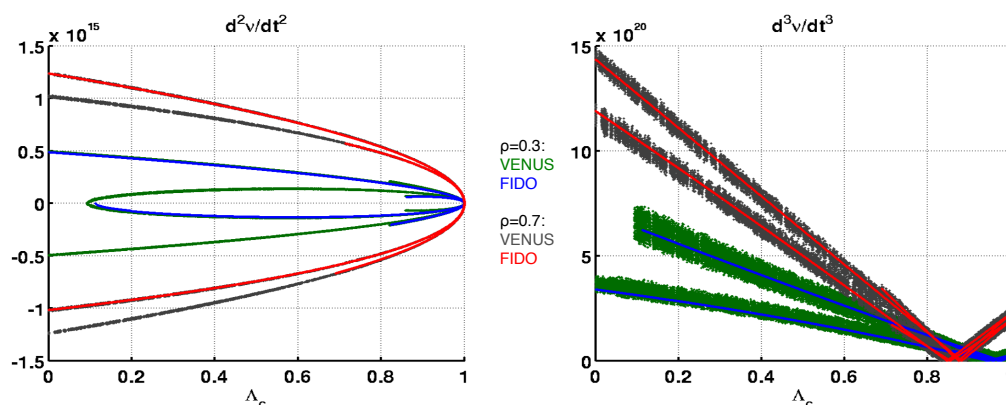
Figure 10.1.: Comparison between the second and third derivatives of the phase ν defined in Eq. (6.30) and entering the interaction times τ_1 and τ_2 defined in Eqs. (6.33a) and (6.33b). The x-axis is the pitch angle $\Lambda_c \equiv \mu B_c / E$. The second derivatives are almost exactly equal, whereas the third derivative in VENUS is more noisy due to the variable time steps.

the equilibrium. The equilibrium for SELFO is concentric with $R_0 = 3\,\text{m}$ and minor radius $a = 1\,\text{m}$, such that the midplane edges are located at $R_{min} = 2\,\text{m}$ and $R_{max} = 4\,\text{m}$. With the Shafranov shift of $4\,\text{cm}$ in VMEC, the magnetic axis at $R_0 = 3\,\text{m}$ and the outer edge at $R_{max} = 4\,\text{m}$, the minor radius is $a = 1.04\,\text{m}$ and $R_{min} = 1.92\,\text{m}$. The bulk plasma is composed of deuterium and a $2\,\%$ hydrogen minority heating scheme is investigated.

10.3. Monte Carlo RF operators

FIDO comprises orbit averaged operators as defined in Ref. 78, whereas VENUS includes the local operators defined in Sec. 6.2.2, and it is prudent to compare the elements of these operators. For these comparisons, the magnetic field strength has been multiplied by a factor of ten, i.e. $B_0 = 34.5\,\text{T}$ in order to diminish the orbit widths, since we want to compare the operators at one given radial position. Of course, also B_c and the RF frequency have been multiplied by a factor of ten. However, the wave codes have not been applied to this scaled equilibrium, but, in order to further simplify the comparison, the wave numbers and electric field have been set to constant values. Explicitly, we employ $k_\parallel = n_\varphi / R$ with $n_\varphi = -27$, $k_\perp = 30$ and $E^\pm = 1\,\text{V/m}$. Fig. 10.1 shows the comparison of the second and third time derivatives of the phase defined in Eq. (6.30), with the first derivative being $\dot{\nu} = \omega - k_\parallel v_\parallel - n\Omega$. The second and third derivatives appear in the computations of the interaction times $\tau_{1,2}$ defined in Eqs. (6.33). For these comparisons we loaded all particles at one given radial position, $\rho \approx \sqrt{s} = 0.3$ and $\rho \approx \sqrt{s} = 0.7$ for VENUS and $R = 3.312\,\text{m}$ and $R = 3.755\,\text{m}$ for FIDO, and on the outboard midplane $\theta = 0$. We also fixed the particle energy to $1\,\text{MeV}$. The pitch angle was chosen at random and no actual heating was applied. The values of $\ddot{\nu}$ and $\dddot{\nu}$ are plotted in Fig. 10.1 as functions of the pitch angle $\Lambda_c = \mu B_c / E$, which equals unity at the resonant layer.
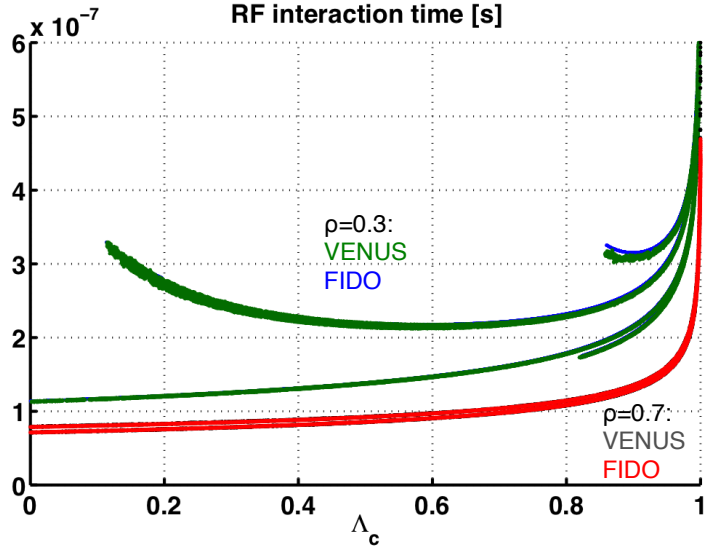
Figure 10.2.: Comparison between the interaction time τ as defined in Eqs. (6.33a) and (6.33b). The x-axis is the pitch angle $\Lambda_c \equiv \mu B_c / E$. Coloring is the same as in Fig 10.1, but the results match so well that not all curves can be seen. The lower (red) curve is the interaction time for the $\rho = 0.7$ radial position, where only the tip points require the Airy function close to $\Lambda_c = 1$. The upper curve shows the interaction time for $\rho = 0.3$, where the Airy function has to be applied more often. In particular, around $\Lambda_c = 0.1$, where a tangent resonance of passing particles forces $\dot{\nu}$ to vanish.

The match is very good, even if the values of $\ddot{\nu}$ are rather noisy in VENUS. The latter is mainly due to the variable time step, which makes precise second derivatives of $\dot{\nu}$ very difficult. We can then compare the interaction time τ defined in Eq. (6.31), which is done in Fig. 10.2. Here, the match is almost exact and it is difficult to distinguish the VENUS and FIDO curves in the figure. The upper (green) curve corresponds to the inner radial position ($\rho = 0.3$), the lower (red) curve the outer position ($\rho = 0.7$). This shows why it is important to consider both radial positions: the outer position has one region where the Airy function has to be used, that is around $\Lambda_c = 1$, where the tip points of the resonant trapped particles are aligned with the resonant layer. The inner position, however, shows a distinct feature around $\Lambda_c = 0.1$, where a tangent resonance of passing particles arises, and the Airy function has to be employed as well. By tangent resonance we mean that a particle's orbit just satisfies the Doppler shifted resonance condition $\dot{\nu} = 0$ at one point on the orbit, namely at $\theta = 0$. There, the resonant layer is exactly tangent to the orbit, hence the name. This shows clearly that the Airy function does not only have to be applied at the turning points, but also when tangent resonances appear.
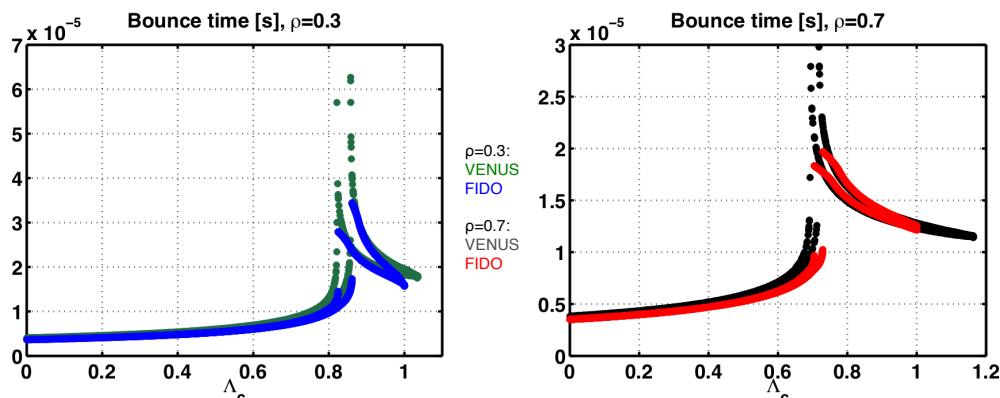
Figure 10.3.: Comparison between the bounce times in FIDO and VENUS for $1\,\mathrm{MeV}$ particles. In FIDO, only resonant particles are considered for this plot, whereas VENUS shows the bounce times for all particles at the given radial position, i.e. also non-resonant deeply trapped particles on the LFS of the resonance. This is why the VENUS pitch angle $\Lambda_c = \mu B_c / E$ extends to higher values. For the resonant particles, the bounce times match reasonably well, and main differences are at the trapped-passing boundary, where the real bounce time goes to infinity. In FIDO, too large bounce times at the trapped-passing boundary are prevented artificially, explaining parts of the discrepancy.

10.4. Bounce time

For the orbit averaged operators of FIDO, the bounce time has to be determined. The bounce time is the time a particle takes to complete one poloidal orbit, and it is found in FIDO by solving analytic expressions in terms of the constants of motion μ, E, P_φ. These expressions can be solved exactly, if the magnetic field is of the form $B = B(R)$, as assumed in the SELFO equilibrium. We can check the validity of the approximation in the magnetic field (or, equivalently, the match of the two equilibria), by checking the bounce times determined by FIDO and VENUS. VENUS follows the full guiding centre orbits, and the bounce time can be computed by saving the time it takes a particle for one poloidal revolution. Fig. 10.3 shows a comparison of the evaluated bounce times as a function of the pitch angle. Note that the FIDO results show only the bounce time for resonant particles, while the VENUS plots include the bounce time for all particles regardless of whether they interact with the wave. Hence the values of Λ_c are larger for the VENUS curves, representing deeply trapped particles on the low field side of the resonant layer, never seeing the resonance during their evolution. The bounce times fit well, except at the trapped-passing boundary, where the real bounce time becomes infinite, and FIDO's algorithm prohibits too large values. Small differences in equilibrium might account for the rest of the differences, since the trapped passing boundary is very sensitive to the magnetic field strength, and small deviations might result in a passing or a trapped particle. In terms of fraction of particles, this region is very small in a full simulation, and these differences should not affect the final results significantly.
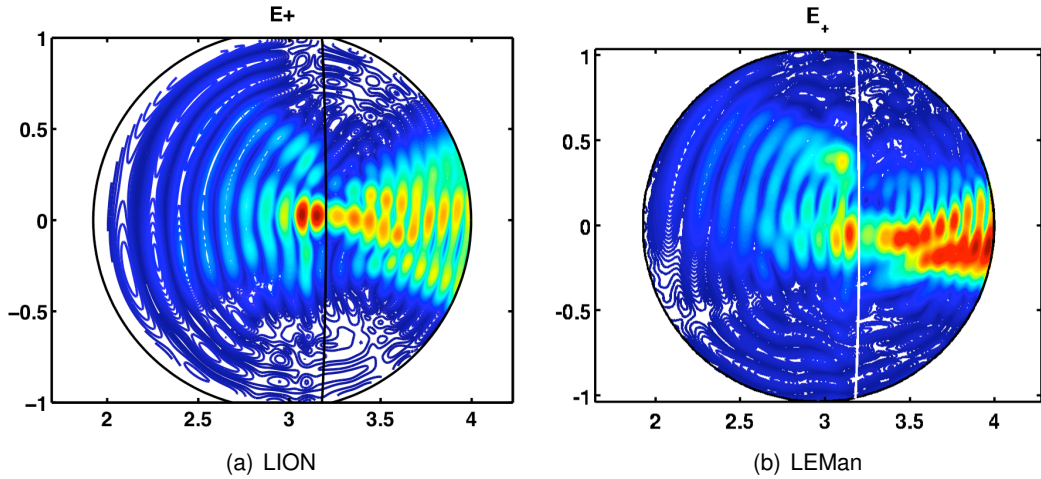
Figure 10.4.: Electric fields $|E^+|$ in the two codes LION and LEMan. The black solid boundary sketches in both plots the VMEC boundary.

10.5. The wave codes

If we want to add the wave fields computed by the wave codes instead of using constant values as in the previous section, we shall first compare the outputs of the wave codes. We use again the magnetic field of $B_0 = 3.45\,\text{T}$ as mentioned in the equilibrium description. The antenna is placed on the low field side, extending in poloidal direction up to $\theta_{ant} = \pm 26°$ in geometrical angle (not Boozer angle). The toroidal mode number is again chosen to be $n_\varphi = -27$, i.e. co-current injection. Note that in LION, the antenna is placed at a certain distance from the plasma, with a vacuum separating them, whereas in LEMan, the antenna touches the plasma. The resulting left hand polarised electric fields are given in Fig. 10.4. The important features for the heating are very similar. Both fields have a local minimum just to the right of the resonant layer (black/white line), and two distinct maxima are visible just to the left of the resonance. The more twisted form of the wave field from LEMan is probably due to a difference in the safety factor profile. The resulting power deposition is plotted in Fig. 10.5. Both codes show two main local maxima of power deposition in the poloidal cuts. The most important one just inside, the secondary just outside the resonant layer. The deposition in LEMan is a little broader, and an additional distinct maximum is visible a bit further from the centre, around ($\rho = 0.4$), which is missing in LION. This is consistent with the differences in the wave fields of Fig. 10.4. The radial power density profiles are normalised to match the maximum value of the two codes, which is why there are no unit indications on the y-axis. In these radial plots, one can see that the profiles of LEMan and LION are displaced by about half a wave length, such that the marked peak in LION is in fact distributed among the two maxima in LEMan just inside and just outside the peak of LION around $\rho = 0.2$. This explains also why in the radial profile from LION three different local maxima are present, whereas in LEMan only two are distinguishable. This difference could be due to either the difference in safety
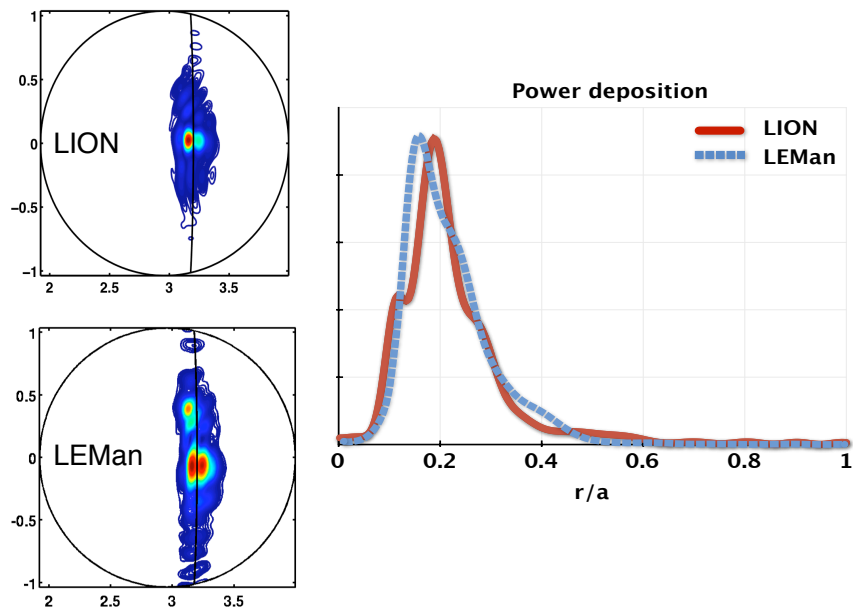
Figure 10.5.: Power deposition in the two codes LION and LEMan.

factor profile, the $B = B(r)$ approximation in SELFO, or, more likely, the differences in how the antennas are modelled in the two codes.

11. Low power simulations

After the previous tests of the operators, the statistics module and examining the numerical behaviour, we are ready to apply SCENIC to ICRF cases. As first examples we will consider $1\,\%$ helium-3 (He^3) minority heating in a deuterium (D) plasma, and apply $3\,\mathrm{MW}$ of power. With this choice, the energetic tails will not be very large, and we will be able to check the consistency of the code package without going to its limits. The equilibrium is JET-like, with major radius $R_0 = 2.99\,\mathrm{m}$ and magnetic field on axis $B_0 = 2.94\,\mathrm{T}$. A detailed description of the equilibrium is given in Appendix D.2. This equilibrium is similar to JET shot 76189, where He^3 minority heating has been applied at the $q = 1$ surface ($r/a \approx 0.25$) for sawtooth control in Refs. 20 and 79. The latter are our motivation to choose this particular scenario, since we know what to expect. However, we do not try to directly compare the results from our simulations to the experimental and numerical data described in those references.

As stated above, we concentrate on this low power scenarios mainly to asses the feasibility of the iterated scheme of SCENIC by using a scenario where we know what kind of results to expect from experiment. An important part of this section is devoted to the comparison between the raw distribution function evolving in VENUS and the analytical model bi-Maxwellian on which the equilibrium and wave field calculations are based.

For avoiding confusion, we introduce the term $\pm 90\,^\circ$ phasing of the injected wave field. Here, $+90\,^\circ$ phasing will always mean co-current injection, i.e. $n_\varphi < 0$ and $k_\parallel < 0$. $-90\,^\circ$ then denotes cases where the RF wave is injected in the counter-current direction, i.e. $n_\varphi > 0$ and $k_\parallel > 0$. Again, the signs of the toroidal mode and parallel wave vector are opposite the Ohmic current, which is why we introduce the new labelling.

11.1. Iterated scheme

As stated in Sec. 7.1, the main diagnostics for the convergence of the iterated scheme is the mean energy per particle defined in Eq. (7.1). Before looking at the converged results, we will check if iterations are indeed needed, and if so, whether the result depends on the number of iterations and the length of each iteration. The above mentioned scenario is employed, with the resonant layer on the high field side of the magnetic axis. Fig.11.1 shows the evolution of the mean energy as a function of time, normalised to the electron slowing down time, for the simulation, but with different number of iterations. In all cases,
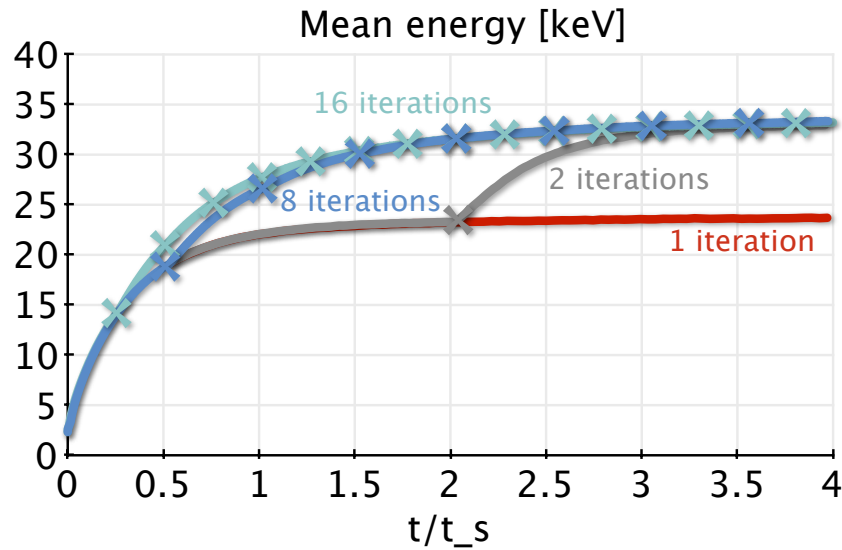
Figure 11.1.: Convergence of the iterated scheme. Comparison of simulations without iterating
(one iteration) and several iterations shows that even if they both reach equilibrium,
the final results are different.

the system reaches a steady-state after a few (electron) slowing-down times. However, Fig. 11.1 shows clearly that iterations are indeed necessary, since the final results differ. The difference is obvious in Fig. 11.1, and it is also visible in the integrated moments of the distribution function. Confirming the difference in energy content of the minority species, Fig. 11.2 gives the difference in the energy distribution $f(E)\sqrt{E}$, i.e. the number of particles at a given energy. For the chosen scenario, two iterations are enough, since convergence is attained against simulations with more and shorter iterations. One requires more iterations for higher power simulations. The splitting parameter is $x = 10$ in both plots, and clearly the simulation with two and more iterations shows a high energy tail (red, squares) peaked at higher energy than the simple simulation with just one iteration. The difference in power deposition can be seen in Fig. 11.3. While the deposition is rather narrow along the resonant layer for one iteration (Fig. 11.3(a)), it becomes somewhat wider at the end of the converged simulations using several iterations (Fig. 11.3(b)). Here,the difference between one iteration and several iterations may be attributed to the Doppler broadening of the resonance at higher energies and a change in electric field polarisation during the iterated simulations. Also, the radial deposited power density in Fig. 11.3(c) reflects the difference in local maxima of Fig. 11.3, and this plot will give an explanation for the difference in hot particle density, Fig. 11.4(b).

Fig. 11.4 illustrates the differences occurring in the profiles of pressure and density. For the cases using multiple iterations, the pressure is generally higher than for the case with one iteration, confirming the higher energy content proportional to the surface under the curves of Fig. 11.2. The density plot with one iteration clearly shows local maxima, separated by a regular distance. It is important to remember that for these plots, only the
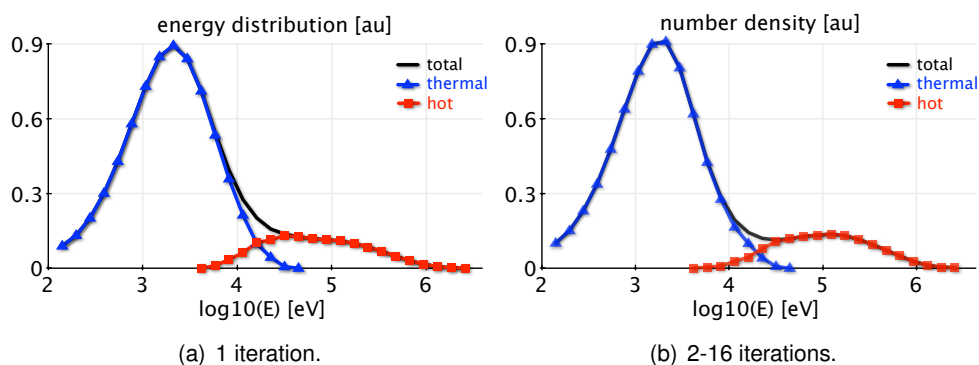
(a) 1 iteration.

(b) 2-16 iterations.

Figure 11.2.: Comparisons of the energy distribution $f(E)\sqrt{E}$. The tail of the iterated simulations is peaked just above $100\,\mathrm{keV}$, whereas the tail in the simple simulation with one iteration has its maximum well below this mark.

resonant particles with energies higher than E_c are considered. A direct relationship between the hot particle density (Fig. 11.4(b)) and the radial power deposition (Fig. 11.3(c)) should be expected, since particles are heated where the power is absorbed. In the beginning of the simulation, the minority is thermal and its density in the resonant region rather low. Single pass absorption is therefore not very important, and the RF wave takes on the structure of a standing wave. The initial power density profile of Fig. 11.3(c) is indeed characteristic for a standing wave. The important heating around $r/a = 0.25$ in the beginning of the simulation (during the complete simulation for one iteration) creates a main hot particle density peak. The changed density then changes (together with the action of enhanced anisotropy) the power deposition after the initial iteration, enhancing single pass absorption. Thus, the standing wave patterns disappear , resulting in the shown differences between one and multiple iterations. These plots thus demonstrate that an iterated scheme is necessary for finding consistent solutions when performing ion cyclotron heating simulations.

After these convergence considerations, we will now concentrate on the converged iterated results for low and high field side application of $3\,\mathrm{MW}$ power.

11.2. Distribution function

At the heart of the self-consistent simulations in SCENIC is the evolution of the fast particle distribution function. We will therefore first investigate the changes induced in the latter and compare the original distribution obtained in VENUS to the bi-Maxwellian model distribution from the equilibrium and wave field computations.

(a) One iteration.

(b) Last of 16 iterations.
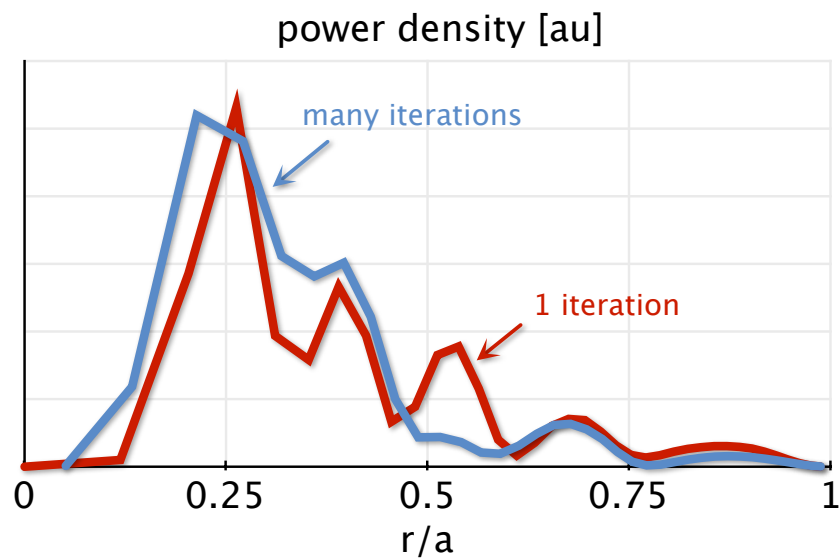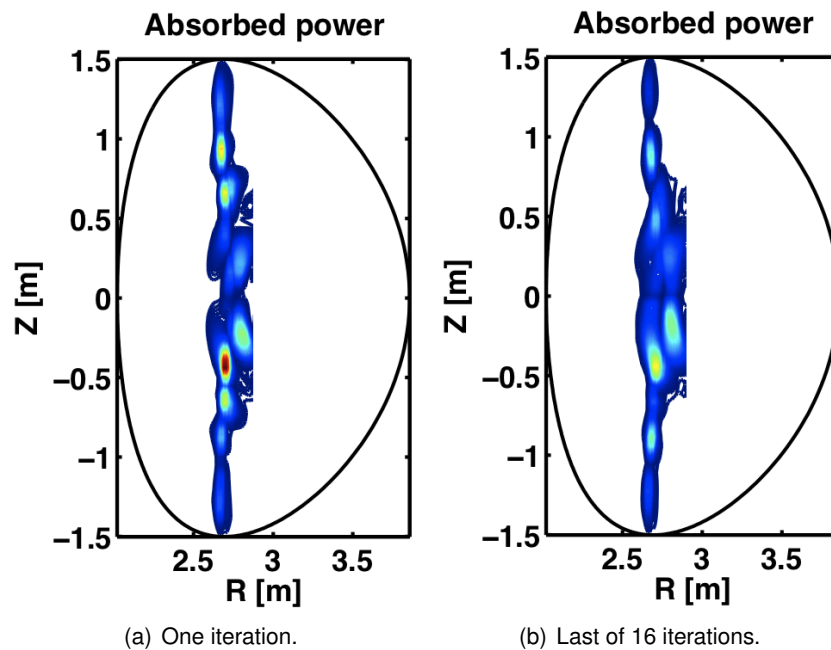
(c) Radial (poloidally averaged) deposited power density. Note that the grid points for the two curves are not at the same positions.

Figure 11.3.: Power deposition in VENUS. The power deposition becomes broader, and the single maxima along the resonance of (a) are less isolated in (b). The sharp border in (b) is due to the limited diagnostics grid size.
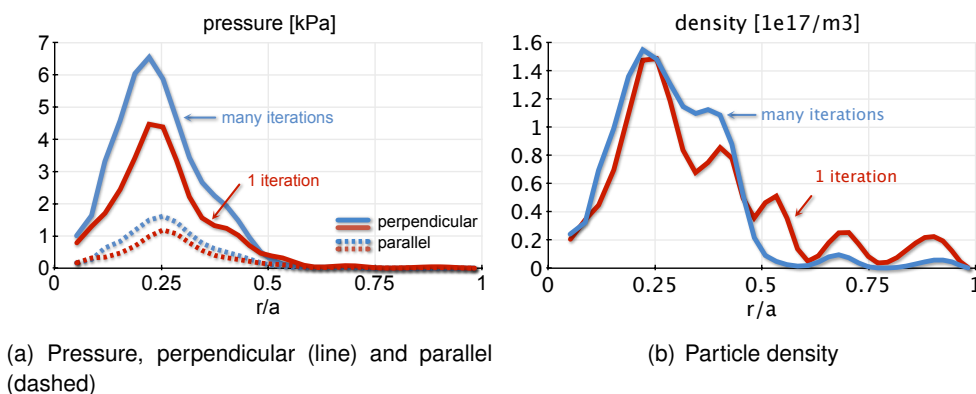
(a) Pressure, perpendicular (line) and parallel (dashed)

(b) Particle density

Figure 11.4.: Comparing integrated moments of the distribution function for pressure and density between one (red) and 2-16 (blue) iterations. Higher pressure is consistent with higher energy content in Fig. 11.1. The difference in density profiles (only the hot particle density is plotted) is directly linked to the difference in power deposition in Fig. 11.3.

11.2.1. Energy distribution

A convenient way of representing the distribution function where a high energy tail develops is the distribution in terms of energy, $f(E)\sqrt{E}$, vs. $\log 10(E)$, which corresponds to a histogram showing the relative number of particles at a given energy. Fig. 11.5 shows such plots for the four scenarios of Low Field Side (LFS), High Field Side (HFS), co-($+90°$) and counter-current ($-90°$) wave injection. The minority distribution function is divided into a thermal and a hot part as described in Sec. 7.2, with $E_c = 10T_e$. The hot part is shown in red/squares, the thermal in blue/triangles. The model (green/hollow) shows how well the obtained bi-Maxwellian agrees in the high energy tail. The thermal part of the distribution function is modelled Maxwellian, but we concentrate on the modelling of the hot anisotropic tail. The latter is one of the specialities of SCENIC and we therefore do not discuss the Maxwellian thermal part in further detail. In general, the VENUS tail is broader than the bi-Maxwellian model, but the differences are rather small. The tails for LFS heating are more pronounced than for the HFS cases, with peaks well above $100\,\mathrm{keV}$, whereas the HFS tails peak at $20 - 30\,\mathrm{keV}$ (remember that the x-axis is in logarithmic scale). Also, $+90°$ injection is more efficient than $-90°$ in terms of the quantity of hot against thermal population.

(a) HFS, $+90°$, 16% hot

(b) HFS, $-90°$, 11% hot
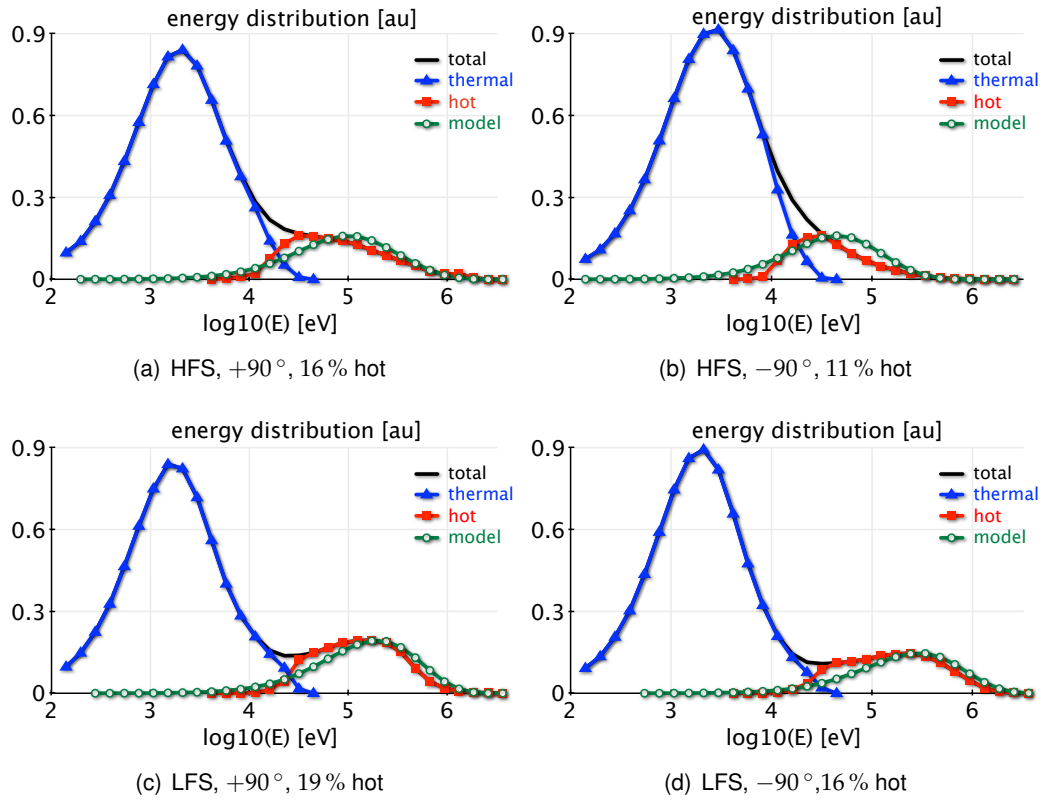
(c) LFS, $+90°$, 19% hot

(d) LFS, $-90°$, 16% hot

Figure 11.5.: Comparison of the energy distribution $f(E)\sqrt{(E)}$, i.e. the distribution integrated over space and pitch angle multiplied by the Jacobian. The hot minority is defined by the particles having an energy higher than $10T_e(s)$ for any given radial position. The largest tail arises for LFS $+90°$, the lowest for HFS $-90°$. The model (green,hollow) corresponds to Eq. (4.1) for the hot minority.

11.2.2. Velocity distribution

Plotting the distribution as a function of $v_\parallel$ and $v_\perp$ at a given position in space can provide a somewhat more detailed view of the effects of the RF field. An isotropic Maxwellian would simply draw circles in such a plot, and it is therefore very straightforward to see the difference between the distribution function generated by VENUS and a pure Maxwellian in such a plot. The bi-Maxwellian model implemented in SCENIC, Eq. (4.1), however, is not as simple, and we need to compare the plots directly in order to quantify to what extent the analytical model represents an approximation. Considering Eq. (4.1), we recall that we can model asymmetries in parallel velocity, $v_\parallel \to -v_\parallel$, in the limit where they correspond to finite orbit widths. For the contour plots, a spatial position has to be chosen. This is in general on the outboard midplane, $\theta = 0$. If we use the poloidal flux function as radial variable for convenience, we can write the distribution function in terms of $\overline{\psi}$, $v_{\parallel 0} = v_\parallel(\theta = 0)$, and $v_{\perp 0} = v_\perp(\theta = 0)$ as

$$
F_h(\overline{\psi}, v_{\parallel 0}, v_{\perp 0}) = \mathcal{N}(\overline{\psi}) \left(\frac{m_h}{2\pi T_\perp(\overline{\psi})} \right)^{3/2}
$$

$$
\exp \left[-\frac{m v_{\perp 0}^2}{2 T_\perp(\overline{\psi})} \frac{B_c}{B(\psi_0, \theta = 0)} - \frac{m \left| v_{\parallel 0}^2 + v_{\perp 0}^2 \left(1 - B_c/B(\psi_0, \theta = 0)\right) \right|}{2 T_\parallel(\overline{\psi})} \right] . \quad (11.1a)
$$

Recalling the discussion about finite orbit widths in Sec. 2.2.2, and in particular Eqs. (2.42) and (2.47), we can show that the distribution function at the average radial position $\overline{\psi}$ contains contributions from all orbits with radial positions ψ_0 and orbit width $\Delta \psi$ defined by

$$
\overline{\psi} = \psi_0 + \Delta \psi \approx \psi_0 + \begin{cases} \frac{m}{Q} \left[R(\psi_0, \theta = 0) v_{\parallel 0} + R_0 v_\parallel(\psi_0, \theta = \pi/2) \right] & , \text{passing} \\ \\ \frac{m}{Q} R(\psi_0, \theta = 0) v_{\parallel 0} & , \text{trapped} \end{cases}
$$

$$(11.1b)$$

If we write the distribution function (11.1)) in terms of $\overline{\psi} = \psi_0 + \Delta\psi(v_{\parallel 0})$, and assume small orbit width, we can Taylor expand around ψ_0 to get

$$
F_h(\overline{\psi}) \approx F_h(\psi_0) + \Delta\psi(v_{\parallel 0}) \left. \frac{\partial F_h}{\partial \overline{\psi}} \right|_{\overline{\psi} = \psi_0}
$$

$$
= F_h(\psi_0) + \Delta\psi(v_{\parallel 0}) \left[\frac{F_h(\psi_0)}{\mathcal{N}(\psi_0)} \left. \frac{\partial \mathcal{N}}{\partial \overline{\psi}} \right|_{\overline{\psi} = \psi_0} \right.
$$

$$
\left. + \frac{F_h(\psi_0)}{T_\perp(\psi_0)} \left(\frac{b}{T_\perp(\psi_0)} - \frac{3}{2} \right) \left. \frac{\partial T_\perp}{\partial \overline{\psi}} \right|_{\overline{\psi} = \psi_0} + \frac{F_h(\psi_0)}{T_\parallel(\psi_0)} \frac{c}{T_\parallel(\psi_0)} \left. \frac{\partial T_\parallel}{\partial \overline{\psi}} \right|_{\overline{\psi} = \psi_0} \right], \quad (11.2)
$$

where $b = m v_{\perp 0}^2 B_c / 2 B(\psi_0, \theta = 0)$ and $c = m | v_{\parallel 0}^2 + v_{\perp 0}^2 (1 - B_c/B(\psi_0, \theta = 0)) | / 2$. From the definition of $\Delta\psi(v_{\parallel 0})$ in Eq. (11.1b), the asymmetry in $v_\parallel$ of the distribution

function $F_h(\overline{\psi})$ can now be attributed to the velocity dependence (including the sign) of the radial excursion $\Delta\psi$. It is proportional to the orbit width $\Delta\psi(v_{\|0})$ and the radial derivatives of $\mathcal{N}$, $T_\perp$ and $T_\|$. Consequently, thanks to the way of writing the distribution function in terms of an orbit averaged radial variable, currents due to finite orbit width effects can be captured in the model distribution. On the other hand, processes which create a large excess of co- or counter-passing ions, independently of their orbit width, are not included in the model. The most important example of such a process is undoubtedly the Fisch currents.[69] If a wave with an asymmetric toroidal spectrum is injected into the plasma, particles with a parallel velocity having the same sign as the wave number will interact with the wave. As a result, more particles moving in the same direction as the wave are heated than particles moving in the opposite direction. Particles with higher energy suffer fewer Coulomb collisions due to the energy dependency of the collisionality, and the distribution function becomes asymmetric with respect to parallel velocity. As a result, currents are generated with the same sign as the wave vector. Hence, if we inject one co-current propagating wave into the plasma, we would expect positive passing current to develop, whereas for a counter-current propagating wave, the passing current would be negative. Another example is asymmetric detrapping of resonant ions due to wave-particle interactions. We will show that more co-passing particles are generated if the heating is applied on axis or on the low field side, resulting in a potentially large passing current. This chapter confirms these effects and that in such cases, the induced currents will not be consistent with the model distribution function. This is an important reason why the toroidal current is directly fed to VMEC, without the fitting to the model distribution. Recall that the sign definition is such that RF induced current is positive if it is in the same direction as the Ohmic current and negative otherwise. Thus, the contour plots $f(v_\|, v_\perp)$ have been created by changing the sign of $v_\|$ corresponding to a negative Ohmic current. In order to consistently include the finite orbit width effects in the bi-Maxwellian in these comparisons, we use the lookup table described in Sec. 6.3 for reloading the marker distribution in VENUS according to Eq. 11.1) at the end of each converged simulation. Figs. 11.6 and 11.7 show the contour plots at the outboard midplane at $r/a = 0.25$. For the HFS cases, this is exactly opposite the heating location, at the same distance from the magnetic axis, but $B \neq B_c$ at that location, so that the characteristic ear-shaped contours can be seen. For the LFS, the plots are exactly at the position the heating is applied, i.e. $B = B_c$, and we expect more oval contours. These features are described in more detail in Ref. 50. In both cases, the maximum anisotropy can be expected to be located around the position chosen for the plots. Note that the model plots have not been created analytically, but by reloading all the particles in VENUS using the model distribution function. From the VENUS distributions Figs. 11.6(a) and 11.6(c) we see again what we discussed when considering the energy distribution, namely that the high energy tail for $+90°$ phasing is larger than for $-90°$ phasing. The asymmetries of the VENUS contours are missing in the model at that particular radial position, and considerably higher current due to passing particles is present in the VENUS distribution function. Nevertheless, the characteristic ear-shaped contours can be seen in all HFS plots of Fig. 11.6, and the elongated oval shaped contours in the LFS plots of Fig. 11.7. Such contours can only be described analytically by a bi-Maxwellian containing a poloidal dependence, explicitly made visible
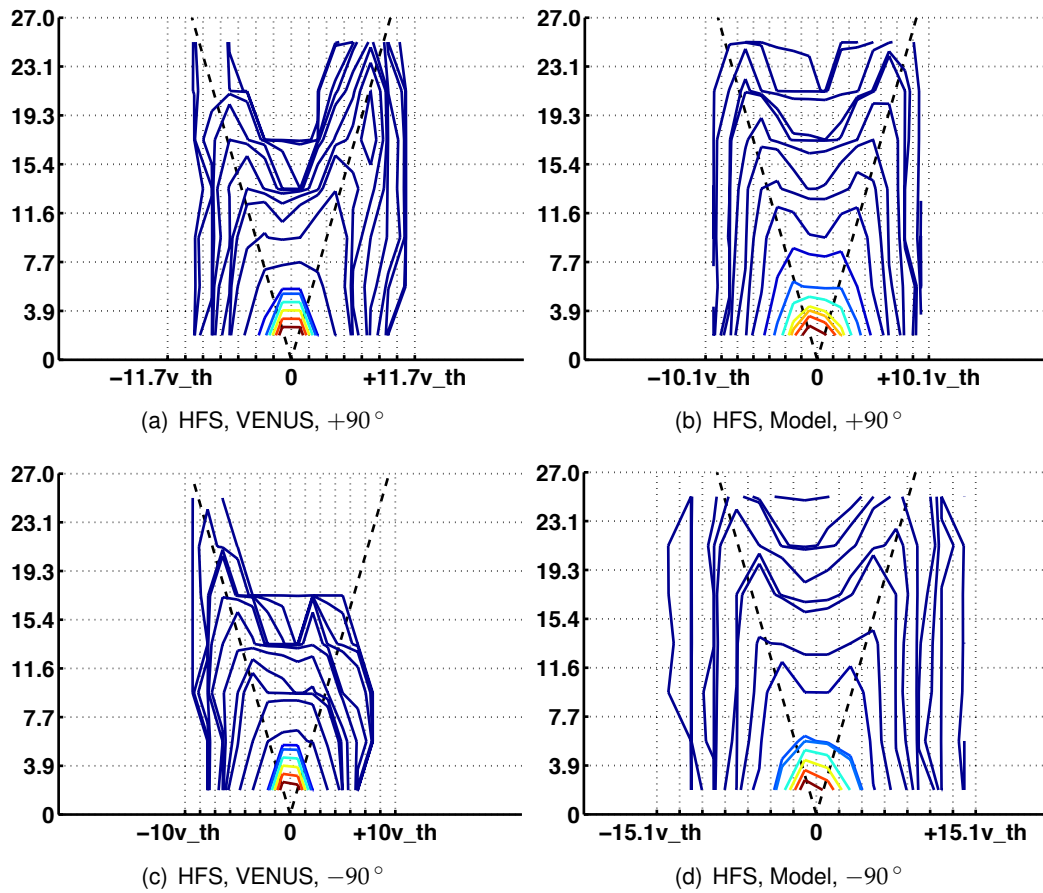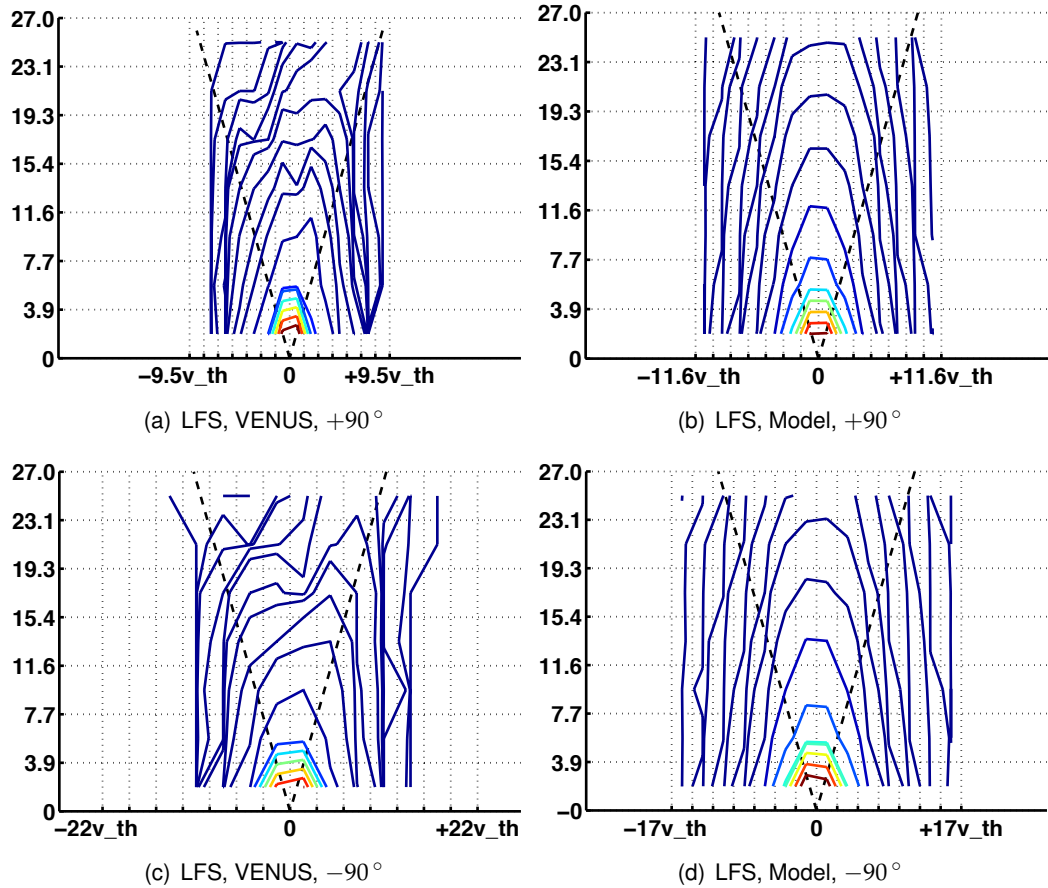
Figure 11.6.: Contour plots of the distribution functions coming from VENUS and modelled by the bi-Maxwellian (4.1) for HFS heating at $r/a = 0.25$. The spatial position was chosen to be at the same distance from the magnetic axis as the heating location, but on the LFS, such that the ear-shaped contours emerge. The dashed lines denote the trapped passing boundary, and the velocities are normalised to the local thermal velocity $v_{th} = 4.2 \times 10^5 \, \text{m/s}$.

(a) LFS, VENUS, $+90°$

(b) LFS, Model, $+90°$

(c) LFS, VENUS, $-90°$

(d) LFS, Model, $-90°$

Figure 11.7.: Contour plots of the distribution functions coming from VENUS and modelled by the bi-Maxwellian (4.1) for LFS heating at $r/a = 0.25$. The spatial position was chosen to be at the same location as the heating location ($r/a = 0.25$), such that the contours are oval instead of the ear-shapes. The dashed lines denote the trapped-passing boundary, and the velocities are normalised to the local thermal velocity $v_{th} = 4.2 \times 10^5 \, \mathrm{m/s}$.
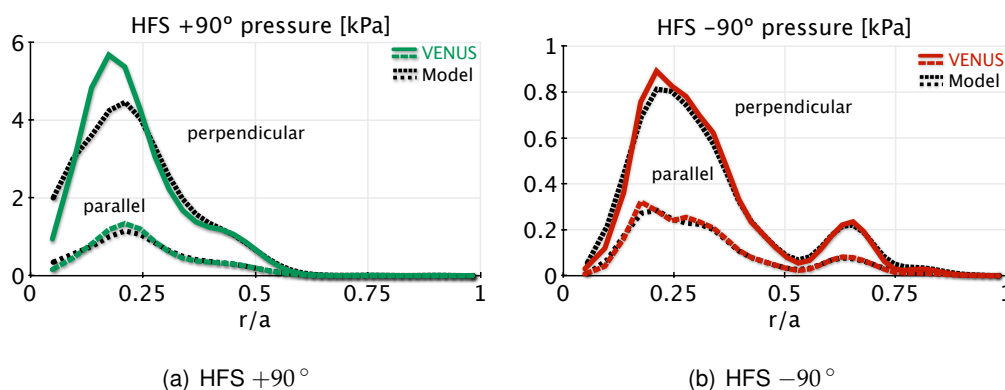
Figure 11.8.: Pressure profiles for the HFS heating scenarios. Co-current injection $(+90°)$ produces higher pressure than counter-current $(-90°)$, which is consistent with Fig. 11.5, and the $-90°$ pressure profile is broader. Note the scale difference between the two plots.

in terms of B_c/B in Eq. (11.1) . We can conclude that the model distribution represents indeed a very satisfying approximation if one keeps in mind the discussed features which cannot be included. We will now turn to some of the integrated moments of the distribution function, and also compare the VENUS outputs to the model.

11.3. Moments of the distribution function

11.3.1. High field side heating

The higher energy content in Fig. 11.5(a) compared to Fig. 11.5(b) can be seen in the resulting pressure profiles, Fig. 11.8. Indeed, the maximum pressure of the HFS $+90°$ case is about five times higher than for the HFS $-90°$ case, and the $-90°$ pressure profile is not only lower, but also broader than the $+90°$ profile. This is in agreement with the findings in Ref. 67, where it was shown experimentally that the radial pressure profile is larger in amplitude and more peaked for $+90°$, and lower and broader for $-90°$. This effect is due to the RF particle pinch in the presence of toroidally propagating waves, as shown in Eqs. (6.40) and (6.41). Note how well the bi-Maxwellian models the parallel and perpendicular currents. The slight deviations in peak perpendicular pressure are mostly due to the applied smoothing to the radial profiles fed to VMEC and LEMan. Especially in the $+90°$ case, anisotropy has been prevented from peaking too much. We chose a conservative profile smoothing to make sure that the effects are rather under- than over-estimated.

The total toroidal current is directly fed into the equilibrium without approximations due to the model distribution function, as described in Sec. 7.4. We can plot the current densities due to passing and trapped particles, allowing for more detailed physical studies. This is shown in Fig. 11.9. As mentioned before, the model distribution function is formu-

(a) HFS $+90°$ (b) HFS $-90°$
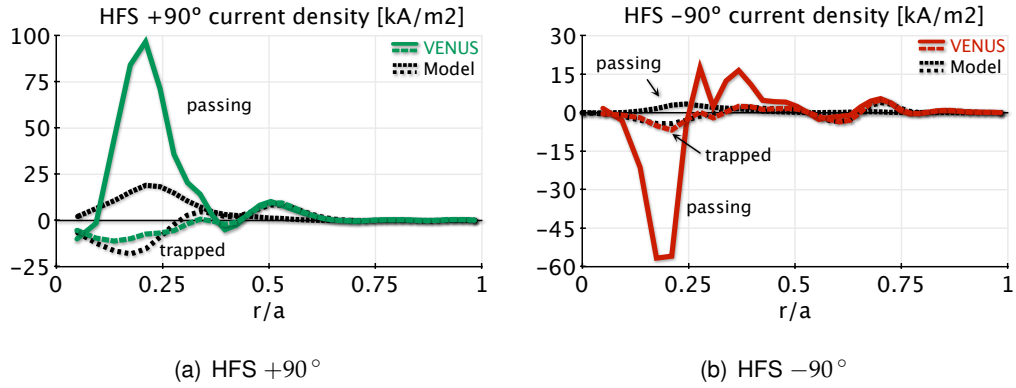
Figure 11.9.: Current profiles for HFS heating scenarios. Trapped particle current is mainly due to finite orbit effects, which can be modelled to a large proportion. However, the passing current is dominating, created through detrapping of resonant particles.

lated in terms of orbit averaged radial position, allowing for finite orbit width effects. We can therefore plot the current densities the model allows for, but it is important to keep in mind that these model currents are not required for any computations in SCENIC. The currents coming from VENUS show high (dominating) current due to passing particles, which changes sign when the phasing of the RF field changes. This passing current can be attributed mainly to the above discussed Fisch currents, which are expected to be in the direction of wave propagation, and is exactly what we see in Fig. 11.9. Another (smaller) contribution can be assigned to the particles located just below the passing-trapped boundary in Fig. 11.6, i.e. it is coming from detrapping resonant trapped particles. For HFS scenarios, detrapping is symmetric with respect to the resonant layer position, with $k_\parallel v_\parallel > 0$ for $B < B_c$ and $k_\parallel v_\parallel < 0$ for $B > B_c$ (due to the Doppler shifted resonance $\omega = \Omega + k_\parallel v_\parallel$).[80] The result is co- (counter-) passing current with $v_\parallel < 0$ ($v_\parallel > 0$) inside the resonant layer (since then $B < B_c$ along the complete flux surfaces) for co- (counter-) injection, i.e. $k_\parallel < 0$ ($k_\parallel > 0$). The model does not contain the Fisch currents or detrapping, but the finite orbit width effects. Therefore, we expect the bi-Maxwellian to include the trapped particle current, and the current from barely passing particles. This is why the passing current is much lower in absolute values and does not change sign when going from $+90°$ to $-90°$. The trapped particle current, however, is due to finite orbit widths, and does not change sign between the co- or counter-current phasing cases. This is to be expected, since trapped particles always propagate co-current on the outer leg, and counter-current on the inner leg, resulting in negative current inside and positive current outside the resonance.[80] Indeed the trapped particle currents of the VENUS outputs and the model are very similar. This gives confidence in the bi-Maxwellian model, since we are representing the tail of the distribution function well, because these currents come from wide orbits, and thus highly energetic particles.
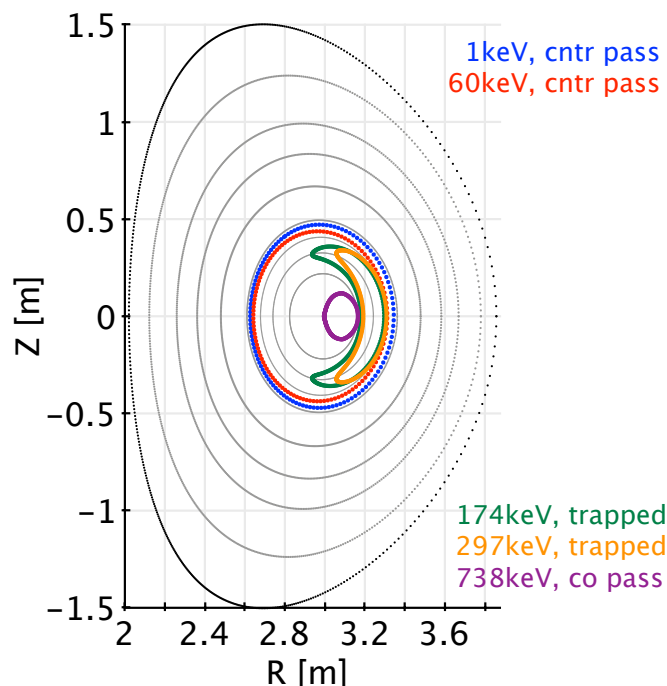
Figure 11.10.: Evolution of an initially counter-passing low energy particle into a LFS co-passing high energy particle.

11.3.2. Low field side heating

For LFS heating, detrapping is asymmetric and generates almost exclusively co-passing orbits inside the resonant layer.[81] Fig. 11.10 shows an extreme example of an initially counter-passing particle, which is being trapped while being heated to very high energy, and eventually detrapped into a co-passing non-standard orbit. In fact, this non-standard passing orbit stays on the LFS of the magnetic axis, between the latter and the resonant layer. Note that this example is very high up in the energetic tail, and for the low power scenarios, only very few particles describe such orbits. Nevertheless, the currents in Fig. 11.12 are dominated by co-passing particles, and the result is independent of whether the wave is propagating parallel or anti-parallel to the Ohmic current. Clearly, the Fisch currents, which switch sign and were dominant for the high field side heating cases, are not dominant anymore. The asymmetric detrapping is indeed more important than the Fisch currents for low field side heating.

Once the particles detrapped into co-passing orbits inside the resonant layer, the only difference between the $+90°$ and $-90°$ simulations is the sign of the parallel wave number. In the $+90°$ case, $k_\parallel < 0$, and therefore the resonance condition $\omega = \Omega + k_\parallel v_\parallel$ with $R < R_c$, and thus $\Omega > \omega$, yields that only counter-passing orbits continue to interact with the RF field on the high field side of the resonance ($R < R_c$). Therefore, the detrapped co-passing particles do not interact with the wave anymore and are slowing down. In
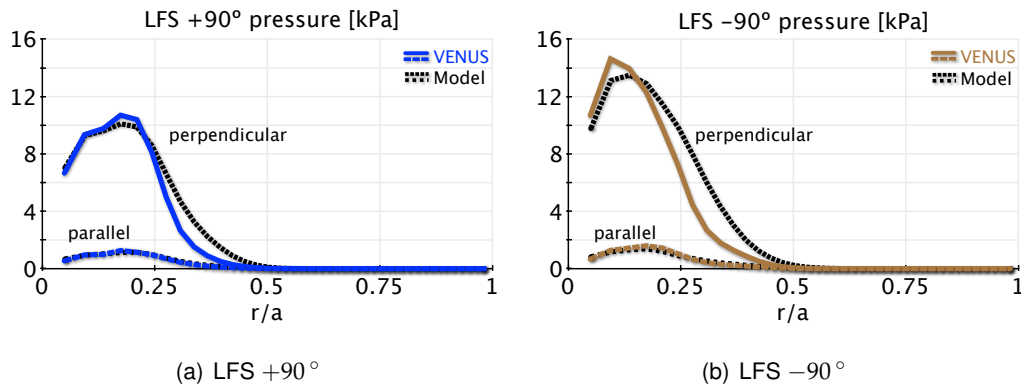
Figure 11.11.: Pressure profiles for the LFS heating scenarios. Non-standard orbits dominate the hot population and more efficient co-passing detrapping for $-90°$ create more peaked pressure.

the $-90°$ case, $k_\parallel > 0$, and the inverse is true, i.e. the detrapped co-passing particles can still resonate. As a result, for low field side heating, the currents are dominated by co-passing particles, and are larger for $-90°$ than for $+90°$. This is the exact contrary to the high field side case.

The non-resonant detrapped particles are slowing down. While doing so, the orbits move towards the magnetic axis, where they become trapped again.[12] This allows the now trapped particles to interact with the wave again, and increase their perpendicular energy, which is why the perpendicular pressure in Fig. 11.11(a) is still considerable inside the resonant layer. Fig. 11.11 also shows that $+90°$ perpendicular pressure is broader but lower than the perpendicular pressure. It is important to note that the total energy content of the plasma, which is slightly higher for $+90°$ in the energy distribution plots of Fig.11.5 represents a volume integral of these pressure profiles. Therefore, even if the $+90°$ pressure profile is lower, it is at the same time broader and the volume integral has the effect that the energy content is still higher for the $+90°$ case than for the $-90°$: The co-current heating is still more efficient in terms of total power deposition on the minority population, although in contrast to the HFS cases the pressure profiles are flatter. We can also observe that the model distribution generates very similar pressure profiles as the raw integrated pressures from VENUS. The amplitudes of the trapped currents are larger than in the HFS cases, since the resonant particles are deeply trapped and not barely trapped as before, and are therefore less easily detrapped. Even so, as in the HFS case, the trapped currents in Fig. 11.12 are very well modelled by the bi-Maxwellian. Since asymmetric detrapping generates an excess of co-passing particles, the passing current profiles are lower from the analytical model, similar to the HFS scenarios before, where Fisch currents were dominating. We can note again that although the $-90°$ current density is smaller in amplitude than for $+90°$, the surface integral reveals a slightly higher total toroidal current for the co-current injection. We do not show here the effects on the equilibrium, since in these low power scenarios no significant changes can be observed,
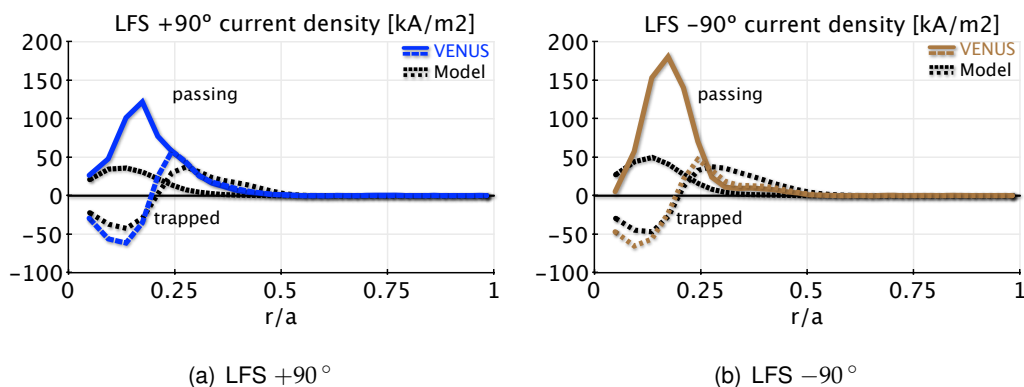
Figure 11.12.: Current profiles for LFS heating scenarios. Again, passing current is much more important than trapped current, although trapped current is larger than for the HFS cases. The model distribution is able to model the trapped currents quite precisely.

and the importance of the iterative scheme lies in the updating of the dielectric tensor. We will concentrate on the equilibrium change in Chapter 12, where we apply high power and a change in equilibrium can indeed be observed.

11.4. Effect of hot particles on the dielectric tensor

11.4.1. Numerical study

It is difficult to directly see the effects of temperature and anisotropy in relations (5.1). Only the effect of the density factor $\mathcal{N}(\bar{s})$ is rather obvious, since all terms depend linearly on this quantity. The latter is therefore chosen to be constant in what follows. The anisotropic dielectric tensor is applied to the minority population, which will be called hot population, even if it is at the same temperature as the background ions for this particular study. It is important to note that the background is treated with a warm dielectric tensor as well, but based on a Maxwellian distribution function. The equilibrium is circular with flat profiles and a magnetic field on axis of $3.45\,\mathrm{T}$, and described in more details in Appendix D.1. For a comparison between the background and the hot dielectric tensor, the RF frequency was chosen to be $33\,\mathrm{MHz}$, which allows for a resonant layer of the helium-3 minority on the Low Field Side (LFS) around $R_c = 3.19\,\mathrm{m}$ and a second resonance for the background D on the High Field Side (HFS) around $R = 2.4\,\mathrm{m}$. It is thus possible to directly compare the values of the dielectric tensor of the background (Maxwellian) and hot (bi-Maxwellian) species. Since $\mathcal{N}(\bar{s})$ is chosen to be $1\,\%$ of the D density, we can expect that the amplitude of the hot dielectric tensor will be about $100/\sqrt{T_\perp/T_\parallel}$ smaller than the amplitude of the background ion tensor. Fig. 11.13 shows a comparison between the components of the dielectric tensor for a case where $T_\parallel^{\mathrm{He}^3} = 9.1\,\mathrm{keV}$ (i.e. about twice the D temperature) and $T_\perp/T_\parallel = 10$. One can see from the color bars on the plots that there is indeed a factor of $\sim$30 between the maxima of the background and

the hot dielectric tensor amplitudes (Figs. 11.13(c) and 11.13(d)), confirming the scaling in density.

If one compares the power deposition by species, Fig. 11.14(a) shows that more power is going to the hot species than to the background ions. This is mainly due to the high single pass absorption on the minority He^3 , such that the fields are much weaker at the HFS, where the resonance for the background deuterium lies. Comparing Figs. 11.13(c) and 11.13(d) with 11.14(c) and 11.14(d) illustrates how the deposition of the power is along the respective resonances and maxima of the dielectric tensor.

We now turn our attention towards the newly derived hot anisotropic dielectric tensor as given in Eq. 5.1), and try to determine what effect a change in temperature and anisotropy has on its real and imaginary parts. Here, we do not compare the complete dielectric tensors, but, for simplicity, only the terms in the sum of Eqs. (5.1aa) and (5.1ba) corresponding to the chosen species (electrons, background ions, minority ions). It is important to define which parameter is changed and which held constant, since it is impossible to change parallel, perpendicular temperature and anisotropy (denoted A) independently. First, we want to know if the pressure has an effect and thus we kept the average pressure constant together with the density, such that for the scan in Fig. 11.15(a) $T_\parallel + T_\perp$ was held constant. The values were chosen for having equal hot and thermal beta. In all plots of Fig. 11.15 same color means same scenario, continuous line real and dashed line imaginary parts of the dielectric tensor. It shows the profiles of the hot dielectric tensor on the midplane $Z = 0$. Fig. 11.15(a) shows considerable differences between the different cases, even if the pressure is kept constant, suggesting that it is the temperatures and the density having distinct effects rather than the pressure as macroscopic quantity. In the case of Fig. 11.15(b), the perpendicular temperature was kept constant at $91\,\mathrm{keV}$. Evidently, when going from ($T_\parallel = 9.1\,\mathrm{keV}$,$A = 10$) to ($T_\parallel = 910\,\mathrm{keV}$,$A = 1/10$), the dielectric tensor becomes much flatter, going from being very localised around the resonance to almost constant over the whole plasma. Also, the imaginary part is not only more localised and higher amplitude for lower $T_\parallel$ and higher A, but also less symmetric at the LFS and HFS of the resonance. From here, one can conclude that the dependence is not explicitly on $T_\perp$ either, and the differences must lie in the parallel temperature and the anisotropy. Therefore, we keep the parallel temperature constant, $T_\parallel = 91\,\mathrm{keV}$ and vary the anisotropy. The amplitudes are now very similar (Fig. 11.15(c)) and the only clear difference is the asymmetry to the left and the right of the resonance for $A = 10$, an asymmetry which is almost completely missing if $A \leq 1$. The last scan in Fig. 11.15(d) is then to keep the anisotropy constant at $A = 10$ and to vary the temperatures. One can see that the asymmetry in the imaginary part, including the peaking at the resonance, is conserved for all values of the temperature, only the amplitudes of the curves vary. Introducing the physical density along the resonant layer, $n_c(\bar{s}) \equiv n^h(\bar{s}, B = B_c)$, we conclude that the dielectric tensor is proportional to the density factor $\mathcal{N} = n_c \sqrt{T_\perp / T_\parallel}$ (i.e. proportional to the density and the square root of anisotropy), inversely proportional to the parallel temperature $T_\parallel$ and that the form of the imaginary part of the dielectric tensor depends on the anisotropy $A = T_\perp / T_\parallel$, peaking more for stronger anisotropy. As a result, we expect a larger impact on the hot particle contribution to the dielectric tensor as
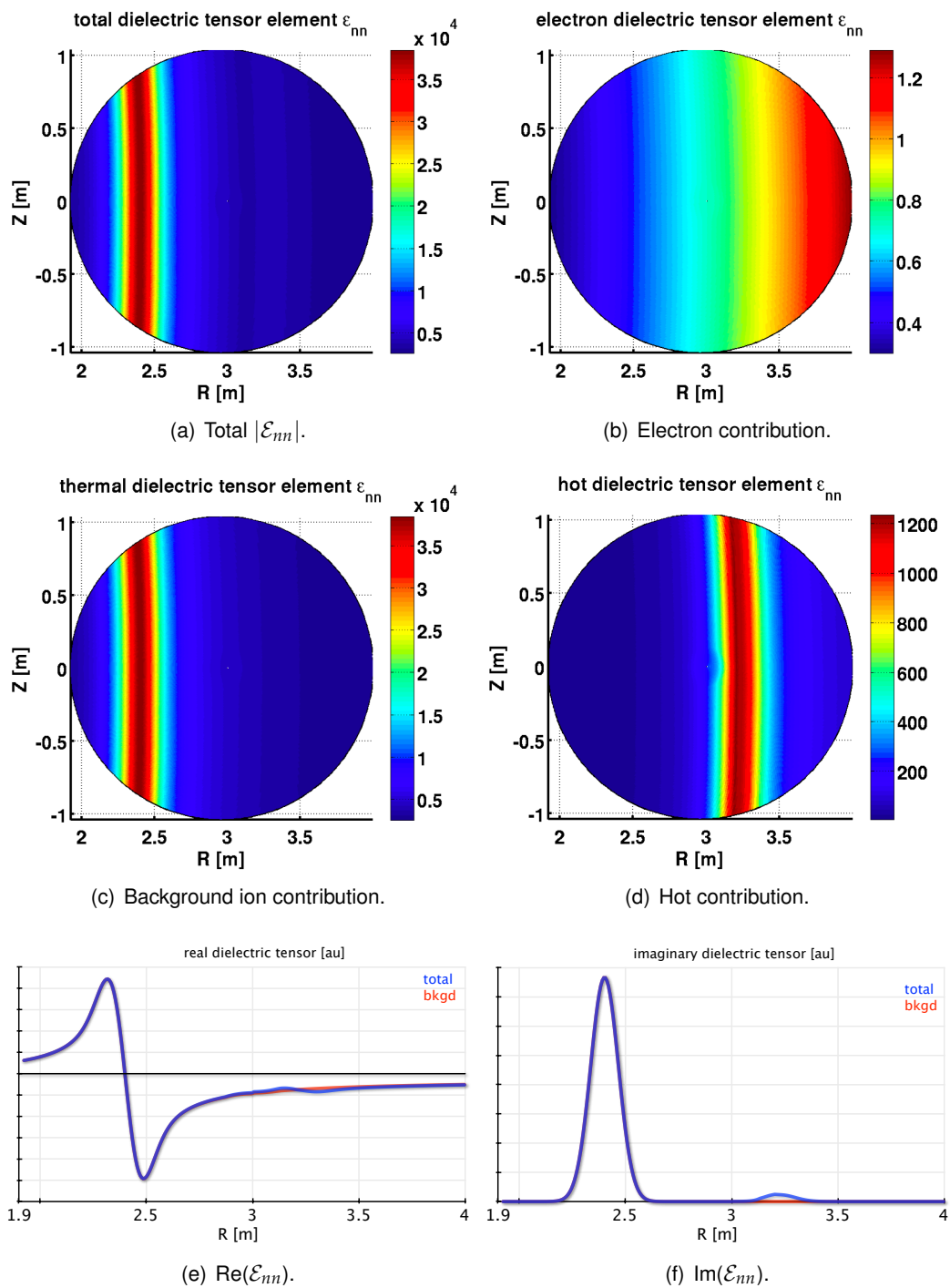
(a) Total $|\mathcal{E}_{nn}|$.

(b) Electron contribution.

(c) Background ion contribution.

(d) Hot contribution.

(e) $\mathrm{Re}(\mathcal{E}_{nn})$.

(f) $\mathrm{Im}(\mathcal{E}_{nn})$.

Figure 11.13.: The $\mathcal{E}_{nn}$ element. 2D plots represent absolute values. The background ion contribution is by far the largest, about four orders of magnitude larger than electron contribution, and about $100/\sqrt{T_\perp/T_\parallel}$ larger than the hot contribution. On the profiles (along the midplane $Z = 0$), the variation of $\mathcal{E}_{nn}$ due to the hot population can be estimated.

(a) Total power deposition.

(b) Electron contribution.

(c) Background ion contribution.

(d) Hot contribution.
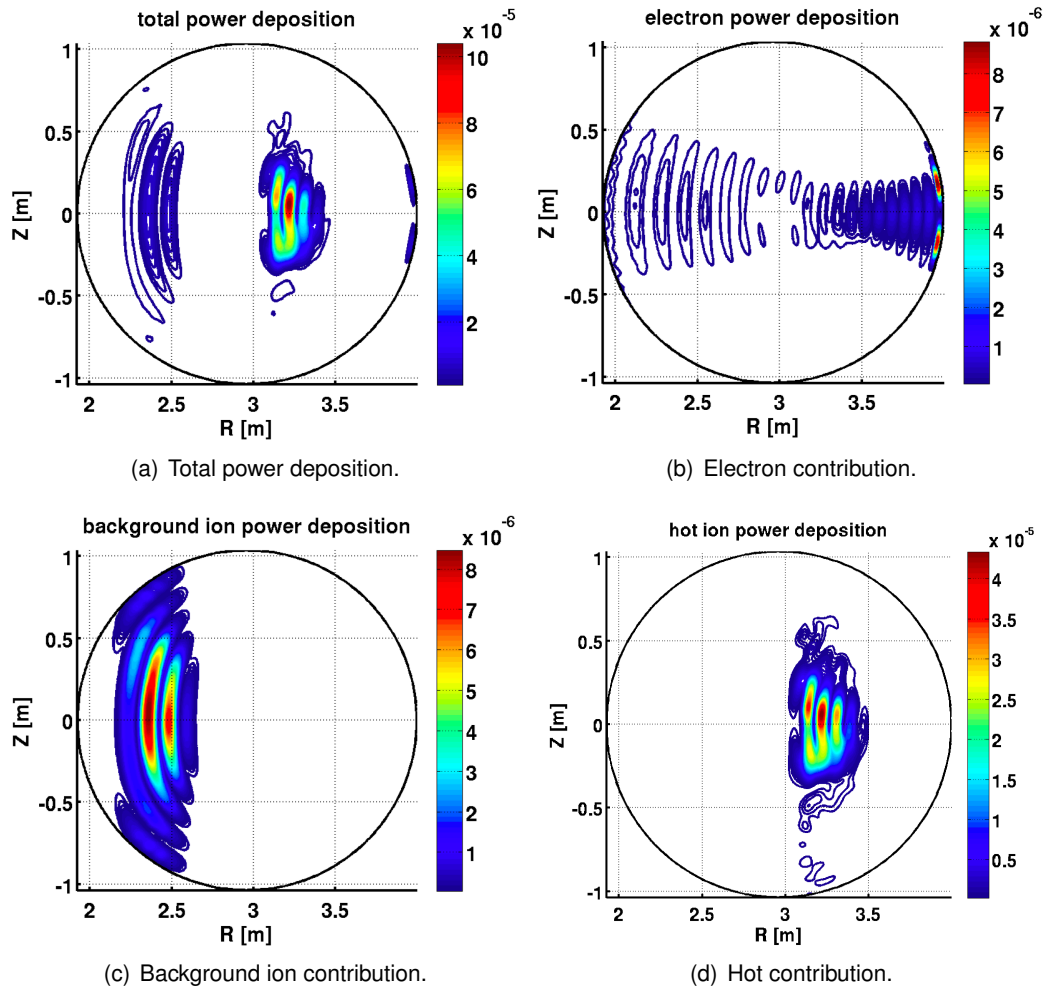
Figure 11.14.: 2D plots of the power deposition. The location of power deposition corresponds to maximum dielectric tensor, but more power is deposited on the minority hot population than on the background ions.

(a) Constant pressure.

(b) Constant $T_\perp = 91\,\mathrm{keV}$.

(c) Constant $T_\parallel = 91\,\mathrm{keV}$.

(d) Constant $T_\perp / T_\parallel = 10$.
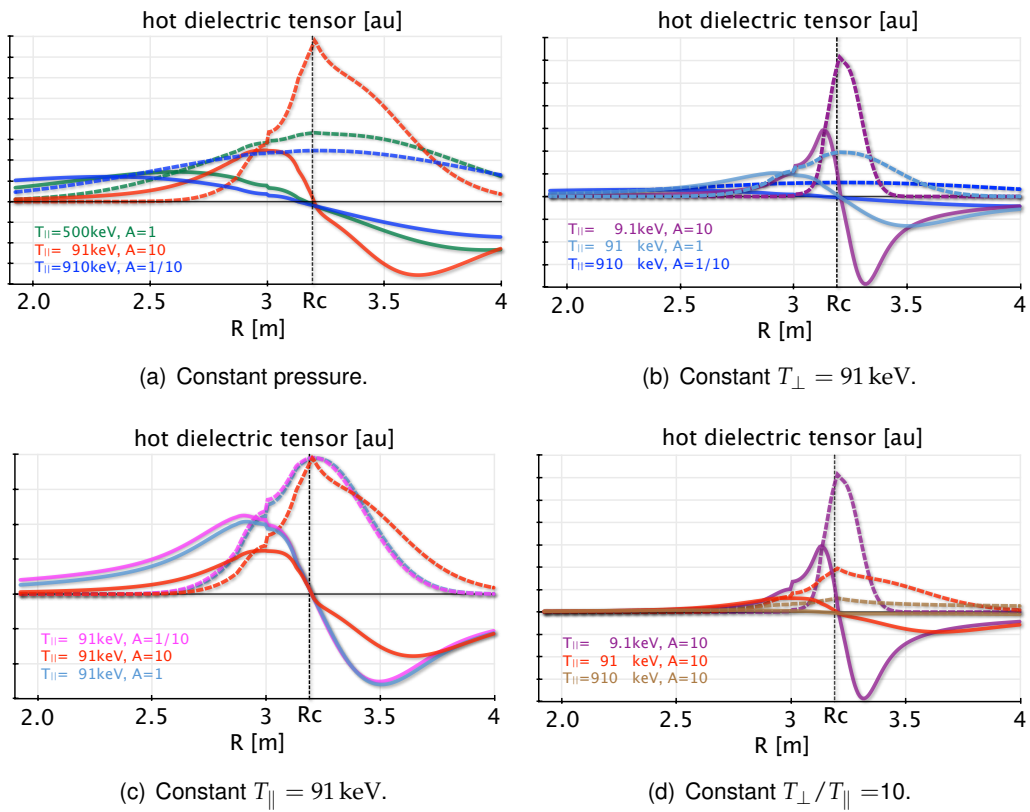
Figure 11.15.: Effect of temperature and anisotropy on hot dielectric tensor. Profiles along the midplane $Z = 0$. The resonant layer is at $R_c = 3.19$ m, the axis at $R_0 = 3$ m. Continuous lines represent the real part, dashed lines the imaginary part.

(a) Background ions.   (b) Thermal minority.   (c) Hot minority.
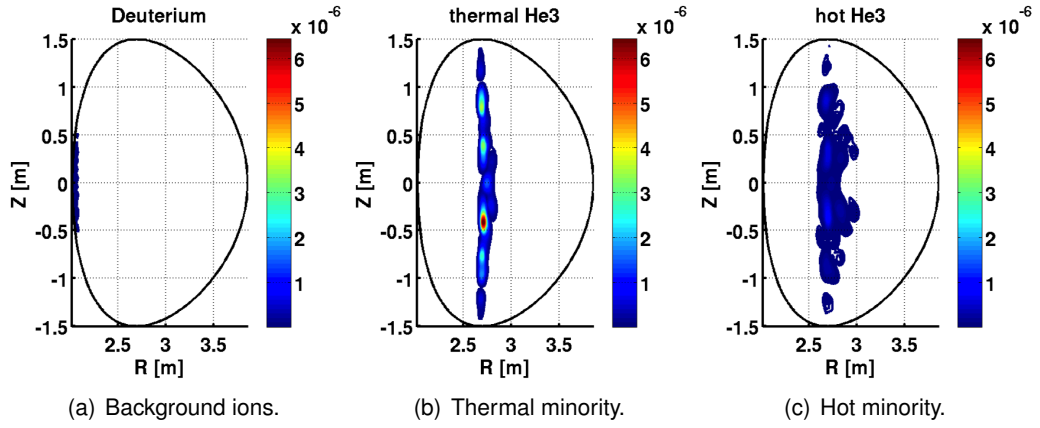
Figure 11.16.: HFS $-90\,^{\circ}$: Absorbed power. Same scale used for all plots. Deposition on hot He^3 is broader but lower than on the thermal He^3 .

$\mathcal{N}(\bar{s})$ is increased. This will be largest for off-axis heating on the LFS, and will increase with minority concentration.

11.4.2. Simulation results

The study in the previous section suggested that the hot anisotropic dielectric tensor is proportional to $n_c\sqrt{T_\perp/T_\parallel}$ and inversely proportional to $T_\parallel$. We will now turn to the more realistic simulations of Secs.11.2 and 11.3 to see if the emergence of anisotropy together with the particle diffusion towards the resonance are strong enough to compensate the effect of the higher parallel temperature and effectively make the hot minority population more important in terms of dielectric tensor than the thermal minority or even the background ions. For illustration we picked the $-90\,^{\circ}$ cases, one on the HFS and one on the LFS. For HFS (LFS), Figs. 11.16 (11.19) show the deposited power on the background deuterium, thermal and hot He^3, (the coloring being the same scale), Figs. 11.17 (11.20) the corresponding absolute values of the first dielectric tensor element $|\mathcal{E}_{nn}|$ (for thermal and hot He^3 same scale is used), and Figs. 11.18 (11.21) the thermal and hot He^3 densities, the resulting hot density factor $\mathcal{N}(\bar{s})$ and the absolute values of the dielectric tensor contributions. For HFS heating, one can see the broadening of the power deposition (and dielectric tensor maximum) for the hot relative to the thermal He^3 population, but most of the power (79 %) is absorbed by the thermal population. Fig. 11.18 demonstrates that although the hot density factor $\mathcal{N}(\bar{s})$ is of the same order as the thermal density along the resonance (due to anisotropy), the hot dielectric tensor contribution is much lower than the thermal contribution, the latter being of the order of the background value in the region of maximum power deposition.

A very different picture is drawn in the case of LFS heating: The high localisation of the resonant particles results in the hot particle density being locally higher than the thermal He^3 density (even if the total hot population is only as large as 16 % of the minority
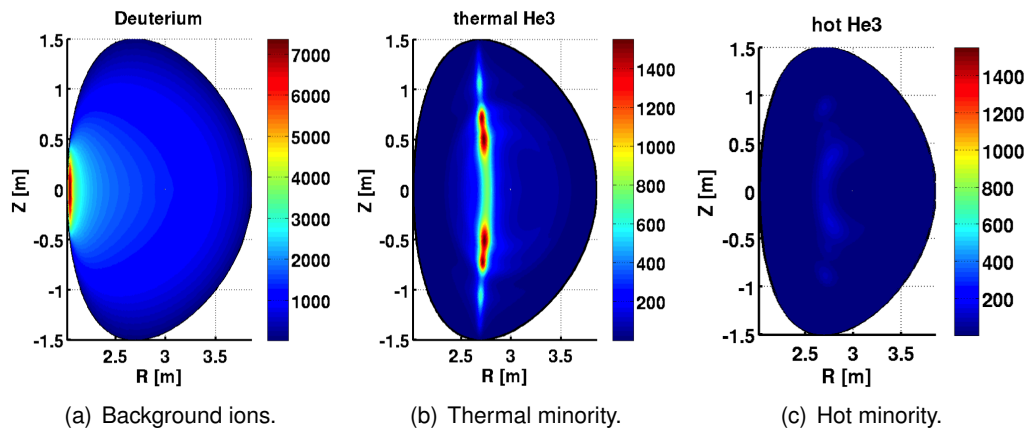
(a) Background ions.   (b) Thermal minority.   (c) Hot minority.

Figure 11.17.: HFS $-90\,°$: Dielectric tensor $|\mathcal{E}_{nn}|$. For He^3 same scale is used. Again, we observe Doppler broadening for hot part, but with a lower amplitude.
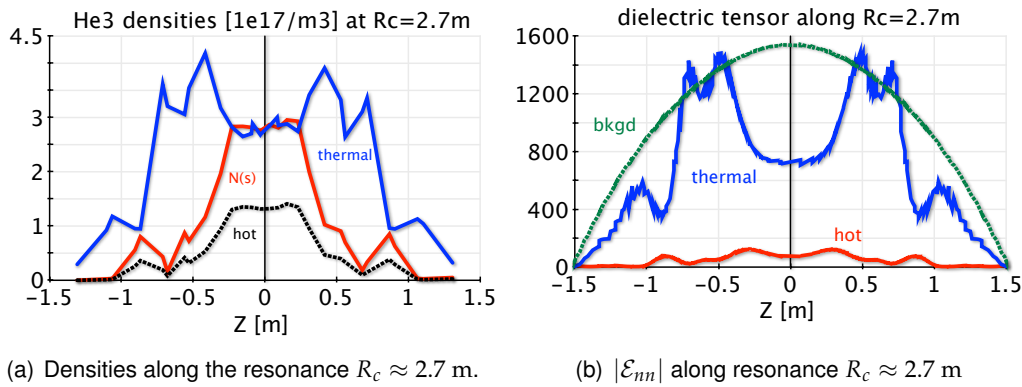

(a) Densities along the resonance $R_c \approx 2.7$ m.   (b) $|\mathcal{E}_{nn}|$ along resonance $R_c \approx 2.7$ m

Figure 11.18.: HFS $-90\,°$: Density and dielectric tensor along the resonant layer. Even though maximum $\mathcal{N}(\bar{s})$ is comparable to thermal density, $T_\parallel$ is high enough to diminish the amplitude of the hot dielectric tensor.

(a) Background ions.   (b) Thermal minority.   (c) Hot minority.
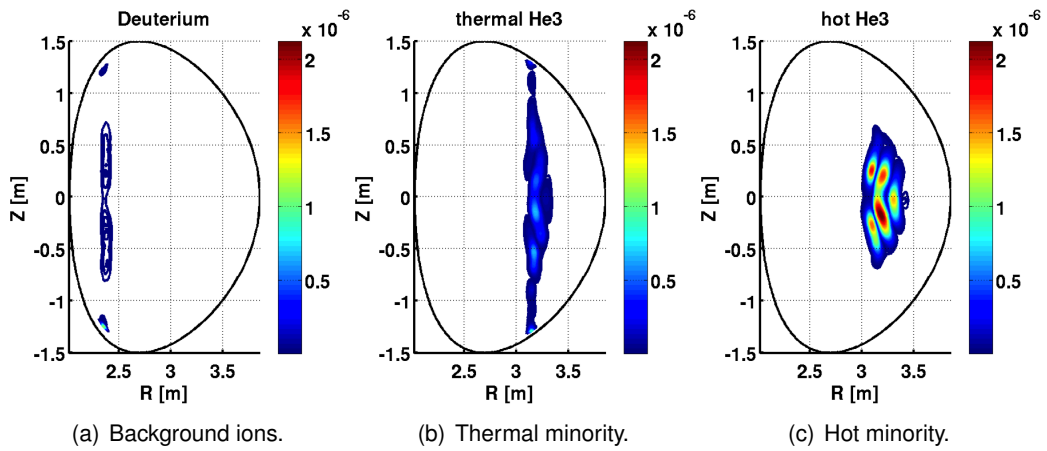
Figure 11.19.: LFS $-90\,^\circ$: Absorbed power. Same scale is used for all plots. Deposition is broader and larger for hot than for thermal He^3. Also, it is more localised around the midplane for the hot part.

(a) Background ions.   (b) Thermal minority.   (c) Hot minority.
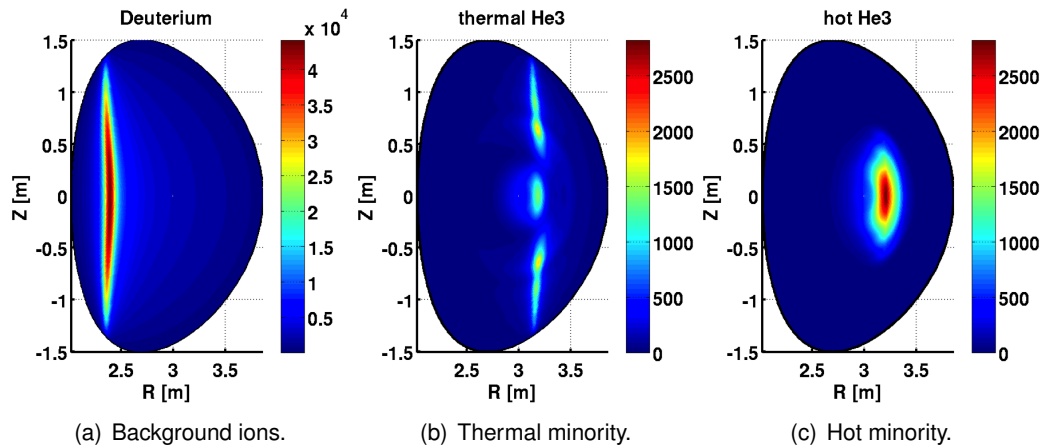
Figure 11.20.: LFS $-90\,^\circ$: Module of dielectric tensor element $|\mathcal{E}_{nn}|$. For He^3 same scale is used. Again, we observe broader and more localised features for hot He^3.

(a) Densities along the resonance $R_c \approx 3.17$ m. (b) $|\mathcal{E}_{nn}|$ along resonance $R_c \approx 3.17$ m
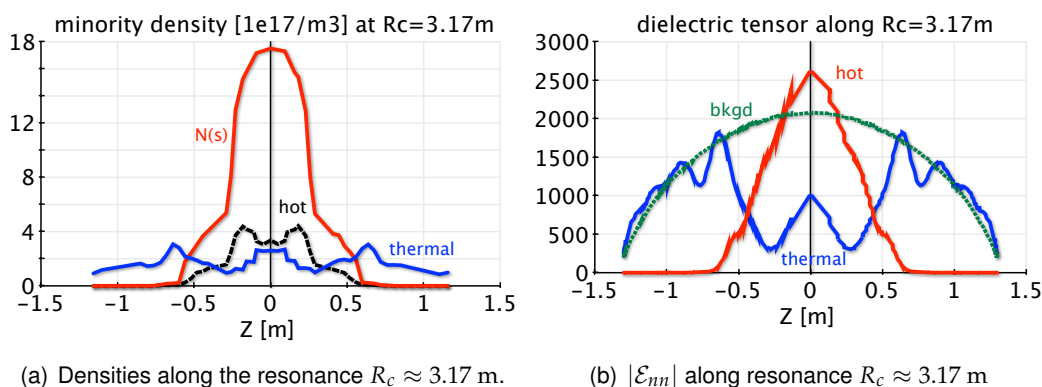
Figure 11.21.: LFS $-90°$: Density and dielectric tensor along resonant layer. Hot density is comparable to thermal density thanks to RF induced particle diffusion. Anisotropy makes $\mathcal{N}(\bar{s})$ much larger, creating a localised peak in the hot dielectric tensor, surmounting even the value of the background around the midplane.

species) and the large number of (deeply) trapped particles drive anisotropy high enough to make the hot dielectric tensor dominant over both thermal minority and background ion contributions (Fig. 11.21). Here, the effect of anisotropy is important enough to outweigh the $1/T_\parallel$ dependence in the dielectric tensor. Resultingly, the hot dielectric tensor has a larger amplitude than the thermal dielectric tensor (Fig. 11.20) and the power is deposited to 85% to the hot minority. Not that this is a very localised phenomenon, and the hot dielectric tensor is only large at the resonant layer and around the midplane.

After these low power He^3 simulations, we will in the next chapter apply four times more power, i.e. $12\,MW$. Also, due to the charge/mass ratio of helium-3, the highly energetic tails are not going to be very large, and it will therefore be more interesting to consider hydrogen. We will then be able to see if the equilibrium does indeed evolve during the self-consistent calculations.

12. High power simulations

In this chapter, we will base the simulation on the same JET-like equilibrium as in the low power simulations of the previous chapter. However, we consider now a 3% hydrogen (H) minority, having the exact same initial temperature and density profiles as the background deuterium . A more detailed description of the equilibrium is given in Appendix D.2. The reason why we switch from a He^3 to a H minority is that we can expect higher tails in the distribution for the lighter hydrogen minority. Here, heating with a given amount of power will result in higher particle velocities due to the lower mass, resulting in a lower critical energy as defined in Eq. (7.2). Therefore, slowing down will be predominantly on the electrons, and pitch angle scattering will be less important, resulting in higher pressure anisotropy. We will again inject two waves, one co- and one counter-passing. One reason is to verify the RF induced particle pinch as described in Eq. (6.41), both for validating the code and showing why it is important to include variations in parallel velocity in the RF Monte Carlo operators. Another reason is to minimise the Fisch currents,[69] which we have seen in the high field side simulations of the low power simulations in the last chapter. The interest in this is to remove the directly induced toroidal momentum and therefore current which exists even when orbit widths are small. Without this, only finite orbit width effects remain in the current, and these are inherent in the model distribution. The toroidal wave numbers are $n_\varphi = \pm 17$, and we will study the evolution for heating on the High Field Side (HFS), On Axis (OA) and on the Low Field Side (LFS). The RF wave frequencies are $52.6\,\mathrm{MHz}$ (HFS), $48.5\,\mathrm{MHz}$ (OA) and $38.7\,\mathrm{MHz}$ (LFS), with a total deposited power of $12\,\mathrm{MW}$. The resonant layers are shown in Fig. 12.1

12.1. Asymmetric wave spectrum

For studying the RF induced particle pinch,[66,67,82] we have run the HFS case not only using two waves with $n_\varphi = \pm 17$, but also one simulation per wave, i.e. one with $n_\varphi = -17$ and one with $n_\varphi = +17$. As before we try to avoid confusion due to sign conventions, and will therefore continue naming the two cases $+90°$ and $-90°$ phasing respectively. As a reminder, Eq. (6.41) states that we expect a net inward drift of resonant particles for $+90°$ phasing and a net outward drift for $-90°$. As a result, $+90°$ phasing produces narrower but larger peaks inside the tangent resonant layer of density and pressure, whereas $-90°$ phasing produces wider peaks outside the tangent resonant layer.[78] This is con-
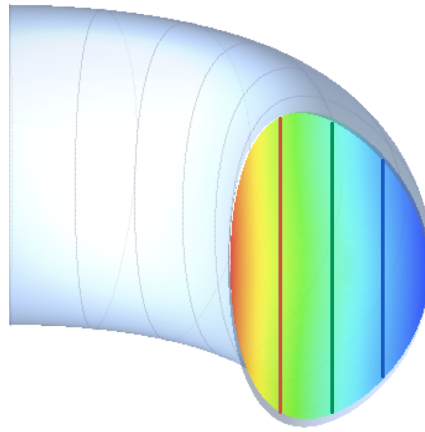
Figure 12.1.: Locations of the resonant layers for HFS (red,left), OA (green,middle) and LFS (blue,right). These are the locations of $B = B_c$, marking the cold resonances, and the true resonances are Doppler broadened.

firmed in Figs. 12.2(a) and 12.2(b), where the density and most of all the perpendicular pressure shows a sharp peak inside the resonant layer (solid vertical line) for the $+90°$ case, whereas the profile is much broader and peaked outside the resonant layer for $-90°$ phasing. Having assessed that this particle drift due to interactions with the wave are included and important enough to be visible, we will be able to include this mechanism in the interpretation of the results in the subsequent sections. We can also verify the projection made earlier in Eq. (11.2), which states that the asymmetry in $v_\parallel$ of the distribution function can be expected to be proportional to the density and temperature gradients (to lowest order in orbit width). This asymmetry is the source for the RF induced currents, and we can therefore compare the total current densities in Fig. 12.2(c) with the density and pressure profiles. Even if the currents are computed directly in VENUS without the application of the bi-Maxwellian model, these plots agree well with the analytical projection from in the previous chapter. We have chosen to place the resonance on the high field side for this study, since for on axis and low field side heating, non standard orbit effects become important, as we will see later in this chapter. We will now turn to symmetric wave spectra, in order to minimise Fisch currents and concentrate on finite orbit width effects, and apply the heating both on the low field side, on axis, and on the high field side.
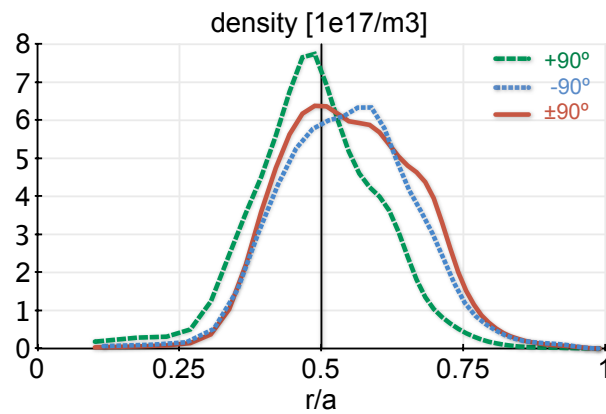
(a) Hot particle density
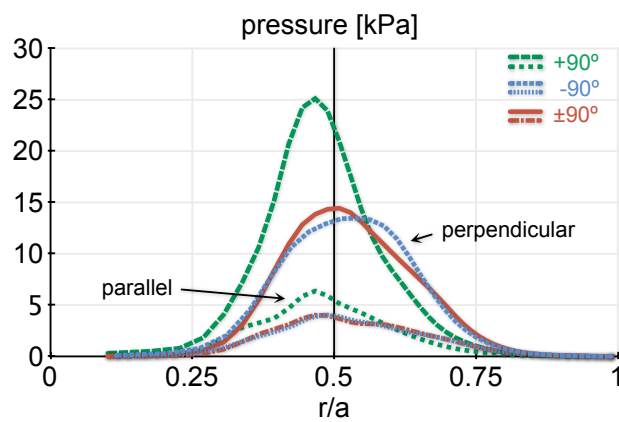
(b) Hot particle pressure. The upper and more continuous line shows the perpendicular, the lower and lighter line parallel pressure for each case.
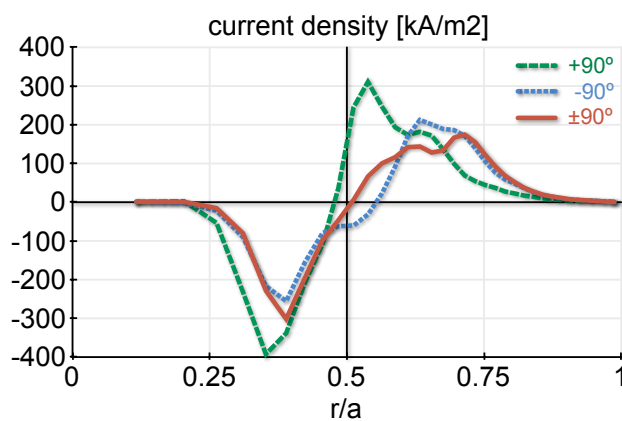
(c) Total RF induced current density. One can verify Eq. 11.2), which states that the current density (to lowest order in orbit width) is proportional to the density and temperature gradients.

Figure 12.2.: The RF induced particle pinch causes density and pressure profiles to be peaked sharply inside (broadly outside) the tangent resonant layer for co- (counter-) current wave injection. $+90°$ corresponds to co-current injection. The solid line marks the tangent resonant layer, located on the HFS.
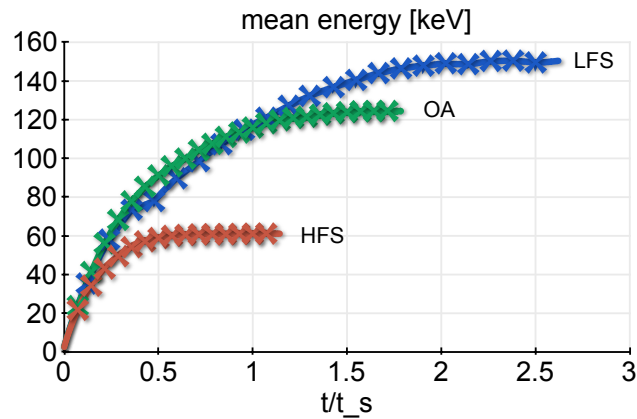
mean energy [keV]

Figure 12.3.: Temporal evolution of the mean energy, Eq. (7.1). On axis heating is about twice as efficient as HFS heating in terms of total minority energy content, LFS another 25 % more efficient than OA. Note also that the higher the final energy content, the longer the total simulation needs to be for reaching steady-state.

12.2. Temporal evolution

At the end of every iteration, we can read the stored data in order to study the temporal evolution. Fig. 12.3 shows the evolution of the mean energy per particle of the minority species as defined in Eq. (7.1). For the High Field Side (HFS) case, we ran $16 \times 15\,\mathrm{ms}$ simulations, for the On Axis (OA) case, $25 \times 15\,\mathrm{ms}$ simulations, and the Low Field Side (LFS) heating needed $22 \times 25\,\mathrm{ms}$ iterations. In the plots in Fig. 12.3, the time on the x-axis has been normalised to the electron slowing down time of $210\,\mathrm{ms}$. The mean energy comprises the thermal and the hot parts, i.e. the total minority species. Therefore, the energies shown in Fig. 12.3 are much lower than the tail temperatures. We will discuss the effective tail temperatures later in this section, and they are plotted in Fig. 12.8.

In terms of heating the minority species, LFS and OA heating is more efficient than HFS heating, since the mean energy (and thus the total energy content) of the hydrogen is higher at the end of the simulation (about twice as high for LFS compared to OA). Now, in all three cases, the simulation converges when the absorbed RF power equals the slowing down power, and the RF power is kept constant at $12\,\mathrm{MW}$. Then, the lower energy content for the HFS heating can be translated into the information that if the resonance is on the HFS, the slowing down on background is more important than for the other cases. Indeed, the resonant particles of the HFS case are mainly at the trapped-passing boundary, completing almost one full poloidal rotation before interacting again. Also, the orbits are wider for barely trapped particles than for the deeply trapped resonant particles in the LFS case, and thus the resonant particles spend more time out of resonance, and lose more energy to the background than the resonant particles of the other cases. Therefore, more power is going to the background, and the steady state is achieved at lower energies. We will study the power balance at steady state more in detail at a later point in this chapter.

In Figs. 12.4(a) to 12.4(c) we show the temporal evolution of the total perpendicular pressure in the HFS heating scenario, which is initially dominated by the background pressure. We show the initial and an intermediate state together with the final state after iteration 16. The colors are to the same scale in all figures of one given case (i.e. horizontally). Perpendicular pressure builds up rather quickly along the resonant layer, and the hot (minority) pressure becomes locally more important than the background pressure, even if the thermal volume averaged beta is always larger than its hot equivalent. Figs. 12.4(d) to 12.4(f) show the same plots but for the on axis heating case. The colors are to the same scale, which is why the initial pressure plot differs from Fig. 12.4(a), even if it shows the exact same absolute values. As before, an elongated feature appears in the total perpendicular pressure along the resonant layer. However, as opposed to the HFS heating, it is much more local and at the magnetic axis, where the initial pressure already is maximum before the RF interaction. Finally, the LFS case in Figs. 12.4(g) to 12.4(i) is similar to the on axis case, in that the final peak perpendicular pressure is larger than the initial pressure, and it is localised around the outboard midplane. The main difference is that the final pressure maximum is not so much along the cold resonant layer, but rather halfway between the magnetic axis and the tangent layer. We will discuss this last item later on.

Possibly the most interesting example of radial profiles is the current induced by Ion Cyclotron Current Drive (ICCD), Fig. 12.5. For the HFS case, a simple dipolar structure forms initially around the resonant layer at $r/a = 0.5$, a structure which is growing and changing shape during the evolution. This dipole is due to finite orbit widths, and the fact that trapped particles always move in the counter-current direction on the inner and in the co-current direction on the outer leg of the orbit. As the wave spectrum is symmetric, Fisch currents are expected to be negligible, and the parallel current is following the trapped current, as symmetric detrapping causes the parallel current to be similar to the trapped current. The current due to detrapping is the dominant for the on axis (OA) and low field side (LFS) heating cases, Figs. 12.5(d) to 12.5(f) and 12.5(g) to 12.5(i). For OA and LFS heating, the passing current does not show the dipolar structure we have seen for HFS heating. These results are of course similar, though stronger in amplitude, to the results discussed in the last chapter. However, the higher energies for these high power scenarios have the effect that non-standard orbits such as potato orbits are more abundant for these scenarios. Especially when depositing power on the low field side, the turning points move inwards for negative wave numbers ($+90°$), after Eq. (6.41), and the counter-current inner leg of the trapped orbits becomes smaller and smaller as the turning points move towards each other. By the time the two turning points merge and a passing orbit forms, only the co-current outer leg of the orbits is left.[11] For $-90°$, the turning points move outwards, but the orbits are still non-standard due to the fact that the turning points of the initially standard trapped orbits lie on the low field side of the magnetic axis. As the turning points slide along the resonance outwards and the particles gain further energy, the particles start describing potato orbits. Detrapping, although due to collisions and not the meeting of the turning points on the midplane, has then the same effect as for $-90°$.[80,81] As a result, preferentially co-passing particles are produced, and we see a large positive passing current forming, whereas the trapped particle current still

(a) HFS Initial.   (b) HFS Iteration 3.   (c) HFS Iteration 16.

(d) OA Initial.   (e) OA Iteration 4.   (f) OA Iteration 25.

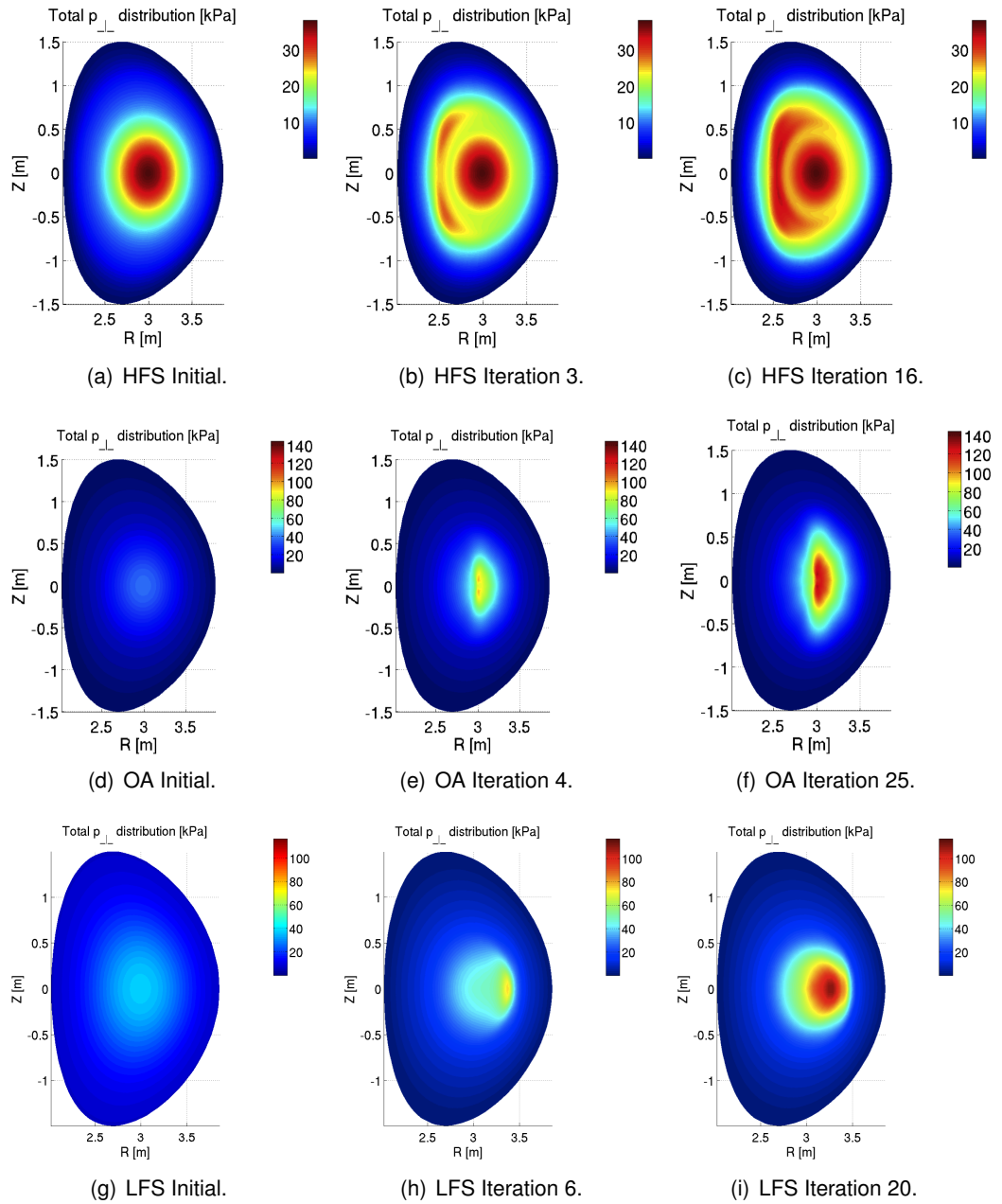(g) LFS Initial.   (h) LFS Iteration 6.   (i) LFS Iteration 20.

Figure 12.4.: Evolution of the total perpendicular pressure for HFS, OA and LFS heating. The iteration for the centre figure has been chosen for the best illustration the temporal evolution. Color scaling is constant for each given resonance position.
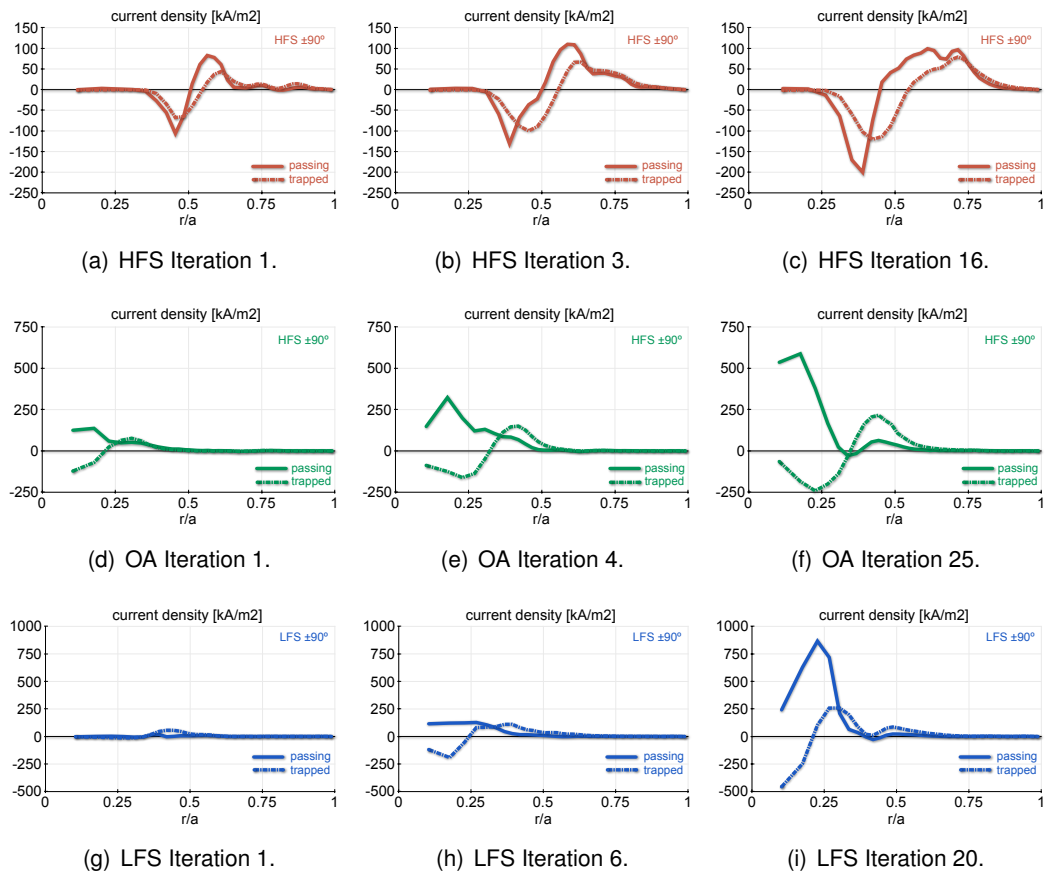
(a) HFS Iteration 1.

(b) HFS Iteration 3.

(c) HFS Iteration 16.

(d) OA Iteration 1.

(e) OA Iteration 4.

(f) OA Iteration 25.

(g) LFS Iteration 1.

(h) LFS Iteration 6.

(i) LFS Iteration 20.

Figure 12.5.: Evolution of the RF induced current density for HFS, OA and LFS heating.
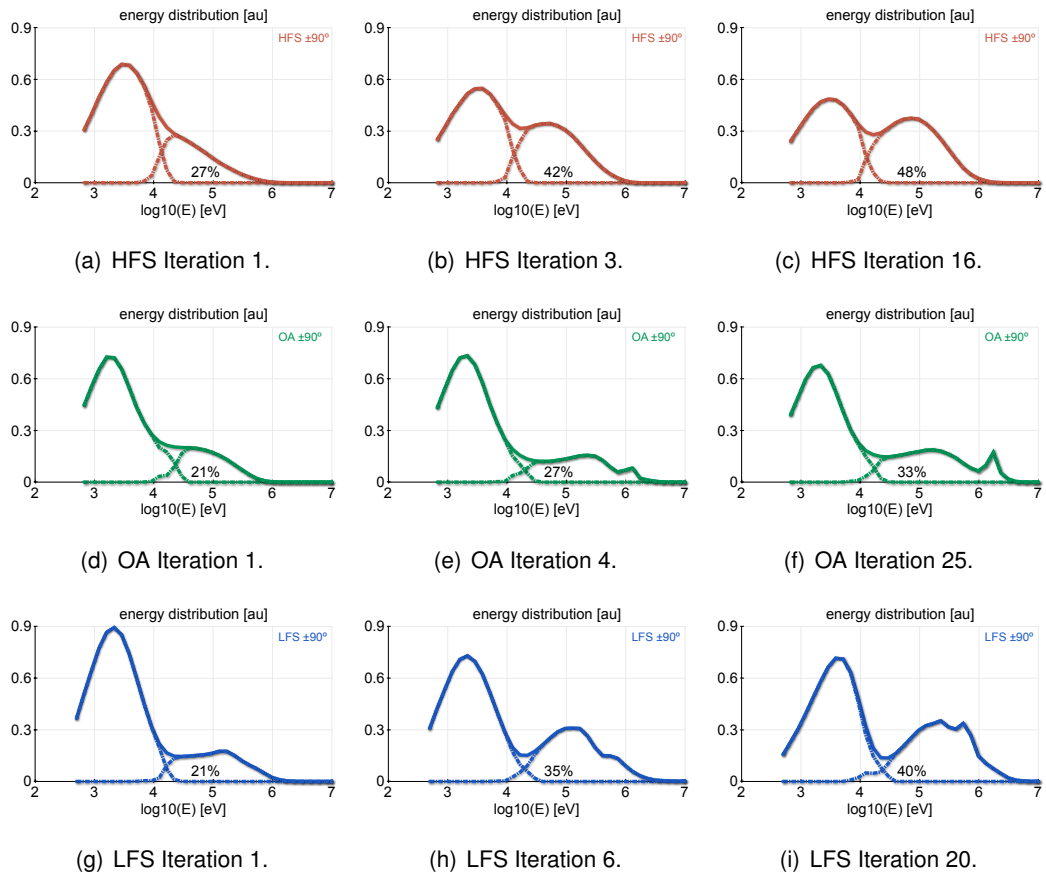
Figure 12.6.: Evolution of the total minority distribution function for HFS, OA and LFS heating. Shown is $f(E)\sqrt{E}$, and the percentage denotes the fraction of hot particle density compared to total minority density.

assumes the dipolar structure we have seen before. A slight speciality in the evolution of the current density for the LFS case is that trapped particle current is dominant at first, since the resonance on the low field side produces deeply trapped particles which are not de-trapped as easily as the orbits for the high field side heating. The final currents are most important for LFS heating, which is in agreement with the highest energy content of Fig. 12.3.

We can also show the evolution of the distribution function. In Fig. 12.6, the building of the high energy tails is visualised for the three cases. The critical energy for splitting the distribution function defined in Eq. (7.3) is set to $E_c = 10T_e$, and the percentages in the plots denote the fraction of hot particle density compared to the total minority density. The high energy tail is created rather quickly, and except for the HFS case, only small changes occur after an initial phase. One can note that the highest percentage of hot particles is found for the HFS case. In the latter case, however, the tail is centered around about $100\,\mathrm{keV}$, which is considerable lower than e.g. in the LFS case. Therefore, even
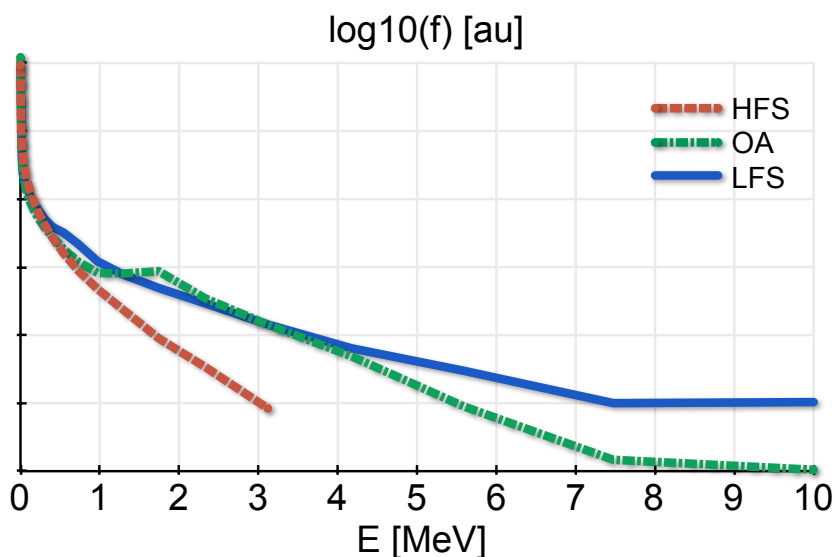
Figure 12.7.: Energy distribution functions with tails in the MeV range for the HFS, OA and LFS cases.

if more particles are considered hot, the total energy content of the hydrogen minority is lower. It is also interesting that in the on axis case, the tail is rather flat, but spans over a wide area in energy space. Also, a distinct feature above $1\,\mathrm{MeV}$ is clearly visible, creating a secondary MeV tail within the distribution. Something similar, although less detached, develops in the LFS case. In Fig.12.6(h), a secondary tail starts forming just below $1\,\mathrm{MeV}$, but in this case it gets almost absorbed by the primary tail which builds up at more comparable energies.

If we then turn towards the final converged state, we can look at the high energy tails in a bit more detail. Fig. 12.7 shows the distribution functions without the Jacobian. $\log f(E)$ is plotted against a linear scale in energy, focusing on the regions with the highest energy. The tails for on axis (OA) and low field side (LFS) heating are more energetic than the tail of the high field side (HFS) resonance. Again, we find the distinct feature just below $1\,\mathrm{MeV}$ for the LFS and around $2\,\mathrm{MeV}$ for the OA case, which is due to a secondary tail forming for the highest energies. In all three cases, particles in the MeV range are present, which gives another confirmation of the importance of including finite orbit effects in such computations. In Fig. 12.8, the effective temperature has been defined as

$$T_{\mathrm{eff}} = -\left(\frac{\mathrm{d}\ln f(E)}{\mathrm{d}E}\right)^{-1}, \tag{12.1}$$

and is plotted together with the average temperatures determined by VENUS. These average temperatures are neither the perpendicular nor the parallel temperatures, since
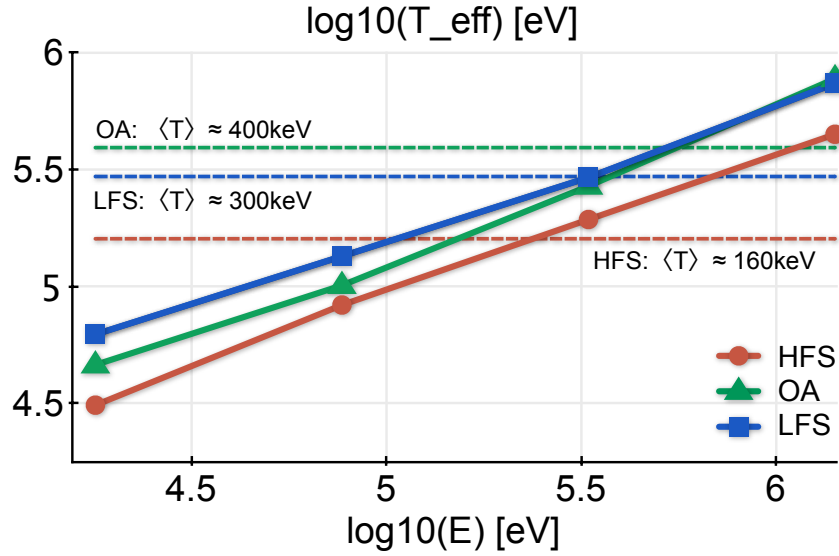
Figure 12.8.: Effective tail temperatures as defined in Eq. (12.1) for the HFS, OA and LFS cases. The dotted lines show the average temperature (12.2) coming from the integrated moments. Maximum effective temperatures are $775\,\mathrm{keV}$ for OA and LFS, and $450\,\mathrm{keV}$ for HFS.

those have radial profiles. The dotted lines in Fig. 12.8 have been created computing

$$\langle T \rangle = \left\langle \frac{p_\perp + p_\parallel}{n} \right\rangle, \tag{12.2}$$

where the average is over the radial variable. This is done only to give an order of magnitude for an effective temperature based on the integrated moments of f, since the latter are the quantities passed on in the iterative scheme of SCENIC. The effective temperatures are not constant, reflecting the fact that the tails are indeed not Maxwellian. Nevertheless, the average temperatures confirm that the representation of the high energy tails with the implemented algorithms is indeed accurate. Even more so if we recall that the tails are in SCENIC represented by different parallel and a perpendicular temperatures, and that the latter can vary in radial direction. This is of course all included in the varying effective temperatures in Fig. 12.8, but not in the constant average temperatures.

Finally, we investigate the secondary tails in the distribution functions of Figs. 12.6(f) and 12.6(i) in a little more detail. The local peak is very clear for the OA case, and we will therefore especially concentrate on this case, where this tail contains about $5\,\%$ of the minority particles. Compared to the total $33\,\%$ of the hot minority, that means that $15\,\%$ of the hot particles are in this secondary tail (recall Table 7.1 for species designation definitions). If we only consider particles in this peak, which are in fact particles having an energy of about four hundred times the electron temperature and energies around $1.6\,\mathrm{MeV}$, we get the density and pressure profiles shown in Fig. 12.9. Density and pressure profiles
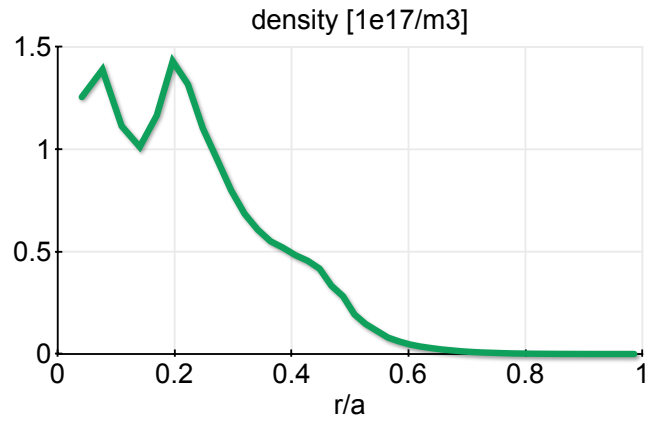
(a) Density profile of the particles in the secondary tail of Fig. 12.6(f). To be compared to total hot density in Fig. 12.15(c).
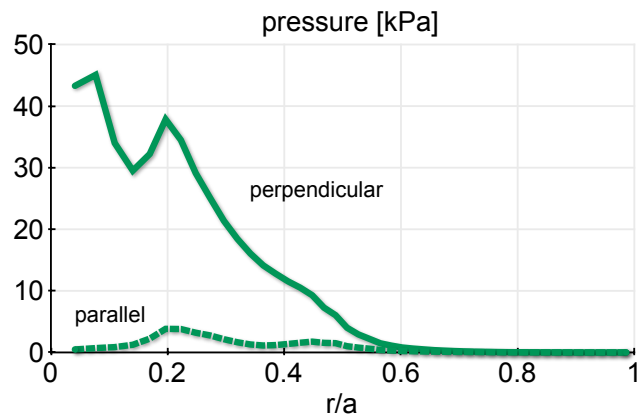
(b) Pressure profiles of the particles in the secondary tail of Fig. 12.6(f). To be compared to total hot pressure in Fig. 12.15(d).
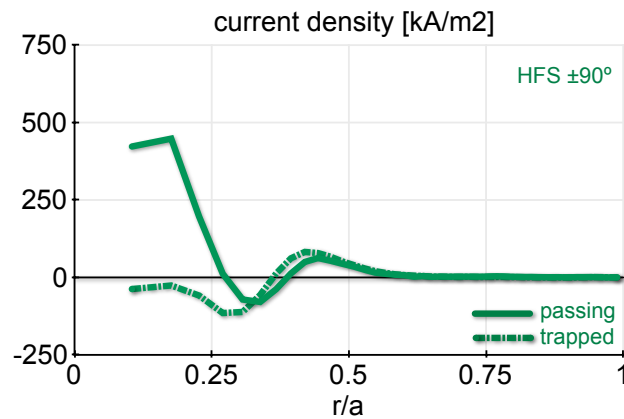
(c) Current profiles of the particles in the secondary tail of Fig. 12.6(f).   To be compared to total minority current in Fig. 12.5(f).

Figure 12.9.: Density, pressure and current density profiles of the secondary tail in the OA distribution function. Perpendicular pressure is much larger than parallel pressure, and the total passing current density from Fig. 12.5(f) is entirely dominated by these contributions.

(a) Inner maximum, $r/a = 0.04$ (b) Middle minimum, $r/a = 0.14$ (c) Outer maximum, $r/a = 0.20$
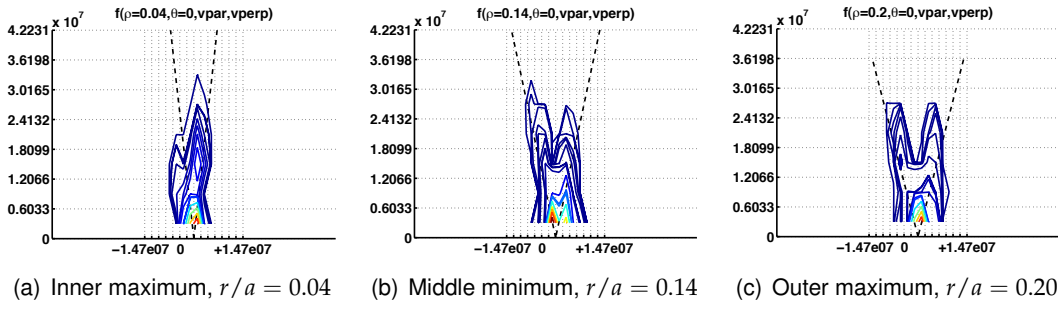
Figure 12.10.: The contour plots for the three positions of the local maxima and minimum show that the particles in the secondary tail are dominated by highly energetic particles on the passing-trapped boundary.

are clearly peaked towards the magnetic axis and thus the resonant layer. Fig. 12.10 shows the distribution function contours at the radial positions of $r/a = 0.04, 0.14$ and 0.20, which correspond to the two local maxima and the local minimum of the two profiles. Almost all the particles at this high energy are situated along the trap cone in all three positions. The typical banana width in the large aspect ratio limit is approximated by[12] $qv_\perp/\Omega \sqrt{\epsilon}$, with the standard notations as defined in this thesis. If we take a characteristic perpendicular velocity from the contour plots, say $v_\perp \sim 15 \times 10^6 \, \mathrm{m/s}$, a safety factor close to unity and with $r = 0.2a = 0.23 \, \mathrm{m}$ the outer maximum position, we get a banana width estimation of about $20 \, \mathrm{cm}$. Fig. 12.11 shows example orbits of particles in the secondary tail. Two are trapped, one passing, all three having an orbit width of about 30cm, which is much closer to the estimation of the potato orbit width[12] $(qv_\perp/\Omega_0 R_0)^{2/3} R_0 \approx 32 \, \mathrm{cm}$. In fact, the results for the OA and LFS cases shown in this chapter are largely dominated by non-standard orbits such as potato orbits, similarly to what we have observed in the low field side low power scenario described in Chapter 11. In particular, the passing current density of Fig. 12.5(f) is completely dominated by the current density from these non-standard orbits, shown in Fig. 12.9(c).

12.3. Power deposition

The wave-particle resonance is satisfied if $\omega = n\Omega + k_\parallel v_\parallel$. The Doppler shift $k_\parallel v_\parallel$ is responsible for a broadening of the power deposition at high parallel temperatures. This is shown in Fig. 12.12, where the initially thin deposition along the resonant layer is broadened by the RF heating, and especially for on axis heating power is deposited almost up to the plasma edge.

Resonant particles describe trajectories whereof only a small portion is located in the resonant region. Typically, a trapped particle interacts four times, a passing particle twice during a full poloidal revolution. The Coulomb interactions with the background ions and electrons, however, are continuous. As a result, the power deposition on the background, i.e. the power lost by the minority ions, is expected to define a broader region than the RF
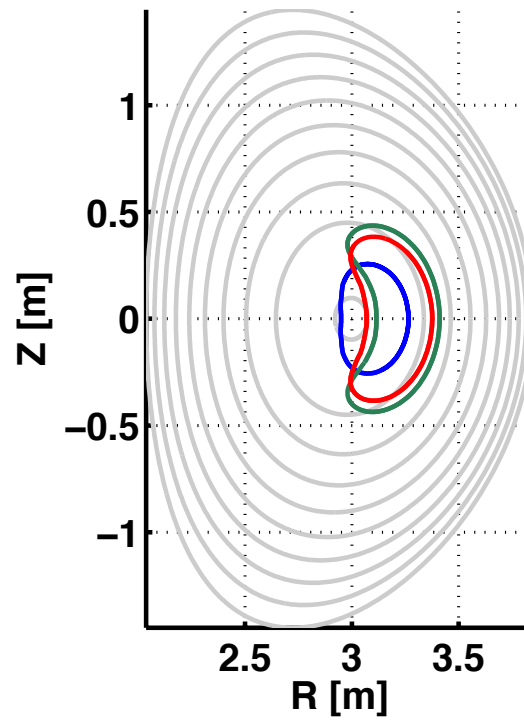
Figure 12.11.: Three examples of orbits in the secondary tail of the OA heating case. The orbit widths are about 30cm, which compares well with potato orbit width estimations for these $1.6\,\mathrm{MeV}$ particles.
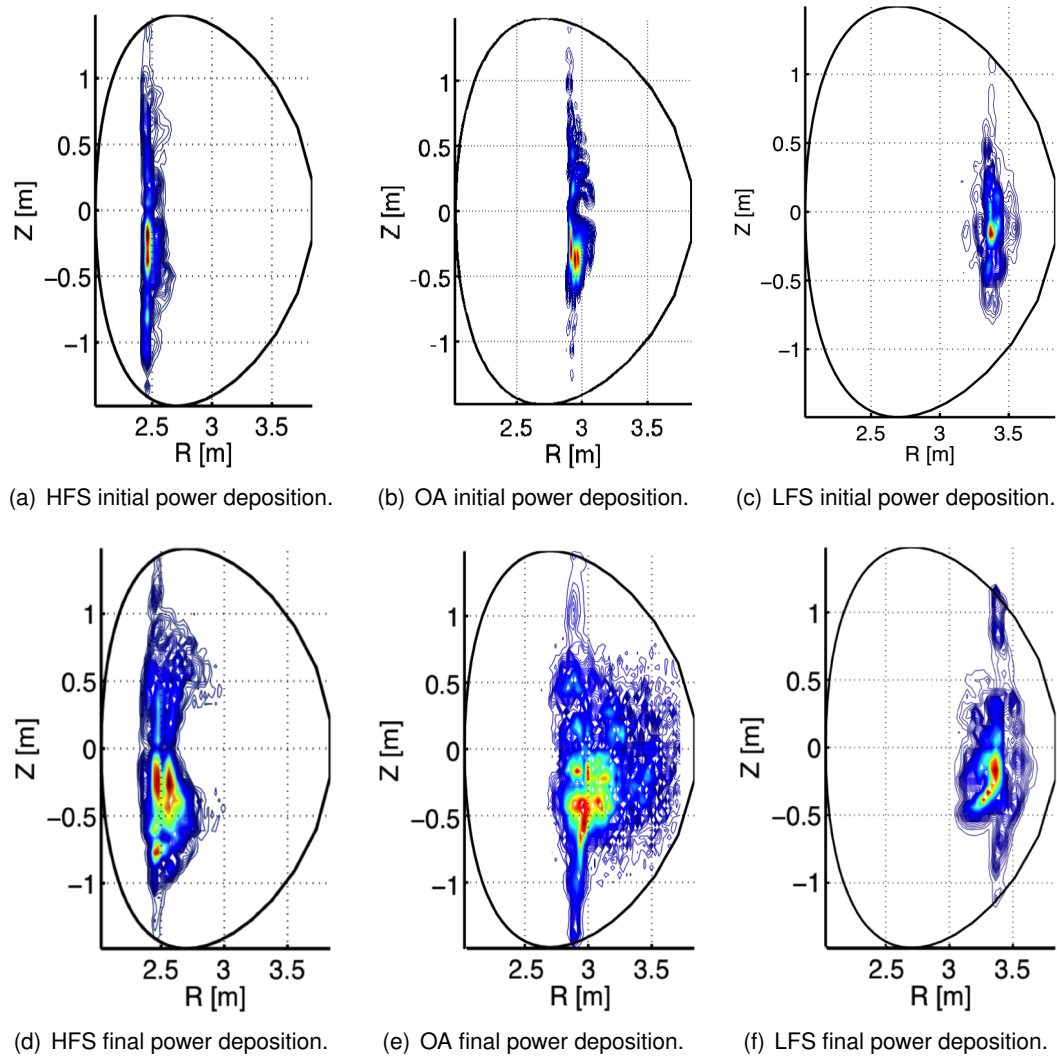
(a) HFS initial power deposition.   (b) OA initial power deposition.   (c) LFS initial power deposition.

(d) HFS final power deposition.   (e) OA final power deposition.   (f) LFS final power deposition.

Figure 12.12.: Doppler broadening of the resonant layer. Shown is the deposition in the RF operators in VENUS at the end of the simulation.

power deposition. In steady state, the power absorbed by the minority from the RF wave balances the power lost to the background in total, but there are regions in the plasma where one process is dominant over the other. Fig. 12.13 shows the steady state radial power density profiles, with the sign convention that positive power means absorbed by the minority from the wave, P_{ICRH}, negative meaning lost by the minority to the background, P_{Coul}. The red curve is the sum of the two, and green shading denotes regions of net heating ($|P_{ICRH}| > |P_{Coul}|$), whereas regions of net slowing down ($|P_{ICRH}| < |P_{Coul}|$) are indicated in blue shading. These regions have to balance each other when integrated, such that

$$\int \left(P_{ICRH} + P_{Coul} + P_{loss} \right) \mathrm{d}^2 x = 0, \tag{12.3}$$

where P_{loss} incorporates the power absorbed but not yielded to the background due to particle losses. As expected, the region of net slowing down (shaded blue) is broader for the HFS than for the other cases, since the resonant particles describe larger orbits, resulting in lower energy content of the minority species. As a conclusion, if the goal is to heat the background plasma, HFS heating is preferable, since the minority is heated less and the background is heated in a broader region. But before investigating the effects on the equilibrium, we want to check whether the bi-Maxwellian model in the equilibrium and wave field calculations represents a good approximation.


12.4. Model bi-Maxwellian

As in the last chapter, we will compare the distribution function from VENUS with the bi-Maxwellian model. These two chapters used the same equilibria, but the resonant layer was chosen slightly further from the magnetic axis for HFS and LFS heating. For the contour plots $f(v_\parallel, v_\perp)$, we chose again the flux surface of the resonant layer, and at $\theta = 0$ on the outboard midplane. For on axis heating, we decided to show the contours at $r/a = 0.25$, since there is no special position with respect to B/B_c except the magnetic axis, where we do not have any grid points for statistics. At the chosen point. however, the currents from VENUS and the model are similar (see Fig. 12.17(b) which will be described later), such that we expect a good match between VENUS and the model at that position. In Fig. 12.14, the ear-shaped features for the HFS can very accurately be reproduced by the model, with the tips along the (dashed) trapped-passing boundary, suggesting high number of barely trapped/passing particles as expected. For the on axis (OA) case, the ears are inside the trapped-passing boundary, meaning that a large population is being trapped. The model shows slightly less extreme ears than VENUS, containing more deeply trapped particles ($v_\parallel \approx 0$) than the distribution function from VENUS. However, the same asymmetries appear in both contours, with somewhat more trapped particles for negative parallel velocity and more co-passing particles. The LFS contours show both the characteristic oval shapes, with a slightly more important asymmetry in the VENUS distribution. This might again be attributed to the secondary tail in the VENUS distribution function, which is less separated from the primary tail than in the OA case. Overall, Fig. 12.14 confirms that the model distribution is indeed a very adequate approximation
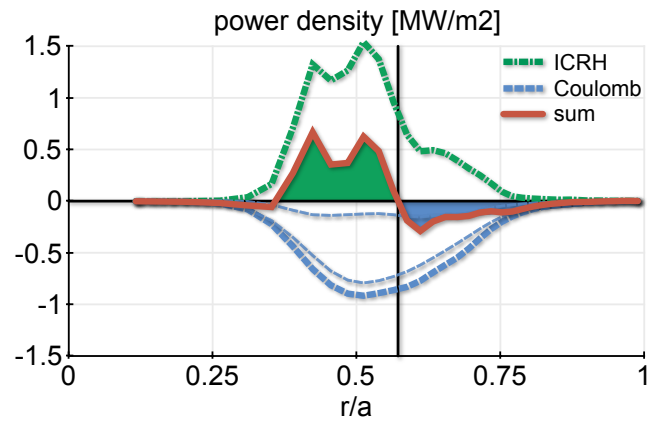
(a) HFS. Net heating between $r/a = 0.35$ and $\rho = 0.57$, net slowing down outside.
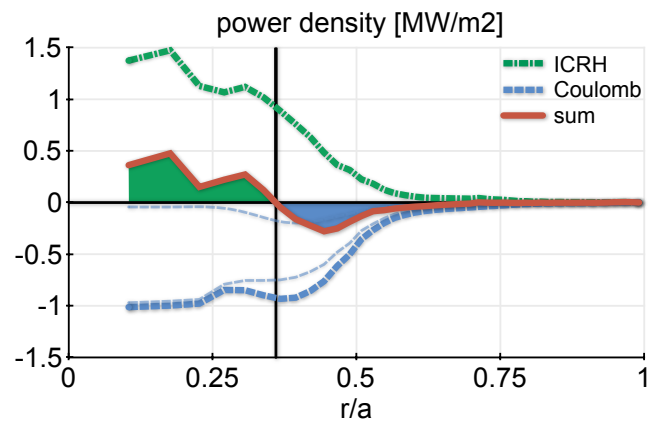
(b) OA. Net heating inside $r/a = 0.36$, net slowing down outside.
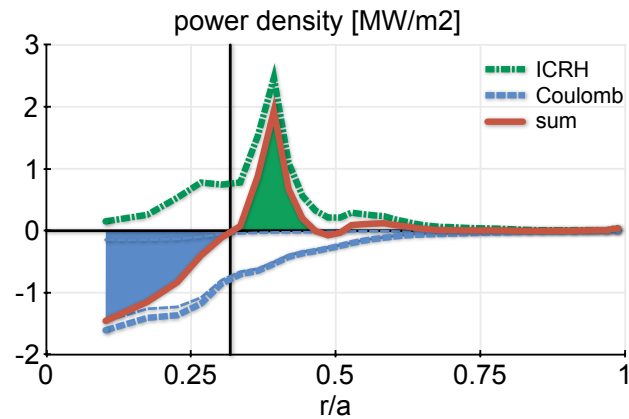
(c) LFS. Net heating between $r/a = 0.32$ and $\rho = 0.46$, net slowing down inside.

Figure 12.13.: Radial power densities, showing regions of net heating (red shaded) and net slowing down (blue shaded). Note that the integral of the resulting (red, thick) curve plus the small losses is zero in steady state. The thin dashed lines show the electron and ion contributions to the total slowing down.

of the raw self-consistent distribution function from VENUS. For the equilibrium, we need the model to match integrated moments of the distribution function, most importantly the density and pressure profiles as discussed in Sec 7.4. In Fig. 12.15, hot particle density and pressures are compared between the distribution function in VENUS and the profiles resulting from the model. As already mentioned in the previous chapter, the analytical model only knows about the smoothed profiles passed to VMEC and LEMan from VENUS. The smoothing has been implemented in such a way that the anisotropy is under-estimated rather than over-estimated, and therefore its peak value is lower than in the VENUS distribution. This is the main difference between the raw distribution and the model, with a deviation of about 20% in anisotropy ($\sim p_\perp/p_\parallel$) at the resonance for HFS and OA resonance. For the LFS, anisotropy in VENUS is very large, most of all towards the centre, and therefore the difference in perpendicular pressure is somewhat larger. For the same scenario, the hot particle density gradient is very large, which has been mitigated in the model distribution. For the OA case, we can compare the total hot density and pressures from VENUS with the same quantities coming from the secondary tail only, Fig. 12.9. First of all, the relative contribution from the secondary tail is most important in the perpendicular pressure, suggesting that the importance of this feature in the distribution function is mainly in the perpendicular temperature. Indeed, the perpendicular pressure comes in the relevant region inside $r/a = 0.25$ to about 64% from the secondary tail, whereas only about 23% of the density can be attributed to the latter in the same region.

While the density and pressure profiles can be compared between VENUS and the model, no such comparison is possible for the dielectric tensor. Nevertheless we can compare the initial and final form of the real and imaginary parts of the hot dielectric tensor in LEMan. In Fig. 12.16 the Doppler broadening can be observed by the regions of maxima and minima, which are much larger at the end of each simulation. Also, the maxima assume a certain poloidal dependence, which is due to the pressure anisotropy. The reason the maxima are not extending up to the wall in the final state is that the resonant particle density is vanishing faster after applying RF than in the initial state, thus decreasing the amplitude of the dielectric tensor. Even if the total energy content is highest for the LFS case, the Doppler broadening is not as extreme. The reason lies in the fact that most of the energy density is stored in perpendicular direction, which does not contribute to the Doppler shift.

Fig. 12.17 compares the current densities from VENUS with the currents contained in the model. Recall that this comparison is done purely out of interest, since the currents are directly fed to the equilibrium from VENUS, without modelling. The high field side trapped current is again similar. The passing current, however, is mainly generated through detrapping, and is therefore different in VENUS and the model. The on axis and low field side cases are dominated by asymmetric detrapping into co-passing particles, and non-standard orbits. Therefore, the model currents are further away from the raw currents than e.g. the density, pressures, or even the currents in the low power scenarios from the previous chapter. This shows clearly the importance of feeding the current directly from VENUS to VMEC, whereas Fig. 12.15 yields very satisfying results for density and pressure. We are therefore confident that setup of the model and the linking of the
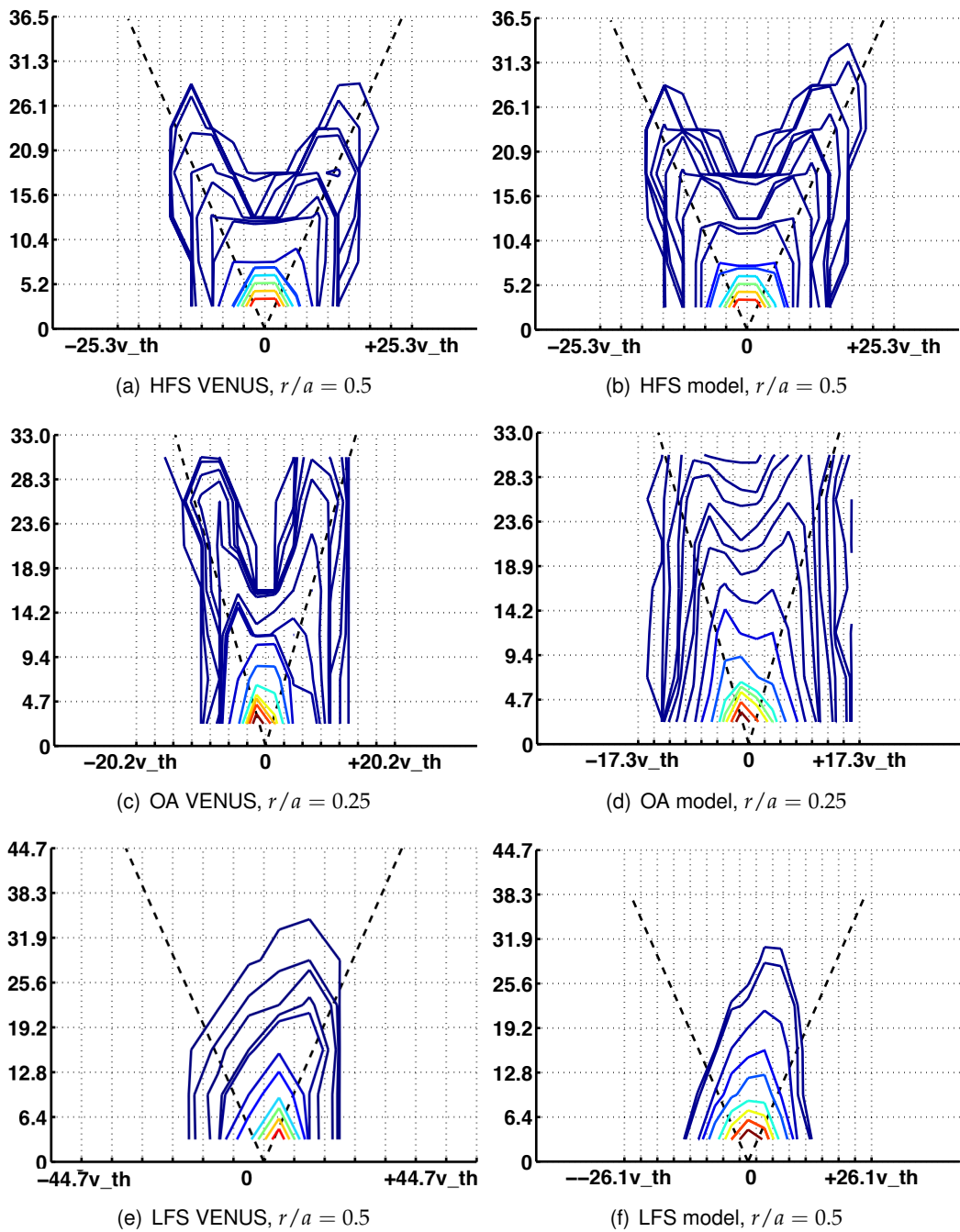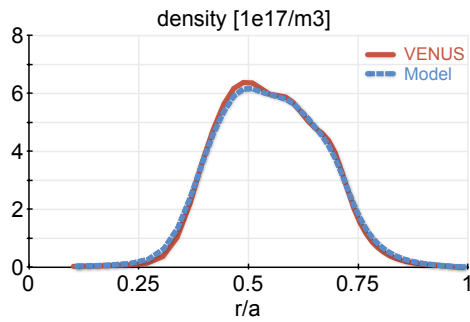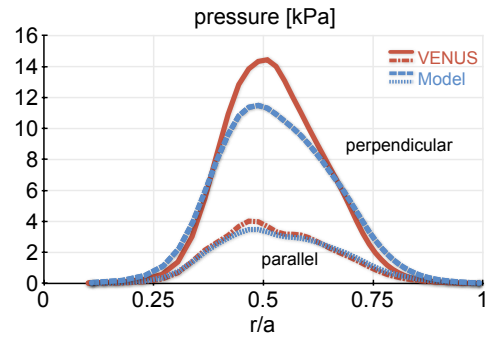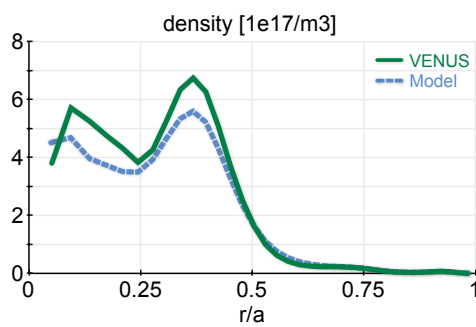
Figure 12.14.: Comparison between VENUS and the model. Both the ear-shaped and the oval characteristic forms are present in VENUS and the bi-Maxwellian. The strong asymmetries in (c) correspond to the secondary tail in the distribution and are not included in the model. The dotted lines show the trapped-passing boundary as defined in Eq. (2.37). The parallel and perpendicular velocities have been normalised to the thermal velocity $v_{th} = 5.4 \times 10^5 \, \text{m/s} (7.3 \times 10^5 \, \text{m/s})$ for $r/a = 0.5(0.25)$.
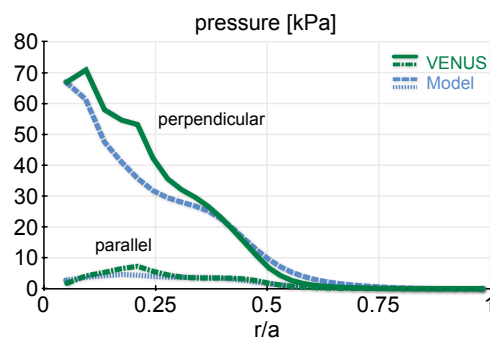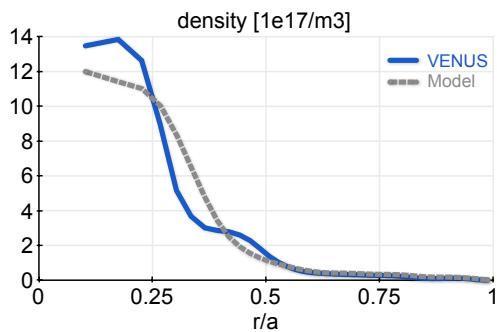
(a) HFS hot density profiles.
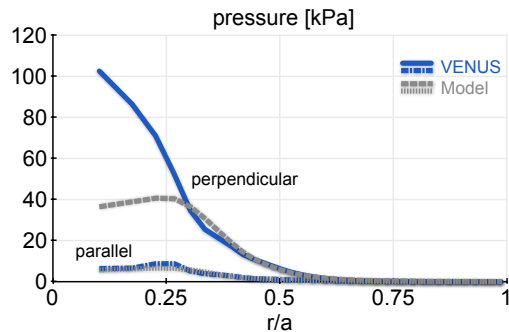

(b) HFS pressure profiles.

(c) OA hot density profiles.

(d) OA pressure profiles.

(e) LFS hot density profiles.

(f) LFS pressure profiles.

Figure 12.15.: Comparison of the first and second moments from VENUS and the model distribution function. The upper curve in the pressure plots shows perpendicular, the lower parallel pressure. hot particle density from the model is used in LEMan for the dielectric tensor, the pressure profiles are read by VMEC for the equilibrium computations.

(a) HFS initial.

(b) HFS final.

(c) OA initial.

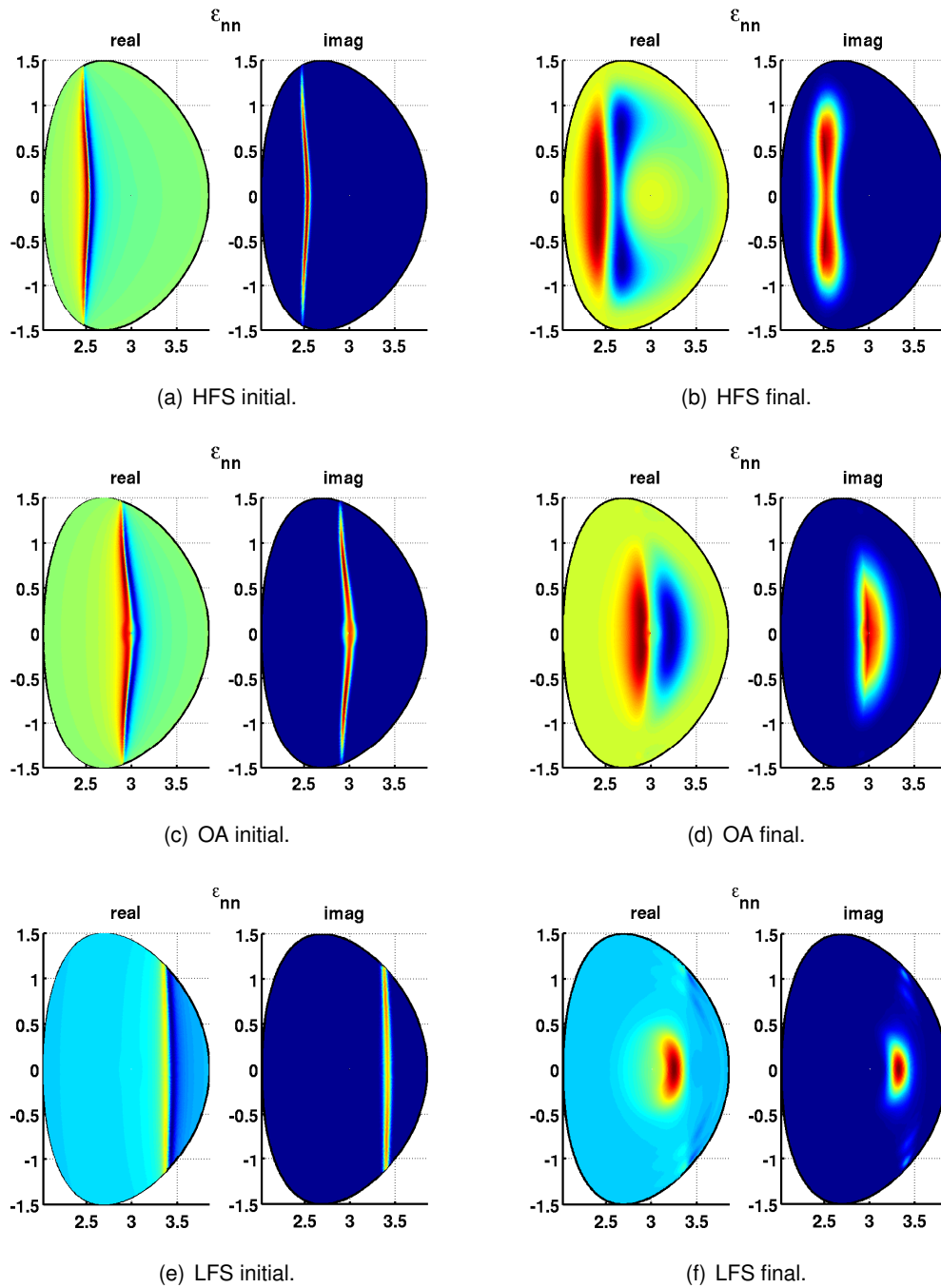(d) OA final.

(e) LFS initial.

(f) LFS final.

Figure 12.16.: $\mathcal{E}_{\perp\perp}$ elements as defined in Eq. (5.1) in the beginning and the end of the simulations. The maxima (and minima) broaden considerably around the cold resonance. They are not extended up to the wall anymore due to the hot particle density vanishing more rapidly at the end of simulation. For the HFS case, the color scale is one order of magnitude lower for the final plots, whereas the scale is comparable for the OA case and exactly equal for LFS.
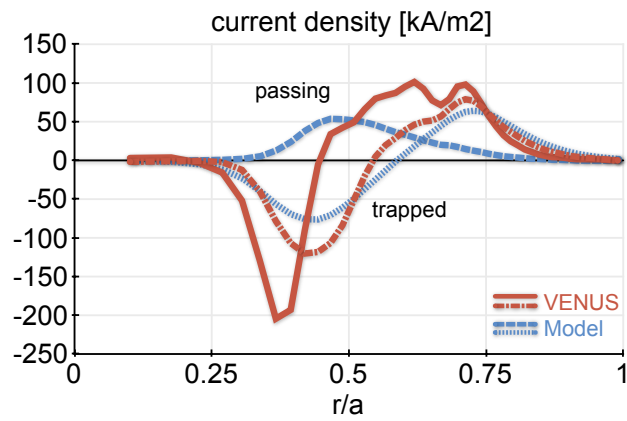
(a) HFS
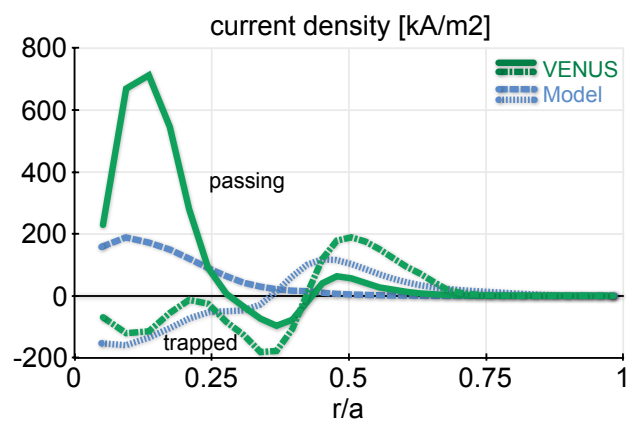
(b) OA
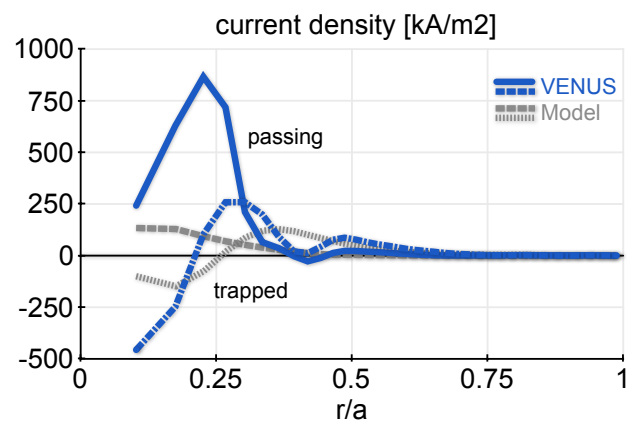
(c) LFS

Figure 12.17.: Comparison of the RF driven currents from VENUS with the currents contained in the analytical model distribution function. Trapped particle current can be modeled more accurately since its origin lies in finite orbit width effects. Lighter lines always denote trapped particle current, more solid lines passing current. Note that the current is fed directly from VENUS into the equilibrium, as defined in Sec. 7.4 and Eq. (7.9). and not the current coming from the model.

codes in the package SCENIC is very well suited for simulating ICRH scenarios. The next step is therefore to investigate the effects of the hot particles on the equilibrium in the next section.

12.5. Effects on the equilibrium

The changes in pressure and current can have effects on the equilibrium, such as the safety factor and the Shafranov shift as discussed in Sec. 2.1.2. In Sec. 6, we described that the current from the VENUS simulations does not include the reaction of the background ions and electrons, and has to be diminished by the drag current, Eq. (7.9), for the equilibrium computations. Fig. 12.18 shows the current density from VENUS together with the corrected current density fed to VMEC, and the effect on the safety factor profile at the end of each simulation. For these simulations, we did not consider any impurities, such that $Z_{\text{eff}} = Z_h = 1$ and $m_i = 2m_h$, and the drag current formula simplifies a lot to

$$j^{RF}_{VMEC} = j^{RF}_{VENUS} 1.46 \sqrt{\frac{r}{R_0}} A(1) 0.5 \tag{12.4}$$

This means that the effective current in VMEC is underestimated with respect to a more realistic case with $Z_{\text{eff}} > 1$, and the RF current effect on the safety factor would be greater in reality. This is why we have added the safety factor using the "raw" RF current density, without drag current, in Fig. 12.18(f) in order to show the maximum effect at $Z_{\text{eff}} \rightarrow \infty$. Even with the drag current, one can see that the $q-$profile does change in these simulations. The change is rather low for the LFS scenario, which has to do with the fact that $\sqrt{(r/R_0)}$ becomes very small towards the axis, where the RF induced current is largest, so almost cancelling its effect. Indeed, due to the drag current without impurities, the HFS case is more effective in terms of altering the safety factor profile than the LFS case, even if the total energy content is considerably smaller. The effect on the Shafranov shift Δ, defined in Eq. (2.12), is shown in Fig. 12.19 together with its second derivative. As shown in Chapter 8, the latter plays an important role in the toroidal drift frequency and related MHD stability. Here, the pressure building up has its full effect on the magnetic flux surfaces, and the Shafranov shift varies between $2\,\%$ and $9\,\%$, whereas $\Delta''(r)$ shows a very localised variation for the LFS case, which is due to the localised pressure of Fig. 12.4(i).

For the High Field Side (HFS) case, the hot volume averaged beta increased from $3\,\%$ to $30\,\%$ of the thermal beta during the simulation. For On Axis (OA) heating, the final hot minority contribution was $60\,\%$, and for the Low Field Side (LFS) heating the final hot beta reached $50\,\%$ of the thermal beta. The values of hot beta is shown in Fig. 12.20, where the local values of $\beta(R,Z) = \mu_0 P(R,Z)/2B^2(R,Z)$ are plotted to same scale. Surfaces of constant beta are changed locally in all three cases with respect to the initial state. Whereas for HFS the region of intermediate beta values (between $0.1\,\%$ and $0.2\,\%$) is wider than initially, the OA and LFS contours show that the peak value increased, and for LFS heating, the latter moved slightly towards the resonance. The maximum local beta value changed from initially $0.28\,\%$ to $0.34\,\%$ for the LFS case,

(a) HFS: Current

(b) HFS: Safety factor

(c) OA: Current

(d) OA: Safety factor

(e) LFS: Current
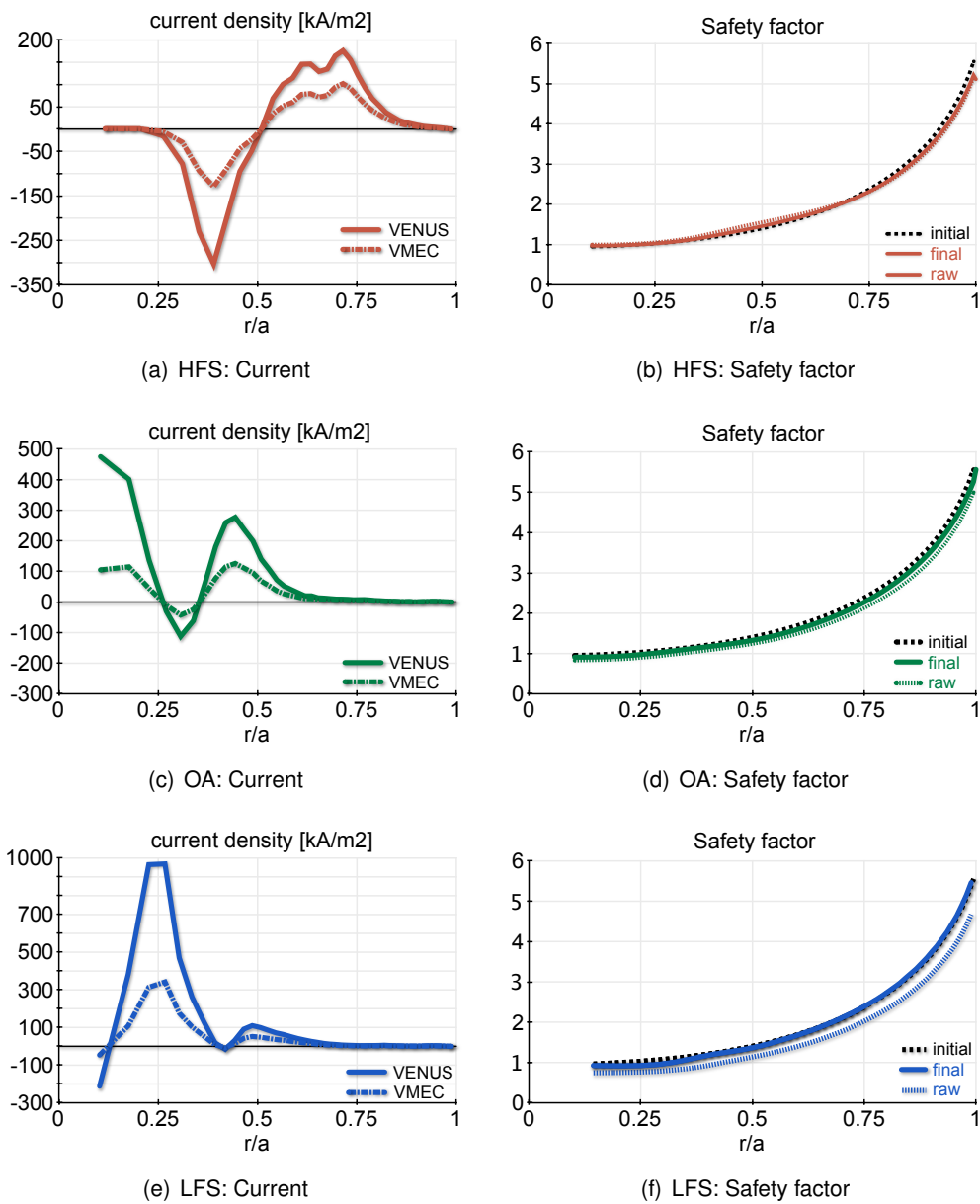
(f) LFS: Safety factor

Figure 12.18.: Direct RF and corrected current densities together with the resulting initial and final safety factor profiles. The higher current densities from the OA and LFS cases are more diminished by the drag current than in the HFS case. The "raw" curves indicate the maximum change in safety factor if the drag current is neglected.

(a) HFS $\Delta(r)$

(b) HFS $\Delta''(r)$

(c) OA $\Delta(r)$

(d) OA $\Delta''(r)$

(e) LFS $\Delta(r)$

(f) LFS $\Delta''(r)$

Figure 12.19.: Changing of the Shafranov shift and its second derivative.

Figure 12.20.: Total beta surfaces initially and for the three converged solutions. Coloring is to scale on all plots.

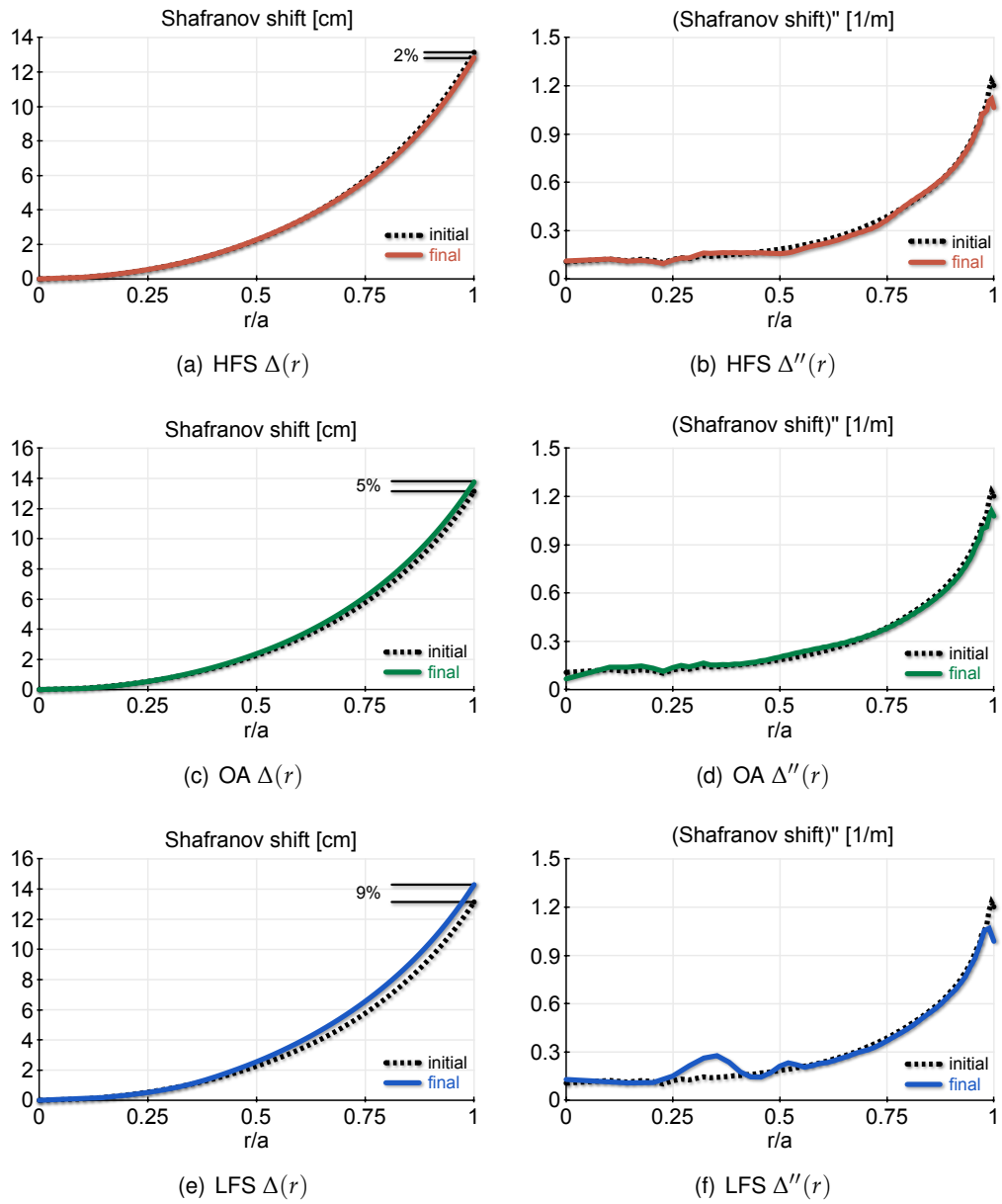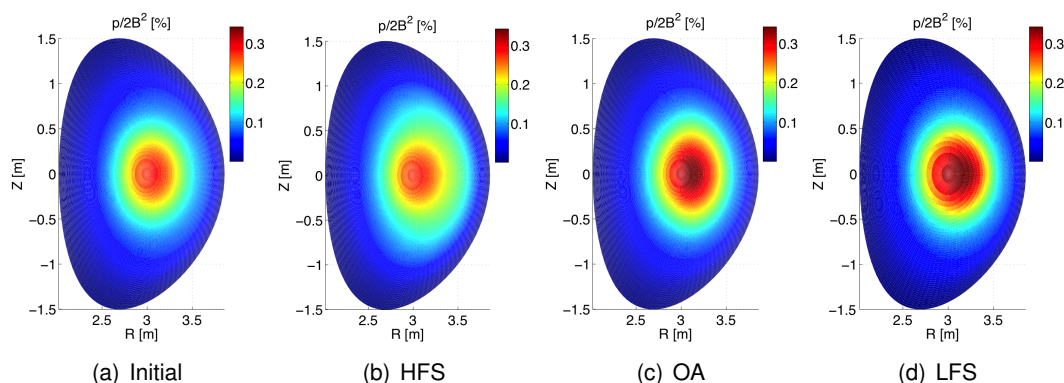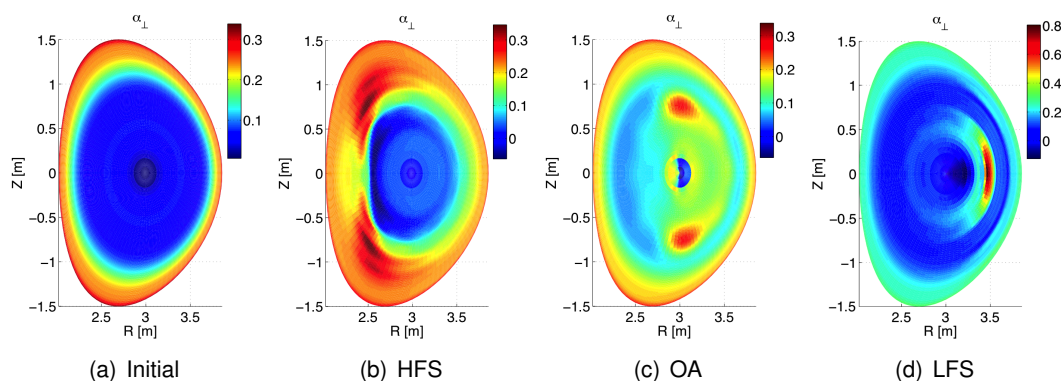Figure 12.21.: Total $\alpha_\perp$ as defined in Eq. (8.4) initially and for the three converged solutions. Note the difference in scale.

which represents a relative increase of about $20\,\%$. As already seen in Chap. 8, one important quantity for MHD stability is the perpendicular ballooning parameter $\alpha_\perp$ directly related to the perpendicular pressure gradient, defined in Eq. (8.4). This parameter is plotted in Fig. 12.21 for the initial conditions and the three converged solutions. For a more detailed view, the colors are not to scale, and the plots show rather different effects for each of the chosen heating locations, except that most changes happen along the resonant layer. The pressure peaking along the resonant layer for the off-axis scenarios, shown in Fig. 12.4, has the consequence that the ballooning parameter becomes negative between the resonant layer and the magnetic axis, with a minimum along the resonance, but inside the flux surface tangent to the resonance. On the opposite side of the resonant layer, outside the tangent flux surface, are the maximum values, with the effect that local variations of $\alpha_\perp$ can be extreme. Similar to what we found when discussing other physical quantities, we find that for the HFS these effects are located all along the resonant layer, whereas they are very localised at the outboard midplane, and more extreme, for the LFS

case. The OA case shows two symmetrically localised maxima along the resonant layer, without the regions of $\alpha_\perp < 0$ observed in the off-axis cases. Whereas initially, $\alpha_\perp$ is very small except towards the plasma edge, with values around $\alpha_\perp \approx 0.05$, the very localised maximum in the LFS case shows amplitudes of $\alpha_\perp \approx 0.8$. This is sixteen times higher than the initial value. More importantly, it is large enough that we can expect effects on global MHD stability. The latter has not yet been investigated, but it is expected that the very large local changes in Δ'' and $\alpha_\perp$ will have a very important effect. This is especially true for the internal kink mode, Mercier and ballooning modes.

12.6. Inclusion of the equilibrium in the iterative scheme

In SCENIC, the equilibrium calculations are fully included in the iterative scheme, and the equilibrium is updated from iteration to iteration. We now want to determine whether this inclusion is important or if it would be sufficient to base the wave and particle iterations, and their saturated solution, on an unchanged equilibrium. The final equilibrium could be constructed, including the hot particle effects in pressure and current, once a converged solution with unchanged equilibrium is obtained. We have repeated the simulations for the LFS case, keeping the equilibrium constant during the complete simulation, but still updating the wave fields with the thermal and hot minority contributions from VENUS. An immediate difference is in the number of iterations needed. Whereas the LFS simulation discussed in the previous sections required twenty-two iterations with a total duration of about two and a half slowing down times, the simulation without the equilibrium evolution had to be iterated thirty times with a total duration of three and a half slowing down times to achieve convergence. But most importantly, the high energy tails of the converged solution are lower, as can be observed in Fig. 12.22(a) Clearly, more minority particles remain thermal and do not contribute to the anisotropic high energy tail. As a result, the effects on the equilibrium are substantially underestimated, as shown in Fig 12.22(b). We show as an example the values of the ballooning parameter $\alpha_\perp$, which is a factor of two lower if one omits the equilibrium calculations in the iterative scheme during the simulations. Similar behaviour is visible on all equilibrium relevant quantities: They show the same general features, but the effects due to energetic particles are smaller if we omit the equilibrium evolution in the simulations. As a last example we plot the dielectric tensor element $\mathcal{E}_{nn}$, where the colors in Fig. 12.22(c) are to scale with Fig. 12.16(f), allowing for direct comparison. Clearly, the maxima of the dielectric tensor are less localised in poloidal angle if we omit the equilibrium calculations, due to lower pressure anisotropy. To conclude this study, we can state that the equilibrium has to be included in self-consistent computations of ICRH, and has to be part of the self-consistent scheme, as variations of the equilibrium during the simulation alter e.g. the particle orbits, as discussed in Chap. 8.
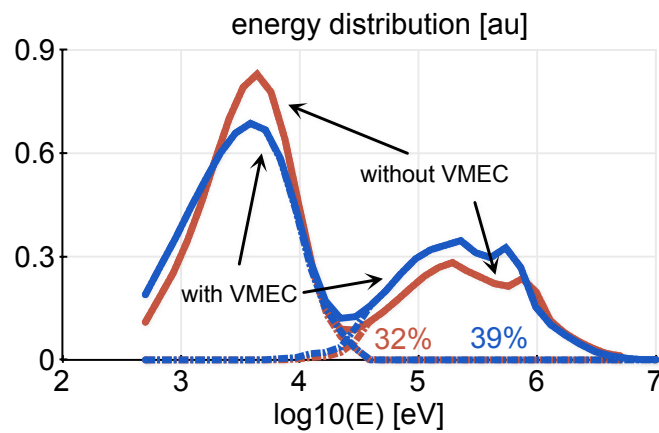
(a) Energy distributions $f(E)\sqrt{E}$. Without the equilibrium evolution in the iterative scheme, the final tails are lower, and more minority particles remain thermal.
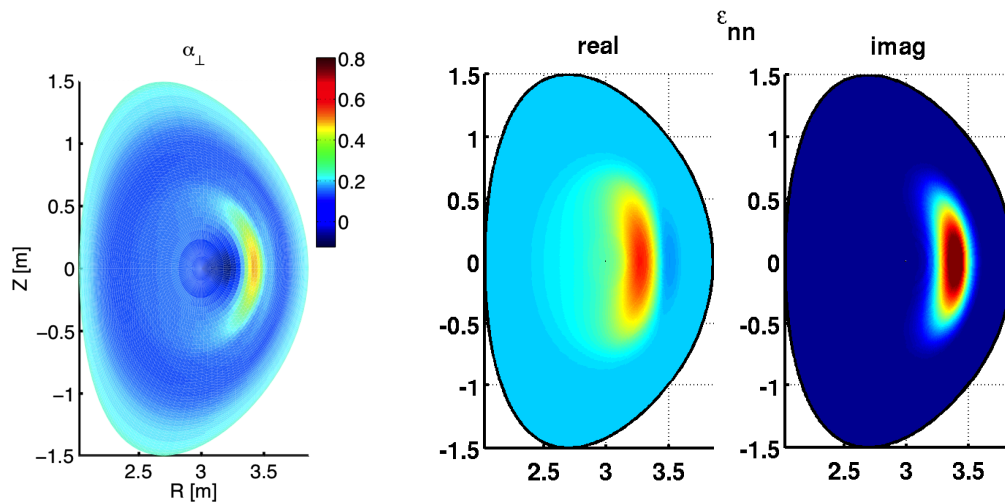
(b) The ballooning parameter $\alpha_\perp$, with the colors to scale with Fig. 12.21(d). The value of this parameter, which is important for global stability, is underestimated by a factor of two if the equilibrium is not updated during the simulation.

(c) The dielectric tensor element $\mathcal{E}_{nn}$ with the colors to scale with Fig. 12.16(f). The smaller tails have the effect that the dielectric tensor maxima are less localised than if the equilibrium is included in the iterative scheme. Moreover, the maxima are closer to the cold resonant layer than in Fig. 12.16(f).

Figure 12.22.: Comparison of the final states for the low field side simulations with and without updating the equilibrium at the end of each iteration. For the simulation without updating, the equilibrium has been re-computed once the simulation including LEMan and VENUS converged. Clearly, the results are different, with a smaller high energy tail for the case without inclusion of the equilibrium. As a result, equilibrium quantities such as $\alpha_\perp$ differ substantially.

13. Conclusions and outlook

13.1. Conclusions

In this thesis, the new code package SCENIC has been designed, tested and applied to relevant cases. The package is the first to include the equilibrium in self-consistent computations of wave injection in the Ion Cyclotron Range of Frequencies (ICRF). SCENIC includes the MHD equilibrium code VMEC, the full wave code LEMan and the guiding centre orbit following code VENUS. In all codes, further improvements with respect to other existing numerical tools for ICRF computations have been included. In particular, all codes are capable of full 3D geometries, and include the effects of pressure anisotropy ($T_\perp \neq T_\parallel$) as well as correct treatment of the spatial localisation of the cyclotron resonance. In the equilibrium and wave field computations, this is achieved by using a bi-Maxwellian for the resonant particles, which includes different parallel and perpendicular temperatures, finite orbit widths and the critical magnetic field strength B_c, defining the cyclotron resonance and allowing for poloidal dependences in pressure and dielectric tensor. In the evolution of the distribution function, represented by following guiding centre orbits, there is no restriction of an analytical model. Non standard orbits and preferential detrapping, together with the effects of a Doppler broadened resonant layer are included.

As a first application, it was possible to study the effects of shaping and pressure on the toroidal drift frequency of fast particles, which is an important quantity for MHD stability. Here, it was shown how the second radial derivative of the Shafranov shift and the radial derivative of the perpendicular pressure (perpendicular ballooning parameter) influence the drift frequency as a function of pitch angle, demonstrating significant reduction, or even sign reversal, of the toroidal drift frequency. After extensive testing and starting benchmarking efforts against SELFO, SCENIC has been applied to different Ion Cyclotron Resonance Heating (ICRH) scenarios, including low and high power heating of hydrogen or helium-3 minorities in deuterium background plasmas. By exploring low power cases, the general development of anisotropic pressure has been illustrated. The effects of anisotropy on the dielectric tensor were studied. While the parallel temperature is directly related to the Doppler broadening of the resonant region, the anisotropy (increasing perpendicular with constant parallel temperature) can result in a dominant hot dielectric tensor even if the hot particle density is considerably lower than that of the majority. Furthermore, geometric effects (poloidal variations) are important when anisotropy

157

is large. For the same low power simulations, the applicability of the bi-Maxwellian model could be confirmed, by showing both the convergence of the iterative scheme and the difference in the final distribution compared to the non-iterative case. The latter has been achieved in the high power simulations as well, where additionally the effects on the equilibrium could be highlighted. Large local perpendicular pressure affects the shaping mainly through enhanced Shafranov shift, and the resulting strong local variations in ballooning parameter and local shear indicate important changes in global stability. Moreover, the effect of the RF induced current on the safety factor profile could be quantified. Finally, the RF induced particle pinch could be verified. All of the results shown suggest that the newly developed code package SCENIC can be applied successfully to minority ICRH scenarios, and the inclusion of the equilibrium in the self-consistent computations is a great improvement in the research related to ion cyclotron resonance.

13.2. Outlook

For the future, many possible applications can be explored. We have limited our studies to fixed boundary equilibrium computations. The application of heating can cause the boundary shape to change through the enhanced Shafranov shift and possibly also through the impact of pressure anisotropy. It would therefore be interesting to exchange the fixed boundary with an anisotropic free boundary version of VMEC.[49] Furthermore, the studies conducted have indicated that ICRH could directly affect MHD stability. Applying the results from SCENIC to a stability code presents one logic application of the code. In particular, the stability code TERPSICHORE is already linked to the equilibrium code VMEC, including the bi-Maxwellian fast particles, and it would be straightforward to use this tool for studying the effects of ICRH on stability. Furthermore, the same code can pass perturbed fields to the equations of motion of the guiding centre drifts in VENUS, and therefore the effects of field perturbations on the distribution function can be studied without further code development. All of these studies can also be done in three dimensions, so another possible use of SCENIC would of course be to investigate self-consistently 3D effects in relation to ICRF. Here, the only development work to be performed would be to generalise the implemented statistics modules in VENUS from the axisymmetric (s, θ) to the general (s, B), which is a relatively undemanding task. With this, the effects of magnetic ripple and self-generated internal 3D magnetic structures[83] in tokamaks or general simulations in stellarator geometries become possible. Yet another possible extension of SCENIC is to add the NBI and anomalous transport modules implemented in VENUS by M. Albergante,[84] in order to include Neutral Beam injection and turbulent transport in the computations. Again, three dimensionality would come as a free asset.

A. Computation of the anisotropic dielectric tensor

As said in Chapter 5, we consider the bi-Maxwellian distribution function F_h from Eq. (4.1) in order to find the dielectric tensor analytically. As the calculations are rather tedious, we shall only show the computation of $\mathcal{E}_{\parallel\parallel}$, as the principles are the same for finding the other components. We will start from the Vlasov equation (2.51). Then we linearise this equation around the equilibrium state $f = F + \tilde{f}$, $\mathbf{E} = \mathbf{E}$, $\mathbf{B} = \mathbf{B}_0 + \tilde{\mathbf{B}}$ and $\mathbf{v} = \mathbf{v}$, where F and $\mathbf{B}_0$ are the equilibrium quantities and $\tilde{f}$, $\mathbf{E}$, $\tilde{\mathbf{B}}$ and $\mathbf{v}$ are small perturbations. Retaining only first order perturbation terms, the linearised Vlasov equation reads

$$\frac{\partial}{\partial t}\tilde{f} + \mathbf{v} \cdot \nabla \tilde{f} + \frac{Q}{m}\mathbf{B_0} \cdot \frac{\partial}{\partial \mathbf{v}}\tilde{f} + \frac{Q}{m}\mathbf{E} \cdot \frac{\partial}{\partial \mathbf{v}}F = 0. \tag{A.1}$$

As explained in Sec. 5.1, we will only retain terms of 0:th order in the small parameters $\epsilon_e = \rho/L$ and $\epsilon_p = \rho/\lambda_\perp$, such that the latter equation simplifies further to

$$\left[\frac{\partial}{\partial t} + v_\parallel \nabla_\parallel + \Omega\frac{\partial}{\partial \alpha}\right]\tilde{f} = -\frac{Q}{m}\mathbf{E} \cdot \frac{\partial}{\partial \mathbf{v}}F, \tag{A.2}$$

where we adopted the cylindrical velocity coordinates $\mathbf{v} = v_\perp(\cos\alpha\,\hat{\mathbf{e}}_\mathbf{n} + \sin\alpha\,\hat{\mathbf{e}}_\mathbf{b}) + v_\parallel\hat{\mathbf{e}}_\parallel$, with α the gyro angle, and $\Omega = QB_0/m$. The derivative with respect to velocity takes the form

$$\frac{\partial}{\partial \mathbf{v}} = \left(\cos\alpha\frac{\partial}{\partial v_\perp} - \frac{\sin\alpha}{v_\perp}\frac{\partial}{\partial \alpha}\right)\hat{\mathbf{e}}_\mathbf{n} + \left(\sin\alpha\frac{\partial}{\partial v_\perp} + \frac{\cos\alpha}{v_\perp}\frac{\partial}{\partial \alpha}\right)\hat{\mathbf{e}}_\mathbf{b} + \frac{\partial}{\partial v_\parallel}\hat{\mathbf{e}}_\parallel, \tag{A.3}$$

and it follows that

$$\mathbf{E} \cdot \frac{\partial}{\partial \mathbf{v}}F = \frac{1}{2}\left[E_n\left(e^{i\alpha} + e^{-i\alpha}\right) - iE_b\left(e^{i\alpha} - e^{-i\alpha}\right)\right]\frac{\partial F}{\partial v_\perp} + E_\parallel e^{i0\alpha}\frac{\partial F}{\partial v_\parallel}$$
$$+ \frac{1}{2v_\perp}\left[E_b\left(e^{i\alpha} + e^{-i\alpha}\right) + iE_n\left(e^{i\alpha} - e^{-i\alpha}\right)\right]\frac{\partial F}{\partial \alpha}. \tag{A.4}$$

159

To zeroth order in Larmor radius, $\partial F / \partial \alpha = 0$, and only the first line has to be computed. The perturbed distribution function can also be considered periodic in gyro angle, such that we can further decompose

$$\tilde{f} = \sum_{l=-\infty}^{\infty} \tilde{f}_l e^{il\alpha}. \tag{A.5}$$

Since there are terms with the same exponential form on the right hand side of Eq. (A.2), explicitly given in Eq. (A.4), only three terms in the expansion of $\tilde{f}$ will contribute, namely for $l = \{-1, 0, 1\}$. We will only consider one frequency for the injected wave, such that we can further expand $\tilde{f}_l$ using an exponential dependence in time, $\exp(-i\omega t)$, and we also assume one parallel wave vector $k_\parallel$. Note that for every mode in the plasma, $k_\parallel$ differs, and thus the value of the dielectric tensor differs. We can now write

$$\sum_{l=\{-1,0,1\}} i \left[\omega + v_\parallel k_\parallel - l\Omega \right] \tilde{f}_l e^{il\alpha} =$$

$$= \frac{Q}{m} \left\{ \frac{1}{2} \left[E_n \left(e^{i\alpha} + e^{-i\alpha} \right) - iE_b \left(e^{i\alpha} - e^{-i\alpha} \right) \right] \frac{\partial F}{\partial v_\perp} + E_\parallel e^{i0\alpha} \frac{\partial F}{\partial v_\parallel} \right\}, \quad \text{(A.6)}$$

yielding

$$\tilde{f}_{-1} = -\frac{Q}{m} \frac{i}{\omega + k_\parallel v_\parallel + \Omega} \frac{E_n + iE_b}{2} \frac{\partial F}{\partial v_\perp} \tag{A.7a}$$

$$\tilde{f}_0 = -\frac{Q}{m} \frac{i}{\omega + k_\parallel v_\parallel} E_\parallel \frac{\partial F}{\partial v_\parallel} \tag{A.7b}$$

$$\tilde{f}_{+1} = -\frac{Q}{m} \frac{i}{\omega + k_\parallel v_\parallel - \Omega} \frac{E_n - iE_b}{2} \frac{\partial F}{\partial v_\perp}. \tag{A.7c}$$

Only the perturbed distribution function $\tilde{f}$ has to be considered in the current, since the equilibrium electric field is zero, and as $\mathbf{j} = \sigma \mathbf{E}$, the equilibrium current is zero as well. The parallel current then reads

$$j_\parallel = Q \int v_\parallel \tilde{f} \mathrm{d}^3 \mathbf{v} = Q \int \mathrm{d}^3 \mathbf{v} v_\parallel \left[\tilde{f}_{-1} + \tilde{f}_0 + \tilde{f}_1 \right]$$

$$= -\frac{Q^2}{m} \int \mathrm{d}^3 \mathbf{v} v_\parallel \left[\frac{i}{\omega + v_\parallel k_\parallel + \Omega} \frac{E_n + iE_b}{2} \frac{\partial F}{\partial v_\perp} \right.$$

$$\left. + \frac{i}{\omega + v_\parallel k_\parallel} E_\parallel \frac{\partial F}{\partial v_\parallel} + \frac{i}{\omega + v_\parallel k_\parallel - \Omega} \frac{E_n - iE_b}{2} \frac{\partial F}{\partial v_\perp} \right] \quad \text{(A.8)}$$

and

$$j_\parallel = \sigma_{\parallel n} E_n + \sigma_{\parallel b} E_b + \sigma_{\parallel \parallel} E_\parallel, \tag{A.9}$$

such that only the middle term has to be included for the calculation of $\sigma_{\parallel\parallel}$. In fact, one can show that all other terms are zero, but this does not matter for finding $\sigma_{\parallel\parallel}$. The wanted

conductivity element then reads

$$\sigma_{\|\|} = -i\frac{Q^2}{m} \int_0^{2\pi} \int_{-\infty}^{\infty} \int_0^{\infty} \frac{v_{\|}}{\omega + k_{\|}v_{\|}} \frac{\partial F}{\partial v_{\|}} v_{\perp} \mathrm{d}v_{\perp} \mathrm{d}v_{\|} \mathrm{d}\alpha. \tag{A.10}$$

The equilibrium distribution function F is the bi-Maxwellian from Eq. (4.1), which can be written in terms of $v_{\|}$ and $v_{\perp}$ as

$$F = \mathcal{N} \left(\frac{m}{2\pi T_{\perp}}\right)^{3/2} \exp\left(-\frac{v_{\perp}^2}{v_{\perp \mathrm{th}}^2} \frac{B_c}{B} - \frac{|v_{\|}^2 + v_{\perp}^2(1 - B_c/B)|}{v_{\|\mathrm{th}}^2}\right), \tag{A.11}$$

where $v_{\perp \mathrm{th}}^2 = 2T_{\perp}/m$ and $v_{\|\mathrm{th}}^2 = 2T_{\|}/m$.

For $B > B_c$, we can remove the absolute value in the argument of the exponential and the derivative takes the form

$$\begin{aligned}
\frac{\partial F}{\partial v_{\|}} &= \frac{\mathcal{N}}{\pi^{3/2}} \frac{1}{v_{\perp \mathrm{th}}^3} \exp\left(-\frac{v_{\perp}^2}{v_{\perp \mathrm{th}}^2} \frac{B_c}{B}\right) \frac{\partial}{\partial v_{\|}} \exp\left(-\frac{v_{\|}^2 + v_{\perp}^2(1 - B_c B)}{v_{\|\mathrm{th}}^2}\right) \\
&= -\frac{\mathcal{N}}{\pi^{3/2}} \frac{2v_{\|}}{v_{\perp \mathrm{th}}^3 v_{\|\mathrm{th}}^2} \exp\left(-\frac{v_{\perp}^2}{v_{\perp \mathrm{th}}^2} \frac{B_c}{B} - \frac{v_{\|}^2 + v_{\perp}^2(1 - B_c/B)}{v_{\|\mathrm{th}}^2}\right).
\end{aligned} \tag{A.12}$$

We can then integrate the distribution

$$j_{\|} = i\frac{\mathcal{N} Q^2}{\sqrt{\pi} m} \frac{4}{v_{\perp \mathrm{th}}^3 v_{\|\mathrm{th}}^2} I_1 I_2 E_{\|}, \tag{A.13}$$

with

$$I_1 = \int_0^{\infty} v_{\perp} \exp\left[-v_{\perp}^2 \left(\frac{B_c/B}{v_{\perp \mathrm{th}}^2} + \frac{1 - B_c/B}{v_{\|\mathrm{th}}^2}\right)\right] \mathrm{d}v_{\perp} = \frac{1}{2\left(\frac{B_c/B}{v_{\perp \mathrm{th}}^2} + \frac{1 - B_c/B}{v_{\|\mathrm{th}}^2}\right)} \tag{A.14}$$

and

$$I_2 = \int_{-\infty}^{\infty} \frac{v_{\|}^2}{\omega - k_{\|}v_{\|}} \exp\left[-\frac{v_{\|}^2}{v_{\|\mathrm{th}}^2}\right]. \tag{A.15}$$

For this integral, we change variables $x = v_{\|}/v_{\|\mathrm{th}}$ and define $z_0 = \omega/k_{\|}v_{\|\mathrm{th}}$, such that

$$I_2 = \frac{v_{\|\mathrm{th}}^2}{k_{\|}} \int_{-\infty}^{\infty} \frac{x^2}{z_0 - x} e^{-x^2} dx. \tag{A.16}$$

Now,

$$\frac{x^2}{z_0 - x} = \frac{-x(z_0 - x) + z_0 x}{z_0 - x} = \frac{z_0 x}{z_0 - x} - x, \tag{A.17}$$

and

$$\frac{x}{z_0 - x} = \frac{x - z_0 + z_0}{z_0 - x} = -1 + \frac{z_0}{z_0 - x},$$ (A.18)

and thus

$$\frac{x^2}{z_0 - x} = -z_0 - x + \frac{z_0^2}{z_0 - x}.$$ (A.19)

We can now compute the second integral

$$I_2 = \frac{v_{\|\text{th}}^2}{k_\|} \left[-\underbrace{\int_{-\infty}^{\infty} z_0 e^{-x^2} dx}_{=z_0 \sqrt{\pi}} - \underbrace{\int_{-\infty}^{\infty} x e^{-x^2} dx}_{=0} + \underbrace{\int_{-\infty}^{\infty} \frac{z_0^2}{z_0 - x} e^{-x^2}}_{=z_0^2 Z^{Sh}(z_0) \sqrt{\pi}/z_0} \right]$$

$$= \frac{v_{\|\text{th}} \omega}{k_\|^2} \sqrt{\pi} \left(Z^{Sh} \left(\frac{\omega}{k_\| v_{\|\text{th}}} \right) - 1 \right),$$ (A.20)

where Z_0^{Sh} is defined in Eq. (5.2). Putting together Eqs. (A.13), (A.14) and (A.20), and introducing the notations defined in (5.2) yields

$$\mathcal{E}_{\|\|\|}^{B > B_c} = 1 + \frac{i}{\omega \epsilon_0} \sigma_{\|\|\|}^{B_c > B} = 1 + \frac{2}{(k_\| v_{\|\text{th}})^2} \frac{\sqrt{T_\| / T_\perp}}{C_+} \left(\tilde{\omega}_p^2 - \omega \tilde{Z}_0^\| \right),$$ (A.21)

which is Eq. (5.1ac) for one species.

For B < B$_c$, one has to split the integral over the perpendicular velocity into two contributions, one for $0 < v_\perp < v_\| / \sqrt{B_c/B - 1}$ and one for $v_\| / \sqrt{B_c/B - 1} < v_\perp < \infty$, because of the absolute value in the exponential. Since the principle of the computations is the same but the algebra is rather tedious, we satisfy ourselves with the computations for the case $B > B_c$. The case $B < B_c$ is shown in the Appendix of Ref. 53.

B. Wave number computation

B.1. Basis vectors.

$$
\begin{aligned}
\mathbf{e}^s &= \nabla s & \text{(B.1)} & & \mathbf{e}_s &= \sqrt{g}\,(\nabla \theta \times \nabla \varphi) & \text{(B.4)} \\
\mathbf{e}^\theta &= \nabla \theta & \text{(B.2)} & & \mathbf{e}_\theta &= \sqrt{g}\,(\nabla \varphi \times \nabla s) & \text{(B.5)} \\
\mathbf{e}^\varphi &= \nabla \varphi & \text{(B.3)} & & \mathbf{e}_\varphi &= \sqrt{g}\,(\nabla s \times \nabla \theta) & \text{(B.6)}
\end{aligned}
$$

with

$$
\sqrt{g} = \frac{1}{\nabla s \cdot (\nabla \theta \times \nabla \varphi)}.
$$

Magnetic field components in Boozer coordinates.

$$
\begin{aligned}
B^s &= 0 & \text{(B.7)} & & B_s &= B_s & \text{(B.10)} \\
B^\theta &= \psi' / \sqrt{g} & \text{(B.8)} & & B_\theta &= \mu_0 J / \sigma & \text{(B.11)} \\
B^\varphi &= \Phi' / \sqrt{g} & \text{(B.9)} & & B_\varphi &= -\mu_0 I / \sigma & \text{(B.12)}
\end{aligned}
$$

with I the poloidal current flux, J the toroidal current flux, ψ the poloidal and Φ the toroidal flux functions. Prime denotes the derivative with respect to s. We will always compute the wave numbers using the scalar potential.

B.2. Alternative basis

For the computation of the wave vectors, let us define new basis vectors as

$$
\begin{array}{llll}
\mathbf{e}^s &=& \nabla s & \text{(B.13)} \\
\mathbf{e}^b &=& (\mathbf{b} \times \nabla s) & \text{(B.14)} \\
\mathbf{e}^\| &=& \mathbf{b} \equiv \dfrac{\mathbf{B}}{B} & \text{(B.15)}
\end{array}
\qquad
\begin{array}{llll}
\mathbf{e}_s &=& \sqrt{\mathcal{J}}(\mathbf{e}^b \times \mathbf{e}^\|) & \text{(B.16)} \\
\mathbf{e}_b &=& \sqrt{\mathcal{J}}(\mathbf{e}^\| \times \mathbf{e}^s) & \text{(B.17)} \\
\mathbf{e}_\| &=& \sqrt{\mathcal{J}}(\mathbf{e}^s \times \mathbf{e}^b) & \text{(B.18)}
\end{array}
$$

The Jacobian is

$$
\sqrt{\mathcal{J}} = \frac{1}{\nabla s \cdot (\mathbf{b} \times \nabla s \times \mathbf{b})} = \frac{1}{\nabla s \cdot ((\mathbf{b} \cdot \mathbf{b})\nabla s - (\mathbf{b} \cdot \nabla s)\mathbf{b})} = \frac{1}{\nabla s \cdot \nabla s}, \qquad \text{(B.19)}
$$

which is as expected since $e^s \perp e^b \perp e^\|$ and $e^s \cdot e^s \neq 1$. Now,

$$
\begin{aligned}
\mathbf{e}_s &= \sqrt{\mathcal{J}}(\mathbf{e}^b \times \mathbf{e}^\|) = \sqrt{\mathcal{J}}\left((\mathbf{b} \times \nabla s) \times \mathbf{b}\right) = \sqrt{\mathcal{J}}\nabla s = \sqrt{\mathcal{J}}\mathbf{e}^s \\
\mathbf{e}_b &= \sqrt{\mathcal{J}}(\mathbf{e}^\| \times \mathbf{e}^s) = \sqrt{\mathcal{J}}(\mathbf{b} \times \nabla s) = \sqrt{\mathcal{J}}\mathbf{e}^b \\
\mathbf{e}_\| &= \sqrt{\mathcal{J}}(\mathbf{e}^s \times \mathbf{e}^b) = \sqrt{\mathcal{J}}(\nabla s \times (\mathbf{b} \times \nabla s)) = \sqrt{\mathcal{J}}(\underbrace{\nabla s \cdot \nabla s}_{1/\sqrt{\mathcal{J}}})\mathbf{b} - (\underbrace{\nabla s \cdot \mathbf{b}}_{0})\nabla s = \mathbf{e}^\|.
\end{aligned}
$$

B.3. Perpendicular wave number $k_\perp$

By definition of the coordinates,

$$
k_\perp^2 = k_s k^s + k_b k^b,
$$

with

$$
\begin{aligned}
k^s &= \frac{1}{\chi}\mathbf{e}^s \cdot \nabla \chi = \frac{1}{\chi}\nabla s \cdot \nabla \chi = \frac{1}{\chi}\left(\frac{\partial \chi}{\partial s}\nabla s + \frac{\partial \chi}{\partial b}\nabla b + \frac{\partial \chi}{\partial \|}\nabla \|\right) \\
&= \frac{1}{\chi}(\nabla s \cdot \nabla s)\frac{\partial \chi}{\partial s} = \frac{1}{\chi\sqrt{\mathcal{J}}}\frac{\partial \chi}{\partial s} &\text{(B.20)} \\
k_s &= \frac{1}{\chi}\mathbf{e}_s \cdot \nabla \chi = \frac{1}{\chi}\sqrt{\mathcal{J}}\mathbf{e}^s \cdot \nabla \chi = \sqrt{\mathcal{J}}k^s = \frac{1}{\chi}\frac{\partial \chi}{\partial s} \\
&\Rightarrow k_s k^s = \frac{1}{\sqrt{\mathcal{J}}}\left(\frac{1}{\chi}\frac{\partial \chi}{\partial s}\right)^2, &\text{(B.21)}
\end{aligned}
$$

and

$$
\begin{aligned}
k^b &= \frac{1}{\chi}\mathbf{e}^b \cdot \nabla\chi = \frac{1}{\chi}\left(\mathbf{b}\times\nabla s\right)\cdot\nabla\chi = \frac{1}{\chi B}\left[\left(\frac{\mu_0 J}{\sigma}\nabla\theta - \frac{\mu_0 I}{\sigma}\nabla\varphi\right)\times\nabla s\right]\cdot\nabla\chi \\
&= \frac{1}{\chi\sigma B}\left[\mu_0 J(\nabla\theta\times\nabla s) - \mu_0 I(\nabla\varphi\times\nabla s)\right]\cdot\left[\frac{\partial\chi}{\partial s}\nabla s + \frac{\partial\chi}{\partial\theta}\nabla\theta + \frac{\partial\chi}{\partial\varphi}\nabla\varphi\right] \\
&= \frac{1}{\chi\sigma B}\left(\mu_0 J\underbrace{(\nabla\theta\times\nabla s)\cdot\nabla\varphi}_{-1/\sqrt{g}}\frac{\partial\chi}{\partial\varphi} - \mu_0 I\underbrace{(\nabla\varphi\times\nabla s)\cdot\nabla\theta}_{1/\sqrt{g}}\frac{\partial\chi}{\partial\theta}\right) && \text{(B.22)}
\end{aligned}
$$

$$
k_b = \sqrt{\mathcal{J}}k^b = -\frac{\sqrt{\mathcal{J}}}{\chi\sigma B\sqrt{g}}\left(\mu_0 J\frac{\partial\chi}{\partial\varphi} + \mu_0 I\frac{\partial\chi}{\partial\theta}\right)
$$

$$
\Rightarrow k_b k^b = \sqrt{\mathcal{J}}\left[\frac{1}{\chi\sigma B\sqrt{g}}\left(\mu_0 J\frac{\partial\chi}{\partial\varphi} + \mu_0 I\frac{\partial\chi}{\partial\theta}\right)\right]^2 \tag{B.23}
$$

Explicitly, using $\sqrt{\mathcal{J}} = 1/g^{ss}$,

$$
k_\perp^2 = g^{ss}\left(\frac{1}{\chi}\frac{\partial\chi}{\partial s}\right)^2 + \frac{1}{g^{ss}}\left[\frac{1}{\chi\sigma B\sqrt{g}}\left(\mu_0 J\frac{\partial\chi}{\partial\varphi} + \mu_0 I\frac{\partial\chi}{\partial\theta}\right)\right]^2 \tag{B.24}
$$

B.4. Parallel wave number $k_\parallel$

Since $\mathbf{e}_\parallel = \mathbf{e}^\parallel$, there is no difference between the co- and contravariant components:

$$
\begin{aligned}
k^\parallel &= \frac{1}{\chi}\mathbf{e}^\parallel\cdot\nabla\chi = \frac{1}{\chi}\mathbf{b}\cdot\nabla\chi = \frac{1}{\chi B}\left[\psi'(\nabla\varphi\times\nabla s) + \chi'(\nabla s\times\nabla\theta)\right]\cdot\nabla\chi \\
&= \frac{1}{\chi B}\left[\psi'(\nabla\varphi\times\nabla s) + \chi'(\nabla s\times\nabla\theta)\right]\cdot\left[\frac{\partial\chi}{\partial s}\nabla s + \frac{\partial\chi}{\partial\theta}\nabla\theta + \frac{\partial\chi}{\partial\varphi}\nabla\varphi\right] \\
&= \frac{1}{\chi B}\left[\psi'\underbrace{(\nabla\varphi\times\nabla s)\cdot\nabla\theta}_{1/\sqrt{g}}\frac{\partial\chi}{\partial\theta} + \chi'\underbrace{(\nabla s\times\nabla\theta)\cdot\nabla\varphi}_{1/\sqrt{g}}\frac{\partial\chi}{\partial\varphi}\right] && \text{(B.25)}
\end{aligned}
$$

That is ($k_\parallel = k^\parallel$),

$$
k_\parallel = \frac{1}{\chi B\sqrt{g}}\left(\psi'\frac{\partial\chi}{\partial\theta} + \chi'\frac{\partial\chi}{\partial\varphi}\right) \tag{B.26}
$$

C. Solution for a single wave-particle resonance passing

Starting from Eq.6.18, we develop

$$
u(t) \exp \left\{ i \int_{t_0}^{t} \mathrm{d}t' \Omega(t') \right\} - u(t_0) = \frac{Q}{m} E^{+} e^{-i\omega t_0} \int_{t_0}^{t} \mathrm{d}t' \exp \left\{ i \int_{t_0}^{t} \mathrm{d}t'' \left[\Omega(t'') - \omega \right] \right\}
$$
$$
+ \frac{Q}{m} E^{-} e^{+i\omega t_0} \int_{t_0}^{t} \mathrm{d}t' \exp \left\{ i \int_{t_0}^{t'} \mathrm{d}t'' \left[\Omega(t'') + \omega \right] \right\}
$$

(C.1)

Now, using the Taylor expansion of $\Omega(t)$ from (6.15),

$$
\Omega(t'') \approx \omega + (t'' - t_{\mathrm{res}})\Omega'
$$

(C.2)

$$
\Omega(t'') - \omega \approx (t'' - t_{\mathrm{res}})\Omega'
$$

(C.3)

$$
\Omega(t'') + \omega \approx 2\omega + (t'' - t_{\mathrm{res}})\Omega'
$$

(C.4)

One can now see that the contribution proportional to E^{-} will not be resonant due to the 2ω term. We will therefore neglect it from here on. Then,

$$
\int_{t_0}^{t'} \mathrm{d}t'' \left[(t'' - t_{\mathrm{res}})\Omega' \right] = \left[\frac{t''^2}{2} \Omega' - t_{\mathrm{res}}\Omega' t'' \right]_{t''=t_0}^{t''=t'}
$$
$$
= \frac{1}{2} \left(t''^2 - t_0^2 \right) \Omega' - (t' - t_0')t_{\mathrm{res}}\Omega'
$$
$$
= \frac{\Omega'}{2} \left[t'^2 - 2t_{\mathrm{res}}t' + 2t_{\mathrm{res}}t_0 - t_0^2 \right]
$$
$$
= \frac{\Omega'}{2} \left[(t' - t_{\mathrm{res}})^2 - (t_{\mathrm{res}} - t_0)^2 \right]
$$

(C.5)

Let us now assume that the cyclotron frequency only changes slowly with time (due to slow change in magnetic field), i.e.

$$t_{\text{res}} - t_0 \quad \gg \quad \frac{1}{\sqrt{\Omega'}} \tag{C.6a}$$

$$t - t_{\text{res}} \quad \gg \quad \frac{1}{\sqrt{\Omega'}} \tag{C.6b}$$

The RHS of (C.1) becomes then

$$
\begin{aligned}
\int_{t_0}^{t} \mathrm{d}t' & \exp\left\{ i \int_{t_0}^{t} \mathrm{d}t'' \left[\Omega(t'') - \omega \right] \right\} \\
&= \exp\left\{ -i\frac{\Omega'}{2}(t_{\text{res}} - t_0)^2 \right\} \int_{t_0}^{t} \mathrm{d}t' \exp\left\{ i\frac{\Omega'}{2}(t' - t_{\text{res}})^2 \right\} \\
&\to \exp\left\{ -i\frac{\Omega'}{2}(t_{\text{res}} - t_0)^2 \right\} \int_{-\infty}^{+\infty} \mathrm{d}t' \exp\left\{ i\frac{\Omega'}{2}(t' - t_{\text{res}})^2 \right\} \\
&= \exp\left\{ -i\frac{\Omega'}{2}(t_{\text{res}} - t_0)^2 \right\} \sqrt{\frac{2\pi}{-i\Omega'}} \\
&= \exp\left\{ -i\frac{\Omega'}{2}(t_{\text{res}} - t_0)^2 \right\} \sqrt{\exp\left\{ i\frac{\pi}{2}\mathrm{sgn}(\Omega') \right\} \frac{2\pi}{|\Omega'|}} \\
&= \exp\left\{ -i\frac{\Omega'}{2}(t_{\text{res}} - t_0)^2 + i\frac{\pi}{4}\mathrm{sgn}(\Omega') \right\} \sqrt{\frac{2\pi}{|\Omega'|}}. \tag{C.7}
\end{aligned}
$$

With this, we get relation (6.19)

$$u(t) \exp\left[i \int_{t_0}^{t} \mathrm{d}t' \Omega(t') \right] - u(t_0) \cong \frac{Q}{m} E^+ e^{-i\psi} \sqrt{\frac{2\pi}{|\Omega'|}}, \tag{C.8}$$

with $\psi = \omega t_0 + \frac{\Omega'}{2}(t_{\text{res}} - t_0)^2 - \frac{\pi}{4}\mathrm{sgn}(\Omega')$. The average change of energy per transit is the result of simple direct calculations and gives directly Eq. (6.20),

$$W_\perp = \frac{m}{2}\langle u(t)u(t)^* - u(t_0)u(t_0)^* \rangle = \frac{m}{2}\left| \frac{Ze}{m} \right|^2 |E^+|^2 \frac{2\pi}{|\Omega'|}. \tag{C.9}$$

In order to find from this the rate of perpendicular power absorption per unit volume, $P_\perp$, we define the number of resonance crossings per unit volume and time, $\nu(\mathbf{x}, v_\perp, v_\parallel)$, and write

$$P_\perp = \nu(\mathbf{x}, v_\perp, v_\parallel) W_\perp(\mathbf{x}, v_\perp, v_\parallel) \tag{C.10}$$

Let x denote the direction of the guiding centre orbit, with $v_g(v_\perp, v_\parallel)$ the guiding centre velocity. If now x changes by Δx, the average number of resonance crossings per time is

$$
\begin{aligned}
\langle \nu \rangle \Delta V &= \langle \nu \rangle \Delta x \Delta A \\
&= \Delta A \underbrace{\int_u^{u+|\Delta u|}}_{\text{resonantptclesonly}} \mathrm{d}v_\parallel \int_0^\infty \underbrace{|v_g|}_{\text{\#ptclespersec}} f(\mathbf{x}, \mathbf{v}) 2\pi v_\perp \mathrm{d}v_\perp
\end{aligned}
\tag{C.11}
$$

We introduced the velocity $u = v_\parallel^{\mathrm{res}} = (\omega - \Omega(x))/k_\parallel$, with $\Delta u = \Delta x \, \mathrm{d}v_\parallel^{\mathrm{res}}/\mathrm{d}x = -\Delta x/k_\parallel \cdot \mathrm{d}\Omega/\mathrm{d}x$. We will also use $\Omega' = \mathrm{d}\Omega/\mathrm{d}t = v_g \mathrm{d}\Omega/\mathrm{d}x$. We can now simplify

$$
P_\perp = \langle \nu W_\perp \rangle = \underbrace{\frac{1}{\Delta V}}_{\text{perunitvolume}} \Delta A |\Delta u| \int_0^\infty |v_g| W_\perp f(\mathbf{x}, v_\perp, v_\parallel^{\mathrm{res}}) 2\pi v_\perp \mathrm{d}v_\perp
\tag{C.12}
$$

Explicitly,

$$
|\Delta u||v_g|W_\perp = \left| \frac{\Delta x}{k_\parallel} \frac{\mathrm{d}\Omega}{\mathrm{d}x} \right| |v_g| \frac{m}{2} \left| \frac{Ze}{m} \right|^2 |E^+|^2 \frac{2\pi}{\left| v_g \frac{\mathrm{d}\Omega}{\mathrm{d}x} \right|},
\tag{C.13}
$$

and thus

$$
P_\perp = \underbrace{\frac{\Delta A \Delta x}{\Delta V}}_{=1} \frac{\pi Z^2 e^2}{m|k_\parallel|} |E^+|^2 \underbrace{\int_0^\infty f(\mathbf{x}, v_\perp, v_\parallel^{\mathrm{res}}) 2\pi v_\perp \mathrm{d}v_\perp}_{\equiv n_{\mathrm{res}}(\mathbf{x}, v_\parallel^{\mathrm{res}})},
\tag{C.14}
$$

which is exactly Eq. (6.21).

D. Detailed scenario description

D.1. Equilibrium for benchmarking against SELFO and dielectric tensor studies

2 % hydrogen in deuterium background. The Shafranov shift of 4cm in VMEC is not included in SELFO, and we decided to match the LFS of the plasma, since this is where the heating resonance was chosen. The magnetic axis is at $R_0 = 3$ m and the LFS edge at $R = 4$ m, giving a minor radius of $a = 1.04$ m. The plasma was circular, i.e. elongation $\kappa = 0$ and triangularity $\delta = 0$. The magnetic field on axis is $B_0 = 3.45$ T. For simplicity, all profiles are chosen constant with $T_e = T_i = 5$ keV and $n_e = 4 \times 10^{19}$ m^{-3}. The total toroidal current is 2.6 MA. The heating is chosen on the LFS at $B_c = 3.23$ T, resulting in a frequency of 49.3 MHz. The toroidal mode number is $n_\varphi = 27$.

D.2. Equilibrium based on JET shot 76189

The equilibrium is based on JET shot 76189 described in Refs. 79 and 20. It is a JET-like D-shaped equilibrium with major radius $R_0 = 2.99$ m, minor radius $a = 1.17$ m, elongation on edge $\kappa_a = 1.4$ and triangularity on edge $\delta_a = 0.4$. The magnetic field strength on axis is $B_0 = 2.94$ T. The background consists of Deuterium and electrons with a temperature on axis of $T_0^e = T_0^i = 3.5$ keV and the electron density on axis $n_0^e = 3.38 \times 10^{19}$ m^{-3}. This yields a volume averaged thermal beta of $\langle \beta_{th} \rangle = 0.13$ %. The profiles are given in Fig. D.2.

D.2.1. Low power simulations

In Chap. 11, a 1 % helium-3 minority is considered, yielding a deuterium density of $n_0^D = 0.98 n_0^e$ and an initial minority density on axis of $n_0^{He^3} = 0.01 n_0^e$. For both low field side (LFS) and high field side (HFS) heating, the resonant layer is defined by the $q = 1$ surface, i.e. $r_1/a = 0.25$. This gives for the two cases

- Low Field Side: $B_c = 2.73$ T, yielding $f_{RF}^{LFS} = 27.2$ MHz

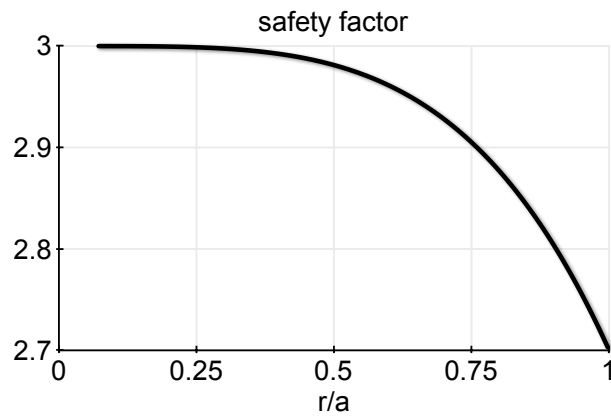- High Field Side: $B_c = 3.18$ T, yielding $f_{RF}^{HFS} = 32.4$ MHz

Figure D.1.: Safety factor profile. The density and temperature profiles are constant.

D.2.2. High power simulations

In Chap. 12, a $3\,\%$ H minority is considered, yielding a deuterium density of $n_0^D = 0.97 n_0^e$ and an initial minority density on axis of $n_0^H = 0.03 n_0^e$. For both low field side (LFS) and high field side (HFS) heating, the resonant layer is approximately defined by $r/a = 0.5$. This gives for the three cases

- Low Field Side: $B_c = 2.54\,\text{T}$, yielding $f_{RF}^{LFS} = 38.7\,\text{MHz}$

- On Axis: $B_c = 2.94\text{T}$, yielding $f_{RF}^{OA} = 48.5\,\text{MHz}$

- High Field Side: $B_c = 3.45\,\text{T}$, yielding $f_{RF}^{HFS} = 52.6\,\text{MHz}$

(a) Background density

(b) Background temperature

(c) Background pressure

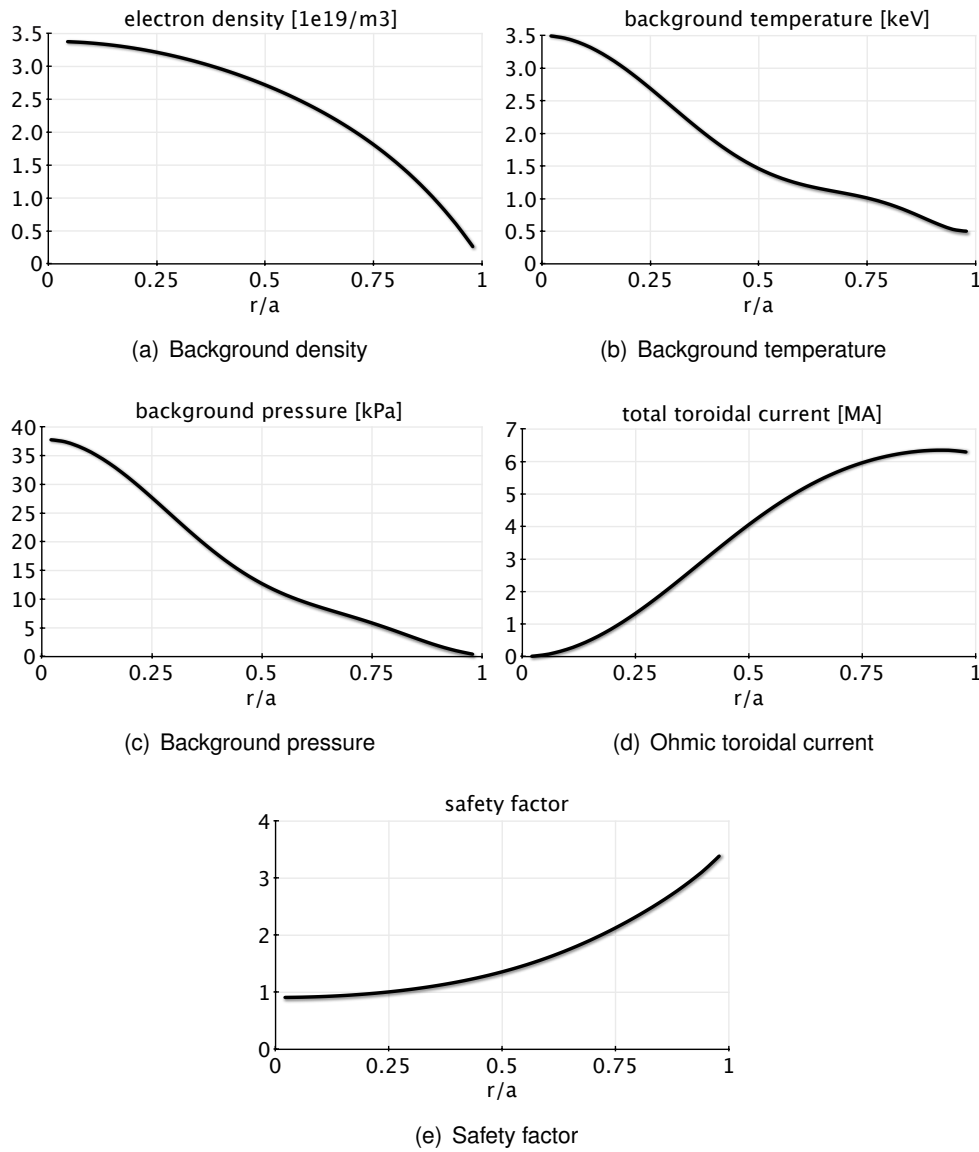(d) Ohmic toroidal current

(e) Safety factor

Figure D.2.: Background profiles. The minority species initially has the same temperature and normalised density profiles. For the low power studies in Chap. 11, the heating is applied at $r/a = 0.25$, where $q = 1$. For the high power studies in Chap. 12, the heating is applied at $r/a = 0.5$.

Bibliography

[1] S. P. Hirshman and O. Betancourt. *Preconditioned Descent Algorithm for Rapid Calculations of Magnetohydrodynamic Equilibria.* J. Comp. Phys, **96**, 99 (1991)

[2] P. Popovich, W. A. Cooper and L. Villard. *A full-wave solver of the Maxwell's equations in 3D cold plasmas.* Comp. Phys. Comm., **175**, 250 (2006)

[3] O. Fischer, W. A. Cooper, M. Y. Isaev and L. Villard. *Neoclassical transport and particle confinement in novel 3-D reactor systems.* Nucl. Fusion, **42**, 817 (2002)

[4] W. A. Cooper, J. P. Graves, M. Jucker and M. Y. Isaev. *Relativistic Hamiltonian guiding center drift formalism in anisotropic pressure magnetic coordinates.* Phys. Plasmas, **13**, 092501 (2006)

[5] G. F. Chew, M. L. Goldberger and F. E. Low. *The Boltzmann Equation and the One-Fluid Hydromagnetic Equations in the Absence of Particle Collisions.* Proc. R. Soc. London, Ser. A, **236**, 112 (1956)

[6] H. Grad. *Velocity Gradient Instability.* Phys. Fluids, **9**, 498 (1966)

[7] W. A. Cooper, S. P. Hirshman, S. Merazzi and R. Gruber. *3D magnetohydrodynamic equilibria with anisotropic pressure.* Comp. Phys. Comm., **72**, 1 (1992)

[8] N. A. Madden and R. J. Hastie. *Tokamak equilibrium with anisotropic pressure.* Nucl. Fusion, **34**, 519 (1994)

[9] J. A. Rome and Y.-K. M. Peng. *The topology of tokamak orbits.* Nucl. Fusion, **19**, 1193 (1979)

[10] J. Hedin, T. Hellsten and L.-G. Eriksson. *The influence of non-standard orbits on ICRH power deposition in tokamaks.* Nucl. Fusion, **40**, 1819 (2000)

[11] T. Hellsten, T. Johnson, J. Carlsson *et al. Effects of finite drift orbit width and RF-induced spatial transport on plasma heated by ICRH.* Nucl. Fusion, **44**, 892 (2004)

[12] L.-G. Eriksson and F. Porcelli. *Dynamics of energetic ion orbits in magnetically confined plasmas.* Plasma Phys. Control. Fusion, **43**, R145 (2001)

175

[13] R. D. Hazeltine. *Recursive derivation of drift-kinetic equation.* Plasma Phys., **15**, 77 (1973)

[14] F. Porcelli, R. Stankiewicz, W. Werner and H. L. Berk. *Solution of the drift-kinetic equation for global plasma modes and finite particle orbit widths.* Phys. Plasmas, **1**, 470 (1994)

[15] A. H. Boozer. *Guiding center drift equations.* Phys. Fluids, **23**, 904 (1980)

[16] R. B. White, A. H. Boozer and R. Hay. *Drift Hamiltonian in magnetic coordinates.* Phys. Fluids, **25**, 575 (1982)

[17] G. A. Cooper, M. Jucker, W. A. Cooper *et al.* *Exact canonical drift Hamiltonian formalism with pressure anisotropy and finite perturbed fields.* Phys. Plasmas, **14**, 102506 (2007)

[18] T. H. Stix. *Waves in Plasmas.* American Institute of Physics, New York (1992)

[19] R. Aymar, V. A. Chuyanov, M. Huguet *et al.* *Overview of ITER-FEAT - The future international burning plasma experiment.* Nucl. Fusion, **41**, 1301 (2001)

[20] J. P. Graves, I. T. Chapman, S. Coda *et al.* *Experimental verification of sawtooth control by energetic particles in ion cyclotron resonance heated JET tokamak plasmas.* Nucl. Fusion, **50**, 052002 (2010)

[21] R. J. Dumont, C. K. Phillips and D. N. Smithe. *Effects of non-Maxwellian species on ion cyclotron waves propagation and absorption in magnetically confined plasmas.* Phys. Plasmas, **12**, 042508 (2005)

[22] R. O. Dendy, R. J. Hastie, K. G. McClements and T. J. Martin. *A model for ideal m=1 internal kink stabilization by minority ion cyclotron resonant heating.* Phys. Plasmas, **2**, 1623 (1995)

[23] M. Brambilla. *Electron Landau damping of ion Bernstein waves in tokamak plasmas.* Nucl. Fusion, **38**, 1805 (1998)

[24] M. Brambilla. *Numerical simulation of ion cyclotron waves in tokamak plasmas.* Plasma Phys. Control. Fusion, **41**, 1 (1999)

[25] J. C. Wright, P. T. Bonoli, E. D'Azevedo and M. Brambilla. *Ultrahigh resolution simulations of mode converted ion cyclotron waves and lower hybrid waves.* Comp. Phys. Comm., **164**, 330 (2004)

[26] M. Brambilla. *Quasi-linear ion distribution function during ion cyclotron heating in tokamaks.* Nucl. Fusion, **34**, 1121 (1994)

[27] M. Brambilla and R. Bilbato. *Simulation of ion cyclotron heating of tokamak plasmas using coupled Maxwell and quasilinear-Foller-Planck solvers.* Nucl. Fusion, **46**, S387 (2006)

[28] M. Brambilla and R. Bilbato. *Advances in numerical simulations of ion cyclotron heating of non-Maxwellian plasmas*. Nucl. Fusion, **49**, 085004 (2009)

[29] E. F. Jaeger, L. A. Berry, J. R. Myra *et al. Sheared Poloidal Flow Driven by Mode Conversion in Tokamak Plasmas*. Phys. Rev. Lett., **90**, 195001 (2003)

[30] E. F. Jaeger, L. A. Berry, E. D'Azevedo *et al. All-orders spectral calculation of radio-frequency heating in two-dimensional toroidal plasmas*. Phys. Plasmas, **8**, 1573 (2001)

[31] E. F. Jaeger, L. A. Berry, E. D'Azevedo *et al. Advances in full-wave modeling of radio frequency heated, multidimensional plasmas*. Phys. Plasmas, **9**, 1873 (2002)

[32] E. F. Jaeger, R. W. Harvey, L. A. Berry *et al. Global-wave solutions with self-consistent velocity distributions in ion cyclotron heated plasmas*. Nucl. Fusion, **46**, S397 (2006)

[33] M. Choi, V. S. Chan, R. I. Pinsker *et al. Monte Carlo orbit/full wave simulation of ion cyclotron resonance frequency wave damping on resonant ions in tokamaks*. Phys. Plasmas, **12**, 072505 (2005)

[34] M. Choi, D. Green, W. W. Heidbrink *et al. Iterated finite-orbit Monte Carlo simulations with full-wave fields for modeling tokamak ion cyclotron resonance frequency wave heating experiments*. Phys. Plasmas, **17**, 056102 (2010)

[35] L. Villard, K. Appert, R. Gruber and J. Vaclavik. *Global waves in cold plasmas*. Comput. Phys. Rep., **4**, 95 (1986)

[36] L. Villard, S. Brunner and J. Vaclavik. *Global marginal stability of TAEs in the presence of fast ions*. Nucl. Fusion, **35**, 1173 (1995)

[37] J. Carlsson, L.-G. Eriksson and T. Hellsten. *FIDO, a Code for Calculating the Velocity Distribution Function of a Toroidal Plasma During ICRH*. In *Theory of Fusion Plasmas (Proc. Joint Varenna-Lausanne Int. Workshop Varenna, 1994)*, 351. Editrice Compositori, Bologna (1998)

[38] J. Carlsson. *Ion Cyclotron Resonance Heating and Current Drive in Tokamaks*. Ph.D. thesis, Royal Inst. of Technology, Stockholm (1998)

[39] J. Hedin, T. Hellsten, L.-G. Eriksson and T. Johnson. *The influence of finite drift orbit width on ICRF heating in toroidal plasmas*. Nucl. Fusion, **42**, 527 (2002)

[40] J. Hedin, T. Hellsten and J. Carlsson. *Self-consistent calculations of parasitic io absorption during fast wave electron current drive*. In J. Connor, E. Sindoni and J. Vaclavik (eds.), *Theory of Fusion Plasmas 1998*, 467–472. Societa Italiana di Fisica (1999)

[41] T. Hellsten, J. Carlsson, L.-G. Eriksson *et al. Parasitic absorption by fusion born -particles in ICRF heated plasmas*. Plasma Phys. Control. Fusion, **40**, 1085 (1998)

[42] A. Fukuyama, E. Yokota and T. Akustu. *Global Analysis of ICRF Waves and Alfvén Eigenmodes in Toroidal Helical Plasmas.* In *Proc. 18th Int. Conf. on Fusion Energy 2000 (Sorrento, Italy)*, http://www.iaea.org/programmes/ripc/physics/fec2000/html/node1.htm. IAEA, Vienna (2000)

[43] S. Murakami, U. Gasparino, H. Idei *et al. 5-D simulation study of suprathermal electron transport in non-axisymmetric plasmas.* Nucl. Fusion, **40**, 693 (2000)

[44] S. Murakami, H. Yamada, M. Sasao *et al. Effect of Neoclassical Transport Optimization on Energetic Ion Confinement in LHD.* Fusion Sci. Technol., **46**, 241 (2004)

[45] S. Murakami, A. Fukuyama, T. Akustu *et al. A global simulation study of ICRF heating in the LHD.* Nucl. Fusion, **46**, S425 (2006)

[46] T. Yamamoto, S. Murakami and A. Fukuyama. *Simulation Study of ICRF Wave Propagation and Absorption in 3-D Magnetic Configurations.* Plasma and Fusion Research, **3**, S1075 (2008)

[47] S. Murakami, T. Yamamoto, A. Fukuyama *et al. Optimization Study of ICRF Heating in the LHD and HSX Configurations.* Contrib. Plasma Phys., **50**, 546 (2010)

[48] M. Jucker, J. P. Graves, G. A. Cooper and W. A. Cooper. *Impact of pressure anisotropy on tokamak equilibria and the toroidal magnetic precession.* Plasma Phys. Control. Fusion, **50**, 065009 (2008)

[49] W. A. Cooper, S. P. Hirshman, P. Merkel *et al. Three-dimensional anisotropic pressure free boundary equilibria.* Comp. Phys. Comm., **180**, 1524 (2009)

[50] W. A. Cooper, J. P. Graves, S. P. Hirshman *et al. Anisotropic pressure bi-Maxwellian distribution function model for three-dimensional equilibria.* Nucl. Fusion, **46**, 683 (2006)

[51] J. P. Graves, K. I. Hopcraft, R. O. Dendy *et al. Sawtooth Evolution during JET Ion-Cyclotron-Resonance-Heated Pulses.* Phys. Rev. Lett., **84**, 1204 (2000)

[52] N. Mellet, W. A. Cooper, P. Popovich *et al. Convolution and iterative methods applied to low-frequency waves in 3D warm configurations.* to be published

[53] N. Mellet, M. Jucker, W. A. Cooper and J. P. Graves. *Effect of a hot particle bi-Maxwellian distribution function on the propagation of low-frequency waves.* to be published in Comp. Phys. Comm.

[54] T. Martin and J. Vaclavik. *Dielectric tensor operator of a nonuniformly magnetized inhomogeneous plasma.* Helvetica Physica Acta, **60**, 471 (1987)

[55] S. Brunner and J. Vaclavik. *Dielectric tensor operator of hot plasmas in toroidal axisymmetric systems.* Phys. Fluids B, **5**, 1695 (1993)

[56] N. Mellet. *Propagation and Absorption of Low Frequency Waves in Two and Three Dimensional Warm Plasmas*. Ph.D. thesis, École Polytechnique Fédérale de Lausanne (2009)

[57] T. H. Stix. *Fast-wave heating of a two-component plasma*. Nucl. Fusion, **15**, 737 (1975)

[58] J. Wesson. *Tokamaks*. Oxford University Press, Great Clarendon Street, Oxford OX2 6DP, 3 ed. (2004)

[59] A. H. Boozer and G. Kuo-Petravic. *Monte Carlo evaluation of transport coefficients*. Phys. Fluids, **24**, 851 (1981)

[60] R. Koch. *Wave-particle interactions in plasmas*. Plasma Phys. Control. Fusion, **48**, B329 (2006)

[61] M. A. Kovanen and W. G. F. Core. *HECTOR: A Code for the Study of Charged Particles in Axisymmetric Tokamak Plasmas*. J. Comp. Phys, **105**, 14 (1993)

[62] T. Johnson, T. Hellsten and L.-G. Eriksson. *Analysis of a quasilinear model for ion cyclotron interactions in tokamaks*. Nucl. Fusion, **46**, S433 (2006)

[63] T. Hellsten, K. Holmström, T. Johnson *et al*. *On ion cyclotron emission in toroidal plasmas*. Nucl. Fusion, **46**, S442 (2006)

[64] G. D. Kerbel and M. G. McCoy. *Kinetic theory and simulation of multispecies plasmas in tokamaks excited with electromagnetic waves in the ion-cyclotron range of frequencies*. Phys. Fluids, **28**, 3629 (1985)

[65] C. F. Kennel and F. Engelmann. *Velocity Space Diffusion from Weak Plasma Turbulence in a Magnetic Field*. Phys. Fluids, **9**, 2377 (1966)

[66] L. Chen, J. Vaclavik and G. W. Hammett. *Ion radial transport induced by RF waves in tokamaks*. Nucl. Fusion, **28**, 389 (1988)

[67] L.-G. Eriksson, M. Mantsinen, D. Borba *et al*. *Evidence of a Wave-Induced Particle Pinch in the Presence of Toroidally Asymmetric ICRF Waves*. Phys. Rev. Lett., **81**, 1231 (1998)

[68] V. P. Bhatnagar, D. F. H. Start, J. Jacquinot *et al*. *Local magnetic shear control in a tokamak via fast wave minority ion current drive: theory and experiments in JET*. Nucl. Fusion, **34**, 1579 (1994)

[69] N. J. Fisch. *Theory of current drive in plasmas*. Rev. Mod. Phys., **59**, 175 (1987)

[70] O. Sauter. private communication

[71] M. N. Rosenbluth and M. L. Sloan. *Finite$-\beta$ Stabilization of the Collisionless Trapped Particle Instability*. Phys. Fluids, **14**, 1725 (1971)

[72] M. A. Beer, G. W. Hammett, G. Rewoldt *et al. Gyrofluid simulations of turbulence suppression in reversed-shear experiments on the Tokamak Fusion Test Reactor.* Phys. Plasmas, **4**, 1792 (1997)

[73] Y. Wu, C. Z. Cheng and R. B. White. *Alpha particle effects on the internal kink and fishbone modes.* Phys. Plasmas, **1**, 3369 (1994)

[74] J. W. Connor, R. J. Hastie and T. J. Martin. *Effect of pressure gradients on the bounce-averaged particle drifts in a tokamak.* Nucl. Fusion, **23**, 1702 (1983)

[75] J. P. Graves. *Internal kink mode stabilization and the properties of auxiliary heated ions.* Phys. Plasmas, **12**, 090908 (2005)

[76] T. Hellsten and T. Johnson. *On Current Drive and Wave Induced Bootstrap Current in Toroidal Plasmas.* In X. Garbet, O. Sauter and E. Sindoni (eds.), *Theory of Fusion Plasmas*, 88–99. American Institute of Physics, Melville, New York (2008)

[77] A. N. Kaufman. *Quasilinear Diffusion of an Axisymmetric Toroidal Plasma.* Phys. Fluids, **15**, 1063 (1972)

[78] L.-G. Eriksson and M. Schneider. *Monte Carlo operators for ions interacting with radio frequency waves.* Phys. Plasmas, **12**, 072524 (2005)

[79] J. P. Graves, I. T. Chapman, S. Coda *et al. A new sawtooth control mechanism relying on toroidally propagating ion cyclotron resonance frequency waves: Theory and Joint European Torus tokamak experimental evidence.* Phys. Plasmas, **17**, 056118 (2010)

[80] M. Laxåback and T. Hellsten. *Modelling of minority ion cyclotron current drive during the activated phase of ITER.* Nucl. Fusion, **45**, 1510 (2005)

[81] J. Carlsson, T. Hellsten and J. Hedin. *New mechanics of minority ion cyclotron current drive.* Phys. Plasmas, **5**, 2885 (1998)

[82] L.-G. Eriksson, T. Johnson, T. Hellsten *et al. Plasma Rotation Induced by Directed Waves in the Ion-Cyclotron Range of Frequencies.* Phys. Rev. Lett., **92**, 235001 (2004)

[83] W. A. Cooper, J. P. Graves, A. Pochelon *et al. Tokamak Magnetohydrodynamic Equilibrium States with Axisymmetric Boundary and a 3D Helical Core.* Phys. Rev. Lett., **105**, 035003 (2010)

[84] M. Albergante, J. P. Graves, A. Fasoli *et al. Numerical modelling of the electromagnetic turbulent transport of energetic ions in burning plasmas.* to be published in Plasma Phys. Control. Fusion

Acknowledgments

It is a great pleasure to thank several persons without whom this work would not have been possible in its present form.

Jonathan Graves Thanks for accepting the adventure of being my thesis (co-) director. All of this besides the birth of two children just before and during this project. I know it is not easy to make me do something I don't want to. Or to convince me that I am wrong, especially when I am. Thanks a lot for still pushing and convincing me in the end.

W. Anthony Cooper Another victim of my thesis. Any problems with VMEC or equations over entire pages have always been sorted out very quickly and efficiently. Also, thanks for fighting for me to obtain the computational resources I needed. And, of course, your BBQs are legendary.

Stephan Brunner Any question about distribution functions, numerical implementation, or Monte Carlo schemes? No problem, ask Stephan! Thanks for always having time when I needed some additional help on the numerical side. Many thanks for your help in finding my postdoc position - your input certainly was crucial for the good outcome of my search.

Laurent Villard Thanks for many interesting discussions about wave fields and related topics. Also, thank you for your efforts when creating the lists for the "assistanat" and always trying to satisfy as many people involved as possible. Of course, a big thank you for your help when I needed numerical resources - I could not have created the here presented results without the resources you where willing to organise for me at once when I needed them. And sorry for using so many CPUh during such a short time.

Thomas Johnson One of the busiest people I know, but you still found the time to work on the benchmarking of our codes. For me it was much more than a benchmark. I learned so much during the three weeks I was in Stockholm, that my code never would have worked as it did without your inputs and help. Tack så mycket!

Nicolas Mellet Thanks to you I got LEMan to work within SCENIC. Also, whenever I needed to know about the workings of the code, you had the answer, even by the time you where already gone from CRPP. Most of all, thanks for all the funny and Ragusa-full coffee breaks (pause!).

Mattia Albergante   What an officemate. Always ready for a good laugh, a geeky comic on the web or a good talk about motorbikes - and, of course, work. Was a pleasure being in the same office. Thanks for all the fun.

The CRPP football team   Now this is serious. A big thank you to all the football players of CRPP. This was the best way to get integrated at CRPP, and to have fun with people outside the usual working environment. Sometimes we did great, sometimes we did poor, but the fun of being a team was always there. And hell - we could have won that tournament!

Gianpaolo Turri   Always there for a good laugh, some football or drinks. But, most of all, you were a good friend when I needed one - thanks.

Emmanuelle Serré   The best thing that could happen in the UNIL rowing club? Meet you. A very deep thank you for your understanding, your support and your company.

Yvonne & Rudolf Jucker   You never questioned my decisions and supported me all along, financing me for longer than you probably would have preferred. I hope I can give back some of it with this thesis.

So long, and thanks for all the fish!

Curriculum vitae

Born on September 4, 1981, in Aarau (AG), Switzerland

EDUCATION

1997-2001	Kantonsschule Wohlen (AG), Maturity in ancient languages (latin)
2001-2006	MSc in Physics at Ecole Polytechnique Fédérale de Lausanne (EPFL)
2003-2004	Exchange year at Uppsala University, Sweden
Sep. 2005-	Master's thesis at Uppsala University, Sweden
Jan. 2006	*Self-consistent model of magnetic electron drift wave turbulence*
2006-2010	PhD at Centre de Recherches en Physique des Plasmas (CRPP), EPFL

FIRST AUTHOR PUBLICATIONS

M. Jucker, Zh.N. Andrushchenko and V.P. Pavlenko, *Large scale magnetic fields and coherent structures in nonuniform unmagnetized plasma*, Phys. Plasmas **13**, 072308 (2006)

M. Jucker and V.P. Pavlenko, *On the modulational stability of magnetic structures in electron drift turbulence*, Phys. Plasmas **14**, 102313 (2007)

M. Jucker and V.P. Pavlenko, *On the kinetic stability of magnetic structures in electron drift turbulence*, Phys. Plasmas **14**, 032303 (2007)

M. Jucker, J.P. Graves, G.A. Cooper and W.A. Cooper, *Impact of pressure anisotropy on tokamak equilibria and the toroidal magnetic precession*, Plasma Phys. Control. Fusion **50**, 065009 (2008)

M. Jucker, J.P. Graves, N. Mellet, T. Johnson and W.A. Cooper, *SCENIC - a code package for iterated 3D Ion Cyclotron Resonant Heating simulations*, submitted to Comp. Phys. Comm.

M. Jucker, J.P. Graves, W.A. Cooper and T. Johnson, *Integrated modeling for Ion Cyclotron Resonance Heating in toroidal systems*, submitted to Plasma Phys. Control. Fusion

OTHER PUBLICATIONS

W.A. Cooper, J.P. Graves, M. Jucker and M.Yu. Isaev, *Relativistic Hamiltonian guiding center drift formalism in anisotropic pressure magnetic coordinates*, Phys. Plasmas **13**, 092501 (2006)

W.A. Cooper, J.P. Graves, M. Jucker et al. *Fluid magnetohydrodynamic stability in a Heliotron with anisotropic fast particle species*, Plasma Phys. Control. Fusion **49**, 1177 (2007)

G.A. Cooper, M. Jucker, W.A. Cooper, J.P. Graves and M.Yu. Isaev, *Exact canonical drift Hamiltonian formalism with pressure anisotropy and finite perturbed fields*, Phys. Plasmas **14**, 102506 (2007)

Zh.N. Andrushchenko, M. Jucker and V.P. Pavlenko, *Self-consistent model of electron drift mode turbulence*, J. Plasma Phys. **74**, 21 (2007)

N. Mellet, M. Jucker, W. A. Cooper and J. P. Graves, *"Effect of a hot particle bi-Maxwellian distribution function on the propagation of low-frequency waves"*, in preparation

INVITED TALKS

"Integrated modeling for Ion Cyclotron Resonance Heating in toroidal systems", Joint Varenna-Lausanne International Workshop, Varenna, Italy, 2010

FIRST AUTHOR CONFERENCE PARTICIPATIONS

M. Jucker, Zh.A. Andrushchenko and V.P. Pavlenko, *Large scale magnetic field structures in nonuniform unmagnetized plasma*, 33th EPS conference on Plasma Physics, Poster, Rome 2006

M. Jucker and V.P. Pavlenko, *Generation and Stability of Large Scale Magnetic Structures in Electron Drift Turbulence*, European Fusion Theory Conference EFTC, Poster, Madrid 2007

M. Jucker, J.P. Graves and W.A. Cooper, *Single particle orbits in anisotropic fully shaped plasmas*, European Fusion Theory Conference EFTC, Poster, Madrid 2007

M. Jucker, J.P. Graves, G.A. Cooper and W.A. Cooper, *Impact of ICRH heating on particle motion in anisotropic toroidal magnetic confinement systems*, Annual meeting of the Swiss Physical Society, Talk, Geneva 2008

M. Jucker, J.P. Graves, W.A. Cooper, N. Mellet and S. Brunner, *Monte Carlo ICRH simulations in fully shaped anisotropic plasmas*, Joint-Varenna-Lausanne International Workshop, Poster, Varenna 2008

M. Jucker, J.P. Graves, W.A. Cooper, S. Brunner, N. Mellet and T. Johnson, *Self-consistent ICRF simulations in fully shaped anisotropic plasmas*, European Fusion Theory Conference EFTC, Poster, Riga 2009